University of Southampton

Faculty of Natural and Environmental Sciences
School of Ocean and Earth Science
National Oceanography Centre Southampton

Numerical Modelling of Overpressure Generation in Deep Basins and Response of Arctic Gas Hydrate to Ocean Warming

by

Héctor Marín Moreno

Thesis for the degree of Doctor of Philosophy

February 2014

For Carla and my Family

"Narrow minds devoid of imagination. Intolerance, theories cut off from reality, empty terminology, usurped ideals, inflexible systems. Those are the things that really frighten me. What I absolutely fear and loathe..."

-Haruki Muarakami, Kafka on the shore

University of Southampton

Abstract

Faculty of Natural and Environmental Sciences
School of Ocean and Earth Science
National Oceanography Centre Southampton

Doctor of Philosophy

NUMERICAL MODELLING OF OVERPRESSURE GENERATION IN DEEP BASINS AND RESPONSE OF ARCTIC GAS HYDRATE TO OCEAN WARMING

by Héctor Marín Moreno

This thesis is split into the two scientific topics studied; overpressure development in deep basins and present-day and future gas hydrate dissociation in the Arctic.

Locating and quantifying overpressure is essential to understand basin evolution and hydrocarbon migration in deep basins and thickly sedimented continental margins. The first part of this thesis develops two new methods, including an inverse model, to impose seismic and geological constraints on models of overpressure generated by the disequilibrium compaction and aquathermal expansion mechanisms. The results provide greater understanding of a low velocity zone (LVZ), inferred from wide-angle seismic data, in the centre of the Eastern Black Sea Basin (EBSB). The application of both methods in the study area indicate that the LVZ located within the Maikop formation, at ∼3500-6500 m depth below the seabed (mbsf), is linked to overpressure generated, mainly, by disequilibrium compaction. The results suggest that the relatively low vertical and horizontal permeabilites of the Maikop formation of ∼1-5x10^{-13} m s^{-1} and of ∼7.5x10^{-12} m s^{-1}, respectively, and the presence of a thin layer, ∼200 m thick, with a significantly low permeability of ∼0.3-1.3x10^{-14} m s^{-1}, below the Maikop formation, would have limited the escape of pore fluids. The rate of fluid flow within the Maikop formation, would not have been enough to accommodate the relatively high sedimentation rate of 0.28-0.29 m ka^{-1} of the Maikop formation during 33.9-20.5 Ma, and an even higher sedimentation rate of 0.91-0.94 m ka^{-1} during 13-11 Ma, and overpressure would have developed with maximum values of 40-51 MPa at ∼6400 mbsf.

Methane is a potent greenhouse gas and large-scale rapid release of methane from hydrate may have contributed to past abrupt climate change. Oceans are warmer than they have been in millions of years and hence, gas hydrates have the potential to release more

methane than in the past. In 2008 over 250 plumes of methane gas emanating from the seabed at ∼400 m water depth (mwd) offshore West Svalbard were discovered. The second part of this thesis employs the TOUGH+HYDRATE code to model the dynamic response of hydrate-bearing sediments over a period of 2300 yr and investigates ocean warming as a possible cause for present-day and likely future dissociation of hydrate offshore West Svalbard. Future seabed temperatures are given by seven climate models under climate-forcing scenarios Representative Concentration Pathways (RCPs) 2.6 and 8.5, which represent low and high greenhouse emissions, respectively. The results show that offshore West Svalbard the potential methane emissions would extend to ∼400-480 mwd (seabed area of ∼71.4 km^2) over the next century releasing 0.97-10.3 Gg yr^{-1} of methane from dissociated hydrate to the Arctic Ocean. Over the next three centuries, the potential methane emissions may extend to ∼400-550 mwd (seabed area of ∼134 km^2) releasing 5.3-29 Gg yr^{-1}. An extrapolation of these results to the entire Eurasian Margin suggests that future methane emissions from dissociated hydrate may be similar to those from other significant methane sources such as Arctic tundra.

Contents

Electronic Material

EM.1 Matlab 7.8.0 Functions for Chapter 3

EM.2 Matlab 7.8.0 Functions for Chapter 4

EM.3 Matlab 7.8.0 Functions for the Ursa Basin Analysis

EM.4 Matlab 7.8.0 Functions, Data and Results for Chapters 5 and 6

EM.5 Matlab 7.8.0 Functions, Data and Results for the Beaufort Sea Analysis

EM.6 Thesis, Papers, Abstracts, Posters and Talks

List of Figures

List of Tables

Declaration of Authorship

I, Héctor Marín Moreno, declare that this thesis, "Numerical Modelling of Overpressure Generation in Deep Basins and Response of Arctic Gas Hydrate to Ocean Warming", and the work presented in it are my own and have been generated by me as the result of my own original research.

I confirm that:

1) This work was done wholly while in candidature for a research degree at this University;

2) Where any part of this thesis has previously been submitted for a degree or any other qualification at this University or any other institution, this has been clearly stated;

3) Where I have consulted the published work of others, this is always clearly attributed;

4) Where I have quoted from the work of others, the source is always given. With the exception of such quotations, this thesis is entirely my own work;

5) I have acknowledged all main sources of help;

6) Where the thesis is based on work done by myself jointly with others, I have made clear exactly what has been done by others and what I have contributed myself;

7) Parts of this work have been published as:

   Marín-Moreno, H., Minshull, T. A., & Edwards, R. A. (2013a). A disequilibrium compaction model constrained by seismic data and application to overpressure generation in The Eastern Black Sea Basin. *Basin Research*, 25(3), 331-347, doi: 10.1111/bre.12001.

   Marín-Moreno, H., Minshull, T. A., & Edwards, R. A. (2013b). Inverse modelling and seismic data constraints on overpressure generation by disequilibrium compaction and aquathermal pressuring: application to the Eastern Black Sea Basin. *Geophysical Journal International*, 194(2), 814-833, doi: 10.1093/gji/ggt147.

Marín-Moreno, H., Minshull, T. A., Westbrook, G. K., Sinha, B., & Sarkar, S. (2013c). The response of methane hydrate beneath the seabed offshore Svalbard to ocean warming during the next three centuries. *Geophysical Research Letters*, 40, doi: 10.1002/grl.50985.

8) Work directly related to this thesis has been presented at numerous conferences:

American Association of Petroleum Geologists AAPG International Conference & Exhibition 2011

Marín-Moreno, H., Minshull, T. A., & Edwards, R. A. (2011). An inverse approach for relating seismic velocity and overpressure to permeability and sedimentation history in deep basins, AAPG 23-26 October 2011, Milan, Italy.

The Geological Society, Deep Water Continental Margins DWCM 2012

Marín-Moreno, H., Minshull, T. A., & Edwards, R. A. (2012). An inverse approach to impose seismic and geological constraints on a disequilibrium compaction model and application to overpressure generation in the Eastern Black Sea Basin, The Geological Society DWCM 1-2 October 2012, London, UK.

American Geophysical Union AGU Fall Meeting 2012

Marín-Moreno, H., Minshull, T. A., & Edwards, R. A. (2012). An inverse approach to impose seismic and geological constraints on a disequilibrium compaction model and application to overpressure generation in the Eastern Black Sea Basin, AGU Fall Meeting 3-7 December 2012, San Francisco, USA.

European Geophysical Union EGU General Assembly 2013

Marín-Moreno, H., Minshull, T. A., Westbrook, G. K., Sinha, B., & Sarkar, S. Determining the response of hydrate offshore Svalbard to ocean warming during the next century, EGU General Assembly 7-12 April 2013, Vienna, Austria.

Signed: Héctor Marín Moreno

Date: 27/02/2014

Aknowledgements

It looks like this is the end of my PhD story...

This unforgettable journey started three years ago and from the very first day, my supervisors, Tim Minshull and Rose Edwards, have been fantastic. I sincerely want to thank them for considering me as an equal, for their guidance, encouragement and confidence in every single science decision I made, and for opening me the doors for a world of opportunities out of my PhD. Part of my future career is thanks to you, and this, I will never forget.

A PhD is full of ups and downs. Moments of tremendous satisfaction... "My model works!" "My manuscript has been accepted!" together with moments of tremendous frustration... (allow me not to mention them). These moments need to be shared, need to be remembered, and **YOU** were there. Carla, we left Catalonia together (not so sure who was following who). We started our adventure, each with our own fears. Three years later, most fears behind and about to submit my thesis, I want to tell you: **this is the best decision I have ever made**. Thanks for being who you are and standing by my side.

My family... what can I say. I feel enormously proud of being part of it. Yes, dad, mum, brother, aunty. You have been always there, always supportive. Thanks for being different, genuine, unique.
Sabéis que no soy muy dado a sentimentalismos, pero me gustaría recordaros una de mis controvertidas frases... ¡Os quiero porque sois mi ejemplo y no porque seáis familia!

I would like to thank my office-mates, James Hunt, Giuseppe Malgesini, and Chris Stevenson. Although I was the outsider in the "turbidites office", I always enjoyed your never ending discussions in the white board. It has been great fun!

What can I say about my adoptive family in Southampton? Giuseppe and Georgios, thanks for introducing me to the mid-day coffee break from our already retired friend, "the vending bad coffee machine". Alanoud, Angeliki, Eithne, Konstantina, Lena, Lizeth, Maxi... I have been lucky enough to meet you and to share moments with you. Migue & Daniela, our live in Southampton would have not been the same without you. You have been a very important part! *Merci per compartir estones amb nosaltres!*

When I decided to get involved in the project of modelling warming-induced gas hydrate dissociation, I knew it was going to be challenging. It has been TOUGH, but thanks to Tim Minshull, Graham Westbrook, Bablu Sinha and Sudipta Sarkar, I have learnt a great deal about the fascinating world of natural gas hydrates. Tim Minshull and Graham

Westbrook, thanks for invaluable discussions. Bablu Sinha, thanks for providing me with the climate model data. Sudipta, thanks for you sincere science and not science advices.

Martin Sinha, Karen Weitemeyer, Lawrence North, Ian Tan, Bedanta Goswami and Joan Campanyà. It has been a pleasure to briefly work with you in the field of marine electromagnetics.

Finally, I would like to thank Mark Vardy, Casey, Joe, Simon, Louis and members of the football team.

Chapter 1

Introduction

"You can never solve a problem on the level on which it was created."
–Albert Einstein

This chapter provides the background and motivations behind this thesis, and it is split into the two scientific topics studied; overpressure development in deep basins and present-day and future gas hydrate dissociation in the Arctic. In the first part, I emphasise the importance of overpressure as a factor mobilising subsurface fluids, present the main mechanisms generating overpressure, and introduce the study location, the Eastern Black Sea Basin (EBSB). In the second part, I summarise the current state of knowledge of gas hydrates, focusing in the Arctic, which is used as the scientific framework for the analysis in Chapters 5 and 6. Although the geological settings and aims of each of these studies are different, they both are based on developing and applying numerical models of subsurface fluid behaviour to understand and make the most of some interesting geophysical observations.

1.1 Overpressure Development in Deep Basins

In the XII century, approximately in the year 1126, Carthusian monks from the former French region of Artois, observed that their wells were different from the majority of the wells found and used until that moment. They observed that when drilled, the water flowed upward reaching the surface, and in some circumstances, the water could even overpass the ground surface by a few meters. This type of well, called an artesian well and named after the region where it was used (they were used before by the Egyptian and Syrian civilisations), could be considered the first historical example of overpressure ...

1.1.1 Rationale and Aims

Understanding the mechanisms generating pressure above the hydrostatic (overpressure) in the subsurface, and estimating the amount of overpressure using geophysical techniques have traditionally been two strongly related overpressure study fields that have rarely been brought together by either practitioners or researchers. Many methods have been developed to estimate and locate overpressure in sedimentary basins and accretionary prisms, both in industry and academia, but most of them use uncoupled approaches and the physics governing the possible generation of overpressure is not directly linked to the constraints imposed by geological and geophysical observations.

Characterising overpressured systems using only geophysical and geological data, without considering the hydrodynamics of the sedimentary basin, may be an ambiguous problem, as it is likely that more than one possible answer explains the data anomalies that are usually linked to high pore pressure; anomalies such as low resistivity zones (LRZ), low velocity zones (LVZ) and extremely low density zones (LDZ). One reason is the heterogeneity of the sediments and hence their different geomechanical and fluid properties (e.g, porosity, mineralogy, pore fluid, effective stress). Another limitation is inherently derived from the nature of the data. The data usually used for overpressure prediction consist of compressional and shear wave velocities or resistivity, which are not physically correlated with pore pressure directly, and hence the use of site dependent semi-empirical models, such as the Eaton method (den Boer *et al.*, 2006; Eaton, 1969, 1975), and discrete pore pressure measurements is required.

Approaches that do consider the physics of the problem, often lack real evidence to validate the results for laterally extensive and deep overpressured zones. However, if there are available data to constrain the results, it is most likely that a few runs of the model changing the parameters are required to match model results to pore pressure measurements. Even if the combination of selected parameters is such that the overpressure calculated matches that observed, how do we know that those parameters are actually the in-situ ones? and, how do we know that the model parameters selected are the physically "best" fit to data, and there is not another combination that gives a "better" fit?

There is gap in the literature to overcome the above mentioned limitations of using forward numerical models and/or geophysical data for overpressure prediction independently. Therefore, the methods presented in this thesis are a step forward in the current state of knowledge in pore pressure prediction, and aim to "couple" seismic and geological observations with overpressure generated with forward numerical models to better understand the hydrodynamics of deep basins.

In addition to the purely development of novel methods for pore pressure prediction, these methods were tested in the Black Sea Basin, a frontier basin for hydrocarbon exploration (Robinson *et al.*, 1996). In the centre of the Eastern Black Sea Basin (EBSB), and based on wide-angle seismic data, Scott *et al.* (2009) inferred a LVZ which they linked to overpressure using two geophysical-based methods. They proposed disequilibrium compaction to be the dominant mechanism generating the overpressure, but no robust physical evidence of the mechanisms and parameters generating that LVZ can be obtained from a overpressure analysis using only semi-empirical relationships. The application of these new methods provides a better understanding of the hydrodynamic behaviour of the centre of the basin.

1.1.2 Importance of Overpressure

Understanding, locating, and quantifying overpressure is essential in geoscience, as it has a fundamental control on numerous shallow Earth processes. Overpressure plays an important role in basin evolution and hydrocarbon migration in deep basins and thickly continental margins. It can affect the fluid-flow pattern within a basin (Harrison & Summa, 1991) and knowledge of it can help provide a prior understanding of the consequences of seal failure, primary oil migration and reservoir porosity (Swarbrick & Hillis, 1999). From a well engineering point of view, the link between overpressure, seal effectiveness and reservoir porosity can also help to drill wells safely and economically (Bekele *et al.*, 2001; Fertl *et al.*, 1994; Sayers, 2006), minimising the possibility of a well blowout, and to avoid fracturing the formation due to an excessively high mud weight (Sarker & Batzle, 2008). Overpressure is one of the factors affecting the structural mechanics of fault surfaces through its control on effective normal stress (e.g, Hubbert & Rubey, 1959a), fault localisation and mediation of earthquake slip (Dugan & Sheahan, 2012), and propagation of rupture and migration of microseismicity (e.g, Tsuru *et al.*, 2005). In subduction environments, overpressure in the underthrust sediments of a décollement influences its location and deformation in accretionary prisms (e.g, Davis *et al.*, 1983; Saffer & Tobin, 2011), with examples observed all over the world, such as the Makran accretionary prism in the Gulf of Oman (Minshull & White, 1989), the southwest Alaska accretionary prism (Byrne & Fisher, 1990), the Barbados accretionary prism (Moore & Tobin, 1997; Saffer, 2003; Saffer & Tobin, 2011), the Nankai accretionary prism of the Muroto Peninsula, southwestern Japan (Saffer, 2003; Tobin & Saffer, 2009; Tsuji *et al.*, 2008), and the Costa Rican Margin (Saffer, 2003; Saffer & Tobin, 2011). Large submarine slope failures, such as the massive Storegga Slide in the Vøring Plateau west of Norway, one of the largest submarine slides in the Holocene,(e.g, Leynaud *et al.*, 2007; Solheim *et al.*, 2005) or the giant Sahara Slide on the northwest African continental margin (e.g, Georgiopoulou *et al.*, 2010), may have

been highly influenced by shallow overpressure caused by high sedimentation rates and low permeability strata. Therefore, overpressure prediction is a primary requirement to ensure the safety of offshore infrastructure. Overpressure may also be a mechanism driving warm fluid flows to the subsurface forming and/or altering ore (Garven & Freeze, 1984; Noble, 1963) and other mineral deposits (Cathles & Smith, 1983; Sharp, 1978).

1.1.3 Overpressure Mechanisms

Various mechanisms have been proposed in the literature to explain the generation of overpressure in sedimentary basins, accretionary prisms and continental margins. They can be grouped into three main types:

- Overpressure generation due to changes in porosity.
- Overpressure generation due to changes in fluid volume.
- Overpressure generation because of fluid movement.

The rate of overpressure generation depends upon the balance between the mechanisms generating it and the rate of overpressure dissipation by fluid motion, which mainly depends on the hydraulic conductivity of the sediment (Eq. 1.1). Overpressure generated by these mechanisms can build up until it exceeds the tensile strength of the rock and hydraulic fracturing occurs.

$$\boldsymbol{C_H} = \frac{\boldsymbol{K} A}{L} = \frac{\boldsymbol{K_i} k_r A}{L \mu} \tag{1.1}$$

In Eq. 1.1 $\boldsymbol{C_H}$ is the hydraulic conductivity tensor, $\boldsymbol{K}$ is the permeability tensor, $\boldsymbol{K_i}$ is the intrinsic permeability tensor, k_r is the relative permeability (equal to one for a monophase 100% water saturated fluid system), A and L are the surface area and distance through which the fluid flows, respectively, and μ is the fluid viscosity.

Overpressure Generation Due to Changes in Porosity

Changes in porosity generating overpressure can occur mainly by: sediment deposition, tectonic compression, smectite dehydration to illite and cementation.

The mechanism where the deposition of overlying sediments is rapid enough to not allow the underlying sediments to compact to their normal or equilibrium porosity is known as disequilibrium compaction in the geoscience discipline and underconsolidation in the geotechnical community. This situation appears when fine-grained sediments with low intrinsic permeabilities and high sediment compressibilities are unable to release the fluid pressure rapidly enough, to allow normal gravitational compaction, in comparison to the sedimentation rate. Consequently, the fluids support part of the sediment loading. The

magnitude of overpressure generated is a coupled effect between the total vertical stress application (Eq. 1.2) compared to the coefficient of consolidation (Eq. 1.3).

$$\frac{\partial \sigma_z}{\partial t} = \rho g \omega \tag{1.2}$$

$$c_v = \frac{K}{(\beta \rho_f g)} \tag{1.3}$$

In Eq. 1.2 and Eq. 1.3 K is the permeability, g is the gravitational acceleration, t is the time, β is the sediment compressibility, σ_z is the total vertical stress, ω is the sedimentation rate, and ρ and ρ_f are the sediment and fluid densities, respectively. The term disequilibrium has to be understood in the framework of an evolving process and hence the entire history of the geologic setting must be known (Neuzil, 1995).

One of the overpressured basins most extensively studied is the Gulf of Mexico. In the 1970's, research was focused on the overpressured zones of the Gulf of Mexico as a source of mechanical and thermal energy and of dissolved methane (e.g, Wallace Jr *et al.*, 1979). Due to intensive study, the majority of mechanisms capable of producing overpressure have been identified in the basin, with disequilibrium compaction assumed to be the dominant one (e.g, Bredehoeft & Hanshaw, 1968; Harrison & Summa, 1991; Sharp & Domenico, 1976), mainly because of sedimentation rates as high as 5 m ky^{-1} (Neuzil, 1995). Harrison & Summa (1991) stated that only 1% of the total overpressure comes from fluid expansion, and overpressure due to fluid release from smectite-illite transformation is not significant. The three conditions satisfied in the basin that allow the development of abnormally high pressure by disequilibrium compaction are: (1) low intrinsic permeability, (2) thick shale sequences and (3) sedimentation rates higher than 1 mm yr^{-1} for overpressure approaching the lithostatic, and higher than 0.1 mm yr^{-1} for moderate overpressure (Harrison & Summa, 1991). In general, high sedimentation rates are associated with low geothermal gradients, and the typical geothermal gradient in the Gulf of Mexico basin is relatively low, 25 °C km^{-1} (Barker, 1972). In the Gulf of Mexico, offshore Louisiana, Hart *et al.* (1995) concluded that overpressure was produced mainly by disequilibrium compaction, although 25% of the total overpressure may be generated by other mechanisms at depths below 2 km. In the same geological location, Gordon & Flemings (1998) demonstrated that the overpressure predicted below 1500-2000 m, from drilling mud density, could be explain by the two main factors controlling disequilibrium compaction, rapid sediment loading and low intrinsic permeability deposits.

Bekele *et al.* (2001) analysed the overpressure in the Barrow sub-basin, northwest Australia, using a forward basin model and considering two mechanisms, disequilibrium compaction and organic maturation. They concluded that the dominant mechanism generating the observed overpressure was disequilibrium compaction, due to the low intrinsic permeability

of the shale layers, and calculated that only 15% of the total overpressure was from organic maturation. They pointed out that the major uncertainty in estimating the magnitude of overpressure with forward basin models comes from the estimation of the initial intrinsic permeability of the shale.

The degree of overpressure generated by tectonic compression depends upon the balance between the rate of tectonic strain, which produces the changes in porosity, and the rate of groundwater flow. Loss of porosity and sediment deformation can be attributed to tectonic compression associated with geological environments such as tectonically active convergent margins and related orogenic zones (Neuzil, 1995). Using the forcing table presented by Neuzil (1995), stable plate interiors and passive margins may not develop overpressure due to tectonic compression because the tectonic forcing is not big enough (with the possible exception of unfractured crystalline rocks). However, in more tectonically active geological settings the forcing can be greater and lead to its development. This mechanism has been considered responsible of overpressure in several tectonically active regions such as the Potwar plateau of the Punjab in Pakistan, south of the Himalayan foothills (Hubbert & Rubey, 1959a), and in the Barbados accretionary complex (Screaton *et al.*, 1990).
In the California Coast Ranges, Berry (1973) demonstrated the existence of overpressure in the low permeability fined-grained sediments of the Franciscan sequence using drilling data. He suggested that the overpressure was generated by tectonic compression because the Franciscan sediments are being compressed from the northwest and southwest by granitic blocks that limit them. In the same geological setting, McPherson & Garven (1999) developed a 2D model to explain the dominant mechanism generating the overpressure, and proposed tectonic compression as the most likely mechanism on a regional scale. However, they also mentioned that disequilibrium compaction may explain some overpressure, but just for local extremely high sedimentation rates. They pointed out that, in general, sediment compaction models require the introduction of either unrealistically high sedimentation rates, or extremely low intrinsic permeabilities and really high compressibilities of the overpressured layers, whereas in the published tectonic models, normal compressibilities are used and shortening rates are consistent with observed tectonic rates.

The diagenetic transformation of smectite to illite releases water molecules from the structure of smectite into pore spaces increasing fluid pressure. Smectite is a layered silicate which contains a large quantity of water between the layers, keeping them apart. Illite is another clay mineral with very similar composition to smectite but with different chemical and physical properties. The transformation of smectite to illite occurs at temperatures above 60 °C. The reaction is very slow and controlled by the temperature and the amount of potassium (Cuadros, 2008). Assuming that a shale is initially 100% smectite and compacts normally, Osborne & Swarbrick (1997) calculated a maximum increase in volume

of 4% when the smectite is totally transformed to illite. Unless the sediment has an extremely low intrinsic permeability, such a small increase in volume is unlikely to generate significant overpressure. However, the transformation of smectite to illite also releases silica which reduces the porosity by cementation and hence the intrinsic permeability of the shale (Foster, 1982), and increases the compressibility (Lahann & Swarbrick, 2011). These changes in clay properties can favour the generation of overpressure if they occur without fluid release from the shale (Lahann & Swarbrick, 2011).

Overpressure Generation Due to Changes in Fluid Volume

Changes in fluid volume generating overpressure can occur mainly by: thermal expansion of water, transformation of kerogen into hydrocarbons and dissociation of gas hydrate.

The thermal expansion of water due to an increase in temperature, for temperatures above 4 ^{o}C, causing overpressure is commonly known as aquathermal pressuring. Chapman (1980) argued two necessary but unlikely conditions that must be satisfied by the aquathermal pressuring mechanism, the existence of a perfect seal and the maintenance of constant porous volume. Sharp (1983) suggested that aquathermal expansion can considerably contribute to the total overpressure if the geothermal gradients are high and permeabilities are sufficiently small. Bethke (1989) and Neuzil (1995) considered that temperature can be a second important driving force for abnormally high pressure in rapidly subsiding sedimentary basins. Shi & Wang (1986) compared both aquathermal pressuring and disequilibrium compaction and demonstrated that, although both mechanisms are responsible for generating overpressure, the effect of mechanical loading due to the sedimentation process is greater than aquathermal pressuring in sedimentary basins under normal geological conditions, because the change in fluid volume is small (Luo & Vasseur, 1992). In contrast, Shi & Wang (1986) also stated that aquathermal pressuring may be significant in basins with a rapid increase in temperature due to a nearby intruding igneous body or during unloading due to uplift and erosion, and where permeabilities are very low (e.g, impermeable evaporite sequences). In the Gulf of Mexico basin, Harrison & Summa (1991) calculated that only 1.5% of the total overpressure comes from aquathermal pressuring, which is in agreement with the 1% estimated by Bethke (1985) for intracratonic sedimentary basins. Offshore Louisiana, Gordon & Flemings (1998) demonstrated that, considering irreversible compaction, aquathermal pressuring accounts for the 8% of the total pore pressure.

The transformation of kerogen into hydrocarbons and the dissociation of gas hydrate creates porosity. However, the resulting fluid, oil or gas, tends to increase the pressure because its density is lower than the density of the kerogen and hydrate. The transformation of kerogen into gas provokes the largest increase in volume, and hence its presence in overpres-

sured basins may indicate kerogen transformation as a source of overpressure. Although gas pressurisation is considered to be a secondary mechanism, it helps to maintain the overpressure generated by disequilibrium compaction in deep sedimentary basins (Hansom & Lee, 2005; Swarbrick & Osborne, 1998). Chi *et al.* (2010) observed that the overpressure related to hydrocarbon generation was insignificant compared to the overpressure created by disequilibrium compaction in the Paleozoic Anticosti Basin, eastern Canada.
The amount of overpressure generated by gas hydrate dissociation is governed by the balance between kinetic dissociation rate and pressure dissipation (Holtzman & Juanes, 2011), and depends on initial pressure, temperature, hydrate fraction, gas solubility and sediment compressibility (Kwon *et al.*, 2008; Sultan *et al.*, 2004). Some authors suggest that this mechanism can be important, and up to several MPa of overpressure can be generated in confined pore spaces at low initial pressure (Xu & Germanovich, 2006). In contrast, Holtzman & Juanes (2011) suggested, based on a pore scale model, that the timescale for pressure buildup by dissociation is much larger than that for pressure dissipation by drainage, even for low permeability sediments. However, much faster rates of dissociation than of pressure dissipation can be expected during thermal stimulation of fine grained sediments, where the thermal diffusion coefficient is typically higher than the pressure diffusion coefficient (by one order of magnitude or more in high plasticity clays) (Kwon *et al.*, 2008). The growth of fractures, sediment decementation or liquefaction driven by overpressure from gas hydrate dissociation, could also induce landslides (Xu & Germanovich, 2006). Sultan *et al.* (2004) suggested that overpressure from gas hydrate dissolution, at the top of the hydrate layer, may be the origin of a retrogressive failure at the lower part of the Storegga slope.

Overpressure Generation Because of Fluid Movement

An elevation of the water table in a highland region above the pressure of the subsurface of a basin, i.e., lateral variations in the hydraulic potential due to the topographic relief, can cause relatively minor overpressure (Neuzil, 1995). However, if a significantly low permeability layer overlies the basin sediments, this overpressure can increase considerably. This mechanism is considered the dominant driving force for groundwater motion in stable continental areas (Bredehoeft, 2002). It explains the existence of an artesian groundwater system in the Dakota Sandstone in South Dakota (Bredehoeft *et al.*, 1983) and in the Australia's Great Artesian Basin (Habermehl, 1980), and is thought to generate overpressure in the central United States Basin and Range Province (Swarbrick & Osborne, 1998).

Steep gradients in the salinity of pore fluids can induce fluid transfer across a semi-impermeable membrane due to osmosis and generate overpressure (Marine & Fritz, 1981). However, it has been observed that overpressured zones are less salty than the fluids in

the surrounding areas and this situation will actually reduce the overpressure (Osborne & Swarbrick, 1997).

1.1.4 The Eastern Black Sea Basin

The Black Sea Basin (BSB) is a large semi-isolated marine basin located within the Alpine orogenic belt, represented by the Balkanides-Pontides to the south and southwest, the Caucasus in the northeast and the Crimean range in the north (Fig. 1.1). It can be subdivided into the western and eastern Black Sea extensional basins, based on deep seismic reflection data (Zonenshain & Lepichon, 1986). These basins are separated by the Mid Black Sea High (MBSH), running through the centre of the BSB from SW-NE (Fig. 1.1). The EBSB opened in a NE-SW direction by the rotation of the Shatsky Ridge away from the MBSH (Robinson *et al.*, 1996) and although the timing of opening remains controversial, a recent study using a strain-rate inversion suggests that extension continued into the early Cenozoic (Shillington *et al.*, 2008). The infill of the EBSB is largely composed of post-rift, Cenozoic sediments (Finetti *et al.*, 1988), with older pre-rift sediments identified on the shelf (Robinson *et al.*, 1995a). A detailed description of the geological setting can be found in section 3.2.1.

Wide-angle seismic data were collected, using ocean bottom seismometers, in the EBSB during February - March 2005, onboard the RV *Iskatel*. Scott (2009) interpreted these data, focusing on the structure of deep sediments and the structure of the crust and mantle. The velocity model that Scott *et al.* (2009) proposed for the deep sediments contains a LVZ in the centre of the EBSB at ∼5500-8000 m depth below sea level (Fig. 1.1) in the Maikop formation (33.9-20.5 Ma), a thick and homogeneous mud layer rich in organic matter (Robinson *et al.*, 1996). They linked this LVZ to overpressure using the equivalent depth method (e.g, Westbrook, 1991), and the Eaton method (den Boer *et al.*, 2006; Eaton, 1969, 1975) with an Eaton factor of 8, calibrated using pore pressure measurements in a borehole near the east coast. They suggested that the overpressure was mainly generated by disequilibrium compaction because rapid sedimentation, bypassing the margins and depositing straight into the centre of the basin, may have occurred in the Late Eocene-Early Miocene during the deposition of the Maikop formation (Robinson *et al.*, 1995a). However, there is no direct evidence that the sedimentation rates were high enough to generate overpressure in the centre of the basin, and no direct pore pressure measurements are available in the area. The closest measurements are in a borehole near the east coast and these may be influenced by compressional tectonics affecting the coast (McClusky *et al.*, 2000) but not the basin centre (Shillington *et al.*, 2008).

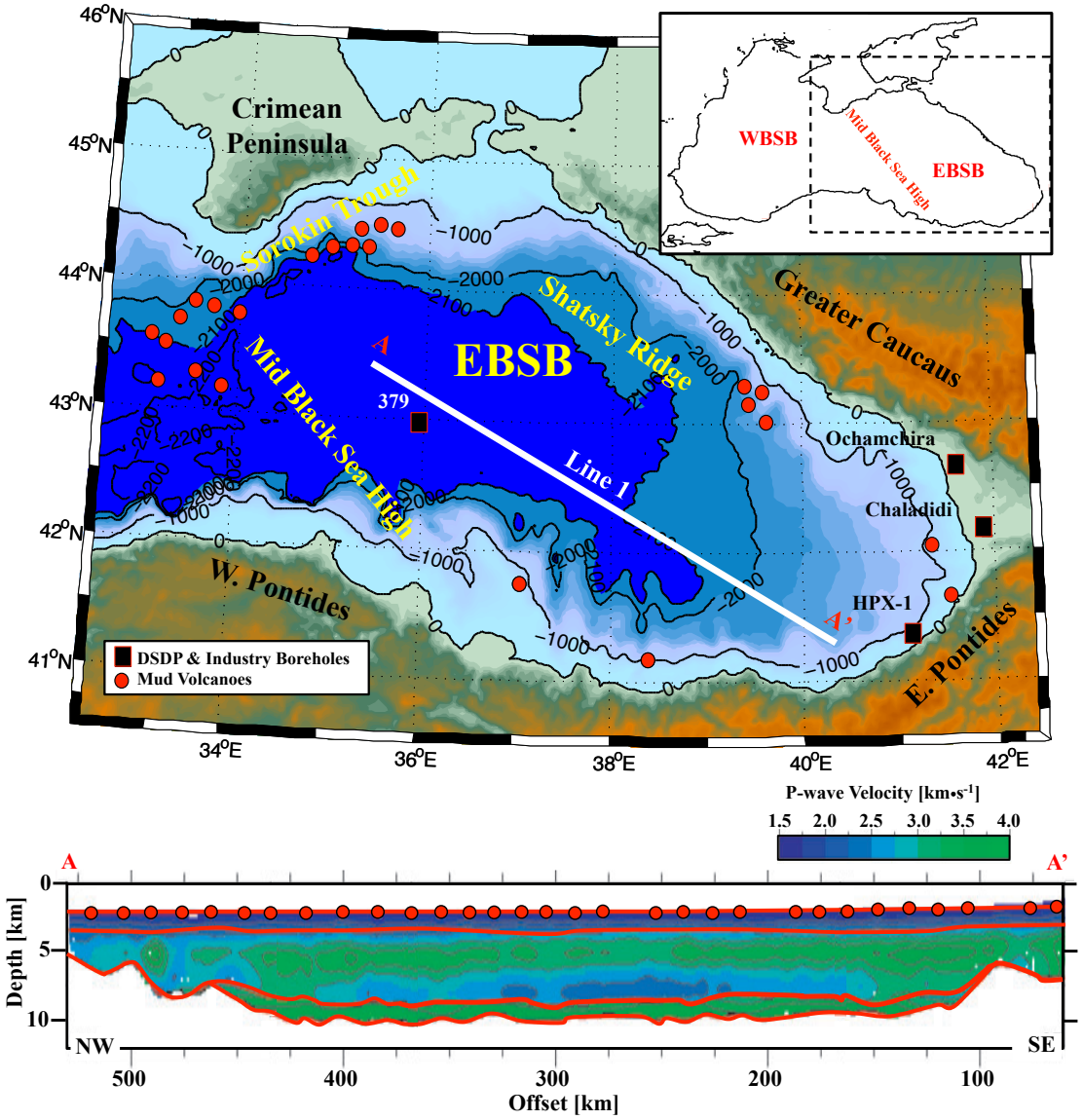

Figure 1.1: Top, map of the eastern Black Sea showing the location of wide-angle seismic profile (white line) with bathymetry and elevation taken from the National Oceanic and Atmospheric Administration (NOAA, http://www.ngdc.noaa.gov/mgg/global/relief/ ETOPO2/ETOPO2v2-2006/ETOPO2v2g/). Red circles indicate known locations of mud volcanoes (Ivanov *et al.*, 1996; Krastel *et al.*, 2003; Kruglyakova *et al.*, 2004) and black squares indicate the location of industry and Deep Sea Drilling Program (DSDP) boreholes. The inset in the upper right hand corner gives the location with respect to the entire Black Sea. Bottom, P-wave velocity structure along the wide-angle seismic profile. Red dots indicate the location of every ocean bottom seismometer (adapted from Figure 5 in Scott *et al.*, 2009).

1.2 Methane Hydrate in the Arctic and its Future Response to Ocean Warming

1.2.1 Rationale and Aims

The discovery in 2008 of over 250 plumes of methane gas escaping from the seabed along the West Spitsbergen continental margin, offshore West Svalbard, at ~400 m water depth (Westbrook *et al.*, 2009; Fig. 1.2a and 1.2b), and of bubble plumes and high dissolved methane concentrations in ocean waters above regions of subsea permafrost on the East Siberian Arctic Shelf (Shakhova *et al.*, 2005, 2010) suggest that large-scale methane release from warming-induced gas hydrate dissociation may be occurring in the present-day Arctic. Previous transient numerical modelling studies of hydrate dissociation in the Arctic, using various simplified past and future climate change scenarios (Reagan & Moridis, 2009; Reagan *et al.*, 2011; Thatcher *et al.*, 2013), show that increasing ocean temperatures will liberate significant amounts of methane from hydrate to the oceans, and that warming-induced gas hydrate dissociation may explain the observed methane bubble plumes offshore West Svalbard, and the corresponding reduction of the extent of the GHSZ (Westbrook *et al.*, 2009; Fig. 1.2c). This process is farther supported by the increase in the temperature of the West Spitsbergen current, due to Atlantic warming, over the latter part of the 20th century (about 1 °C over the last 30 yr; Westbrook *et al.*, 2009).

The above cited numerical modelling studies of the response of the methane hydrate system offshore west of Svalbard to increasing ocean temperatures have not undertaken several aspects considered in this thesis. These are: (1) the present-day gas hydrate system was not arbitrarily defined but was "grown" over the past ~2000 yr driven by a model of changing ocean temperatures from proxy data close to the study area for the period 1-1900 CE, and from oceanographic measurements for the period 1900-2005 CE, (2) some of the parameters controlling the gas hydrate system were determined based on seismic data that image the bottom simulating reflector (BSR) in water depths of more than 580 m and the upper limit of gas-related reflectors in shallower water, and (3) the future changes in climate came from published global climate models and were interpolated to our study location. These model improvements allow us to understand better how Arctic marine gas hydrate may react to future global warming and to reduce the uncertainty on the potential methane release to the ocean, and perhaps to the atmosphere, from dissociated hydrate over the next three centuries in the Svalbard archipelago and in the Arctic.

Methane release from hydrate dissociation is not included in the current published climate models, but the results presented here, although showing a smaller amount than previously speculated, may enable its Arctic contribution to be added in their future versions.

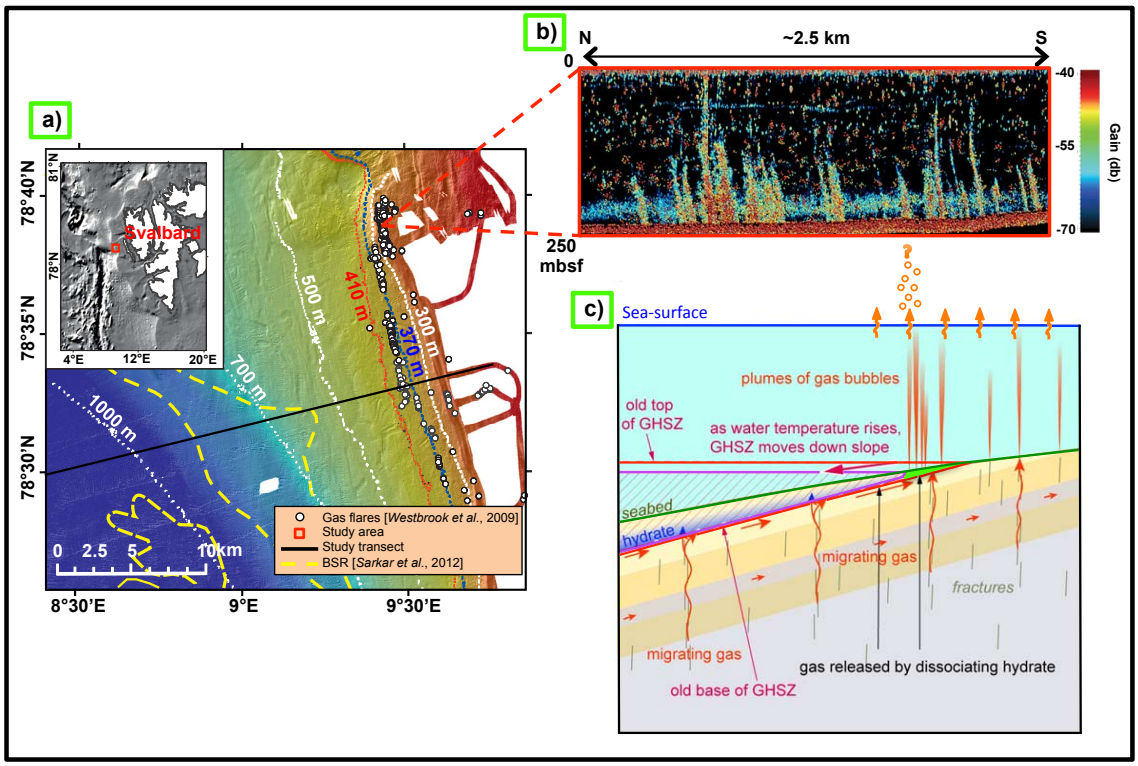

Figure 1.2: a) Map of the study area (Chapters 5 and 6) with bathymetry derived from multibeam echo-sounding data acquired on Cruise JR211 between 23 August and 24 September 2008 (Westbrook *et al.*, 2009). The dotted blue and red bathymetric contours represent the upper limit of the modelled steady state bottom of the gas hydrate stability zone (GHSZ) at 2°C and 3°C seabed water temperatures, respectively, and assuming a 3.5% salinity, pure methane hydrate and hydrostatic pressures (Sarkar *et al.*, 2012). b) Part of record of observed bubble plumes (the location of the bubble plumes is approximated) from an EK60 acoustic survey on board JR211 (adapted from Figure 1 in Westbrook *et al.*, 2009). c) Conceptual cartoon showing a down slope contraction of the GHSZ (green area) driven by an increase in temperature offshore West Svalbard. Where the GHSZ is removed completely and beyond, significant methane gas from the dissociated hydrate escapes from the seabed as bubble plumes through the sea column. Most of the methane gets dissolved in the water and part of this methane will enter the atmosphere by equilibration. Some large methane fluxes may arrive directly to the atmosphere. In thinner parts of the GHSZ, gas from dissociated hydrate at the base of the GHSZ can migrate to shallower depths and reform hydrate or may also migrate up slope (adapted from Figure 3b in Westbrook *et al.*, 2009).

1.2.2 Background

Gas hydrates are naturally occurring solid crystalline compounds that are formed when small guest molecules of natural gas are trapped in cages of water at low temperature (commonly less than 300 K) and high pressure (greater than 3.8 MPa of hydrostatic pressure at 277 K) (Sloan, 2004) and if the dissolved methane concentration in the sediments within the gas hydrate stability zone (GHSZ) is at saturation value (Fig. 1.3). These compounds look like ice and have a similar density, but contain significant concentrated methane

(Buffett & Archer, 2004); 1 m^3 of hydrate contains approximately 163 m^3 of methane at Standard Temperature and Pressure (STP) conditions, 1 atm and 273 K (Sloan, 2004). Gas hydrates can form in the presence of gas molecules over the size range of 0.48-0.90 nanometers (nm). Three distinct structural types can form depending on the size of the largest guest molecules. Methane and ethane individually form Structure I (sI) hydrate, but in certain combinations also form Structure II (sII) hydrate. Propane and isobutane form sII hydrate, either individually or in combination with ethane and methane. Normal-butane and neopentane form sII hydrate only when methane is present as well, and larger hydrocarbon molecules (C5-C9) form Structure H (sH) hydrate, again where methane is present (Collett *et al.*, 2011).

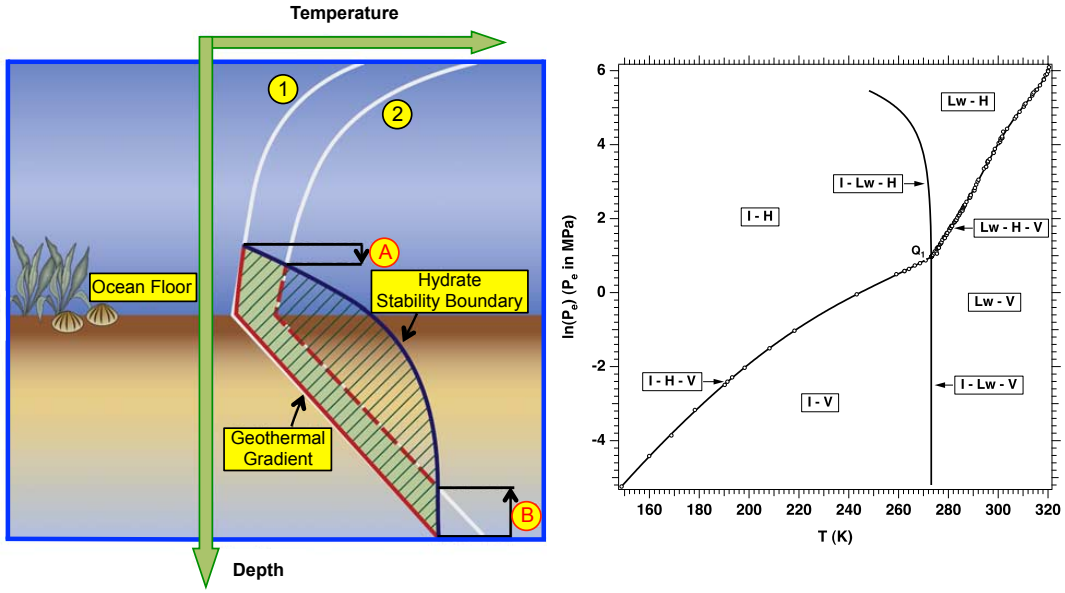

Figure 1.3: Left, conceptual cartoon of the GHSZ in the seafloor environment (not to scale). In this example the top boundary of the GHSZ is above the seafloor, but it may exist above or below it depending on the P-T conditions. Increasing temperatures (moving from temperature profile (1) to profile (2), shown by the white lines) decreases the thickness of the GHSZ , lowering the position of the top boundary (A) and raising the position of the bottom boundary (B). The zone of hydrate stability is defined by the intersection of the temperature profile with the phase envelope (blue dashed area). Modified from Reagan & Moridis (2008). Right, Pressure-Temperature (P_e-T) equilibrium relationship in the phase diagram of the water-CH_4-hydrate system (Fig. 2.5 in Moridis *et al.*, 2012). In the diagram, **Lw** is liquid water, **V** is vapor, **I** is ice and **H** is hydrate.

Marine sediments, including shallow continental margins, slopes, and deep waters, and permafrost sediments are the two main areas that favour hydrate stability in nature (Kvenvolden, 2002; Fig. 1.4). From gas hydrate samples, it is known that the physical nature of in-situ gas hydrates is highly variable, and they are formed and can be observed in (1) the porosity of coarse-grained sediment, (2) nodules disseminated within fine grained sediment,

(3) a solid substance, filling fractures and (4) a massive unit composed mainly of solid gas hydrate with minor amounts of sediment (Boswell & Collett, 2011). However, from gas hydrate sampling, their occurrence is mostly controlled by the presence of fractures and/or coarser grained sediments in which gas hydrate fills fractures or is disseminated in the pores of sand-rich reservoirs (Collett, 1993; Yang *et al.*, 2008).

The P-T controls on the formation of hydrates have been reasonably well understood since the 1960s (Boswell & Collett, 2011). However, other factors controlling the distribution of hydrates are still under investigation (Boswell *et al.*, 2011). The distribution of methane hydrate deposits in marine sediments is mainly inferred from the presence of bottom simulating reflectors (BSR) in seismic reflection and wide-angle seismic data (Shipley *et al.*, 1979). The BSR shows the acoustic boundary between the hydrate and the underlaying free gas bearing sediments and tends to be parallel to the seafloor because the isotherms within the sediment column tend to be parallel to the seafloor (Archer, 2007). However, gas hydrates also may exist in zones where the BSR is not observed (Kvenvolden *et al.*, 1993).

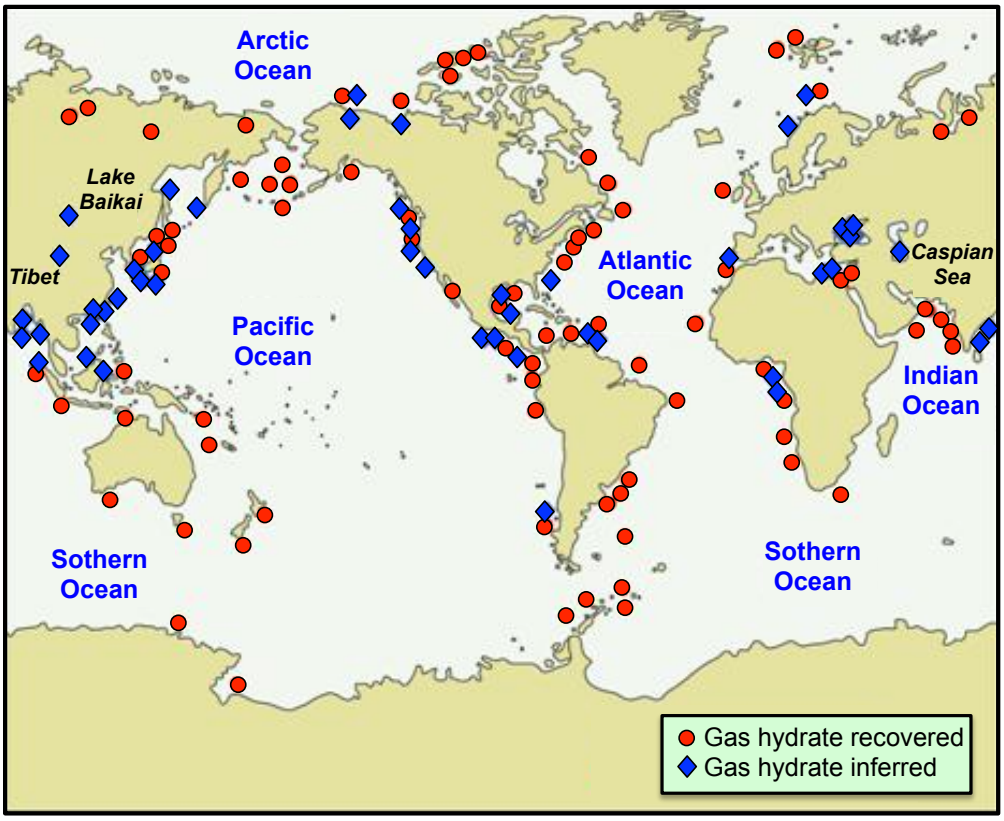

Figure 1.4: Known and inferred locations of gas hydrate occurrence. Adapted from the map compiled by the United States Geological Survey (USGS; http://woodshole.er.usgs.gov /project-pages/hydrates/primer.html).

Supply of hydrate-forming gases into the GHSZ is essential for hydrate formation and these may have a biogenic origin as a product of organic matter degradation, or may have a thermogenic origin from hydrocarbons generated much deeper (Archer, 2007). Thermogenic gas from deep geological carbon stores is relatively rich in ^{13}C whereas gas sourced from biological methanogenesis at shallow levels is richer in ^{12}C (Fisher *et al.*, 2011). The majority of the hydrate deposits on Earth are composed of biogenic methane (Archer, 2007; Collett *et al.*, 2000; Kvenvolden & Lorenson, 2001), as indicated by their isotopic composition and the lack of other short hydrocarbons such as ethane (Archer, 2007). However, there are other hydrate systems such as the Gulf of Mexico (Milkov, 2005) and the Siberian gas fields (Grace & Hart, 1986) dominated by thermogenic methane. Methane hydrate makes up 80% of the total inventory of naturally occurring gas hydrates (Kvenvolden, 1993) and is composed of roughly six molecules of water for each molecule of methane and, hence, the dissociation reaction can be represented by,

$$(CH_4 \cdot 6H_2O)_{\text{solid}} \rightarrow (CH_4)_{\text{gas}} + 6\,(H_2O)_{\text{liquid}} \tag{1.4}$$

Estimates of the total amount of methane stored in hydrates have been reduced in the past two decades from a starting "consensus" value of 10000 Gt (Kvenvolden, 1988; MacDonald, 1990) to 2500-455 Gt (Archer *et al.*, 2009; Burwicz *et al.*, 2011; Milkov, 2004; Piñero *et al.*, 2013; Wallmann *et al.*, 2012), with the most recent estimate being ∼550 Gt of carbon (Piñero *et al.*, 2013), as a result of growing knowledge of gas hydrate distribution and concentration in sediment based in recent Deep Sea Drilling Project (DSDP) and especially Ocean Drilling Program (ODP) drilling results (Milkov, 2004). Despite this decrease, the inventory of hydrates may be comparable in size to other reservoirs of organic carbon such as soil and dissolved organic matter (Buffett & Archer, 2004).

Gas hydrates may have a significant potential as a future energy resource as their energy density (volume of CH4 at STP conditions per volume of sediment) is 10 and 2-5 times greater than that of coal bed methane and conventional natural gas (Englezos & Lee, 2005), respectively, and the energy value of the produced gas is approximately 10 times the energy required to dissociate hydrate in typical reservoirs (Holder *et al.*, 1982). Gas hydrate reservoirs could supply 10% of the global methane consumption in the coming decades (Grauls, 2001; Kerr, 2004), but their use is likely to be limited because of the technical difficulty of extracting most of them (Archer, 2007), with a recent estimate of ultimate global recoverable volumes of ∼ 150 Gt of carbon (Boswell & Collett, 2011). From a technical point of view, all potential schemes of gas production from hydrate need to economically and safely achieve, at least, the following objectives (Pooladi-Darvish, 2004): (1) bring the temperature and pressure conditions of the hydrate-bearing sediments

out of the GHSZ, (2) maintain the latent heat required for the endothermic reaction, and (3) provide a system to transfer the dissociation products to the production wells.

Gas hydrates are vulnerable to dissociation with ocean warming of a few degrees Celsius (Buffett & Archer, 2004; Dickens *et al.*, 1997, 1995; Kennett *et al.*, 2000; Nisbet, 2002). Methane is a greenhouse gas that oxides to another greenhouse gas CO_2 in about a decade, and this accumulates in the Earth's carbon cycle and continues to impact climate for many millennia (Archer, 2005; Archer & Brovkin, 2008). Hydrates may have accumulated over millions of years (Davie & Buffett, 2001; Dickens, 2001), with the gradual cooling of the ocean over geologic time, and it could take millennia to release the carbon from melting the gas hydrate pool (Archer, 2007; Kennett *et al.*, 2003). However, human release of CO_2 from hydrocarbon combustion since the industrial revolution has accelerated ocean warming. Oceans are warmer than they have been in millions of years (Martin *et al.*, 2002; Stouffer & Manabe, 2003) and hence, hydrates have the potential to dissociate faster and release more methane than during the repeated glacial-interglacial periods (Sowers, 2006), and thereby create a positive feedback loop of warming (Nisbet, 1989, 1990). A strong correlation has been found between those climate switches and methane concentrations from two Antarctic ice-core records for the past 650 kyr (Spahni *et al.*, 2005), but no clear indicator has been found confirming that glacial-interglacial transitions were triggered by global methane fluxes (Fischer *et al.*, 2008). The significant negative $\delta^{13}C$ excursions during the "Paleocene-Eocene Thermal Maximum" (PETM) and other past hyperthermal events have also been linked to episodes of large amounts of methane release from dissociated gas hydrate (Dickens, 2011).

1.2.3 Present Day Arctic Gas Hydrate

Hydrates in the Arctic are estimated to contain ~100-600 Gt of methane carbon (Archer *et al.*, 2009). Marine hydrates are commonly found at water depths of 1000-3000 m (Kvenvolden, 1993), and are unlikely to form at water depths below 600 m because the bottom water is too warm for stability, except in the Arctic Ocean where the low water temperatures allow hydrates to form at water depths of only 250 m (Buffett & Archer, 2004). Based on model-derived predictions of sub-seabed conditions in the continental shelf of the Arctic Ocean, sub-sea permafrost hydrates may be stable only up to 120 m water depth (Collett *et al.*, 2011). However, downhole log data in the Alaska Beaufort continental shelf suggest the occurrence of permafrost and gas hydrate beneath the continental shelf of the Arctic Ocean at a maximum water depth of only ~50 m (Collett *et al.*, 1988), perhaps because of the limited number of direct measurements of permafrost occurrence on the

shelf (Collett *et al.*, 2011).

Ocean warming triggers and/or accelerates methane hydrate dissociation and significant amounts of methane are being liberated in the Arctic (e.g, Shakhova *et al.*, 2005, 2010; Westbrook *et al.*, 2009). However and depending on water depth, the escaping methane bubbles from melting hydrate may not reach the atmosphere, unless there is a large methane gas upward flow at shallow water depth (McGinnis *et al.*, 2006), because they are likely to get oxidised and dissolved in the water column (Judd, 2004; Westbrook *et al.*, 2009) accelerating ocean acidification (Biastoch *et al.*, 2011). In permafrost environments, in addition to ocean warming, gas hydrates are also currently affected by marine transgressions because during these transgressions comparatively warm waters flood over cold permafrost areas of the Arctic Shelf (Paull *et al.*, 2007). This mechanism could rapidly release significant amounts of methane from dissociated hydrate (Maslin *et al.*, 2010). Emissions of methane from melted hydrate have been inferred along the Siberian coastline (Shakhova *et al.*, 2005, 2010), resulting in 2500% supersaturation concentrations of methane relative to the atmosphere in Siberian shelf waters, and surface waters over the North Slope of Alaska have shown similar methane supersaturations (Kvenvolden, 1999). Terrestrial permafrost thawing and methane release in these areas are also being observed (Christensen *et al.*, 2004; Isaksen *et al.*, 2011), but it is not clear if the source of the observed methane is dissociated hydrate. Arctic marine hydrates may be affected more rapidly by global warming than hydrate at lower latitudes, because the Arctic colder seabed waters allow hydrate to form shallower than elsewhere and, the most intense warming is predicted in the Arctic (Hassol, 2004).

1.3 Thesis Structure

Chapter 2 sets out the methods used in this thesis and it is split into the two scientific topics studied. The first part describes the two methods developed in this thesis to impose seismic and geological constrains to the overpressure generated by a 1D/2D forward disequilibrium compaction and aquathermal expansion model (DCAEM). The second part describes the method used to calculate the response of gas hydrate-bearing sediments to ocean warming using the TOUGH+HYDRATE (T+H) v1.2 Code (Moridis *et al.*, 2012), and introduces the governing physics for the simulation of system behaviour in hydrate-bearing sediments in T+H.

Chapter 3 proposes a new method to calculate overpressure that uses the observed thickness of the layers and P-wave velocity data (V_p) to constrain the overpressure calculated with a 1D numerical disequilibrium compaction model. It includes an accurate description

of the sediments comprising the EBSB, proposes an explanation for the observed LVZ and discusses some limitations of the previous pore pressure analysis on the area (Scott *et al.*, 2009).

Chapter 4 describes the derivation of a 1D/2D forward numerical model to calculate pore pressure generated by the disequilibrium compaction and aquathermal pressuring mechanisms. It presents a novel 1D/2D inverse model to calculate overpressure and model parameters using the physical principles governing the generation of overpressure due to the above mechanisms, and the constraints imposed by V_p and density data, and the depth of layer interfaces. It builds on the findings of Chapter 3 for the EBSB, giving an explanation for the observed normal V_p below the LVZ.

Chapter 5 presents a modelling study of the dynamic response of hydrate-bearing sediments to ocean warming and present-day and likely future methane release from dissociated hydrate offshore west of Svalbard, over a period of 2300 yr and for water depths 350-800 m. In this chapter, future temperatures are given by two climate models, the Community Climate System model (CCSM4; Gent *et al.*, 2011), and the Met Office Hadley Centre model (HadGEM2; Collins *et al.*, 2011; Jones *et al.*, 2011) and two climate-forcing scenarios, Representative Concentration Pathways (RCPs) 2.6 and 8.5 (Moss *et al.*, 2010), which represent low and high greenhouse emissions, respectively.

Chapter 6 builds on the results from Chapter 5, and presents a more detailed analysis on the response of gas hydrate to ocean warming over the next century and for water depths between 400-500 m, using RCPs 8.5 and 2.6, and seven different climate models: the CCSM4, the Geophysical Fluid Dynamics Laboratory model (GFDL; Gordon & Stern, 1982), the HadGEM2 model, the Institute Pierre-Simon Laplace model (IPSL; Marti *et al.*, 2010), the Max-Plank Institute model (MPI; Marsland *et al.*, 2003), the Meteorological Research Institute model (MRI; Yukimoto *et al.*, 2001), and the Norwegian Climate Centre model (NorESM1; Bentsen *et al.*, 2012; Iversen *et al.*, 2012).

Chapter 7 gives a summary of the advances in knowledge derived from the work presented in this thesis and presents some ideas for future work. It also includes some preliminary results from an ongoing study of overpressure generation in the Ursa Basin, Gulf of Mexico, and of gas hydrate dissociation trigger by ocean warming in the Beaufort Sea, north Alaska.

The Appendix describes the main functions coded in Matlab 7.8.0 for the overpressure methods (Chapters 3 and 4) and those used to input annually variable seabed temperatures into T+H and to extract the results from the T+H output files (Chapters 5 and 6). These functions are included in the electronic material EM.1 (functions used in Chapter

3), EM.2 (functions used in Chapter 4) and EM.4 (functions used in Chapters 5 and 6).

Chapters 3-4 and Chapters 5-6 were prepared as individual papers, therefore they contain some overlapping introductory information. The work presented in Chapter 3 has been published in Basin Research (Marín-Moreno *et al.*, 2013a), that presented in Chapter 4 has been published in Geophysical Journal International (Marín-Moreno *et al.*, 2013b), and that presented in Chapter 5 has been published in Geophysical Research Letters (Marín-Moreno *et al.*, 2013c). Chapter 6 was prepared for submission in a short format type journal. The development and coding of the methods presented in the papers was done exclusively by me and these papers were written primary by me, with guidance and contribution from my supervisors Tim Minshull and Rose Edwards for the papers in Chapters 3-4 and from Tim Minshull, Graham Westbrook, Bablu Sinha and Sudipta Sarkar for the paper in Chapter 5.

Chapter 2

Methodology

2.1 Introduction

This chapter sets out the methods used in this thesis to locate and estimate overpressure zones, and to predict the future response of the Arctic gas hydrate system to ocean warming. The methods for overpressure prediction presented in this thesis are only applied to the centre of the Eastern Black Sea Basin (EBSB; Chapters 3 and 4), however these are general approaches that could be adapted to any sedimentary basin.

In Chapter 3, the overpressure structure in the centre of the EBSB was found using a new method to impose seismic constraints (P-wave velocity, and thickness of sedimentary layers) to the overpressure calculated by forward modelling using a 1D sediment compaction model. This analysis provided an initial idea of the expected overpressure structure in the centre of the basin and some knowledge on the lithological and fluid flow parameters and sedimentation rates of the layers generating the overpressure. A summary of this approach is given in section 2.1.2, and a more detailed description is given in section 3.2.3. The limitations of this method and the lack of understanding of some of the physical processes that may have been involved in the generation and dissipation of overpressure in the centre of the EBSB, motivated the development of a more robust approach to calculate overpressure and lithological and fluid flow parameters.

In Chapter 4, the overpressure structure in the centre of the EBSB was found using an inverse method. The overpressure was calculated using a 1D/2D forward disequilibrium compaction and aquathermal expansion model (DCAEM), and was constrained by seismic and density data, by means of automatic variation of some forward model parameters. The derivation of the mathematical and numerical 1D/2D forward DCAEM can be found in sections 2.2.1 and 4.2. The description of the inverse model can be found in sections 2.2.3

and 4.3. The overpressure structure predicted with the above methods was compared with that obtained using two P-wave velocity semi-empirical approaches, the equivalent depth method (e.g, Westbrook, 1991) and the Eaton method (den Boer *et al.*, 2006; Eaton, 1969, 1975). The description of those can be found in sections 2.2.4, 3.2.2, and 4.4.

To determine the response of gas hydrate to ocean warming in the Arctic the TOUGH+ HYDRATE (T+H) v1.2 Code (Moridis *et al.*, 2012) was used. Past temperatures were given by oceanographic measurements and proxy data and the predictions of future changes in temperature were given by published global climate models. Seismic and geological data were used to constrain some of the physical parameters controlling the gas hydrate system. A description of the method and an introduction to the physical and thermodynamic principles of the T+H v1.2 code can be found in sections 2.3.1 and 2.3.2, respectively. The method used to construct the temperatures over the period 1-2300 CE can be found in section 5.5.

2.2 Estimating Overpressure

2.2.1 1D/2D Disequilibrium Compaction and Aquathermal Expansion Model

The mathematical model developed here for estimating overpressure is based on Gibson's (1958) model. He was the first to estimate the generation of pore pressure due to disequilibrium compaction using Terzaghi's (1943) 1D small strain equation, and considering a single sedimentation rate and constant lithological properties (porosity, compressibility, density and permeability). Bethke (1985) extended that model by introducing 2D, non-isothermal conditions and non-linear variation of lithological properties, while Audet & Fowler (1992) and Wangen (1992) introduced a non-dimensionalised, non-linear and large strain formulation of Gibson's (1958) model.

The derivation of the equation governing the evolution of the total pore pressure through time due to sediment loading and fluid thermal expansion is given below.
The conservation of solid grains mass per unit of volume is given by

$$\frac{\partial}{\partial t}\left(\rho_s\left(1-\phi\right)\right)+\nabla\cdot\left(\rho_s\left(1-\phi\right)\mathbf{u}\right)=0 \tag{2.1}$$

where $\mathbf{u}=(u_x,u_y,u_z)$ is the solid grain velocity vector, ρ_s is the solid grain density and ϕ is the porosity.

The conservation of fluid mass per unit of volume is given by

$$\frac{\partial}{\partial t}\left(\rho_f \phi\right) + \nabla \cdot \left(\rho_f \phi \mathbf{v} + \rho_f \phi \mathbf{u}\right) = 0 \tag{2.2}$$

where $\mathbf{v} = (v_x, v_y, v_z)$ is the fluid velocity vector and ρ_f is the fluid density. The second term in the divergence operator describes the movement of the fluid because of the displacement of the solid grains.
The sediment density ρ in saturated conditions is given by

$$\rho\left(\phi, \rho_f\right) = \rho_s\left(1 - \phi\right) + \rho_f \phi \tag{2.3}$$

Eqs. 2.1 and 2.2 are reformulated according to a material description where the reference frame is fixed on the solid grains. The material derivative of a property DX/Dt following a specific particle of the continuous medium is given by

$$\frac{DX}{Dt} = \frac{\partial X}{\partial t} + \mathbf{u} \cdot \nabla X \tag{2.4}$$

By applying the material derivative to Eqs. 2.1 and 2.2 the solid grains and fluid conservation equations in a material formulation are obtained (Eqs. 2.5 and 2.6).

$$\left(1 - \phi\right)\frac{D\rho_s}{Dt} - \rho_s \frac{D\phi}{Dt} + \rho_s\left(1 - \phi\right)\nabla \cdot \mathbf{u} = 0 \tag{2.5}$$

$$\phi \frac{D\rho_f}{Dt} + \rho_f \frac{D\phi}{Dt} + \nabla \cdot \left(\rho_f \mathbf{v} \phi\right) + \rho_f \phi \nabla \cdot \mathbf{u} = 0 \tag{2.6}$$

Substituting the term $D\phi/Dt$ of Eq. 2.5 into Eq. 2.6 and dividing it by ρ_f gives

$$\frac{\phi}{\rho_f}\frac{D\rho_f}{Dt} + \frac{\left(1 - \phi\right)}{\rho_s}\frac{D\rho_s}{Dt} + \frac{1}{\rho_f}\nabla \cdot \left(\rho_f \mathbf{v} \phi\right) + \nabla \cdot \mathbf{u} = 0 \tag{2.7}$$

where the term $\nabla \cdot \mathbf{u}$ can be expressed in the form

$$\nabla \cdot \mathbf{u} = \frac{\partial u_x}{\partial x} + \frac{\partial u_y}{\partial y} + \frac{\partial u_z}{\partial z} = \frac{D}{Dt}\left(\varepsilon_x + \varepsilon_y + \varepsilon_z\right) = \frac{D\varepsilon_v}{Dt} \tag{2.8}$$

where ε_x, ε_y, ε_z are Cartesian strains and ε_v is the volumetric strain.
Equation. 2.7 describes that changes in the water content of a unit-volume of sediment must be balanced by changes in the fluid density, solid grain density and deformation of the sediment. To express Eq. 2.7 in terms of pore pressure, three constitutive equations relating fluid density, porosity and fluid flow to pore pressure are required (the solid grains density is considered a constant). The fluid density changes are assumed to be a function of changes in pore pressure and temperature and are given by International Association

for the Properties of Water and Steam's (2007) density model. The evolution of porosity is controlled by mechanical and chemical compaction (Bjørlykke & Høeg, 1997; Schneider *et al.*, 1996), but here only mechanical compaction is considered. The Athy's (1930) law in terms of vertical effective stress is used. The effective stress principle (Terzaghi, 1943) states that any variation in porosity is due to a variation in the effective stress. The porosity evolution as a function of the vertical effective stress is given by

$$\phi\left(\beta, \sigma'_{zz}\right) = \phi_0 \exp\left[-\beta\sigma'_{zz}\right] \tag{2.9}$$

where β is an empirical compaction factor, ϕ_0 is the initial porosity or porosity at surface conditions (zero effective stress) and σ'_{zz} is the vertical effective stress (Eq. 2.10). Here, the empirical factor β is assumed to be equivalent to the bulk compressibility of the saturated sediments (Hart *et al.*, 1995).

$$\sigma'_{zz}\left(z, \rho, \rho_f\right) = \int_0^z \left(\rho - \rho_f\right) g dz - P^* = P_L - P = P_L - \left(P_h + P^*\right) \tag{2.10}$$

In Eq. 2.10 g is the gravitational acceleration, z is the depth, P is the total pore pressure, P_h is the hydrostatic pressure, P^* is the overpressure, and P_L is the vertical or lithostatic pressure. The change in lithostatic pressure over time can be expressed in terms of sediment thickness h (Fig. 2.1a) by

$$\frac{DP_L\left(h, \rho\right)}{Dt} = \rho g \frac{Dh}{Dt} \tag{2.11}$$

Equation. 2.9 when differentiated with respect to time, and considering here that changes in β with time are significantly smaller compared to those in σ'_{zz} and therefore assuming that β is a constant, gives

$$\frac{D\phi}{Dt} = -\phi\beta \frac{D\sigma'_{zz}}{Dt} \tag{2.12}$$

The term $D\phi/Dt$ in Eq. 2.12 can also be expressed in terms of volumetric deformation by

$$\frac{D\phi\left(V_\phi, V_s\right)}{Dt} = \frac{D}{Dt}\left(\frac{V_\phi}{V_\phi + V_s}\right) = \frac{\frac{D}{Dt}V_\phi\left(V_\phi + V_s\right) - V_\phi \frac{D}{Dt}V_\phi}{\left(V_\phi + V_s\right)^2} = \frac{D\varepsilon_v}{Dt}\left(1 - \phi\right) \tag{2.13}$$

where V_ϕ and V_s are the pores and solid grains volume respectively.
Fluid flow is described by Darcy's equation

$$\rho \mathbf{v} \phi = \frac{-\boldsymbol{K}\left(k_i, \rho, \mu\right)}{g} \cdot \nabla\left(P - \rho_f g z\right) \tag{2.14}$$

where $\boldsymbol{K}$ is the permeability tensor, with eigenvalues K_{xx}, K_{yy}, K_{zz} (assuming Cartesian principal directions).

Using expressions 2.8, 2.10, 2.11, 2.12, 2.13 and 2.14 in Eq. 2.7 the evolution of the total pore pressure through time due to sediment loading and fluid volume change is governed by

$$\frac{DP\left(\boldsymbol{K},\beta,\phi,\rho_f,h\right)}{Dt}=\nabla\cdot\left(\frac{(1-\phi)}{\phi\beta\rho_f g}\boldsymbol{K}\cdot\nabla\left(P-\rho_f g z\right)\right)+\rho g\frac{Dh}{Dt}-\left(\frac{(1-\phi)}{\beta\rho_f}\right)\frac{D\rho_f}{Dt}$$
$$K_{zz}\left(k_i,\rho_f,\mu\right)=\frac{k_i\rho_f g}{\mu};\quad K_{xx}=K_{yy}=\alpha K_{zz};\quad \beta\left(\rho,\rho_f\right)=\frac{c}{\left(\rho-\rho_f\right)g};$$
$$\rho_f=g_1(P,T);\quad \mu=g_2(T,\rho_f);\quad k_i=g_3(k_{i0},\gamma,\phi,\phi_0); \tag{2.15}$$

In Eq. 2.15 T is the temperature, c is the depth compaction factor (Sclater & Christie, 1980), k_i is the intrinsic permeability (geometric permeability), k_{i0} is the initial intrinsic permeability, α is the ratio between the horizontal and vertical permeability (considered only in the 2D model), γ is the parameter controlling how the intrinsic permeability evolves with porosity, ϕ_0 is the surface porosity, and μ is the viscosity. In Eq. 2.15 the first term on the right-hand side of the first equation is the fluid flow term, the second is the sediment loading term, and the third is the term that considers changes in fluid volume. In normal geological environments, water volume changes by changes in temperature are dominant over pressure changes for an equal increment in depth. Therefore, as water tends to expand with increasing depth and so its density decreases, the minus sign in the third term of Eq. 2.15 is required. Equation 2.15 considers the non-linear variation of the lithological properties porosity, intrinsic permeability and compressibility and changes in water density and viscosity with pressure and temperature.

The 1D/2D DCAEM (Eq. 2.15) was coded in Matlab 7.8.0 and was solved numerically using an implicit finite difference scheme with backward differences to approximate the time derivative and centred differences in space (Eq. 2.16) a fully compacted coordinate system for the depth axis (Gutierrez & Wangen, 2005), and an harmonic average to estimate the permeability at the interface between cells. The implicit finite difference scheme is an unconditionally stable algorithm with a first order approximation in time and second order in space.

$$\left[\frac{\partial P}{\partial t}\right]_{m,n}^{t_i}=\frac{P|_{m,n}^{t_i+1}-P|_{m,n}^{t_i}}{\Delta t}+\xi\left(\Delta t\right)$$
$$\left[\frac{\partial^2 P}{\partial z^2}\right]_{m,n}^{t_i}=\frac{P|_{m-1,n}^{t_i}-2P|_{m,n}^{t_i}+P|_{m+1,n}^{t_i}}{\Delta z^2}+\xi\left(\Delta z^2\right)$$
$$\left[\frac{\partial^2 P}{\partial x^2}\right]_{m,n}^{t_i}=\frac{P|_{m,n-1}^{t_i}-2P|_{m,n}^{t_i}+P|_{m,n+1}^{t_i}}{\Delta x^2}+\xi\left(\Delta x^2\right) \tag{2.16}$$

Equation 2.16 expresses the derivative approximations used in the numerical model (Eq. 2.17) and Δt is the time step, Δx and Δz are the horizontal and vertical dimensions of the finite difference cell, respectively, the superscript t_i is the time index, the subscripts m and n are the z and x dimensions indexes, and the second term on the right-hand side of the equations are the truncation errors in the approximation.

The fully compacted depth coordinate axis measures a sediment column where all the pores have been removed (Fig. 2.1b). The fully compacted depth coordinate ζ-axis was obtained from the real depth coordinate z-axis using the transformation $\Delta\zeta = \Delta z\,(1-\phi)$. Every new sedimented layer was also added in the fully compacted coordinate system H_ζ using the transformation $H_\zeta = H_0\,(1-\phi_0)$, where H_0 is the uncompacted sediment thickness, i.e. thickness at the time of deposition.

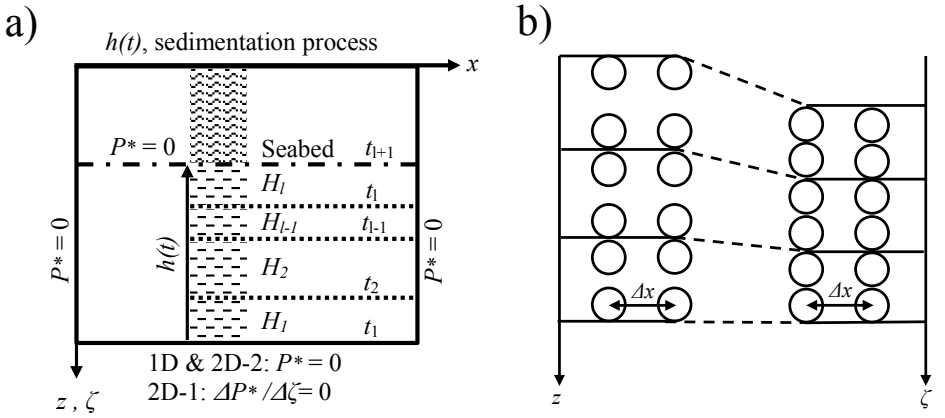

Figure 2.1: (a) Conceptual diagram for the application of the forward numerical model (Eq. 2.17), showing the sedimentation process and the boundary conditions imposed at all boundaries. The subscript l varies between one and the maximum number of stratigraphic layers in the model. The sedimentation time interval Δt_s is calculated using the ages of the top and base of each stratigraphic layer. (b) Schematic diagram of the fully compacted coordinate system ζ. It shows two conceptual columns of sediment separated by a distance of Δx in the real and in the fully compacted depth coordinate system.

Following Bethke (1985) 2D finite difference discretisation of the geometrical domain and the fully compacted description of the depth coordinate axis (Fig. 2.1b), the finite difference approximation to Eq. 2.15 can be expressed as:

$$\frac{\Delta P}{\omega \Delta t_s} = \frac{1}{\Delta\zeta}(1-\phi)\left(\frac{K_{\zeta\zeta}\,(1-\phi)^2\,\Delta x}{V_c \phi\beta\rho_f g}\frac{\Delta P^*}{\Delta\zeta}\right)\Delta\zeta + \frac{1}{\Delta x}\left(\frac{K_{xx}\,(1-\phi)\,\Delta\zeta}{V_c\phi\beta\rho_f g}\frac{\Delta P}{\Delta x}\right)\Delta x + \frac{H_0\,(1-\phi_0)}{\Delta t_s}\rho g - \left(\frac{(1-\phi)}{\beta\rho_f}\right)\frac{\Delta\rho_f}{\omega\Delta t_s} \quad (2.17)$$

where K_{xx} and $K_{\zeta\zeta}$ (K_{zz} in the fully compacted coordinate system) are the horizontal and vertical permeabilities, respectively, V_c is the area per unit of width of a finite difference cell,

Δt_s is the sedimentation time interval of each stratigraphic layer, and ω is a parameter with values between $0 < \omega < 1$. Therefore, the length of the numerical time step is $\Delta t = \omega \Delta t_s$. Assuming a constant sea level, the term $\Delta P / \Delta x$ in Eq. 2.17 was expressed in terms of overpressure $\Delta P^* / \Delta x$, which allowed the boundary and initial conditions in terms of overpressure to be imposed. The top boundary condition was set to zero overpressure $P^* = 0$, and the bottom, left and right boundary conditions were set to either $P^* = 0$ or $\Delta P^* / \Delta \zeta = 0$. The top boundary condition is a moving boundary condition that is imposed at each newly deposited layer (Fig. 2.1a). The initial condition was set to zero overpressure $P^*(t = 0) = 0$. Equation 2.17 describes the generation of overpressure as the balance between the third and fourth terms on the right hand side (sediment loading and fluid volume changes terms, respectively) which tend to increase the overpressure, and the first and second terms (vertical and horizontal fluid flow terms, respectively) which tend to decrease the overpressure.

The 1D/2D contour problem is formed by Eq. 2.17, two (1D) or four (2D) boundary conditions and a initial condition. Its implicit finite difference numerical scheme can be expressed in matrix form by,

$$\left(\underset{(M\times N, M\times N)}{\mathbf{A}}\right) \cdot \left(\underset{(M\times N,1)}{\mathbf{P}^*}\right)^{t_i+1} = \underset{(M\times N, M\times N)}{\mathbf{I}} \cdot \left(\underset{(M\times N,1)}{\mathbf{P}^*}\right)^{t_i} + \left(\underset{(M\times N,1)}{\mathbf{F}}\right) \tag{2.18}$$

where $\mathbf{A}$ is the coefficients matrix (Eq. 2.19) and has the form of a triband and pentaband matrix in the 1D and 2D problem, respectively (it was assumed that the fluid flow can be decomposed into its horizontal and vertical components and so each cell has a maximum of two (1D) or four (2D) connections), $\mathbf{I}$ is the identity matrix, $\mathbf{F}$ includes the contribution of the initial and boundary conditions, and source terms (sediment loading and aquathermal expansion terms), and M and N are the maximum number of rows and columns, respectively.

$$\begin{pmatrix} a_{1,1} & a_{1,2} & \dots & a_{1,1+N} & 0 & 0 & 0 \\ a_{2,1} & a_{2,2} & a_{2,3} & \dots & a_{2,2+N} & 0 & 0 \\ \vdots & \ddots & \ddots & \ddots & \dots & \ddots & \vdots \\ a_{1+N,1} & \dots & a_{i,i-1} & a_{i,i} & a_{i,i+1} & \dots & a_{i,i+N} \\ \vdots & \ddots & \dots & \ddots & \ddots & \ddots & \vdots \\ 0 & 0 & a_{L-1,L-N} & \dots & a_{L-1,L-2} & a_{L-1,L-1} & a_{L-1,L} \\ 0 & 0 & 0 & a_{L,L-N} & \dots & a_{L,L-1} & a_{L,L} \end{pmatrix}; \quad \begin{matrix} L = M \times N \\ i = 1, 2, \dots, L-1, L \end{matrix} \tag{2.19}$$

In Eq. 2.19 the subscripts in the a coefficients indicate how the cells are connected assuming a row natural ordering of the discretised model geometry.

2.2.2 Layer Thickness and P-Wave Velocity Constraints in Modelling Overpressure

A new method in which observed sediment thickness and P-wave velocity (V_p) data are used to constrain the overpressure predicted with a 1D disequilibrium compaction model was developed and applied to the EBSB (Chapter 3). A more detailed description of the method can be found in section 3.2.3, and so here just an introduction to the conceptual algorithm and main equations are shown.
Figure 3.2 illustrates the method's workflow.

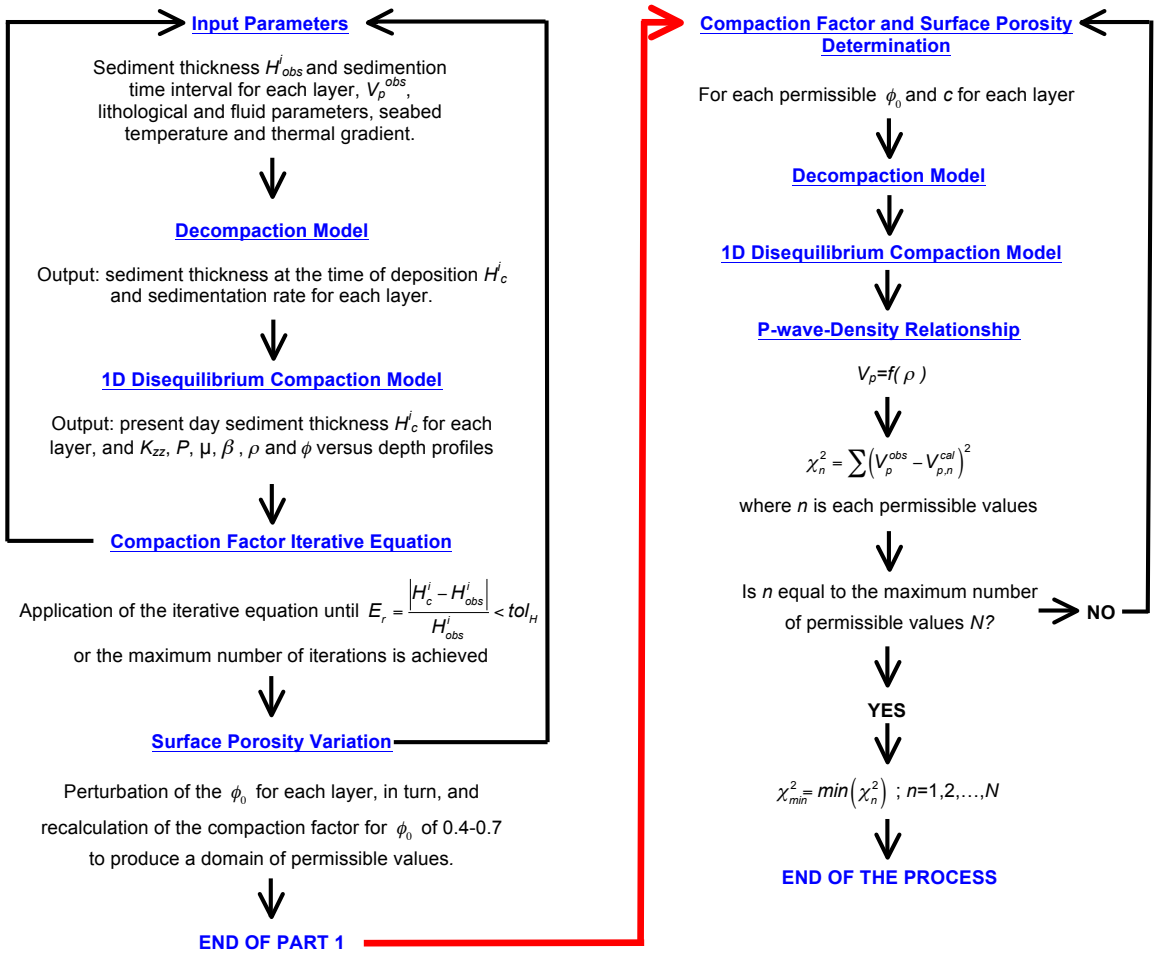

Figure 2.2: Conceptual algorithm to impose observed sediment thickness and V_p constraints in the overpressure predicted with a 1D disequilibrium compaction model. The superscript i in H_{obs} and H_c denotes layer number and varies between one and the maximum number of layers considered.

This method starts with a set of initial input parameters. Using these input parameters and a decompaction model based on Sclater & Christie (1980) (Eq. 2.20) the sedimentation

rate of each modelled layer is estimated.

$$z'_2 - z'_1 = z_2 - z_1 - \frac{\phi_0}{\beta}\left[\exp\left(-\beta\sigma'_{z_1}\right) - \exp\left(-\beta\sigma'_{z_2}\right)\right] + \frac{\phi_0}{\beta}\left[\exp\left(-\beta\sigma'_{z'_1}\right) - \exp\left(-\beta\sigma'_{z'_2}\right)\right] \tag{2.20}$$

In Eq. 2.20 z_1 and z_2 are the present top and base depths of a layer and z'_1 and z'_2 are the top and base depths at the moment of deposition assuming instantaneous deposition. Equation 2.20 keeps the mass of the solid constant, and considers the change in volume and so in thickness due to the change in the volume of water assuming hydrostatic conditions. It represents the removal of the sediment above each layer, allowing the layer to decompact. The decompacted layer thicknesses are then used to estimate the sedimentation rates, assuming that the ages range for each layer is known. From the estimated sedimentation rates and the original input parameters, the 1D disequilibrium compaction model (Eq. 2.15), only considering the vertical fluid flow component and neglecting the contribution to overpressure from fluid thermal expansion) is applied. Next, the observed and calculated layer thicknesses are compared. If they are similar within a tolerance, the input surface porosities are changed and, for each layer in turn, the process above is applied again. If they are not, an ad-hoc iterative equation (Eq. 2.21) is applied to obtain the input compaction factors that give calculated layer thicknesses within a tolerance.

$$c^i_{j+1} = \frac{\ln\left(\phi^i_0\right) - \ln\left(1 - \varepsilon + \varepsilon\phi^i_0 \exp\left[-c^i_j z^i_{(1/2)j}\right]\right)}{z^i_{(1/2)obs}} \qquad i = 1, 2..., N_{layers} \qquad j = 1, 2..., N_{iterations} \tag{2.21}$$

In Eq. 2.21 the subscript j is the iterative index, the superscript i is the layer index, $N_{iterations}$ and N_{layers} are the number of iterations and layers respectively, $z_{(1/2)}$ and $z_{(1/2)obs}$ are the calculated and observed present middle point layer depth respectively, and ε is the ratio between the calculated and observed present-day layer thickness. The logarithm of a negative number is not defined. Therefore, if $\left(1 - \varepsilon + \varepsilon\phi^i_0 \exp\left[-c^i_j z^i_{(1/2)j}\right]\right) < 0$, the iterative equation is not solved in that iteration and $c^i_{j+1} = c^i_j$. To control the rate of change of the compaction factor, the equation $c^{i\varpi}_{j+1} = c^i_j + \varpi\left(c^i_{j+1} - c^i_j\right)$ is applied, where ϖ is a weighting parameter with values between 0 and 1. In Eq. 2.21 an exponential porosity-depth relationship was introduced ($\phi = \phi_0 \mathrm{e}^{-cz}$). At this stage, a set of permissible surface porosities and compaction factors in terms of layer thicknesses have been determined, but those may not represent the observed present-day V_p structure. The permissible parameter space is further constrained by comparing the observed and calculated V_p structure. For the

permissible values, both the decompaction model and the 1D disequilibrium compaction model are applied again, and the density output from the latter model is introduced into a V_p-density relationship to calculate the V_p. Finally, a least-squares approach is used to select the best-fitting model.

2.2.3 Modelling Overpressure with an Inverse Approach

Introduction to Inverse Problems

Scientists and engineers frequently try to relate physical model parameters m, to observations making up a dataset d. In this process, it is commonly assumed that the fundamental physics or mathematical model G governing the system is understood. The *forward problem* ($G(m) = d$) consists of finding d given m, i.e. given an adequate description of the physical system, we can predict the outcome of some measurements. The *forward problem* may involve evaluating an integral, solving a Ordinary Differential Equation (ODE), a Partial Differential Equation (PDE), or, as in this thesis, applying an algorithm for which there is no explicit analytical formula. The *inverse problem* consists in finding m given d and while in deterministic physics the *forward problem* has a unique solution, the *inverse problem* does not, so many models may adequately fit the data. Therefore, it is essential to determine how accurate the solution is in terms of the physical plausibility and how consistent it is with other constraints. Three important considerations are: *solution existence*, *solution uniqueness*, and *instability of the solution process* (Aster *et al.*, 2005).

- *Existence.* There may be no model that exactly fits the data because, in practice, either the data may contain noise or the forward model is an approximation of the real physics of the system.
- *Uniqueness.* If there is an exact solution, this may not be unique.
- *Instability.* Inverse problems are often extremely unstable and a small change in the measurement can drive big changes in the estimated model.

Solving the Inverse Problem with a Non-Linear Least Squares Approach

The inverse model presented in this thesis and applied to the EBSB (Chapter 4) is given by minimising the functional:

$$\chi^2 = \frac{1}{N}\sum_{n=1}^{N}\left(\frac{V_{p,n}^{Obs} - V_{p,n}^{Cal}(\mathbf{m})}{s_n\left(V_p^{Obs}\right)}\right)^2 + \frac{1}{N}\sum_{n=1}^{N}\left(\frac{V_{p,n}^{Norm} - V_{p,n}^{NormCal}(\mathbf{m})}{s_n\left(V_p^{Norm}\right)}\right)^2 + \frac{1}{N}\sum_{n=1}^{N}\left(\frac{\rho_n^{Obs} - \rho_n^{Cal}(\mathbf{m})}{s_n\left(\rho^{Obs}\right)}\right)^2 + \frac{1}{L}\sum_{l=1}^{L}\left(\frac{z_{b,l}^{Obs} - z_{b,l}^{Cal}(\mathbf{m})}{s_l\left(z_b^{Obs}\right)}\right)^2 ; \mathbf{m}_{\mathrm{L}} \leqslant \mathbf{m} \leqslant \mathbf{m}_{\mathrm{U}} \quad (2.22)$$

where L and N are the number of sediment layers and data points respectively, $\mathbf{m}$ is the vector containing the model parameters, $\mathbf{m}_{\mathrm{L}}$ and $\mathbf{m}_{\mathrm{U}}$ are the lower and upper bound vectors of model parameters, respectively, and contain their *a-priori* state of information, V_p is the P-wave velocity, z_b is the depth of a layer interface, s is the error associated with the data, and the superscripts, Obs, $Norm$ and Cal mean observed, normal and calculated, respectively. I defined V_p^{Norm} as the V_p assuming hydrostatic conditions and V_p^{Obs} as the V_p obtained from a tomographic analysis of wide-angle seismic data (see section 1.1.4). Equation 2.22 uses a non-linear least squares approach (Aster *et al.*, 2005; Tarantola, 2005), the constraints imposed by the disequilibrium compaction and aquathermal pressuring mechanisms, and seismic (V_p and layer interface depth), density, and geological data to obtain the model parameters for each layer: ϕ_0, c, k_{i0}, γ, α (considered only in the 2D model), and H_0. The second term in Eq. 2.22 drives the model to zero overpressure in layers where it is assumed that the V_p^{Obs} is normal, and penalises models with abrupt changes in V_p^{Obs} derived from significant changes in lithology (and therefore, compressibility and porosity) of the sediments. Without the second term, if the model tried to represent non-compaction derived changes in V_p^{Obs}, these could be given by either overpressure or by significant changes in lithological parameters. However, with the second term and because V_p^{Cal} and $V_p^{NormCal}$ are calculated with the same lithological parameters, differences between both profiles are necessarily given by overpressure. In Eq. 2.22 z_b^{Cal} and ρ^{Cal} are direct outputs from the forward model (Eq. 2.15) whereas V_p^{Cal} and $V_p^{NormCal}$ are not. To calculate them, the density outputs from the forward model and a P-wave velocity density relationship were used.

This inverse model assumes that the data space is linear, and the data uncertainties are gaussian. It also assumes that the forward model is approximately linear in the fitted parameters, so the posterior probability density of model parameters is approximately gaussian (Tarantola, 2005). This model does not consider uncertainties on the forward physical model. If the physical model uncertainties were known and gaussian, the associated covariance matrix could be simply added to the data covariance matrix (Tarantola, 2005).

The global minimum value of χ^2 within the parameters bounds was found using the trust-region reflective method implemented in Matlab 7.8.0 and based on Coleman & Li (1994, 1996). The trust-region reflective method is a deterministic method and so it tends to be a more exploitative than explorative algorithm (Sambridge & Mosegaard, 2002). This type of algorithm only uses the previous sampling or the current best fit model to decide where to sample next. In contrast, more explorative, Monte Carlo type algorithms, try to reduce the error by looking randomly to the parameter space without considering what is known from previous sampling. The more explorative the algorithm is, the less likely it will fall into a lo-

cal minima, but less efficient it will be at converging on a solution. Conversely, exploitative algorithms, such as the one used here, are more efficient at convergence but prone to entrapment, and so prone to find a local minima instead of the global minima and hence, the solution depends on the starting point. For smooth non-linear forward models with approximately known parameter bounds, such as the one considered here, a exploitative algorithm is a sensible choice (Sambridge & Mosegaard, 2002). Convergence was defined when either, $\left|\chi^2\left(\mathbf{m}^{\mathrm{i}+1}-\mathbf{m}^{\mathrm{i}}\right)\right| \leqslant 10^{-6}\left(\chi^2\left(\mathbf{m}^0\right)\right)$ or $\left(\mathbf{m}^{\mathrm{i}+1}-\mathbf{m}^{\mathrm{i}}\right)\left(\mathbf{m}^{\mathrm{i}+1}-\mathbf{m}^{\mathrm{i}}\right)^{\mathrm{T}} \leqslant 10^{-6}\left(\mathbf{m}^0\left(\mathbf{m}^0\right)^{\mathrm{T}}\right)$, is satisfied. Here $\mathbf{m}^0$ is the initial model parameters vector and the superscript i means iteration.

2.2.4 Overpressure Prediction with Geophysical Methods

Geophysical methods for overpressure prediction use semi-empirical relationships to transform geophysical data, such as P and S wave velocities, resistivity and density, to pore pressure. These are the most commonly used methods in the oil industry because the estimated pore pressure is indirectly constrained by geophysical observations, and are less time consuming than other methods. However, such methods do not consider the hydrodynamics of the sedimentary basin, generally have considered a single lithology, and most of them are site dependent.

In Chapters 3 and 4 two V_p based methods, the equivalent depth method (e.g, Westbrook, 1991) and the Eaton method (den Boer *et al.*, 2006; Eaton, 1969, 1975) were used to compare with the outcome of the methods presented in this thesis. V_p methods for pore pressure prediction assume that changes in V_p are a function of changes in the vertical effective stress alone, as an approximation to the mean effective stress. Under hydrostatic conditions, V_p typically increases with burial, and hence with vertical effective stress, due to the reduction in porosity and increased grain contact. Therefore, any decrease in V_p may be attributed to a decrease in the vertical effective stress, that is, an increase of pore pressure above hydrostatic. This overpressure results in undercompacted sediments with porosity and intrinsic permeability values more appropriate to shallower depths.

The equivalent depth method assumes that effective stress at depth z in a low velocity zone (LVZ) is equal to that at the shallower depth $z^{'}$ when V_p is the same but the pressure is hydrostatic, and is given by Eq. 2.23. The V_p in the overpressured zone V_p^{Obs} at depth z was matched with a normal V_p in hydrostatic conditions V_p^{Norm} at depth $z^{'}$ within a tolerance of $\pm$ 0.01 km/s.

$$P\left(z\right) = P_L\left(z\right) - P_L\left(z^{'}\right) + P_h\left(z^{'}\right) \tag{2.23}$$

The Eaton method estimates pore pressure from the ratio between V_p^{Obs} and V_p^{Norm} and is given by Eq. 2.24.

$$P(z) = P_L - (P_L - P_h)\left(\frac{V_p^{Obs}}{V_p^{Norm}}\right)^E \tag{2.24}$$

The Eaton factor E controls the sensitivity of the V_p to the vertical effective stress (den Boer *et al.*, 2006) and should ideally be obtained by calibration using measurements of pore pressure in boreholes in the study area. Equation 2.24 may only be valid for over-pressure generated primary by disequilibrium compaction (Sarker & Batzle, 2008), and in the presence of other dominant mechanisms may not be the most accurate method (Ebrom *et al.*, 2003). To apply Eq. 2.24 the V_p^{Norm} must be known or, in its absence, must be estimated.

2.3 Modelling Gas Hydrate Dissociation in Response to Ocean Warming offshore West Svalbard with TOUGH+HYDRATE (T+H) v1.2 Code

In order to understand the causes of methane release from gas hydrate dissociation and its likely future development offshore West Svalbard, it is necessary to predict the gas hydrate-bearing sediments response to changing temperatures in the overlying ocean. This was done using TOUGH+HYDRATE v1.2 Code (Moridis *et al.*, 2012) from Lawrence Berkeley National Laboratory. The analyses presented in Chapters 5 and 6, build on a previous numerical modelling study in the same area (Thatcher *et al.*, 2013), that explains the present-day methane release, extending it to the future using predicted future temperatures from published global climate models. Offshore west of Svalbard is an ideal location to study the effects of ocean warming in Arctic gas hydrate-bearing sediments because it satisfies the following criteria:

1) Hydrate is known to be widespread from observations of a characteristic bottom simulating reflector (BSR; Rajan *et al.*, 2012; Sarkar *et al.*, 2012; Vanneste *et al.*, 2005) that marks the base of the region where hydrate is stable and the boundary with gas bearing sediments beneath, and from direct sampling of hydrate nearby (Fisher *et al.*, 2011).

2) Sufficient geophysical and geological data exist to estimate the amount of hydrate present (Chabert *et al.*, 2011; Westbrook *et al.*, 2008) and other key parameters for modelling such as the thermal gradient, heat flow and the thermal conductivity (Crane *et al.*, 1991; Eldholm *et al.*, 1999; Rajan *et al.*, 2012; Sarkar *et al.*, 2012; Vanneste *et al.*,

2005), porosity (Haacke *et al.*, 2008) and permeability (from modelling studies; Reagan *et al.*, 2011; Thatcher *et al.*, 2013) of the seabed sediments.

3) Hydrate is inferred to be present where its limit of stability approaches the seabed, and therefore is vulnerable to changing ocean temperatures on timescales of decades to centuries.

2.3.1 Method

A range of 1D models were run from water depths where the present-day gas hydrate-bearing sediments did not change, even after three centuries of increasing ocean temperatures, to water depths where they were already out of the GHSZ. A 1D approach was applied to reduce the computational cost of the calculation and to allow a wide range of climate models, and because given the low hydrate saturations and slopes of the study area, the error in the 1D approximation was small (Reagan *et al.*, 2011).

For each water depth, the following steps were completed:

1) Construct a model of past ocean temperatures at the geographical locations and water depths of interest, using temperatures from historical oceanographic measurements for the period 1900-2005 and from foraminifera proxy data for the period 1-1900.

2) Sample future published climate models at the same locations and water depths. These consisted of Atmosphere-Ocean General Circulation Models (AOGCM) and Earth System Models (ESM), the latter incorporating additional earth system components such as biogeochemical cycles and atmospheric chemistry (Hunter *et al.*, 2013). Seven climate models were used, five of which cover the period to 2100: the Geophysical Fluid Dynamics Laboratory model (GFDL; Gordon & Stern, 1982), the Institute Pierre-Simon Laplace model (IPSL; Marti *et al.*, 2010), the Max-Plank Institute model (MPI; Marsland *et al.*, 2003), the Meteorological Research Institute model (MRI; Yukimoto *et al.*, 2001) and, the Norwegian Climate Centre model (NorESM1; Bentsen *et al.*, 2012; Iversen *et al.*, 2012). Two further models extend to 2300: the Community Climate System model (CCSM4; Gent *et al.*, 2011), and the Met Office Hadley Centre model (HadGEM2; Collins *et al.*, 2011; Jones *et al.*, 2011). The most extreme future climate-forcing scenarios, Representative Concentration Pathways (RCPs) 8.5 and 2.6 for the period 2005-2100 (Moss *et al.*, 2010) and their extended versions to 2300, Extended Concentration Pathways (ECP; Meinshausen *et al.*, 2011), which represent high and low greenhouse emissions, respectively, were used to cover the full range of future scenarios. In this thesis, the term RCP has been used for the period 2005-2300.

3) Determine from seismic and geological data, and literature the appropriate set of physical parameters required by the model. These include heat flow and methane supply into

the base of the model, thermal conductivity, porosity, intrinsic permeability, starting hydrate and gas content, and irreducible gas saturation.

4) Initialise the model with a set of physical parameters (defined by point 3 above), the seabed temperature at 1 CE (defined by point 1 above), hydrostatic pressure, a constant heat flow, and a hydrate-free sediment in the top 7 m to approximate the sulphate reduction zone (Borowski *et al.*, 1996). Several model runs using the constructed temperature series for the past 2000 years (defined by point 1 above), were necessary to ensure that the combination of parameters used resulted in a present-day state of the system that matched the geophysical observations, including the depth of the hydrate BSR, the distribution and saturation of hydrate beneath the seabed, and present-day observations of methane escape. The present-day temperature, gas hydrate, and free gas distribution beneath the seabed depend upon the historical temperature, so model runs needed to start far in the past. The models were started the year 1 CE, but no sensitivity analysis was performed to see the influence of starting the model even farther in the past. This would only change the results if, within a time scale of a few millennia, there were warmer periods before year 1 CE. Based on temperature proxy data, Hald *et al.* (2004) showed that temperatures in the West Spitsbergen continental margin were warmer than present between 11200-8800 yr BP, cooler between 8800-4000 yr BP, and have remained stable and cold for the past 4000 yr. Therefore, our initial temperatures may simulate those of the last 4000 yr. However, when and how the model was initialised does not significantly influence our predictions regarding the future behaviour of the gas hydrate system and on methane emissions, because these are driven by present-day observations rather than assumptions about initial conditions.

5) Run the model for the next 100-300 yr using future seabed temperatures (defined by point 2 above).

2.3.2 Introduction to T+H v1.2 Code: Underlying Physics and Thermodynamics

This subsection is a brief introduction to the main physical and thermodynamical principles governing the behaviour of hydrate-bearing geologic systems in T+H v1.2 code. For more details about the code, including the mathematical principles, the reader should refer to Moridis *et al.* (2012) user's manual.

T+H v1.2 solves the coupled equations of mass and heat balance (Eq. 2.25) and can model the non-isothermal gas release, phase behaviour and flow of fluids and heat under conditions typical of common methane hydrate deposits (in the permafrost and in deep ocean sediments) and in porous/fracture media at any scale (from laboratory to reservoir), at

which the Darcy's law is valid. It accounts for heat and up to four mass components; water, CH_4, hydrate and water-soluble inhibitors. Inhibitors, such as salts or alcohols, cause the decomposition of a gas hydrate by shifting its thermodynamic-equilibrium curve, and they are a remediation measure when unwanted plugging occurs in pipelines and in the vicinity of a wellbore, to reopen flow paths (Pooladi-Darvish, 2004). The four mass components are partitioned among four possible phases; gas, liquid, ice and hydrate. It also includes both an equilibrium and a kinetic model of hydrate formation and dissociation. In the equilibrium model, hydrate is considered only as a phase whereas in the kinetic model hydrate is both a phase and a component. In this thesis the equilibrium model has been employed. Hydrate dissociation or formation, phase changes (Fig. 2.3) and the corresponding thermal effects are fully described.

$$\frac{d}{dt}\int_{V_n} M^k dV = \int_{\Gamma_n} \mathbf{F}^k \cdot \mathbf{n} \; dA + \int_{V_n} q^k dV \tag{2.25}$$

In Eq. 2.25 V and V_n are the volume and volume of subdomain n, respectively, M^k is the mass accumulation term of component k (including heat), A and Γ_n are the surface area and surface area of the subdomain n, respectively, $\mathbf{F}^k$ is the flux vector of component k, $\mathbf{n}$ is the inward unit normal vector, q^k is the source and sink term of component k, and t is the time. The mass accumulation terms for the mass components (Eq. 2.26) and for heat (Eq. 2.27) are given by

$$M^k = \sum_{A,G,I,H} \phi S_\beta \rho_\beta X^k_\beta \,, \qquad k = w, m, i, h \tag{2.26}$$

$$M^\theta = (1-\phi)\rho_R C_R T + \sum_{\beta=A,G,I,H} \phi S_\beta \rho_\beta U_\beta + Q_{diss} \quad \text{, where}$$
$$Q_{diss} = \begin{cases} \Delta\left(\phi \rho_H S_H \Delta U_H\right) & \text{for equilibrium dissociation} \\ 0 & \text{for kinetic dissociation} \end{cases} \tag{2.27}$$

In Eq. 2.26 ϕ is the porosity, S_β is the saturation in phase β, ρ_β is the density of phase β, A,G,I,H mean aqueous, gas, ice, and hydrate phases, respectively, w, m, i, h, mean water, methane, water-soluble inhibitor (salt of organic substance), and hydrate components, respectively, and X^k_β is the mass fraction in phase β of component k. Equation 2.26 is formulated for the kinetic model, and if using the equilibrium model the component hydrate is not considered in the summation. Equation 2.27 is also formulated for the kinetic model and ρ_R is the density of the rock, C_R is the heat capacity of the dry rock, U_β is the specific internal energy of phase β and includes the contribution of all its components, $\Delta()$ means the change in the quantity in parenthesis over the current time step, and ΔU_H is

the specific enthalpy of hydrate dissociation/formation.

T+H v1.2 includes heat exchanges due to: (1) conduction, (2) advection/convection, (3) radiation, (4) hydrate reaction (dissociation or formation), (5) latent heat related to phase changes (ice melting, water fusion, water evaporation and vapor condensation), (6) gas dissolution, and (7) inhibitor dissolution. It considers the advective and molecular diffusive transport, using Fick's law, of water-soluble gases and inhibitors (such as salts and alcohols) in the aqueous and gas phases, the heat flux due to conduction (in the aqueous, gas, hydrate, and ice phases), advection (in the aqueous and gas phases) and radiative heat transfer, the effects of water soluble inhibitors on the hydrate behaviour, and allows consideration of the effects of changes on the intrinsic permeability and capillary pressure driven by changes in saturation of solid phases (ice and/or hydrate).

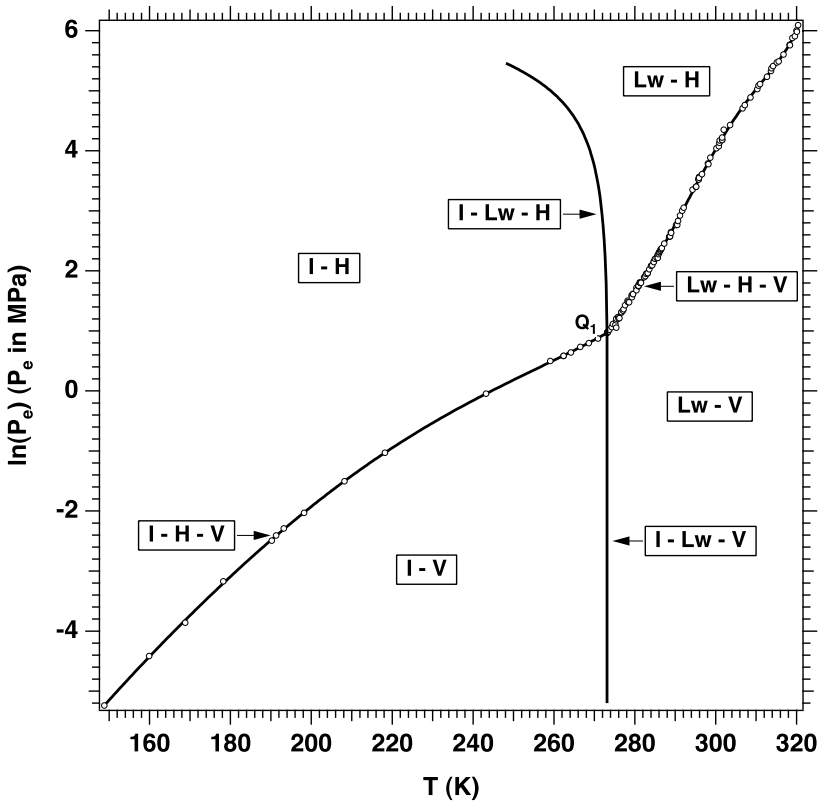

Figure 2.3: Pressure-temperature equilibrium relationship in the phase diagram of the water-CH_4-hydrate system in T+H (Fig. 2.5 in Moridis *et al.*, 2012). In the diagram, **Lw** is liquid water, **V** is vapor, **I** is ice and **H** is hydrate.

T+H v1.2 assumes the following simplifications:

1) The Darcy's law is valid in the simulated domain under the conditions of study. The

fluid flow inside the pores in my analysis is expected to be laminar, so Darcy's law applies (Charbeneau, 2006, section 2.2.5).

2) In the transport of dissolved gases and inhibitors, mechanical dispersion is small compared to advection, and so mechanical dispersion can be neglected. This is a common assumption to reduce the computational cost of the models. Besides, in my analysis, even the advection of dissolved methane is significantly smaller compared to methane flow as a free gas.

3) The only gas component in hydrate is CH_4. In the plume area West Svalbard, gas samples collected at the seabed from bubble plumes in the water column, show a hydrocarbon composition of 99.9% methane (less than 0.01% ethane; James *et al.*, 2011). Therefore, this is a valid assumption.

4) The compressibility and thermal expansivity of hydrate are the same of those of ice. The mechanical response of the system is not within the scope of my analysis, and so this assumption does not influence my results.

5) The movement of the geologic medium while freezing (soil heaving) is not described, and the effects on pressure (caused by the density difference between liquid and ice phases) are accommodated through a relatively high pore compressibility of the geologic medium. As in point 4 above, the mechanical response of the system is not within the scope of my analysis.

6) Dissolved salts do not precipitate as their concentration increases during water freezing. Consequently, the aqueous phase is not allowed to disappear when salts are present. Water does not freeze with the temperature models applied in my analysis, and hence this assumption is valid.

7) The concentration of the dissolved inhibitors is such that it does not affect the thermophysical properties of the aqueous phase. The only dissolved inhibitor used in my analysis is NaCl with an initial concentration of 3.5 wt% (marine water), that ranges from 3.3-3.6 wt% during model runs. These small concentrations of NaCl should not significantly affect the thermophysical properties of the aqueous phase.

8) The inhibitor is non-volatile in the temperature-pressure range of the study. Volatile inhibitors are not used in my models.

9) The pressure-dependent equations describing the hydrate properties and behaviour provide accurate solutions for a P<100 MPa, over nine times larger than the largest pressure at which natural gas hydrates are known to exist (about 11 MPa). The maximum water depth in my models is 800 m (∼8 MPa), hence far from the pressure limit of accurate pressure-dependent equations of hydrate properties and behaviour.

The thermodynamic state and the distribution of the mass components among the four possible phases are determined from the hydrate equation of state, and the system is defined uniquely by a set of primary variables (Tables 2.1 and 2.2) that completely specify the thermodynamic state of the system. The number of primary variables is initially set at the maximum expected in the course of the simulation and does not change during the simulation, but their thermodynamic quantities can change to allow emerging and disappearing phases and components.

The continuum equations (Eq. 2.25) are discretised in space by the integral finite difference method (IFD) (Edwards, 1972; Narasimhan & Witherspoon, 1976) and in time by first-order finite difference. The fluxes are treated as "fully implicit" (Peaceman, 1977). The resultant set of coupled, non-linear, algebraic equations are solved by Newton-Raphson iteration, approximating the Jacobian matrix by numerical differentiation, and using sparse direct matrix methods or iteratively by means of conditioned conjugate gradients (Moridis & Pruess, 1995, 1998; Pruess *et al.*, 1999).

Table 2.1: Primary variables in equilibrium hydrate simulations without inhibitor* (Table 3.1 in Moridis *et al.*, 2012).

Phase	State Identifier	Primary Variable 1	Primary Variable 2	Primary Variable 3
1-Phase: G	**Gas**	*P_gas*	*Y_m_G*	*T*
1-Phase: A	**Aqu**	*P*	*X_m_A*	*T*
2-Phase: A+G	**AqG**	*P_gas*	*S_aqu*	*T*
2-Phase I+G	**IcG**	*P_gas*	*S_ice*	*T*
2-Phase H+G	**GsH**	*P_gas*	*S_gas*	*T*
2-Phase: A+H	**AqH**	*P*	*S_aqu*	*T*
2-Phase: A+I	**AqI**	*P*	*S_aqu*	*X_m_A*
2-Phase: I+H	**IcH**	*P*	*S_ice*	*T*
3-Phase: A+H+G	**AGH**	*S_gas*	*S_aqu*	*T*
3-Phase: A+I+G	**AIG**	*P_gas*	*S_aqu*	*S_gas*
3-Phase: A+I+H	**AIH**	*P*	*S_aqu*	*S_ice*
3-Phase: I+H+G	**IGH**	*S_gas*	*S_ice*	*T*
Quadruple Point: I+H+A+G	**QuP**	*S_gas*	*S_aqu*	*S_ice*

P, pressure [Pa]; P_gas, gas pressure [Pa]; T, temperature [°C]; X_m_A, mass fraction of CH_4 dissolved in the aqueous phase [-]; Y_m_G, mass fraction of CH_4 dissolved in the gas phase [-]; S_aqu, liquid saturation [-]; S_gas, gas saturation [-]; S_ice, ice saturation [-]; X_i_A, mass fraction of inhibitor dissolved in the aqueous phase [-]. * For inhibitor: X_i_A becomes the 3^{rd} primary variable, and the 3^{rd} primary variable (as listed in this table) becomes the 4^{th} primary variable.

Table 2.2: Primary variables in kinetic hydrate simulations without inhibitor* (Table 3.2 in Moridis *et al.*, 2012).

Phase	State Identifier	Primary Variable 1	Primary Variable 2	Primary Variable 3	Primary Variable 4
1-Phase: G	**Gas**	*P_gas*	*Y_m_G*	*S_hyd*	*T*
1-Phase: A	**Aqu**	*P*	*X_m_A*	*S_hyd*	*T*
2-Phase: A+G	**AqG**	*P_gas*	*S_aqu*	*S_hyd*	*T*
2-Phase I+G	**IcG**	*P_gas*	*S_ice*	*S_hyd*	*T*
2-Phase H+G	**GsH**	*P_gas*	*S_gas*	*S_ice*	*T*
2-Phase: A+H	**AqH**	*P*	*S_aqu*	*X_m_A*	*T*
2-Phase: A+I	**AqI**	*P*	*S_aqu*	*X_m_A*	*T*
2-Phase: I+H	**IcH**	*P*	*S_ice*	*S_gas*	*T*
3-Phase: A+H+G	**AGH**	*P_gas*	*S_aqu*	*S_gas*	*T*
3-Phase: A+I+G	**AIG**	*P_gas*	*S_aqu*	*S_hyd*	*S_gas*
3-Phase: A+I+H	**AIH**	*P*	*S_aqu*	*S_ice*	*T*
3-Phase: I+H+G	**IGH**	*P_gas*	*S_gas*	*S_ice*	*T*
Quadruple Point: I+H+A+G	**QuP**	*P_gas*	*S_aqu*	*S_gas*	*S_ice*

P, pressure [Pa]; P_gas, gas pressure [Pa]; T, temperature [°C]; X_m_A, mass fraction of CH_4 dissolved in the aqueous phase [-]; Y_m_G, mass fraction of CH_4 dissolved in the gas phase [-]; S_aqu, liquid saturation [-]; S_gas, gas saturation [-]; S_hyd, hydrate saturation [-]; S_ice, ice saturation [-]; X_i_A, mass fraction of inhibitor dissolved in the aqueous phase [-]. * For inhibitor: X_i_A becomes the 4^{th} primary variable, and the 4^{th} primary variable (as listed in this table) becomes the 5^{th} primary variable.

Chapter 3

A Disequilibrium Compaction Model Constrained by Seismic Data and Application to overpressure generation in The Eastern Black Sea Basin

Locating and quantifying overpressures is essential to understand basin evolution and hydrocarbon migration in deep basins and thickly sedimented continental margins. Overpressures influence sediment cohesion and hence fault slip in seismically active areas or failure on steep slopes, and may drive catastrophic fluid expulsion. They also represent a significant drilling hazard. Here, we present a method to calculate the pore pressure due to disequilibrium compaction. Our method provides an estimate of the compaction factor, surface porosity and sedimentation rate of each layer in a sediment column using a decompaction model and the constraints imposed by seismic data and geological observations. For a range of surface porosities, an ad-hoc iterative equation determines the compaction factor that gives a calculated layer thickness that matches the observed thickness within a tolerance. The surface porosity and compaction factor are then used to obtain a density profile and a corresponding estimate of P-wave velocity (V_p). The selected parameters are those that give a good match with both the observed and calculated layer thicknesses and V_p profiles. We apply our method to the centre of the Eastern Black Sea Basin (EBSB); where overpressures have been linked to a low velocity zone (LVZ) at ∼5500-8500 m depth. These overpressures were generated by the relatively high sedimentation rate of ∼0.28 m ka^{-1} of the low permeability organic-rich Maikop formation at 33.9-20.5 Ma and an even

higher sedimentation rate of ∼0.85 m ka^{-1} at 13-11 Ma. We estimate a maximum pore pressure of ∼138 MPa at ∼8285 m depth, associated with a ratio of overpressure to vertical effective stress in hydrostatic conditions (λ^*) of ∼0.7. These values are lower than those presented in a previous study for the same area.

3.1 Introduction

Pore pressures exceeding hydrostatic pressure (overpressures) can play an important role in basin evolution and hydrocarbon migration in deep basins and thickly sedimented continental margins. Overpressures can significantly affect the fluid-flow pattern within a basin (Harrison & Summa, 1991) and knowledge of them can help provide a prior understanding of the consequences of seal failure, primary oil migration and reservoir porosity (Swarbrick & Hillis, 1999). They are one of the factors controlling the structural mechanics of fault surfaces (Hubbert & Rubey, 1959a,b) and deformation in accretionary wedges (Davis *et al.*, 1983). In subduction environments, the location of the décollement can be influenced by abnormally high pore pressures in discrete layers of underthrust sediments (Saffer, 2003; Tsuji *et al.*, 2008). Overpressures also influence submarine slope failures (e.g, Georgiopoulou *et al.*, 2010; Leynaud *et al.*, 2007). From a more practical point of view, locating and quantifying overpressures is critical in an exploration drilling campaign in order to drill wells safely and economically (Bekele *et al.*, 2001; Fertl *et al.*, 1994; Gordon & Flemings, 1998).

The Black Sea Basin (BSB) is a frontier basin for hydrocarbon exploration, which makes it a primary target for study (Robinson *et al.*, 1996). The Eastern Black Sea Basin (EBSB) is a deep rift basin with a sedimentary cover of up to 9 km in its centre, and with a low velocity zone (LVZ) at ∼5500-8500 m depth below sea level which has been previously linked to overpressures (Scott *et al.*, 2009). The presence of the LVZ was inferred from a two-dimensional tomographic analysis of wide-angle seismic data acquired using ocean bottom seismometers (Scott *et al.*, 2009). The LVZ is located within the Maikop formation, a thick and homogenous mud layer rich in organic material. Organic rich layers are soft, and so can generate a LVZ without the presence of overpressures. Here, however, we explore the contribution of overpressures to generating the LVZ.

Several different mechanisms for generating abnormally high pore pressures have been proposed, and they can be grouped into the following five main types (Neuzil, 1995):

- Lateral variations in hydraulic potential due to topographic relief (e.g, Bredehoeft *et al.*, 1983; Swarbrick & Osborne, 1998).

- Aquathermal pressuring (e.g, Chapman, 1980; Shi & Wang, 1986) due to the thermal expansion of water driven by an increase in temperature.
- Chemical reactions releasing fluids including hydrocarbon generation (e.g, Chi *et al.*, 2010; Hansom & Lee, 2005), smectite dehydration to illite (e.g, Bruce, 1984; Saffer & McKiernan, 2009) gypsum dehydration to anhydrite (Heard & Rubey, 1966) and quartz cementation (Osborne & Swarbrick, 1999).
- Disequilibrium compaction (e.g, Bethke, 1985; Harrison & Summa, 1991; Hubbert & Rubey, 1959a,b).
- Tectonic compression (e.g, Luo *et al.*, 2007; McPherson & Garven, 1999).

Other minor mechanisms have been proposed such as water derived from magmatic intrusions (Platt, 1962) and osmotic membrane phenomena (Hanshaw & Zen, 1965; Marine & Fritz, 1981).

This paper deals only with the disequilibrium compaction mechanism. This mechanism is applicable when fine-grained sediments are unable to compact to their equilibrium porosity by expelling fluids, and consequently the fluids support part of the sediment load. The degree of overpressure is controlled by the balance between the creation of pore pressure by sediment loading and its dissipation controlled by the permeability. Because permeability generally decreases with depth, due to compaction, the generation of abnormally high pore pressures will be more significant with increasing depth. This mechanism is thought to be the dominant source of abnormally high pore pressures in the Gulf of Mexico Basin (e.g, Berhmann *et al.*, 2006), in the South Caspian Basin (e.g, Lee *et al.*, 1999) and in the North Sea (e.g, Gutierrez & Wangen, 2005).

Here we present a method to calculate pore pressures and determine the sedimentation rate, surface porosity and compaction factor, for each sediment layer of a sediment column. We use (1) a 1D large-strain disequilibrium compaction numerical model, (2) a decompaction model (Sclater & Christie, 1980), (3) an ad-hoc iterative equation, (4) a relationship between P-wave velocity and density, and (5) the constraints imposed by geological and seismic data. Overpressures can also be estimated from remote geophysical observations such as P and S seismic velocities. Two velocity-based methods have been used here, the Westbrook (1991) approach and the Eaton method (Eaton, 1969, 1975). The latter method has been previously applied in locations such as the South Caspian Basin (Lee *et al.*, 1999) and the Gulf of Mexico Basin (e.g, den Boer *et al.*, 2006; Ebrom *et al.*, 2003; Kao, 2010).

The goal of this paper is to present a new approach to estimating overpressure due to disequilibrium compaction that satisfies the seismic and geological observations and to

demonstrate that the LVZ in the EBSB may be attributed to overpressures generated by disequilibrium compaction.

3.2 Overpressure Calculation: The EBSB

3.2.1 Geological Setting

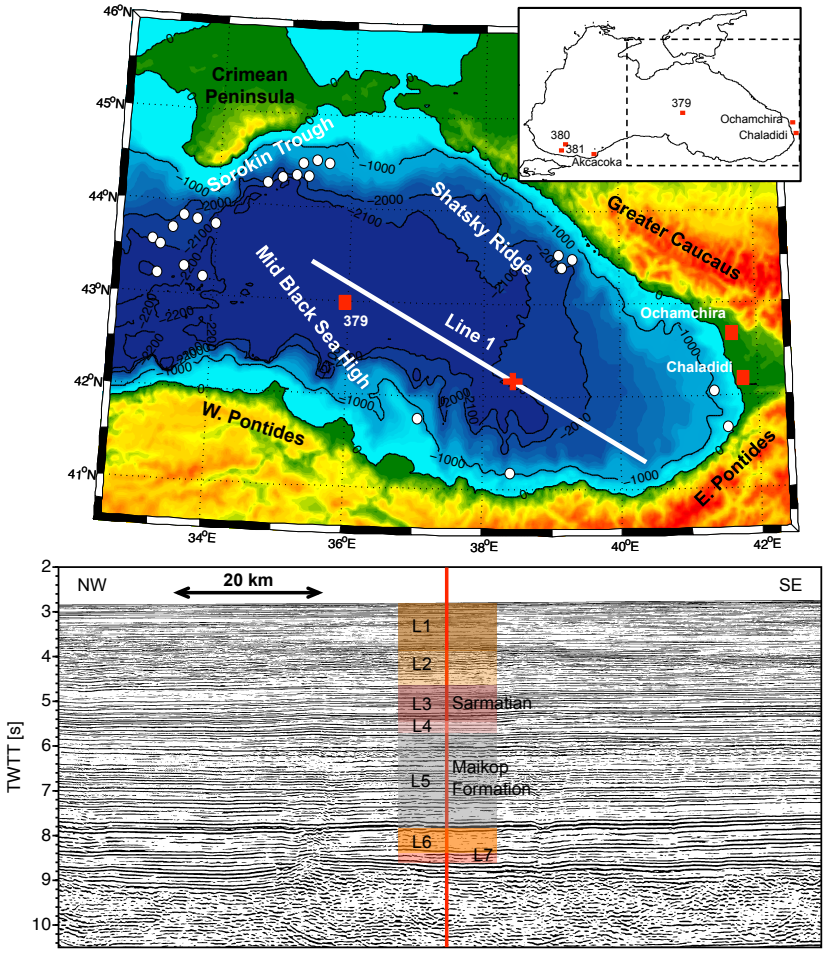

Figure 3.1: Top figure, map of the eastern Black Sea showing the location of line 1 wide-angle seismic profile with bathymetry and elevation taken from the National Oceanic and Atmospheric Administration (NOAA). White circles indicate known locations of mud volcanoes taken from Ivanov *et al.* (1996), Krastel *et al.* (2003) and Kruglyakova *et al.* (2004). Red squares indicate the location of industry and Deep Sea Drilling Project (DSDP) boreholes. Red cross indicates location used for analysis. The inset in the upper right hand corner gives the location of the industry and DSDP boreholes with respect to the entire Black Sea. Bottom figure, section of multichannel seismic data near-coincident to line 1 wide-angle seismic data showing that the modelled layers (Scott *et al.*, 2009; Shillington *et al.*, 2008) are flat in a section around the location used for analysis (red line).

The BSB is a large semi-isolated marine basin located within the Alpine orogenic belt, represented by the Balkanides-Pontides to the south and southwest, the Caucasus in the northeast and the Crimean range in the north (Fig. 3.1). It is linked to the Mediterranean Sea by the Bosporus Strait, the Sea of Marmara and the Dardanelle Strait. Its restricted water exchange with the ocean and freshwater inputs from the Dnieper and Danube rivers results in a salinity below normal levels (Robinson *et al.*, 1995a).

The Black Sea is generally considered to have formed in a back-arc extensional context as a result of its spatial association with evidence of subduction in Turkey, and is linked with the closure of both the Paleo and Neo-Tethys Oceans (Okay *et al.*, 1994; Robinson *et al.*, 1995a; Zonenshain & Lepichon, 1986), but uncertainty remains regarding the time and style of rifting. Görür (1988) constrained the onset of opening as Aptian to Cenomanian. Although of primarily extensional origin, the region has experienced several episodes of extensional and compressional tectonics since the Permian (Robertson *et al.*, 2004; Yilmaz *et al.*, 1997). Currently, it experiences compressional deformation due to the northward movement of the Arabian plate and westward escape of the Anatolian block (McClusky *et al.*, 2000). Although at present the BSB has a single flat abyssal plain at 2200 m depth and is currently considered a single depositional centre (Meredith & Egan, 2002; Robinson *et al.*, 1996), it can be subdivided into the western and eastern Black Sea extensional basins, based on deep seismic reflection data (Zonenshain & Lepichon, 1986). These basins are separated by the Archangelsky and Andrusov Ridges, collectively called the Mid Black Sea High (MBSH), running through the centre of the Black Sea Basin from SW-NE (Fig. 3.1). The Western Black Sea Basin (WBSB) opened by the separation of the Western and Central Pontide continental strip from the Moesian Platform (Robinson *et al.*, 1995a) during the Middle and Upper Cretaceous (Görür, 1988). The EBSB opened in a NE-SW direction by the rotation of the Shatsky Ridge away from the MBSH (Robinson *et al.*, 1996) and although the timing of opening remains controversial, a recent study using a strain-rate inversion suggests that extension continued into the early Cenozoic (Shillington *et al.*, 2008).

The infill of the EBSB is largely composed of post-rift, Cenozoic sediments (Finetti *et al.*, 1988), with older pre-rift sediments identified on the shelf (Robinson *et al.*, 1995a). Drilling at the margins of the Black Sea and mapping of time-correlative units onshore indicates that the acoustic basement is represented by various lithologies, dominated by shallow-water carbonates and significant volcanic material (Robinson *et al.*, 1996). Time correlative formations exposed in the western and eastern Pontides indicate that Early Paleocene-Middle Eocene (65-45 Ma) sediments are dominantly siliciclastic turbidites, shallow and/or deep water mudstones, pelagic mudstones and marls often containing large amounts of volcanogenic sediments (Robinson *et al.*, 1995b; Yilmaz *et al.*, 1997). Formations exposed

in the Pontides in northern Turkey show that Middle Eocene-top Eocene sediments (45-33.9 Ma) are dominantly siliclastic turbidites (Yilmaz *et al.*, 1997) with some carbonate and terrigenous deposits (Zonenshain & Lepichon, 1986). The top Eocene-Early Miocene (33.9-20.5 Ma) unit, known as the Maikop formation, is the most significant hydrocarbon source rock in the Black and Caspian Sea regions, and is attributed to the deposition of muds rich in organic carbon linked to anoxic conditions (Robinson *et al.*, 1996). Samples offshore show very little sand within this formation and low seismic reflectivity suggests homogeneity in physical properties (Zonenshain & Lepichon, 1986). Early Miocene-Middle Miocene (20.5-13 Ma) sediments, sampled by exploration wells on the Crimean peninsula and offshore Romania, are mudstones (Meredith & Egan, 2002; Robinson *et al.*, 1995a). Turbiditic sediments were also identified within this interval using seismic reflection profiles. The Middle Miocene-Late Miocene (13-11Ma) unit, known as the Sarmatian, is thought to comprise terrigenous sediments (Nikishin *et al.*, 2003). Late Miocene-top Pliocene (11-1.8 Ma) sediments comprise sands and conglomerates mapped in north-eastern Turkey (Robinson *et al.*, 1995b) and chalks, siderites, clays and limestones observed by the Deep Sea Drilling Project (DSDP) in the basin centre (Hsü & Giovanoli, 1980; Ross, 1978). Gravity cores and drilling (Robinson *et al.*, 1996; Ross, 1978) indicate that the youngest sediments, top Pliocene-Present (1.8-0 Ma), comprise mostly clays but they also include marls and occasional turbidites (Hiscott & Aksu, 2002; Hsü & Giovanoli, 1980; Ross, 1978).

Mud volcanoes, the surface response of an overpressured layer (Dimitrov, 2002; Yassir, 2003), are found all along the continental shelf of the Black Sea (Kruglyakova *et al.*, 2004), with the greatest density to the south of the Crimean Peninsula within the Sorokin Trough (Dimitrov, 2002; Ivanov *et al.*, 1996) (Fig. 3.1). This location is experiencing compression, which squeezes the sediment laterally and generates overpressures in the low permeability sediments because the fluids cannot escape rapidly enough. These overpressures can create fractures that are used by the pressurised pore fluid to escape vertically (Dimitrov, 2002). The location of mud volcanoes is an indication of the distribution of compressional deformation. The sediments in the centre of the EBSB are relatively undeformed (Shillington *et al.*, 2008) suggesting that deformation due to the current compressional tectonic regime is affecting only the eastern edges of the basin and the Greater Caucasus (McClusky *et al.*, 2000; Rangin *et al.*, 2002).

3.2.2 Pore Pressure Estimation from P-wave Velocities

P-wave velocities in sedimentary rocks typically increase with burial due to the reduction in porosity and the increased grain contact. Most methods of pore pressure prediction from V_p assume that all changes in seismic velocity are a function of the vertical effective stress alone (as an approximation to the mean effective stress). The effective stress principle

(Terzaghi, 1943) states that any variation in porosity is due to a variation in the effective stress. The vertical effective stress σ' is given by

$$\sigma' = \sigma_L - P = \sigma_L - (P_h - u) \tag{3.1}$$

where σ_L is the vertical or lithostatic stress, P is the total pore pressure, P_h is the hydrostatic pressure and u is the overpressure.

Under hydrostatic conditions (zero overpressure), seismic velocity increases with effective stress. Therefore, any decrease in seismic velocity may be attributed to a decrease in effective stress, i.e. an increase of pore pressure above hydrostatic. This overpressure results in undercompacted sediments with porosity and intrinsic permeability values more appropriate to shallower depths.

We use velocities from Scott *et al.* (2009) and the two different approaches described by Scott *et al.* (2009): the Westbrook (1991) approach and the Eaton method (den Boer *et al.*, 2006; Eaton, 1969, 1975). Westbrook (1991) assumed that effective stress at depth z in a low velocity zone is equal to that at the shallower depth z' when the seismic velocity is the same but the pressure is hydrostatic (Eq. 3.2). We match the seismic velocity in the overpressured zone V_p^{obs} at depth z, with a normal seismic velocity in hydrostatic conditions V_p^h at depth z' within a tolerance of ± 0.01 km/s.

$$P(z) = \sigma_L(z) - \sigma_L(z') + P_h(z') \tag{3.2}$$

The Eaton method estimates pore pressure from the ratio between V_p^{obs} and V_p^h (Eq. 3.3)

$$P = \sigma_L - (\sigma_L - P_h)\left(\frac{V_p^{obs}}{V_p^h}\right)^E \tag{3.3}$$

where the Eaton factor E controls the sensitivity of the V_p to effective stress (den Boer *et al.*, 2006). The application of the Eaton method may result in poor estimates of pore pressure if pore pressures are not due to disequilibrium compaction alone (Sarker & Batzle, 2008). E should be obtained ideally by calibration using measurements of pore pressures in boreholes in the study area. In the Gulf of Mexico, where the equation was derived, Ebrom *et al.* (2003) calibrated a value of E equal to 3, den Boer *et al.* (2006) assumed a value between 3 and 5, and Kao (2010) used a value of 2.6. An E value of 3 is widely applicable in the Gulf of Mexico and can be extended to other Tertiary basins (Eaton & Eaton, 1997). Scott *et al.* (2009) estimated an E value of 8 from an industry borehole located near the east coast of the basin and applied this value in the centre of the basin. However, a value as large as 8 indicates insensitivity of the velocities to vertical effective

stress (Sarker & Batzle, 2008), and in this case, another method to estimate overpressures should be applied. In the absence of measurements of V_p^h in the study area, it must be estimated. Following the case 1 assumption of Scott *et al.* (2009), we estimate V_p^h by interpolating the velocity between the top of the low velocity zone, and the base of sediments on the assumption that at these depths, pressures are hydrostatic. This method yields a minimum estimate of the overpressures (Scott *et al.*, 2009). If no density data are available, the Westbrook relationship and the Eaton method both need a function that relates V_p to density to calculate σ_L. Here we use the Hamilton's (1978) relationship (Eq. 3.4) for a silt, clay and turbidite lithology. Using the Gardner *et al.*'s (1974) relationship ($\rho = aV_p^b$) for comparison, with values of the empirical parameters a and b of 1.8 and 0.25, respectively, we obtain a near-coincident density profile except in the first ∼600 m. A value of 1.8 is slightly higher than the value of 1.74 determined by Gardner *et al.* (1974) for sedimentary rocks.

$$\begin{aligned} \rho &= 1.135V_p - 0.190 : \qquad (1.5\text{-}2 \text{ km s}^{-1}) \\ \rho &= 0.917 - 0.714V_p - 0.08V_p^2 : \qquad (>2 \text{ km s}^{-1}) \end{aligned} \tag{3.4}$$

3.2.3 Method

Figure 3.2 illustrates the method's workflow. Our method starts with a set of input parameters. Using these input parameters and a decompaction model we estimate the sedimentation rate of each modelled layer. From the estimated sedimentation rates and the original input parameters, we apply our 1D disequilibrium compaction model. Next, we compare the observed and calculated layer thicknesses. If they are similar within a tolerance, we change the input surface porosities and apply, for each layer in turn, the process above again. If they are not, we apply an ad-hoc iterative equation to obtain the input compaction factors that give calculated layer thicknesses within the tolerance. At this stage, we have a set of permissible surface porosities and compaction factors in terms of layer thicknesses, but these may not represent the present-day V_p structure. We further constrain our permissible parameter space by comparing the observed and calculated V_p. For the permissible values, we apply again both the decompaction model and the 1D disequilibrium compaction model, and we introduce the density output from the latter model into a V_p-density relationship to calculate the V_p. Finally, we apply a least-squares approach to select the best-fitting model.

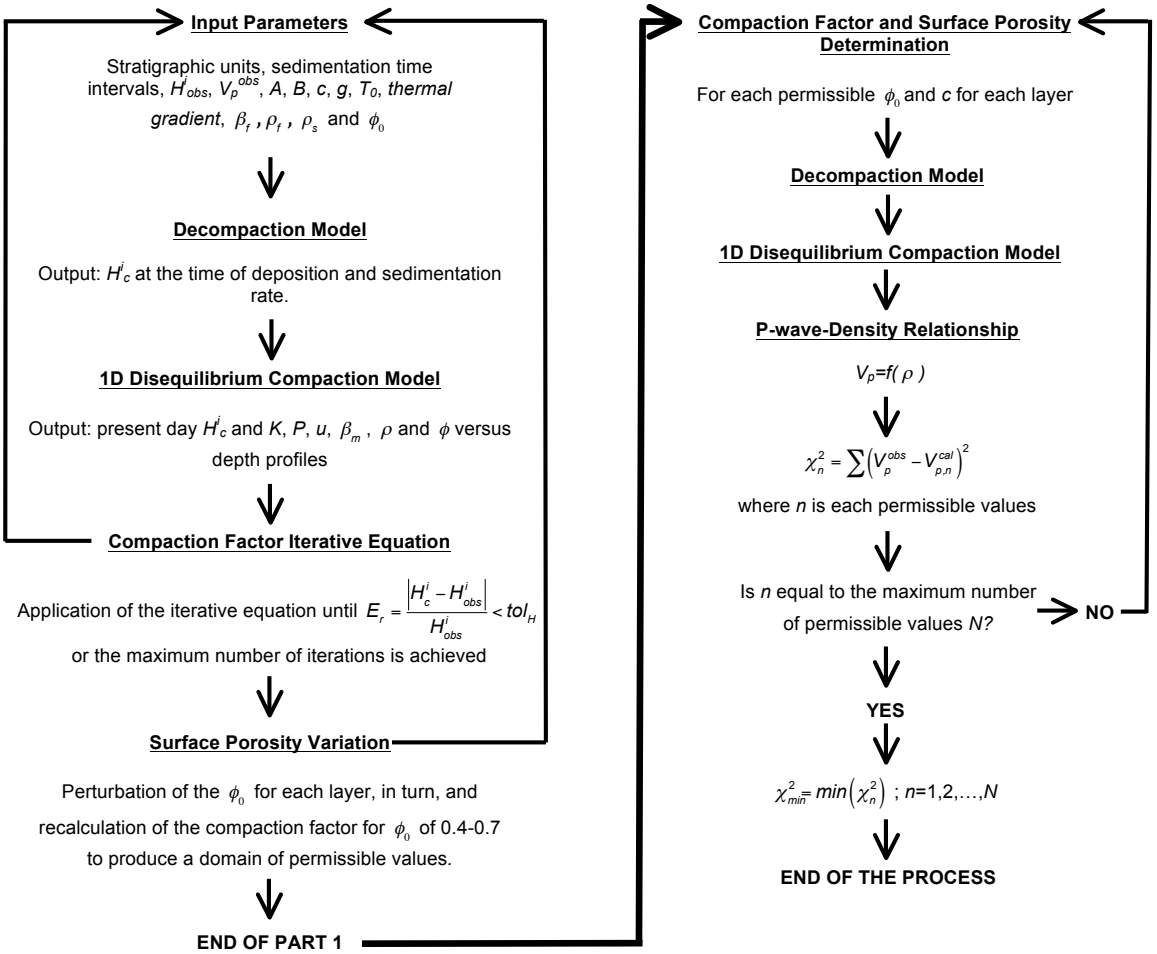

Figure 3.2: Workflow. See text for description of individual parameters.

1D Disequilibrium Compaction Model

Following Gordon & Flemings (1998), the evolution of the total pore pressure P through time t within a sediment column is governed by the equation

$$\frac{DP}{Dt} = \underbrace{(1-\phi)\frac{D}{D\chi}\left[\frac{K(1-\phi)}{S_t\rho_f g}\frac{Du}{D\chi}\right]}_{\text{Diffusive Term}} + \underbrace{\left[\frac{\phi}{S_t(1-\phi)}\beta_m\right]\frac{D\sigma_L}{Dt}}_{\text{Sediment Loading Term}} \tag{3.5}$$

where the storage term S_t is defined by

$$S_t = \left(\frac{\phi}{1-\phi}\beta_m + \phi\beta_f\right) \tag{3.6}$$

Here K is the permeability, g is the gravitational acceleration, χ is the depth from the sediment surface to a grain in a fully compacted coordinate system (Gordon & Flemings, 1998; Gutierrez & Wangen, 2005), β_f is the water compressibility, β_m is the sediment compressibility, ρ_f is the water density, and ϕ is the porosity. The equation used here is formulated in a Lagrangian fully compacted coordinate system χ, where the reference frame is fixed on the solid grains, and measures a sediment column where all the pores have been removed. Every new sediment layer is also added in the fully compacted coordinate system and this is obtained from the real coordinate system z by

$$z = \int_0^{\chi} \frac{1}{1-\phi} d\chi \tag{3.7}$$

$$dz = \frac{D\chi}{1-\phi} \tag{3.8}$$

The boundary conditions of the model are set to zero overpressure (u=0) at the top of the sediment column and zero flow ($Du/D\chi$=0) at the bottom. The top boundary condition is a moving boundary condition that is imposed at the top of each newly deposited layer. The initial condition is set to $u(t$=0)=0. We use an implicit finite difference scheme with backward differences to approximate the time derivative and centered differences in space.

Our model differs from that of Gordon & Flemings (1998) in that we consider the sediment loading as the only source term and we use a different treatment of the sediment compressibility and the fluid viscosity. These differences allow us to incorporate more accurate estimates of the evolution of the matrix compressibility and fluid viscosity with depth.

A 1D disequilibrium compaction model is only applicable in basins with flat and laterally extensive sedimentary layers without compressional tectonic forces, and hence where the horizontal strains are minor in comparison to the vertical strains. In these conditions, the horizontal fluid flow will be small in comparison to the vertical flow. Also, in a 1D disequilibrium compaction model with an impermeable bottom boundary condition the overpressure always remains constant or increases with depth. Therefore, our model cannot generate a sudden decrease in overpressure.

Material Properties

Porosity

The evolution of porosity depends on many physical and chemical factors, but here only mechanical compaction is considered. Athy (1930) proposed an empirical equation where porosity declines exponentially with depth, whereas Palciauskas & Domenico (1989) proposed a linear compaction model. Here, we use Athy's law in terms of vertical effective

stress (e.g, Gordon & Flemings, 1998).

The porosity is given by

$$\phi = \phi_0 \mathrm{e}^{-\beta\sigma'} \tag{3.9}$$

where ϕ_0 is the initial porosity or the porosity at surface conditions (zero effective stress) and the empirical parameter β, or effective stress compaction factor, can be obtained from datasets where σ' is known. We assume that β is equal to the bulk compressibility of the saturated sediments β_m (Hart *et al.*, 1995), which varies with composition, pressure and temperature. According to Domenico & Mifflin (1965) can vary from 2x10^{-6} Pa^{-1} for plastic clay to 6.9x10^{-8} Pa^{-1} for medium hard clay. For sands, it can vary from 10^{-7} Pa^{-1} for loose sand to 1.3x10^{-8} Pa^{-1} for a dense sand.

Equation 3.9 can also be expressed in terms of depth. In this case, a different compaction factor c (Sclater & Christie, 1980) is used. This is related to the effective stress compaction factor by

$$c = (\rho - \rho_f)\, g\beta \tag{3.10}$$

where the saturated density of the sediment ρ is given by

$$\rho = \rho_s\,(1 - \phi) + \rho_f \phi \tag{3.11}$$

where ρ_s is the solid grains density.

Combining Eqs. 3.9 and 3.10 we obtain

$$\phi = \phi_0 \exp\left[\frac{c}{(\rho - \rho_f)\, g}\sigma'\right] \tag{3.12}$$

Equation 3.12 should be solved iteratively because density is itself a function of porosity (Eq. 3.11). Since we use time intervals small enough to avoid large changes in porosity over the time step, the density at each time step is calculated using the porosity from the previous time step.

Permeability

In a saturated medium the permeability K (Eq. 3.13) is a unique function of the intrinsic permeability k_i, fluid density ρ_f and viscosity μ. During burial, permeability changes are caused by changes in intrinsic permeability and viscosity. Intrinsic permeability tends to decrease with depth due to the reduction in porosity. Viscosity also decreases with increasing temperature and pressure. In normal geologic systems, the decrease in intrinsic permeability is more significant than the decrease in viscosity and therefore, permeability generally decreases with depth (Sharp, 1983). Fluid viscosity depends both on pressure

and temperature, but for water it is much more dependent on temperature than pressure (Meyer *et al.*, 1963).

$$K = \frac{k_i \rho_f g}{\mu} \tag{3.13}$$

Intrinsic permeability is a solely geometric parameter that measures the degree of connectivity of the pores in the sediment. Although two sediment types with the same porosity and composition may have different intrinsic permeabilities, here we assume that intrinsic permeability depends only on porosity (Gordon & Flemings, 1998) and is given by

$$k_i = G\mathrm{e}^{(A+B\phi)} \tag{3.14}$$

where A and B are lithology-dependent empirical parameters and G=9.869233x10^{-16} m^2. Ideally, A and B would be estimated from laboratory data. However, the measurement of small permeabilities in a consolidation test is still difficult and even if they are measurable, they may not represent in situ values (Neuzil, 1994).

We estimate the bulk intrinsic permeability of the sediment $k_{sediment}$ using

$$\log\left(k_{sediment}\right) = \sum_{j=1}^{N} f_j \log\left(k_i^j\right) \tag{3.15}$$

where f_j is the fraction of each lithology in the sediment layer, k_i^j is the intrinsic permeability of each individual lithology, and N is the number of different lithologies in the sediment layer.

Parameter Determination: Compaction Factor and Surface Porosity

Sedimentation Rate Calculation

The sedimentation rate for each layer is calculated using a two-stage iterative algorithm (Fig. 3.2):

1) Application of a decompaction model (Sclater & Christie, 1980) to a layered sediment column, with present-day layer thicknesses and compositions determined from seismic data and other observational constraints. Our model differs from that of Sclater & Christie (1980) only in the definition of the exponential compaction law. The decompaction model is given by

$$z'_2 - z'_1 = z_2 - z_1 - \frac{\phi_0}{\beta}\left[\exp\left(-\beta\sigma'_{z_1}\right) - \exp\left(-\beta\sigma'_{z_2}\right)\right] + \frac{\phi_0}{\beta}\left[\exp\left(-\beta\sigma'_{z'_1}\right) - \exp\left(-\beta\sigma'_{z'_2}\right)\right] \tag{3.16}$$

where z_1 and z_2 are the present top and base depths of a layer and z'_1 and z'_2 are the top and base depths at the moment of deposition assuming instantaneous deposition. Equation 3.16 keeps the mass of the solid constant, and considers the change in volume and so in thickness due to the change in the volume of water assuming hydrostatic conditions. It represents the removal of the sediment above each layer, allowing the layer to decompact. This equation is solved using the Trust-Region Method (Powell, 1970). The decompacted layer thicknesses are then used to estimate the sedimentation rates, assuming that the ages range for each layer is known.

2) Application of an iterative process that recalculates the compaction factors until the calculated compacted thickness of each layer matches the observed thickness within a tolerance. The relative error in the calculated thickness is given by

$$E_r = \frac{\left|H_c^i - H_{obs}^i\right|}{H_{obs}^i} \tag{3.17}$$

where H is the thickness, the subscripts c and obs mean calculated and observed respectively, and the superscript i is the layer index.

The iterative equation is obtained using the following steps:

a) Imposing present-day calculated layer thicknesses equal to those observed (Eq. 3.18). If we assume that the imposed surface porosity is correct, Eq. 3.18 reduces to Eq. 3.19.

$$\frac{H_{obs}^i\left(1-\phi_{obs}^i\right)}{\left(1-\phi_{0obs}^i\right)} = \frac{H_c^i\left(1-\phi_c^i\right)}{\left(1-\phi_{0c}^i\right)} \tag{3.18}$$

$$H_{obs}^i\left(1-\phi_{obs}^i\right) = H_c^i\left(1-\phi_c^i\right) \tag{3.19}$$

b) If an exponential porosity-depth curve is introduced in Eq. 3.19 and we impose that the next calculated porosity is the present-day porosity, this results in the following iterative equation

$$c^i_{j+1} = \frac{\ln\left(\phi^i_0\right) - \ln\left(1-\alpha+\alpha\phi^i_0 \exp\left[-c^i_j z^i_{(1/2)j}\right]\right)}{z^i_{(1/2)obs}}$$
$$i = 1, 2 \ldots, N_{layers} \tag{3.20}$$
$$j = 1, 2 \ldots, N_{iterations}$$

where the subscript j is the iterative index, $N_{iterations}$ and N_{layers} are the number of iterations and layers respectively, $z_{(1/2)}$ and $z_{(1/2)obs}$ are the calculated and observed present middle point depth respectively, and α is the ratio between the calculated and observed present-day layer thickness. The logarithm of a negative number is not defined. Therefore, it is imposed that if $\left(1-\alpha+\alpha\phi^i_0 \exp\left[-c^i_j z^i_{(1/2)j}\right]\right) < 0$, the iterative equation is not solved in this iteration and $c^i_{j+1} = c^i_j$. To control the rate of change of the compaction factor the following equation is applied

$$c^{i\omega}_{j+1} = c^i_j + \omega\left(c^i_{j+1} - c^i_j\right) \tag{3.21}$$

where ω is a weighting parameter with values between 0 and 1.

We applied the iterative equation with two different algorithms: (1) with all compaction factors updated per iteration, and (2) with one compaction factor updated per iteration. Although for realistic parameter values both algorithms converge to very similar solutions, the algorithm that varies one compaction factor per iteration is slower because a greater number of evaluations of the 1D disequilibrium compaction model are needed to achieve convergence. To estimate the influence of the surface porosity in the calculation of the layer thicknesses, we apply a perturbation of the surface porosity for each layer, in turn, and recalculate the compaction factors for surface porosities of 0.4-0.7.

The 1D disequilibrium compaction model allows layers to compact due to their own weight, but the applied decompaction model does not, so that the top layer present-day thickness and thickness at the time of deposition are equal. Therefore, the iterative equation finds an unrealistically small compaction factor. A solution to this problem would be to divide the top layer into thinner sublayers; this approach has not been developed to limit the computational cost of the model. In the EBSB there is no indication of overpressures due to disequilibrium compaction at the top of the sediment column and our focus is on the Maikop formation, so the resulting errors are not significant.

P-wave Velocity Constraint

P-wave velocities obtained from seismic data provide a further constraint on the surface

porosities and compaction factors that give a calculated layer thickness within a tolerance. As V_p is not a direct output from our 1D disequilibrium compaction model, and we try to compare the calculated and observed V_p, we estimate the V_p profile corresponding to each model obtained within the thickness tolerance, from the calculated density (Eq. 3.11) using, as above, the Hamilton's (1978) relationship (Eq. 3.4). We then identify a unique surface porosity and compaction factor, for each layer, by minimising the least-squares misfit between the observed and predicted velocities.

Modelling Parameters

Our model comprises seven stratigraphic units (Shillington *et al.*, 2008) based on three DSDP sites in the centre of the basin, industry wells at the margins of the Black Sea (Akcakoca, Chaladidi and Ochamchira; Fig. 3.1) onshore mapping, and the V_p structure obtained from wide-angle seismic data (Scott *et al.*, 2009). The lithology, sedimentation time interval and present-day thickness for the stratigraphic units used in the model are shown in Table 3.1.

Table 3.1: Lithology, time interval and present-day thickness of stratigraphic layers.

Strat. Layers	Lithology[(1)]	Time Interval[(1)] [Ma]	Basin Centre Present Day Thickness [m] [(1,2)]
1	90% sh + 10% sd	0 to 1.8 (Present-Top Pliocene)	665
2	45% sh + 45% ch + 10% sd	1.8 to 11 (Top Pliocene-Late Miocene)	1100
3-Sarmatian	80% sh + 20% sd	11 to 13 (Late Miocene-Middle Miocene)	1300
4	80% sh + 20% sd	13 to 20.5 (Middle Miocene-Early Miocene)	300
5-Maikop	90% sh + 10% sd	20.5 to 33.9 (Early Miocene-Top Eocene)	3000
6	70% sh + 30% sd	33.9 to 45 (Top Eocene-Middle Eocene)	900
7	70% sh + 30% sd	45 to 65 (Middle Eocene-Early Paleocene)	400

(1) Shillington *et al.* (2008) and (2) Scott *et al.* (2009)
sd, sandstone; sh, shale; ch, chalk.

Table 3.2: Fluid and solid grains properties and other modelling parameters.

Property	Value	Units	References
g	9.8	m/s^2	Robinson *et al.*, 1995a
Seafloor depth	2135	m	Scott *et al.*, 2009
T_0	9	°C	Minshull & Keddie, 2010
Thermal gradient	26	°C /km	Minshull & Keddie, 2010
β_f	$5*10^{-10}$	Pa^{-1}	de Marsily, 1986
ρ_f	1030	Kg/m^3	Cloetingh *et al.*, 2003
ρ_s	2700	Kg/m^3	Scott *et al.*, 2009

Table 3.3: Intrinsic permeability parameters of different lithologies making up the stratigraphic layers.

Lithology	Strat. Layers	A	B	References
Sandstone	1,2,5,6,7	-0.4	20	Gordon & Flemings, 1998
	3,6	-0.4	45	this study
Shale	1,2,5,6,7	-22.3	36	Gordon & Flemings, 1998
	3,6	-22.3	45	this study
Chalk	2	-22.3	36	this study

Table 3.4: Sedimentation time interval, calculated compacted and decompacted thickness in the centre of de EBSB, calculated sedimentation rate, porosity and compaction factor, and absolute and relative errors in thickness calculated with the 1D disequilibrium compaction model of stratigraphic layers.

		Basin Centre					Error	
		Present Day	Time of Deposition				1D DCM	
Strat. Layers	Time Interval (1) [Ma]	Thickness [m]	Thickness [m]	Sed. Rate [m/ka]	ϕ_0	$c*10^{-3}$ [m^{-1}]	[m]	||[%]||
1	0 to 1.8	637	665	0.37	0.6	0.1	-28	4.2
2	1.8 to 11	1097	1469	0.16	0.45	0.65	3	0.3
3	11 to 13	1256	1709	0.85	0.4	0.45	-44	3.4
4	13 to 20.5	309	518	0.07	0.5	0.5	9	3.0
5	20.5 to 33.9	2819	3694	0.28	0.4	0.4	-181	6.0
6	33.9 to 45	965	1294	0.12	0.4	0.4	65	7.2
7	45 to 65	438	615	0.03	0.4	0.4	38	9.5

(1) Shillington *et al.* (2008) and (2) Scott *et al.* (2009)
DCM, Disequilibrium Compaction Model

Fluid and solid properties and other modelling constants are given in Table 3.2, while Table 3.3 gives the intrinsic permeability empirical parameters for the different lithologies. Table 3.4 gives the sedimentation time intervals, the present-day thicknesses, and our estimated decompacted thicknesses, sedimentation rates, surface porosities, compaction factors and absolute and relative thickness errors. We used a surface porosity of 0.55 and a compaction factor of 0.4 km^{-1} as initial values for the iterative process described above.

We assume a 10% uncertainty in present-day layer thicknesses, resulting from uncertainties in depth conversion of seismic data. For layer 5, where the low velocity zone was identified (Scott *et al.*, 2009), we derive a thickness 181 m (6.0%) less than the thickness inferred from seismic data (Table 3.4). Scott *et al.* (2009) showed that a perturbation of -200 m in the thickness of the low velocity zone in seismic line 3 results in a travel time perturbation of ∼100 ms (Scott *et al.*, 2009), which is within the picking uncertainty for the corresponding seismic phases.

Limitations of the Method

The three main limitations of our method for the EBSB case study are:

- Our 1D disequilibrium compaction model is only applicable to the centre of the EBSB where the sediments are relatively undeformed (Shillington *et al.*, 2008) and hence the effects of compressional tectonics are minor (Scott *et al.*, 2009).
- The rapid increase in the V_p, and hence decrease in overpressure, at ~6350 m depth (Fig. 3.3), cannot be reproduced with our 1D disequilibrium compaction model for the imposed boundary conditions. This increase in V_p may be attributed either to horizontal flow due to high horizontal permeability below the Maikop formation or to downwards-vertical flow. The latter case would imply that our assumed bottom boundary condition is incorrect.
- The decompaction model does not allow the decompaction of a layer under its own weight but the 1D disequilibrium compaction model does. Therefore, the iterative equation (Eq. 3.21) finds an unrealistically small compaction factor for the top layer (Table 3.4).

3.3 Results

We have estimated the pore pressure using two different approaches: (1) based on the direct application of V_p methods and (2) using our method and based on a 1D disequilibrium compaction model. The results of the first approach are shown in Fig. 3.3, where λ^* is given by

$$\lambda^* = \frac{P - P_h}{\sigma'_h} \tag{3.22}$$

where σ'_h is the vertical effective stress in hydrostatic conditions.

Our method finds the parameters that match the layer thicknesses within 10% and give similar observed and calculated V_p profiles, but does not guarantee that the global best fit has been found. It may be that a small perturbation in the compaction factor and surface porosity gives a better match. To test for this possibility, a sensitivity analysis was carried out in layer 5, where the low velocity zone is mostly located (Fig. 3.3), to study how small perturbations in the compaction factor and in the surface porosity affect the layer thicknesses (Fig. 3.4), and the V_p and pore pressure profiles. In Fig. 3.4, the shape of the contours shows that the surface porosity influences the layer thickness variation more than the compaction factor for a proportionally equal increment in these parameters. From this analysis, we mapped out the range of acceptable models (Fig. 3.5) that result in a layer thickness misfit of less than 10% for all layers.

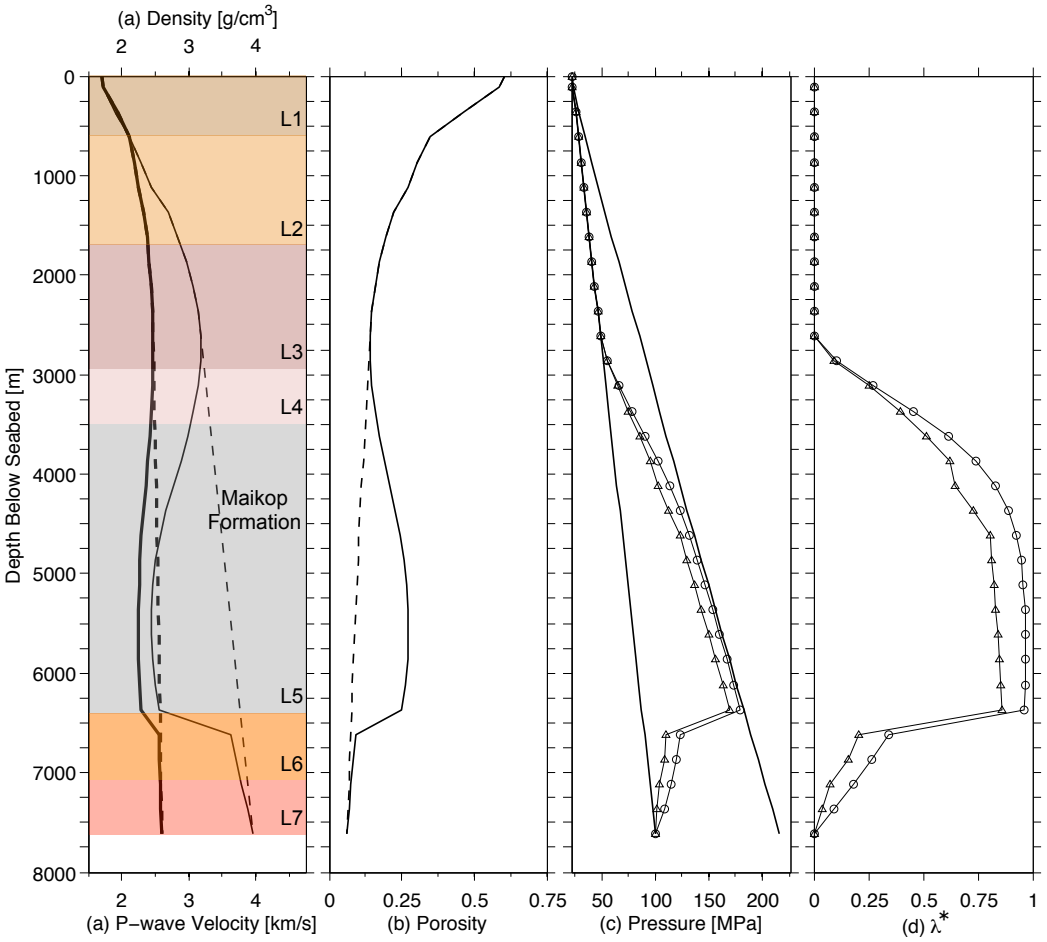

Figure 3.3: Parameter variation with depth at case study site (Fig. 3.1). Plot (a) shows observed P-wave velocity (bold line) and estimated density using the Hamilton's (1978) relationship (Eq. 3.4) while (b) shows porosity calculated from density (Eq. 3.11). Solid lines represent observed conditions, and dashed lines hydrostatic conditions. Plots (c) and (d) show the pore pressure and (Eq. 3.22), respectively, calculated with the Westbrook relationship, triangles, and the Eaton's method with E=8, circles (Scott *et al.*, 2009).

Although models with surface porosities below 0.4 have been considered, they may be rejected because they are unlikely in marine sediments. Models with compaction factors below 0.2 km^{-1} have not been considered since they are unlikely in marine shaley sediments.

The best fit to V_p is obtained with model parameters c = 0.45 km^{-1} and ϕ_0 = 0.425, and the model parameters found with our method are c = 0.4 km^{-1} and ϕ_0= 0.4 for layer 5 (Fig. 3.6). The limitations explained in the previous section of using a decompaction model and a one-dimensional model, can be seen in the top and bottom part of the V_p profile. As the compaction factor in the overpressured layer is reduced, the change in overpressure above and below ∼3300 m depth (where significant overpressures start to be developed)

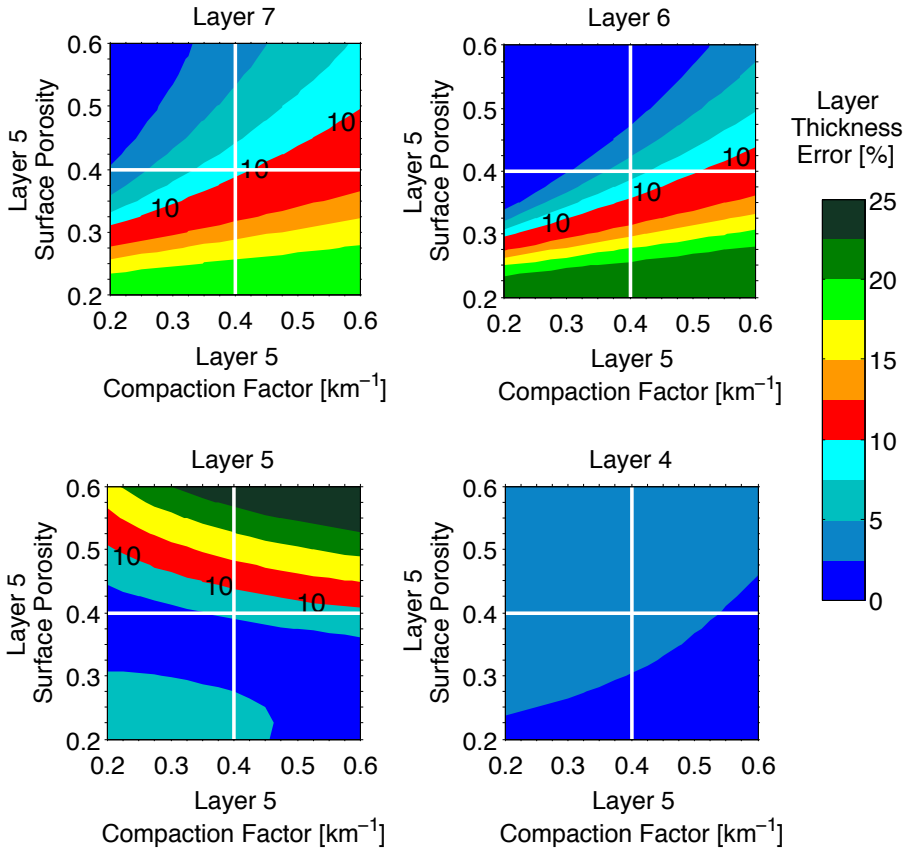

Figure 3.4: Sensitivity of compacted layer thickness error to the best fitting parameters, surface porosity and compaction factor of Layer 5, where the LVZ and the overpressure is located, for layers 7, 6, 5, and 4. The centre of the white cross indicates the best fitting model parameters for layer 5. The contour plots for layers 3, 2, and 1 are not shown because the perturbation has an insignificant effect on them.

is similar but with opposite signs (Fig. 3.7). A reduction in the compaction factor makes the sediment less compressible and hence results in smaller reductions in porosity (Eq. 3.9). Smaller changes in porosity require higher permeabilities (Eqs. 3.13 and 3.14) of the layer of interest and so larger upward flow. This increase in the upward flow provokes a decrease in the overpressure in the layer and the layers below. In contrast, an increase in upward flow results in increased overpressure in the layers above the layer of interest. Both combinations of layer 5 parameters $c = 0.45$ km^{-1} and $\phi_0 = 0.425$, and $c = 0.4$ km^{-1} and $\phi_0 = 0.4$ yield similar results, and so only the results for the latter are discussed below.

We infer the presence of overpressure within layers 3-7 of the model, from ∼2500 m depth to the bottom boundary of the sediment column (Fig. 3.8b). In layer 5, at ∼3300-6150 m depth, the overpressure is linked to a V_p decrease of 0.75-1.00 km s^{-1}, a density decrease of ∼250 kg m^{-3}, a porosity increase of ∼0.15, a sediment compressibility increase

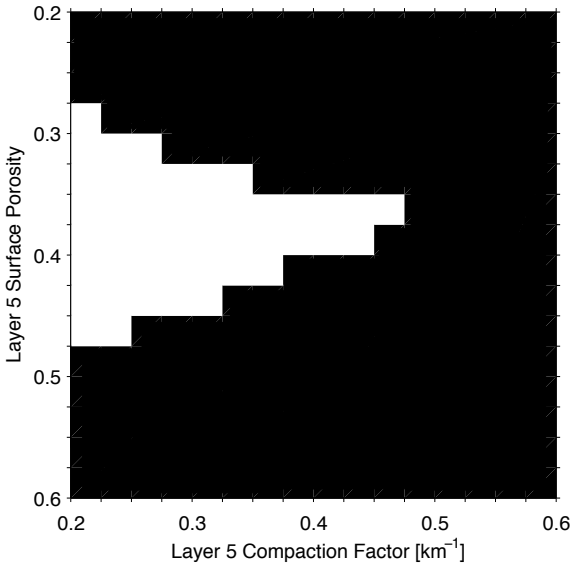

Figure 3.5: Illustration of the uncertainty in the surface porosity and compaction factor in layer 5. White region contains surface porosities and compaction factors that give a thickness error below 10% in all layers. Black region contains models that do not. Compaction factors lower than 0.2 km^{-1} are not considered because they are rarely so low for clay-rich sediments.

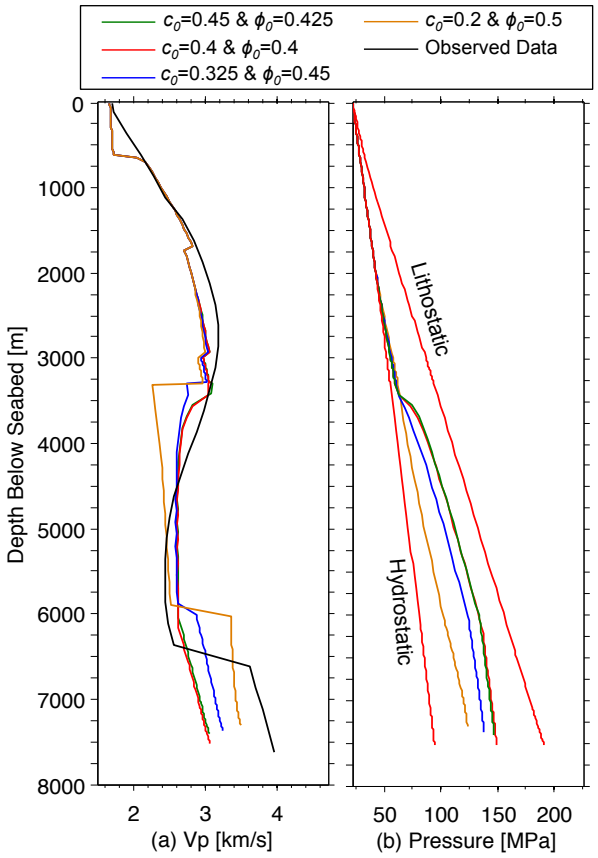

Figure 3.6: (a) Observed P-wave velocity profile (Scott *et al.*, 2009) and calculated profiles for four different permissible values of compaction factors and surface porosities. (b) Calculated pore pressure for the same four values.

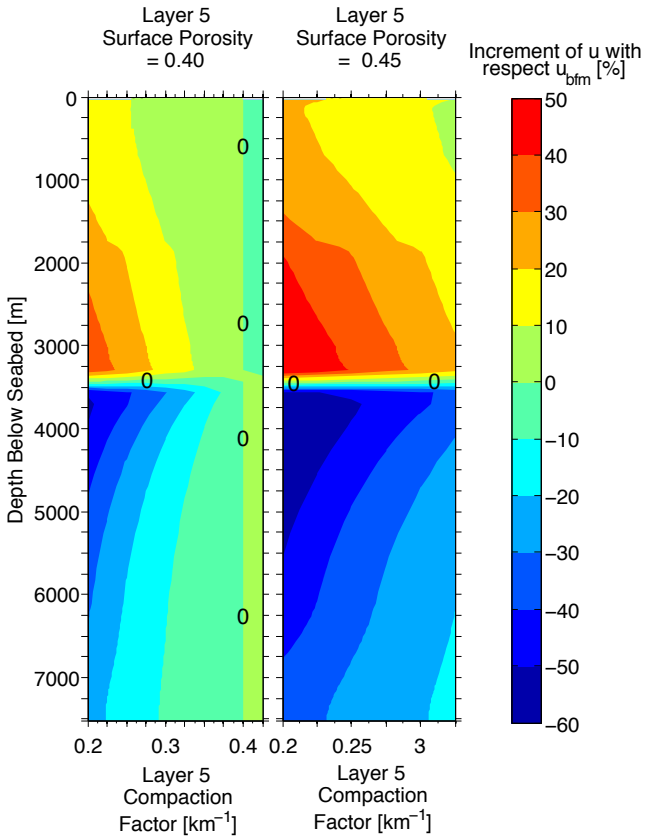

Figure 3.7: Sensitivity of overpressure u to compaction factor of layer 5 relative to the overpressure calculated with its best-fitting model (u_{bfm}).

of ∼0.5x10^{-8} Pa^{-1}, and an increase in the permeability of two orders of magnitude, with respect to the parameter profiles under hydrostatic conditions (Figs. 3.8a and 3.9). Since compressibility, density and permeability are functions of porosity (Eqs. 3.10, 3.11, 3.13 and 3.14), which varies little in the Maikop formation (layer 5), these parameters do not change much within the layer. In the Maikop formation, a compressibility value of ∼3x10^{-8} Pa^{-1} for a layer with 90% shale and 10% sandstone is consistent with published values of the bulk compressibility of sediments (Domenico & Mifflin, 1965). Similarly, a permeability of ∼10^{-13} m s^{-1} for a porosity of ∼0.2 also agrees with laboratory derived values of permeability versus porosity (Neuzil, 1994). The pore pressure profile from our model matches the values estimated from the V_p using the Eaton method, with an exponential factor of 3.5, and the Westbrook relationship (Fig. 3.8b). The Eaton and Westbrook pore pressure profiles bound the profile obtained with our model. The maximum calculated overpressure with our model is ∼138 MPa and is located at the bottom of the Maikop formation, at ∼6150 m depth. The pore pressure gradient of ∼16 MPa km^{-1} is lower than the lithostatic gradient of ∼25 MPa km^{-1} at ∼2500-3300 m depth, higher at ∼40 MPa km^{-1} than the lithostatic gradient of ∼22 MPa km^{-1} at ∼3300-4000 m depth, and approximately equal to the lithostatic gradient of ∼23 MPa km^{-1} until ∼6150 m depth. The largest difference be-

tween overpressures calculated with our model and those estimated from seismic velocities is at the bottom of the overpressure zone, due to the model boundary condition discussed above. The Eaton method and the Westbrook relationship also bound the calculated λ^* profile. The maximum values of λ^* range from 0.7-0.8 (Fig. 3.8c).

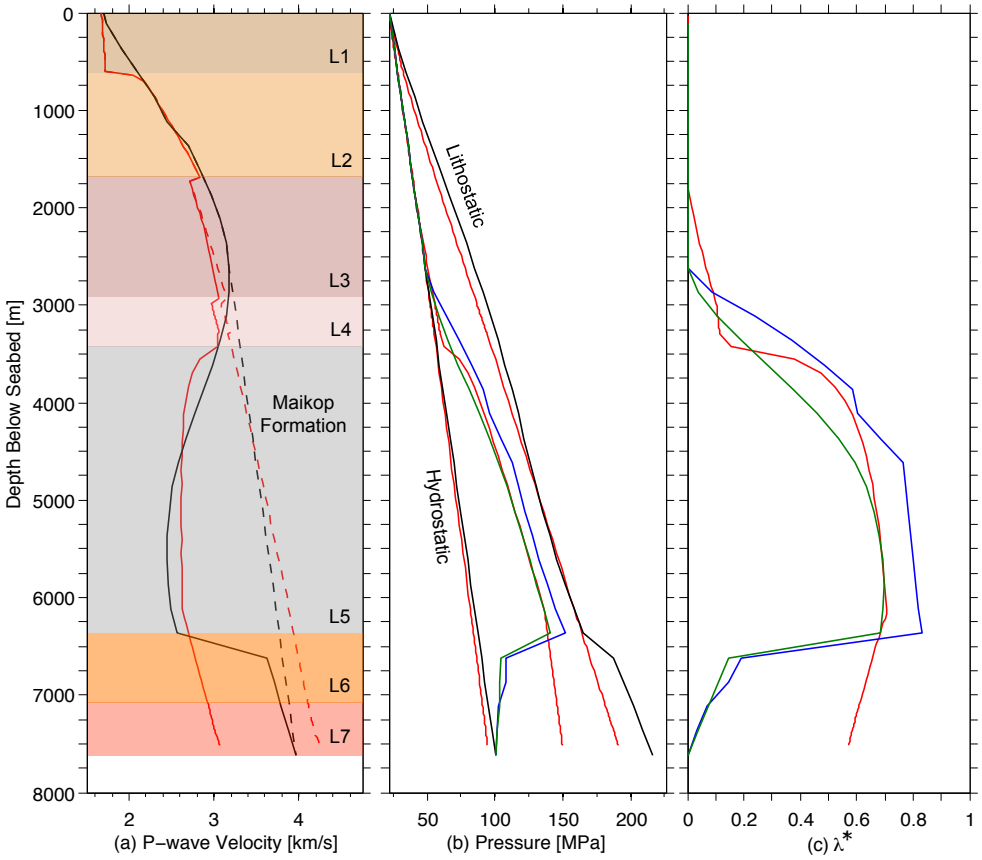

Figure 3.8: (a) Red lines are results from the 1D disequilibrium compaction model and black lines are results from Scott *et al.* (2009). Solid lines represent observed conditions, and dashed lines hydrostatic conditions. In (b) and (c) the red lines are the results using the 1D disequilibrium compaction model and the black, blue, and green lines are the results calculated using the P-wave velocity model in Scott *et al.* (2009). Blue and green lines represent the pore pressure and the λ^* profiles calculated with the Westbrook relationship and the Eaton method with E=3.5, respectively.

3.4 Discussion

We have presented a new method that allows the calculation of overpressures that satisfy both the physical principles governing the development of pore pressures due to sediment loading and the constraints imposed by seismic data and geological observations.

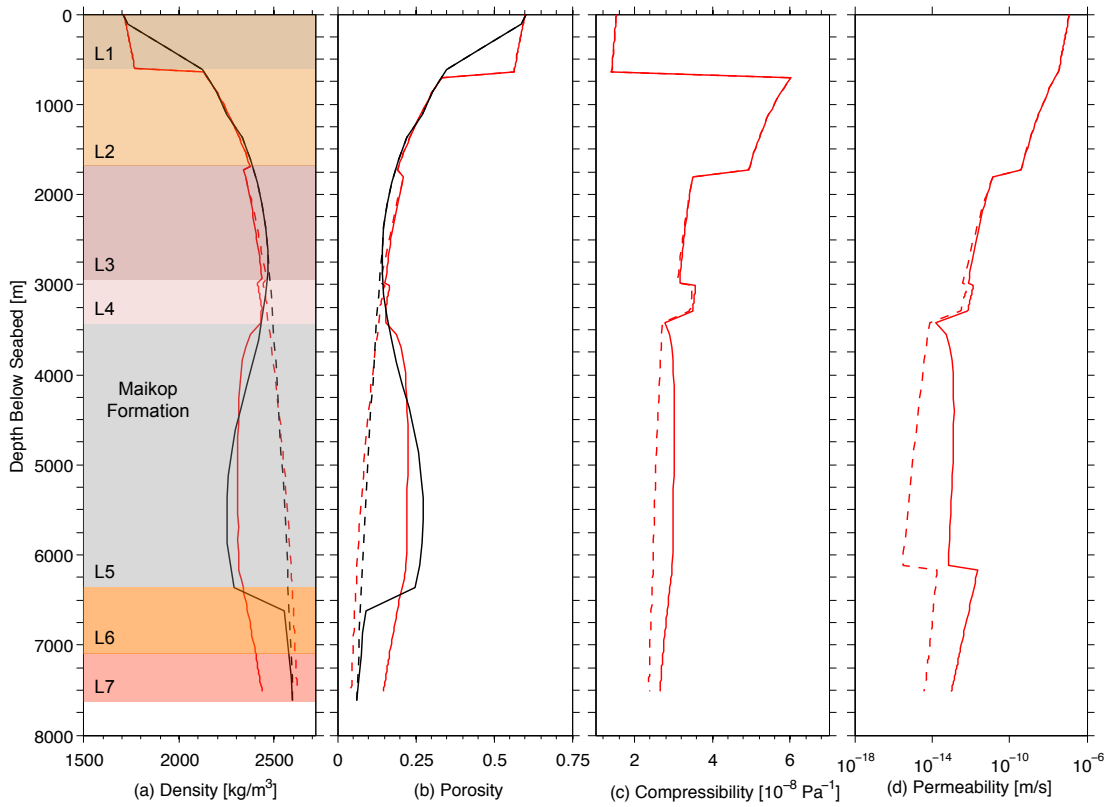

Figure 3.9: Results from best-fitting disequilibrium compaction model (red) compared with those of Scott *et al.* (2009) (black). The four plots show in solid lines the parameters in overpressured conditions, and in dashed lines in hydrostatic conditions.

In our method, the sedimentation rate, compaction factor and surface porosity of each layer are constrained by seismic and geological observations, and so the estimated overpressures are more reliable than values calculated solely with a disequilibrium compaction model.

A common practice in one-dimensional basin modelling is the use of a single sedimentation rate for the whole sediment column (e.g, Gutierrez & Wangen, 2005). If the sedimentation rate has in reality varied over time, the calculated overpressures may not be reliable. Our method estimates the sedimentation rate of each layer using a decompaction model that assumes hydrostatic conditions to calculate the decompacted layer thicknesses, which may not be an accurate assumption. The decompaction model is sensitive to the number of layers used, as it does not consider compaction because of the layer's own weight.

Our method obtains the best-fitting parameters, surface porosity and compaction factor, with a thickness error of each layer below a tolerance, by comparing the observed and calculated V_p. The calculated V_p is estimated using an empirical V_p-density relationship, which should be fairly reliable in the saturated conditions and high effective stresses (Mavko *et al.*,

2009) that we infer in the EBSB. Our method uses the Hamilton's (1978) relationship for marine sediments because it is adequate for the inferred lithologies in our case study, but elsewhere another empirical relationship or rock physics model could be used. Our method does not need to estimate the hydrostatic V_p structure and does not require borehole measurements of pore pressure to calibrate any parameter. Our method can be applied in any basin where disequilibrium compaction is thought to be the dominant mechanism generating overpressures and where the use of a one-dimensional sediment compaction model, i.e., flat and laterally extensive deposits without compressional tectonic forces, is valid.

In our EBSB case study, the calculated V_p profile in overpressured conditions successfully simulates the present-day observed profile (Fig. 3.8a) and hence suggests that the overpressures calculated with our method are reliable. Overpressures estimated with both the Eaton and the Westbrook methods match the overpressures calculated with our method (Fig. 3.8b). We can also compare our results with an empirical approach that has been used to calculate shale pore pressure profiles. This approach assumes that below a certain depth, or Fluid Retention Depth (FRD) (Swarbrick *et al.*, 2002), porosity is constant and so is the vertical effective stress, for the rest of the shale column. It uses the sedimentation rate and FRD to obtain a lithostatic-parallel pore pressure profile. Considering a present-day sediment column equal to the sediment above the top of layer L6, 6300 m (Fig. 3.8), and a rock age of 33.9 Ma (Table 3.1) gives a sedimentation rate of 185 m Ma^{-1}. If we introduce this value into Fig. 3.3 of Swarbrick *et al.* (2002), a FRD of 0.9-1.0 km is obtained. Although the lithostatic-parallel overpressure profile agrees with the pore pressure profile obtained with our method in the overpressure zone (Fig. 3.10), two major differences are observed: (1) the overpressures calculated with the FRD method are slightly higher and (2) the top of the overpressure zone is shallower using the FRD method. As the FRD does not consider pore pressure dissipation, if the FRD has been correctly chosen, the overpressures calculated with this method are always an upper bound. With respect to the differences between depths of the top of the overpressure zone, this is due to the assumption in the FDR method that the lithology is the same in the whole sediment column and so is the intrinsic permeability. Table 3.1 shows that layers L3-Samartian and L4 have 10% more sand than L5-Maikop and hence, higher permeability (Fig. 3.9d). This implies that the FDR should be located deeper in the sediment column, closer to the depth of the top of our overpressure profile. The Eaton factor of 8 estimated by Scott *et al.* (2009) using a borehole located near to the east coast of the EBSB is significantly higher than our best fitting value of 3.5. These different values result in an estimate of the maximum pore pressure of ∼160 MPa in Scott *et al.* (2009) and of ∼140 MPa in our analysis. Our value matches estimated values of 2.6-5.0 in the Gulf of Mexico (Ebrom *et al.*, 2003; Kao, 2010; Swarbrick, 2002), and where overpressures are mainly attributed

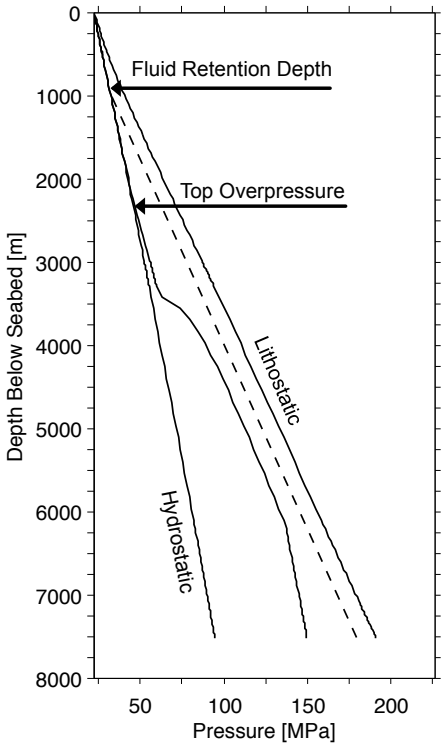

Figure 3.10: Pore pressure profiles obtained from the FRD approach (Swarbrick *et al.*, 2002) (dashed line) and our method (solid line)

to disequilibrium compaction. The large value of Scott *et al.* (2009) suggests that pore pressures in the borehole are affected by processes other than disequilibrium compaction, such as the current compressional tectonics affecting the margins of the EBSB. In the borehole, overpressures approach lithostatic at ∼2600 m depth, with values of λ^*= 0.9-1 (Scott *et al.*, 2009), whereas in the centre of the EBSB we have obtained maximum values of λ^*= 0.7-0.8 at ∼6300 m depth. In a sedimentary basin, it is normally assumed that the vertical effective stress is the maximum principal effective stress and the minimum effective stress is horizontal (e.g, Daigle & Dugan, 2010). In this context, the ratio of horizontal to vertical effective stress K_0 is usually 0.6 (Karig & Hou, 1992). Hydraulic fracturing will occur with pore pressures greater than the minimum-horizontal effective stress, and so with values of $\lambda^* > 0.6$. However, due to the compressional tectonics affecting the margins of the EBSB we can neither assume that the minimum principal effective stress is horizontal or that K_0 is equal to 0.6. The presence of mud volcanoes near the east coast of the EBSB (Kruglyakova *et al.*, 2004) indicates the presence of hydraulic fracturing and so pore pressures greater than the minimum principal effective stress. Although the λ^* value in the centre of the EBSB exceeds 0.6, no mud volcanoes have been observed so far.

The sediments in the centre of the basin are relatively undeformed (Shillington *et al.*, 2008), and the Maikop sediments were rapidly deposited in the centre of the basin bypassing the margins (Robinson *et al.*, 1995a). Therefore, it is reasonable to assume that disequilibrium

compaction is the primary source of overpressures in the centre of the basin. As the Maikop formation is rich in organic matter, hydrocarbon maturation could have been a source of overpressure, but our results suggest that this mechanism is of minor importance. The Maikop formation is a thick, homogenous shale layer with low permeability $\sim 10^{-13}$ m s^{-1}. The relatively high sedimentation rate of $\sim$0.28 m ka^{-1} between 33.9-20.5 Ma, and the high sedimentation rate of $\sim$0.85 m ka^{-1} between 13-11 Ma, were key factors controlling the development of overpressures within the Maikop formation.

In the nearby South Caspian Basin (SCB) low seismic velocities have been linked with the presence of high pore pressures (Knapp *et al.*, 2004) developed by disequilibrium compaction (Lee *et al.*, 1999). Brunet *et al.* (2003) states that the overpressure and undercompaction in the SCB is mainly situated in the Maikop formation. In contrast, Feyzullayev & Lerche (2009) propose that in the upper zone of the SCB at 600-1200 m depth, overpressures were due to disequilibrium compaction but at depths below 5000 m and where the most intense overpressures are localised, they were due to hydrocarbon generation based on the results of analysis of vitrinite reflectivity vs. depth, petroleum biological markers and isotope composition.

Our 1D disequilibrium compaction model is appropriate to understand the general hydrodynamic behaviour in the centre of the EBSB. However, it cannot be extended to the margins, where the assumptions at the base of our 1D model are no longer valid due to the existence of compressional tectonics. In addition, our model cannot reproduce the decrease in overpressure below the Maikop formation given the applied boundary conditions. Moreover, we have used intrinsic permeability parameters (Table 3.2) from an overpressure analysis in the Gulf of Mexico (Gordon & Flemings, 1998), which may not be valid in the EBSB. However, our calculated permeabilities (Fig. 3.9d) agree with laboratory-derived values of permeability versus porosity for the inferred lithologies (Neuzil, 1994).

3.5 Conclusions

From the application of our method to the calculation of overpressures, we conclude that:

i) We have developed a method that can make use of constraints on overpressure both from seismic and geological observations and corresponding disequilibrium compaction.

ii) Our method does not require in situ measurements of pore pressure for calibration.

iii) Our method does not require any assumptions regarding the P-wave velocity of normally compacted sediments.

iv) Our method estimates the sedimentation rate, surface porosity and compaction factor for each layer.

However, our method has also some drawbacks:

i) It cannot reproduce a decrease in overpressure if an impermeable bottom boundary condition is applied.

ii) It needs to impose both a decompaction model and a density-P-wave velocity relationship that incorporates more relationships between variables and assumptions in the model.

From the application of our method in the centre of the Eastern Black Sea Basin, we conclude that:

i) The low velocity zone in the centre of the Eastern Black Sea Basin can be explained by overpressures generated by disequilibrium compaction.

ii) The primary causes of the overpressure are the low permeability of the Maikop formation ($\sim 10^{-13}$ m s^{-1}) and high sedimentation rates of $\sim$0.28 m ka^{-1} during 33.9-20.5 Ma and $\sim$0.85 m ka^{-1} during 13-11 Ma.

iii) Our Eaton's best-fit factor of 3.5 is consistent with factors in other basins where overpressures were also generated by disequilibrium compaction. The high Eaton factor of 8 inferred from borehole data by Scott *et al.* (2009) suggests a tectonic contribution to overpressures at the borehole and is not appropriate for use in the centre of the basin

3.6 Acknowledgements

This work was supported by the Graduate School of the National Oceanography Centre Southampton. We thank Turkish Petroleum Company (TPAO) to provide access to seismic reflection data. We thank two anonymous reviewers for their constructive comments.

3.7 Appendix: The IAPWS Viscosity and Density Models

The viscosity model is defined by

$$\overline{\mu} = \overline{\mu_0}\left(\overline{T}\right)\overline{\mu_1}\left(\overline{T},\overline{\rho_f}\right)\overline{\mu_2}\left(\overline{T},\overline{\rho_f}\right) \tag{3.23}$$

where the upper line in each variable indicates that the viscosity $\overline{\mu}$, temperature $\overline{T}$ and water density $\overline{\rho_f}$ are dimensionless. The reference values to normalise for viscosity, temperature and water density are μ^*=1x10^{-6} Pa·s, T^* =374.82 ^{o}C and ρ_f^*=322 kg m^{-3},

respectively.

The dependence of viscosity on pressure is implicitly incorporated into the water density. As the pressure and temperature used in this study are far from the critical point of the water phase diagram, the $\overline{\mu_2}$ term can be considered equal to 1 (International Association for the Properties of Water and Steam, 2008). The factor $\overline{\mu_0}$ is defined by

$$\overline{\mu_0}\left(\overline{T}\right) = \frac{100\sqrt{\overline{T}}}{\sum_{i=0}^{3} \frac{H_i}{\overline{T}_i}} \tag{3.24}$$

with the coefficients H_i given in the International Association for the Properties of Water and Steam (2008, p.5)

The factor $\overline{\mu_1}$ is defined by

$$\overline{\mu_1}\left(\overline{T}, \overline{\rho_f}\right) = \exp\left[\overline{\rho_f} \sum_{i=0}^{5} \left(\frac{1}{\overline{T}} - 1\right) \sum_{j=1}^{6} H_{ij} \left(\overline{\rho_f} - 1\right)^j\right] \tag{3.25}$$

with the coefficients H_{ij} given in the International Association for the Properties of Water and Steam (2008, p.5)

The application of the International Association for the Properties of Water and Steam's (2008) viscosity model requires the calculation of the water density as a function of pressure and temperature. The International Association for the Properties of Water and Steam's (2007) water density model is defined by the equation

$$\rho_f\left(\pi, \tau\right) = \frac{1}{\nu\left(\pi, \tau\right)} = \frac{P}{RT\pi\gamma_\pi} \tag{3.26}$$

where P is the water pressure, R= 0.461526 kJ kg^{-1} K^{-1} is the specific gas constant, γ_π is a variable, ν is the water specific weight, π is the dimensionless pressure with reference pressure P^*=16.53 MPa, and τ is the dimensionless temperature with reference temperature T^* =1113 °C. The variable γ_π is defined by

$$\gamma_\pi = \sum_{i=1}^{34} -n_i I_i \left(7.1 - \pi\right)^{I_1 - 1} \left(\tau - 1.222\right)^{J_i} \tag{3.27}$$

where I_i, J_i, and n_i are the coefficients given in the International Association for the Properties of Water and Steam (2007, Table 2).

This viscosity model is only applicable for water pressures and temperatures located in region 1 of the water phase diagram (International Association for the Properties of Water

and Steam, 2007). If the calculated water pressures exceed the value of 100 MPa, the pressure is maintained at this value.

Chapter 4

Inverse Modelling and Seismic Data Constraints on Overpressure Generation by Disequilibrium Compaction and Aquathermal Pressuring: Application to the Eastern Black Sea Basin

Pore pressure above the hydrostatic (overpressure) is common in deep basins. It plays an important role in pore fluid migration, represent a significant drilling hazard, and is one of the factors controlling slope stability and deformation in seismically active areas. Here, we present an inverse model to calculate overpressure due to disequilibrium compaction and aquathermal pressuring. We minimise a function that contains the misfits between estimates from our forward model and observed values using a non-linear least squares approach. The inverse model allows the introduction of observed seismic and geological constraints such as P-wave velocity (V_p) and density data, and depth of the layer boundaries, for a better pore-pressure prediction. The model output also provides estimates of: (1) surface porosity, (2) compaction factor, (3) intrinsic permeability at surface conditions, (4) a parameter controlling the evolution of the intrinsic permeability with porosity, (5) the ratio between horizontal and vertical permeability, and (6) uncompacted thickness (so sedimentation rate assuming known time intervals), for each sedimentary layer. We apply our inverse approach to the centre of the Eastern Black Sea Basin (EBSB) where the V_p structure has been inferred from wide-angle seismic data. First, we present results from

a 1D inverse model and an uncertainty analysis based on the Monte Carlo error propagation technique. To represent the observed rapid change from low V_p to normal V_p below the Maikop formation, we impose a zero overpressure bottom boundary, and subdivide the layer below the Maikop formation into two sublayers: an upper layer where the rapid change is located and a lower layer where the V_p is normal. Second, we present the results from a 2D inverse model for the same layers using two alternative bottom boundary conditions, zero overpressure and zero flow. We are able to simulate the observed V_p, suggesting that the low velocity zone (LVZ) at ∼3500-6500 m depth below the seabed (mbsf) can be explained by overpressure generated due to disequilibrium compaction (>90%) and to aquathermal pressuring (<10%). Our results suggest that the upper sublayer, below the Maikop formation, behaves as a seal due to its low permeability ∼0.3-2x10^{-14} m s^{-1}. This seal layer does not allow the fluids to escape downwards, and hence overpressure develops in the Maikop formation and not in the layers below. This overpressure was mainly generated by the relatively high sedimentation rate of ∼0.29 m ka^{-1} of the Maikop formation at 33.9-20.5 Ma and an even higher sedimentation rate of ∼0.93 m ka^{-1} at 13-11 Ma. We estimate a maximum ratio of overpressure to vertical effective stress in hydrostatic conditions (λ^*) of ∼0.62 at ∼5200 mbsf associated with an overpressure of ∼42 MPa.

4.1 Introduction

To understand possible fluid and gas migration pathways in the subsurface of a sedimentary basin it is important to locate and quantify pore pressure above the hydrostatic (overpressure) (Harrison & Summa, 1991). Besides affecting the hydrodynamics of a sedimentary basin, overpressure is one of the factors controlling the structural mechanics of fault surfaces (Hubbert & Rubey, 1959a,b), deformation in accretionary wedges (Davis *et al.*, 1983) and the location of the décollement in subduction environments (Tsuji *et al.*, 2008). It may also drive warm fluids forming mineral deposits (Garven & Freeze, 1984; Sharp, 1978). Understanding overpressure can also contribute to determining the depositional history of a sedimentary basin (Marín-Moreno *et al.*, 2013a). Generation of overpressure has been suggested as a possible factor influencing submarine slope failures (e.g, Georgiopoulou *et al.*, 2010; Leynaud *et al.*, 2007) and so its quantification is essential to ensure the safety of offshore infrastructure. In a hydrocarbon exploration campaign, knowledge of overpressure can help with the assessment of seal effectiveness (Sarker & Batzle, 2008) and to quantify reservoir porosity (Swarbrick & Hillis, 1999). From a well engineering point of view, knowledge of these parameters can also help to drill wells safely and economically (Sayers, 2006), minimising the possibility of a well blowout, and to avoid fracturing the formation due to an excessively high mud weight (Sarker & Batzle, 2008).

Various mechanisms have been proposed to explain the generation of overpressure in sedimentary basins. They can be grouped into three main types: (1) overpressure generation due to changes in porosity, (2) overpressure generation due to changes in fluid volume and (3) overpressure generation because of fluid movement. Changes in porosity developing overpressure can occur either by sediment deposition, tectonic compression (e.g, McPherson & Garven, 1999), cementation (e.g, Osborne & Swarbrick, 1999), and smectite dehydration to illite (e.g, Bruce, 1984; Saffer & McKiernan, 2009). The mechanism where the deposition of overlying sediments is rapid enough to not allow the underlying sediments to compact to their normal or equilibrium porosity is known as disequilibrium compaction. This mechanism usually occurs in fine-grained sediments with low permeabilities under high sedimentation rates. It has been suggested as the dominant mechanism generating overpressure in the Gulf of Mexico (e.g, Berhmann *et al.*, 2006), in the South Caspian Basin (Lee *et al.*, 1999), and in the centre of the Eastern Black Sea Basin (EBSB) (Marín-Moreno *et al.*, 2013a). Cementation and smectite dehydration to illite may generate overpressure through a net reduction in porosity and due to the release of interlayer water into the pores, respectively, if the sediments have low permeability (Osborne & Swarbrick, 1999). Changes in fluid volume generating overpressure include thermal expansion of water (aquathermal pressuring) (e.g, Shi & Wang, 1986) and hydrocarbon generation (e.g, Chi *et al.*, 2010). In normal geological environments, aquathermal pressuring is a secondary mechanism compared to disequilibrium compaction (Shi & Wang, 1986) because the change in fluid volume is small (Luo & Vasseur, 1992). Hydrocarbon generation is usually a secondary mechanism helping to maintain overpressure zones generated by disequilibrium compaction (Hansom & Lee, 2005). Lateral changes in the hydraulic potential due to topographic relief drive fluid movement and this can generate significant overpressure if a seal overlies the basin sediments (Neuzil, 1995).

Gibson (1958) was the first to model the generation of pore pressure due to disequilibrium compaction using Terzaghi's (1943) one-dimensional small strain equation, and considering a single sedimentation rate and constant lithological properties (porosity, compressibility, density and permeability). Bethke (1985) extended that model by introducing two-dimensional, non-isothermal conditions and non-linear variation of lithological properties, while Audet & Fowler (1992) and Wangen (1992) introduced a non-dimensionalised, non-linear and large strain formulation of Gibson's (1958) model. Although these represent important advances in the understanding of the mechanisms generating overpressure and in the numerical models to calculate them, it is still difficult to determine the input parameters and to validate the results of such models for laterally extensive and deep overpressured zones. If the overpressured zone is laterally extensive and the overpressure is variable, the number of available boreholes may not be enough, and if it is deep, valida-

tion by drilling is technically and economically not feasible. Overpressure calculated using empirical methods relating vertical effective stress to any wire-line, seismic or drilling data that can be used as a proxy for porosity, indirectly overcome the validation problem. However, such methods do not consider the hydrodynamics of the sedimentary basin, generally have considered a single lithology, and most of them are site dependent.

This paper presents an inverse approach to model sediment accumulation in a basin that provides: (1) the calculation of overpressure considering the physical principles governing the disequilibrium compaction and fluid thermal expansion mechanisms, and using a 2D non-linear, large-strain forward numerical model, (2) indirect validation of the calculated overpressure using seismic (V_p and layer interface depth), density, and geological data, and (3) constraints on the lithological parameters and sedimentation rates necessary to satisfy the observed data. Using the observed V_p structure as a constraint of our mechanical compaction and aquathermal expansion model, instead of using the pore pressure calculated from V_p, ensures that the calculated pore pressure profile is physically realisable, and excludes pore pressure variations that cannot be generated by disequilibrium compaction or aquathermal pressuring.

We apply our model to Cenozoic post-rift basin fill in the Eastern Black Sea Basin (EBSB). Our EBSB stratigraphic model comprises seven units (Shillington *et al.*, 2008) based on three Deep Sea Drilling Project (DSDP) sites, industry wells at the margins of the Black Sea (Akcakoca, Chaladidi and Ochamchira; Fig. 4.1), onshore geologic mapping, and reflection seismic data (Fig. 4.1). The EBSB is a target basin for hydrocarbon exploration (Robinson *et al.*, 1996) and a low velocity zone (LVZ) has been identified in the Maikop formation at ∼3500-6500 m depth below the seabed (mbsf) (Scott *et al.*, 2009). The P-wave velocity structure was obtained from coincident reflection and ocean bottom seismic data using a two-dimensional tomographic analysis using Jive3D (Hobro *et al.*, 2003) and inverting for refractions, wide-angle reflections and normal incidence reflections simultaneously. This approach provides accurate velocities even within deep sediments (Scott *et al.*, 2009). In the centre of the EBSB, Scott *et al.* (2009) linked this LVZ to overpressure using the empirical Eaton method (den Boer *et al.*, 2006; Eaton, 1969, 1975) and an Eaton factor of 8, calibrated with pore pressure measurements from an industry borehole located near the east coast of the EBSB. They suggested that disequilibrium compaction was likely to be the mechanism generating overpressure because the Maikop formation was rapidly sedimented in the centre of the EBSB bypassing the margins (Robinson *et al.*, 1995a). Marín-Moreno *et al.* (2013a) suggested that this approach might fail because the pore pressure in the borehole is likely to be strongly influenced by compressional deformation, which is absent in the centre of the basin (e.g, Rangin *et al.*, 2002). Instead, they estimated the overpressure with a new method based on a 1D forward disequilibrium compaction model that

allows imposing constraints on P-wave velocity and layer thicknesses indirectly.

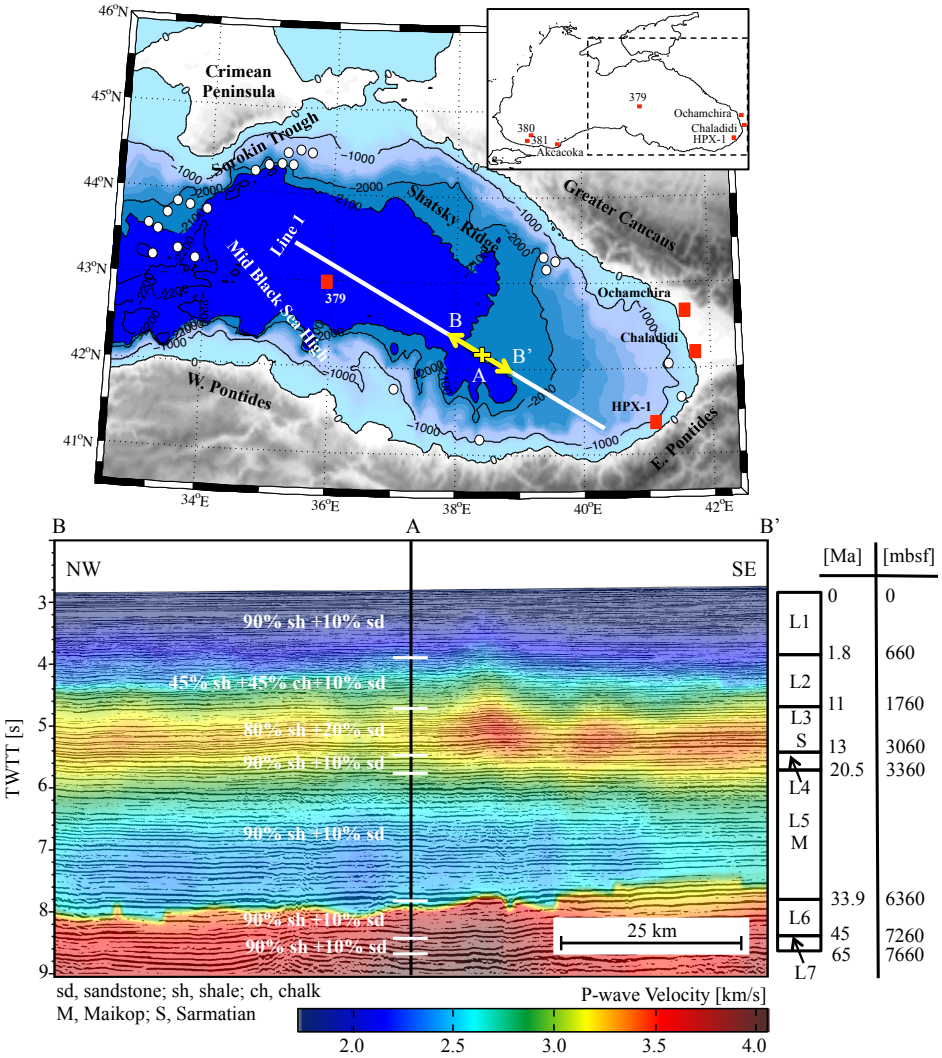

Figure 4.1: Top, map of the eastern Black Sea showing the location of wide-angle seismic profile 1 with bathymetry and elevation taken from the National Oceanic and Atmospheric Administration (NOAA, http://www.ngdc.noaa.gov/mgg/global/relief/ ETOPO2/ETOPO2v2-2006/ETOPO2v2g/). White circles indicate known locations of mud volcanoes (Ivanov *et al.*, 1996; Krastel *et al.*, 2003; Kruglyakova *et al.*, 2004). Red squares indicate the location of industry and Deep Sea Drilling Project (DSDP) boreholes. Yellow cross (A) indicates the location of 1D analysis and yellow arrow (B-B'), 100 km length, the location of the 2D analysis. The inset in the upper right hand corner gives the location with respect to the entire Black Sea. Bottom, part of multichannel seismic profile near-coincident with line 1 in the region for the 2D analysis. The seismic profile is overlaid by P-wave velocities, inferred from wide-angle seismic data (Scott *et al.*, 2009), and shows the lithologies for each stratigraphic layer on the right (Shillington *et al.*, 2008). These lithologies are used as reference but not considered in our inversion. The table in the right gives the ages [Ma] and depth of layer interfaces [mbsf] at the centre of the seismic section (Scott *et al.*, 2009; Shillington *et al.*, 2008)

Using permeabilities based on the lithologies defined by Shillington *et al.* (2008), they demonstrated that overpressure generated by disequilibrium compaction can explain the LVZ in the centre of the EBSB, and that, given the same assumptions as Scott *et al.* (2009) regarding the velocity of normally pressured sediments, the Eaton method with a factor of 3.5, similar to values used elsewhere (e.g, Ebrom *et al.*, 2003; Kao, 2010), gives similar overpressure.

Here, we build on Marín-Moreno *et al.* (2013a) by: (1) extending the analysis to two dimensions, (2) applying both disequilibrium compaction and aquathermal pressuring as possible overpressure mechanisms, (3) allowing the parameters controlling the permeability and porosity functions for each layer to be determined by the inverse model, (4) proposing an explanation for the inferred normal V_p structure below the Maikop formation in the centre of the EBSB.

4.2 Forward Discrete Model

4.2.1 Governing Equations

A concise description of the derivation of the equation governing the evolution of the total pore pressure through time due to sediment loading and fluid thermal expansion is given in this section.
The conservation of solid grains mass per unit of volume is given by

$$\frac{\partial}{\partial t}\left(\rho_s\left(1-\phi\right)\right)+\nabla\cdot\left(\rho_s\left(1-\phi\right)\mathbf{u}\right)=0 \tag{4.1}$$

where $\mathbf{u}=(u_x,u_y,u_z)$ is the solid grain velocity vector, ρ_s is the solid grain density and ϕ is the porosity.
The conservation of fluid mass per unit of volume is given by

$$\frac{\partial}{\partial t}\left(\rho_f\phi\right)+\nabla\cdot\left(\rho_f\phi\mathbf{v}+\rho_f\phi\mathbf{u}\right)=0 \tag{4.2}$$

where $\mathbf{v}=(v_x,v_y,v_z)$ is the fluid velocity vector and ρ_f is the fluid density. The second term in the divergence operator is not considered, but it describes the movement of the fluid because of the displacement of the solid grains.
The sediment density ρ in saturated conditions is given by

$$\rho\left(\phi,\rho_f\right)=\rho_s\left(1-\phi\right)+\rho_f\phi \tag{4.3}$$

We reformulate Eqs. 4.1 and 4.2 according to a material description where the reference frame is fixed on the solid grains. The material derivative of a property DX/Dt following a specific particle of the continuous medium is given by

$$\frac{DX}{Dt} = \frac{\partial X}{\partial t} + \mathbf{u} \cdot \nabla X \tag{4.4}$$

By applying the material derivative to Eqs. 4.1 and 4.2 we obtain the solid grains and fluid conservation equations in a material formulation (Eqs. 4.5 and 4.6).

$$(1-\phi)\frac{D\rho_s}{Dt} - \rho_s \frac{D\phi}{Dt} + \rho_s (1-\phi)\nabla \cdot \mathbf{u} = 0 \tag{4.5}$$

$$\phi \frac{D\rho_f}{Dt} + \rho_f \frac{D\phi}{Dt} + \nabla \cdot (\rho_f \mathbf{v}\phi) + \rho_f \phi \nabla \cdot \mathbf{u} = 0 \tag{4.6}$$

Substituting the term $D\phi/Dt$ of Eq. 4.5 into Eq. 4.6 and dividing it by ρ_f, we obtain

$$\frac{\phi}{\rho_f}\frac{D\rho_f}{Dt} + \frac{(1-\phi)}{\rho_s}\frac{D\rho_s}{Dt} + \frac{1}{\rho_f}\nabla \cdot (\rho_f \mathbf{v}\phi) + \nabla \cdot \mathbf{u} = 0 \tag{4.7}$$

where the term $\nabla \cdot \mathbf{u}$ can be expressed in the form

$$\nabla \cdot \mathbf{u} = \frac{\partial u_x}{\partial x} + \frac{\partial u_y}{\partial y} + \frac{\partial u_z}{\partial z} = \frac{D}{Dt}(\varepsilon_x + \varepsilon_y + \varepsilon_z) = \frac{D\varepsilon_v}{Dt} \tag{4.8}$$

where ε_x, ε_y, ε_z are Cartesian strains and ε_v is the volumetric strain.
Equation. 4.7 describes that changes in the water content of a unit-volume of sediment must be balanced by changes in the fluid density, solid grain density and deformation of the sediment. To express Eq. 4.7 in terms of pore pressure, three constitutive equations relating fluid density, porosity and fluid flow to pore pressure are required (we consider that the solid grains density is a constant). The fluid density changes are assumed to be a function of changes in pore pressure and temperature and are given by International Association for the Properties of Water and Steam's (2007) density model.
The evolution of porosity is controlled by mechanical and chemical compaction (Bjørlykke & Høeg, 1997; Schneider *et al.*, 1996). Mechanical compaction is a function of effective stress and chemical compaction is mainly controlled by time, temperature and mineralogy (Bjørlykke & Høeg, 1997). Mechanical compaction applies to unlithified sediments and dominates at temperatures below 80-100 °C (Mondol *et al.*, 2007). The Maikop formation (33.9-22.5 Ma), which constitutes most of the low velocity layer, is a mudstone-dominated layer (Robinson *et al.*, 1996) with temperatures between 90-170 °C (assuming a constant thermal gradient in the EBSB of 26 °C/km; Minshull & Keddie, 2010). However, chemical compaction is normally only important in basins older than ∼100 Ma (Schneider *et al.*, 1996) and is therefore neglected in this study. Chemical compaction is closely linked to

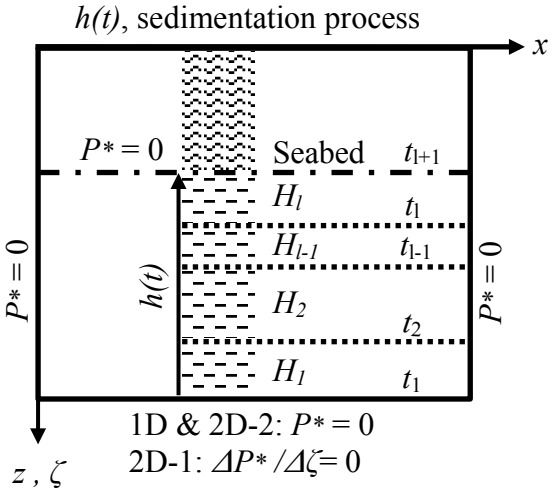

Figure 4.2: Conceptual diagram for the application of our forward numerical model, showing the sedimentation process and the boundary conditions imposed at all boundaries. The subscript l varies between one and the maximum number of stratigraphic layers in the model. The sedimentation time interval Δt_s is calculated using the ages of the top and base of each stratigraphic layer.

overpressure generation by diagenetic reactions (Ramdhan & Goulty, 2010), which are also neglected here.

We use Athy's (1930) law in terms of vertical effective stress. The effective stress principle (Terzaghi, 1943) states that any variation in porosity is due to a variation in the effective stress. The porosity evolution as a function of the vertical effective stress is given by

$$\phi\left(\beta, \sigma'_{zz}\right) = \phi_0 \exp\left[-\beta \sigma'_{zz}\right] \tag{4.9}$$

where β (Eq. 4.12) is an empirical compaction factor, ϕ_0 is the initial porosity or porosity at surface conditions (zero effective stress) and σ'_{zz} is the vertical effective stress (Eq. 4.10).

$$\sigma'_{zz}\left(z, \rho, \rho_f\right) = \int_0^z \left(\rho - \rho_f\right) g dz - P^* = P_L - P = P_L - \left(P_h + P^*\right) \tag{4.10}$$

In Eq. 4.10 g is the gravitational acceleration, z is the depth, P is the total pore pressure, P_h is the hydrostatic pressure, P^* is the overpressure, and P_L is the vertical or lithostatic pressure. The change in lithostatic pressure over time can be expressed in terms of sediment thickness h (Fig. 4.2) by

$$\frac{DP_L\left(h, \rho\right)}{Dt} = \rho g \frac{Dh}{Dt} \tag{4.11}$$

The stress compaction factor β is related to the depth compaction factor c (Sclater & Christie, 1980) by

$$\beta\left(\rho, \rho_f\right) = \frac{c}{\left(\rho - \rho_f\right) g} \tag{4.12}$$

Here, we assume that the empirical factor β is equivalent to the bulk compressibility of

the saturated sediments (Hart *et al.*, 1995). Combining Eqs. 4.9 and 4.12 we obtain

$$\phi\left(\rho, \rho_f, \sigma'_{zz}\right) = \phi_0 \exp\left[-\left(\frac{c}{(\rho - \rho_f)\, g}\right)\sigma'_{zz}\right] \tag{4.13}$$

Equation. 4.9 when differentiated with respect to time, and considering here that changes in β with time are significantly smaller compared to those in σ'_{zz} and therefore assuming that β is a constant, gives

$$\frac{D\phi}{Dt} = -\phi\beta\frac{D\sigma'_{zz}}{Dt} \tag{4.14}$$

The term $D\phi/Dt$ in Eq. 4.14 can also be expressed in terms of volumetric deformation by

$$\frac{D\phi\left(V_\phi, V_s\right)}{Dt} = \frac{D}{Dt}\left(\frac{V_\phi}{V_\phi + V_s}\right) = \frac{\frac{D}{Dt}V_\phi\left(V_\phi + V_s\right) - V_\phi\frac{D}{Dt}V_\phi}{\left(V_\phi + V_s\right)^2} = \frac{D\varepsilon_v}{Dt}\left(1 - \phi\right) \tag{4.15}$$

where V_ϕ and V_s are the pores and solid grains volume respectively.
We use Darcy's equation given by

$$\rho\mathbf{v}\phi = \frac{-\boldsymbol{K}\left(k_i, \rho, \mu\right)}{g} \cdot \nabla\left(P - \rho_f g z\right) \tag{4.16}$$

where $\boldsymbol{K}$ is the permeability tensor, with eigenvalues K_{xx}, K_{yy}, K_{zz} (assuming Cartesian principal directions). We consider that in saturated conditions and in a monophase fluid system, permeability is a unique function of intrinsic permeability k_i (Eq. 4.14), density of the fluid ρ_f and viscosity μ. The vertical permeability K_{zz} and the horizontal permeabilities K_{xx} and K_{yy} are given by

$$\begin{aligned} K_{zz}\left(k_i, \rho_f, \mu\right) &= \frac{k_i \rho_f g}{\mu} \\ K_{xx} = K_{yy} &= \alpha K_{zz} \end{aligned} \tag{4.17}$$

where k_i, intrinsic permeability, is a geometric parameter that measures the degree of connectivity of the pores in the sediment and α is the ratio of horizontal to vertical permeability. Following Audet & McConnell (1994) k_i can be described by

$$k_i\left(\phi\right) = k_{i0}\exp\left[\gamma\left(\phi^2 - \phi_0^2\right)\right] \tag{4.18}$$

where k_{i0} is the intrinsic permeability at surface conditions and γ is a parameter controlling the evolution of the intrinsic permeability with porosity. Several porosity-intrinsic permeability relationships have been proposed, and some of them are compared in section 6. Viscosity depends both on pressure and temperature, but for water it is much more dependent on temperature than pressure (Meyer *et al.*, 1963). For completeness we apply

the International Association for the Properties of Water and Steam's (2008) temperature and pressure dependent viscosity model. During burial, intrinsic permeability decreases with increasing depth due to the reduction in porosity, and viscosity also decreases with increasing temperature. In normal geologic systems, the decrease in intrinsic permeability is more significant than the decrease in viscosity and therefore, permeability generally decreases with depth (Sharp, 1983).
Using expressions 4.8, 4.10, 4.11, 4.14, 4.15 and 4.16 in Eq. 4.7 the evolution of the total pore pressure through time due to sediment loading and fluid volume change is governed by

$$\frac{DP\left(\boldsymbol{K},\beta,\phi,\rho_f,h\right)}{Dt} = \nabla\cdot\left(\frac{(1-\phi)}{\phi\beta\rho_f g}\boldsymbol{K}\cdot\nabla\left(P-\rho_f g z\right)\right)+\rho g\frac{Dh}{Dt}-\left(\frac{(1-\phi)}{\beta\rho_f}\right)\frac{D\rho_f}{Dt} \quad (4.19)$$

In Eq. 4.19 the first term on the right part of the equation is the fluid flow term, the second is the sediment loading term, and the third is the term that considers changes in fluid volume. In normal geological environments, water volume changes by changes in temperature are dominant over pressure changes for an equal increment in depth. Therefore, the minus sign in the third term of Eq. 4.19 indicates that water tends to expand with increasing depth and so its density decreases.

4.2.2 Numerical Model

Equation 4.19 is solved using an implicit finite difference scheme with backward differences to approximate the time derivative and second-order centered differences in space, a fully compacted coordinate system for the depth axis (Gutierrez & Wangen, 2005; Marín-Moreno *et al.*, 2013a), and an harmonic average to estimate the permeability in the interface between cells.
The fully compacted depth coordinate ζ-axis and fully compacted layer thickness H_ζ are obtained from the real depth coordinate z-axis and from the uncompacted layer thickness H_0, respectively, by

$$\begin{aligned}\Delta\zeta &= \Delta z\,(1-\phi)\\ H_\zeta &= H_0\,(1-\phi_0)\end{aligned} \quad (4.20)$$

The fully compacted depth coordinate axis measures a sediment column where all the pores have been removed (Fig. 4.3). Every new sedimented layer is also added in the fully compacted coordinate system. Following Bethke (1985) 2D finite difference discretisation of the geometrical domain, the finite difference approximation to Eq. 4.19 (indicated by the use of Δ instead of D) can be expressed as:

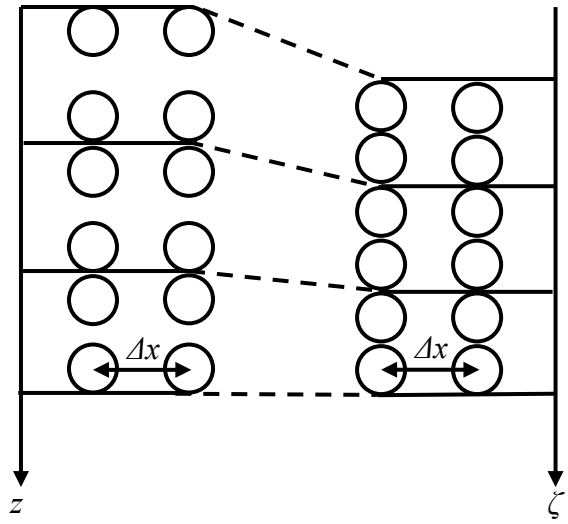

Figure 4.3: Schematic diagram of the fully compacted coordinate system ζ. It shows two conceptual columns of sediment separated by a distance of Δx in the real and in the fully compacted depth coordinate system.

$$\frac{\Delta P}{\omega \Delta t_s} = \frac{1}{\Delta \zeta}(1-\phi)\left(\frac{K_{\zeta\zeta}(1-\phi)^2 \Delta x}{V_c \phi \beta \rho_f g}\frac{\Delta P^*}{\Delta \zeta}\right)\Delta\zeta + \frac{1}{\Delta x}\left(\frac{K_{xx}(1-\phi)\Delta\zeta}{V_c\phi\beta\rho_f g}\frac{\Delta P}{\Delta x}\right)\Delta x + \frac{H_0(1-\phi_0)}{\Delta t_s}\rho g - \left(\frac{(1-\phi)}{\beta\rho_f}\right)\frac{\Delta\rho_f}{\omega\Delta t_s} \quad (4.21)$$

where K_{xx} and $K_{\zeta\zeta}$ (K_{zz} in the fully compacted coordinate system) are the horizontal and vertical permeabilities, respectively, V_c is the area per unit of width of a finite difference cell, Δx and $\Delta\zeta$ are the horizontal and vertical dimensions of the finite difference cell, respectively, Δt_s is the sedimentation time interval of each stratigraphic layer, and ω is a parameter with values between $0 < \omega < 1$. Therefore, the length of the numerical time step is $\Delta t = \omega \Delta t_s$. If we assume constant sea level, the term $\Delta P/\Delta x$ in Eq. 4.21 can be expressed in terms of overpressure $\Delta P^*/\Delta x$ which allows us to impose the boundary and initial conditions in terms of overpressure. The top boundary condition is set to zero overpressure $P^* = 0$, and the bottom boundary condition is set to either $P^* = 0$ or $\Delta P^*/\Delta\zeta = 0$. Similarly, the left and right boundary conditions could be set to either $P^* = 0$ or $\Delta P^*/\Delta x = 0$. Here, to test for the possibility of lateral fluid flow, the lateral boundary conditions are set to $P^* = 0$. The top boundary condition is a moving boundary condition that is imposed at each newly deposited layer (Fig. 4.2). The initial condition is set to zero overpressure $P^*(t = 0) = 0$.

Pore pressure calculated with Eq. 4.21 at each time step can then be used to update fluid density, vertical effective stress (Eq. 4.10) and viscosity. Porosity (Eq. 4.9), vertical effective stress (Eq. 4.10), and compressibility (Eq. 4.12) depend on density (Eq. 4.3). As density is itself a function of porosity (Eq. 4.3), we consider time intervals small

enough to avoid extensive changes in porosity over the time step (maximum of 0.02 porosity changes) and the vertical effective stress, compressibility and porosity at each time step are calculated using the density from the previous time step. The estimated porosity is then used to update the density (Eq. 4.3) and the intrinsic permeability (Eq. 4.18). Then, the fluid and sediment densities are used to update the compressibility (Eq. 4.12). Equation 4.21 is only applicable in basins with flat and laterally extensive deposits without compressional tectonic forces and hence, where the horizontal strains are minor compared to the vertical strains.

4.3 Inverse Model

Our inverse model uses a non-linear least squares approach (Aster *et al.*, 2005; Tarantola, 2005), the constraints imposed by the disequilibrium compaction and aquathermal pressuring mechanisms, and seismic (V_p and layer interface depth), density, and geological data to obtain the model parameters for each layer: (1) the surface porosity ϕ_0, (2) the compaction factor c, (3) the initial intrinsic permeability k_{i0}, (4) the parameter controlling how the intrinsic permeability evolves with porosity γ, (5) the ratio between the horizontal and vertical permeability α (considered only in the 2D model), and (6) the uncompacted sediment thickness H_0, i.e. thickness at the time of deposition, which assuming known sedimentation time intervals, gives the sedimentation rate.
The objective function to be minimised is given by:

$$\chi^2 = \frac{1}{N}\sum_{n=1}^{N}\left(\frac{V_{p,n}^{Obs} - V_{p,n}^{Cal}(\mathbf{m})}{s_n\left(V_p^{Obs}\right)}\right)^2 + \frac{1}{N}\sum_{n=1}^{N}\left(\frac{V_{p,n}^{Norm} - V_{p,n}^{NormCal}(\mathbf{m})}{s_n\left(V_p^{Norm}\right)}\right)^2 + \frac{1}{N}\sum_{n=1}^{N}\left(\frac{\rho_n^{Obs} - \rho_n^{Cal}(\mathbf{m})}{s_n\left(\rho^{Obs}\right)}\right)^2 + \frac{1}{L}\sum_{l=1}^{L}\left(\frac{z_{b,l}^{Obs} - z_{b,l}^{Cal}(\mathbf{m})}{s_l\left(z_b^{Obs}\right)}\right)^2 \quad ; \quad \mathbf{m}_{\mathrm{L}} \leqslant \mathbf{m} \leqslant \mathbf{m}_{\mathrm{U}} \tag{4.22}$$

where L and N are the number of layers and data points respectively, $\mathbf{m}$ is the vector containing the model parameters (ϕ_0, c, k_{i0}, γ, α, and H_0), $\mathbf{m}_{\mathrm{L}}$ and $\mathbf{m}_{\mathrm{U}}$ are the lower and upper bound vectors of model parameters, respectively, and contain their *a-priori* state of information, V_p is the P-wave velocity, z_b is the depth of a layer interface, χ^2 is the chi-squared error between the observed and calculated results, s is the error associated with the data, and the superscripts, Obs, $Norm$ and Cal mean observed, normal and calculated, respectively. Here, we define V_p^{Norm} as the V_p assuming hydrostatic conditions and V_p^{Obs} as the V_p obtained from a tomographic analysis of wide-angle seismic data. The V_p^{Norm} term in Eq. 4.22, drives the model to zero overpressure in layers where we assume that the V_p^{Obs} is normal and penalises models with abrupt changes in V_p, which may

arise from significant changes in lithology (and therefore, compressibility and porosity) of the sediments. In Eq. 4.22 z_b^{Cal} and ρ^{Cal} are direct outputs from our disequilibrium compaction model whereas V_p^{Cal} and $V_p^{NormCal}$ are not. To calculate them, we use the density outputs from our forward model and assume that the seismic velocity of marine sediments is well correlated with density according to Hamilton's (1978) relationship for a silt, clay and turbidite lithology and may be estimated from Eq. 4.23. Hamilton's (1978) relationship has been previously applied in the EBSB (Marín-Moreno *et al.*, 2013a; Scott *et al.*, 2009) and, although P-wave velocity-density relationships depend on clay content (Han *et al.*, 1986), in our inversion we do not make any strong assumption regarding the type of sediment. If we use Gardner *et al.*'s (1974) relationship for comparison, the density differences are not significant (Marín-Moreno *et al.*, 2013a).

$$\begin{aligned} \rho &= 1.135V_p - 0.190 : \qquad (1.5\text{-}2 \text{ km s}^{-1}) \\ \rho &= 0.917 - 0.714V_p - 0.08V_p^2 : \qquad (>2 \text{ km s}^{-1}) \end{aligned} \tag{4.23}$$

Our inverse model assumes that the data space is linear, and the data uncertainties are gaussian. It also assumes that the forward model (Eq. 4.19) is approximately linear, so the posterior probability density of model parameters is approximately gaussian (Tarantola, 2005). Our model does not consider uncertainties on the forward physical model. If the physical model uncertainties were known and gaussian, the associated covariance matrix could be simply added to the data covariance matrix (Tarantola, 2005). We find the global minimum value of χ^2 within the parameters bounds using the trust-region reflective method implemented in Matlab 7.8.0 (R2009a) and based on Coleman & Li (1994, 1996). We define convergence when either, $\left|\chi^2\left(\mathbf{m}^{i+1} - \mathbf{m}^{i}\right)\right| \leqslant 10^{-6}\left(\chi^2\left(\mathbf{m}^0\right)\right)$ or $\left(\mathbf{m}^{i+1} - \mathbf{m}^{i}\right)\left(\mathbf{m}^{i+1} - \mathbf{m}^{i}\right)^{\mathrm{T}} \leqslant 10^{-6}\left(\mathbf{m}^0\left(\mathbf{m}^0\right)^{\mathrm{T}}\right)$, is satisfied. Here $\mathbf{m}^0$ is the initial model parameters vector and the superscript i means iteration.

4.4 Pore Pressure Prediction from V_p

We use two independent empirical methods, the equivalent depth method (e.g, Westbrook, 1991) and the Eaton method (den Boer *et al.*, 2006; Eaton, 1969, 1975), to compare with the outcome from our inverse model. Empirical methods for pore pressure prediction from V_p assume that changes in V_p are a function of changes in the vertical effective stress alone, as an approximation to the mean effective stress. Under hydrostatic conditions, V_p typically increases with burial, and hence with vertical effective stress, due to the reduction in porosity and increased grain contact. Therefore, any decrease in V_p may be attributed to a decrease in the vertical effective stress, i.e. an increase of pore pressure above hydrostatic. This overpressure results in undercompacted sediments with porosity

and intrinsic permeability values more appropriate to shallower depths.

The equivalent depth method assumes that effective stress at depth z in a LVZ is equal to that at the shallower depth $z^{'}$ when the V_p is the same but the pressure is hydrostatic, and is given by Eq. 4.24. We match the V_p in the overpressured zone V_p^{Obs} at depth z, with a normal V_p in hydrostatic conditions V_p^{Norm} at depth $z^{'}$ within a tolerance of ± 0.01 km s^{-1}.

$$P\left(z\right) = P_L\left(z\right) - P_L\left(z^{'}\right) + P_h\left(z^{'}\right) \tag{4.24}$$

The Eaton method estimates pore pressure from the ratio between V_p^{Obs} and V_p^{Norm} and is given by Eq. 4.25.

$$P\left(z\right) = P_L - \left(P_L - P_h\right)\left(\frac{V_p^{Obs}}{V_p^{Norm}}\right)^E \tag{4.25}$$

The Eaton factor E controls the sensitivity of the V_p to the vertical effective stress (den Boer *et al.*, 2006) and should be obtained ideally by calibration using measurements of pore pressure in boreholes in the study area. Equation 4.25 is only valid for overpressure generated primary by disequilibrium compaction and in the presence of other dominant mechanisms an alternative method should be applied. To apply Eq. 4.25 the V_p^{Norm} must be known or, in its absence, must be estimated. We estimate V_p^{Norm} by interpolating the velocity between the top of the LVZ and the base of sediments on the assumption that in the EBSB at depths above and below the LVZ, the pressure is hydrostatic and V_p^{Norm} is equal to V_p^{Obs} (Marín-Moreno *et al.*, 2013a; Scott *et al.*, 2009). If no density data are available, the equivalent depth method and the Eaton method both need a function that relates V_p to density. Therefore, as above, the Hamilton's (1978) relationship for a silt, clay and turbidite lithology is applied.

4.5 Case Study: The Eastern Black Sea Basin

4.5.1 Geological Setting

The Black Sea Basin is a semi-isolated marine basin located within the Alpine orogenic belt, with the Balkanides-Pontides to the south and southwest, the Caucasus in the north-east and the Crimean Peninsula in the north (Fig. 4.1). The Black Sea was formed in a back-arc extensional context (Okay *et al.*, 1994; Zonenshain & Lepichon, 1986) and Görür (1988) constrained the onset of opening as Aptian to Cenomanian. It currently experiences compressional deformation due to the northward movement of the Arabian plate and westward escape of the Anatolian Block (McClusky *et al.*, 2000). Although at present the BSB has a single flat abyssal plain at 2200 m depth and is considered a single de-

pocentre (Meredith & Egan, 2002; Robinson *et al.*, 1996), based on deep seismic reflection data (Zonenshain & Lepichon, 1986) it is divided into the Western and Eastern Black Sea basins, separated by the Mid Black Sea High (MBSH) (Fig. 4.1). The EBSB opened in a NE-SW direction by the rotation of Shatsky Ridge away from the MBSH (Robinson *et al.*, 1996), with extension continuing into the early Cenozoic based on a strain-rate inversion method (Shillington *et al.*, 2008).

The acoustic basement of the basin is thought to be composed of various lithologies, including shallow water carbonates and significant volcanic material (Robinson *et al.*, 1996). The basin infill is mainly post-rift, Cenozoic sediments (Finetti *et al.*, 1988; Shillington *et al.*, 2008), with older pre-rift sediments identified on the shelf (Robinson *et al.*, 1995a). Early Paleocene-Middle Eocene (65-45 Ma) sediments are dominantly siliciclastic turbidites, shallow and/or deep water mudstones, pelagic mudstones and marls often containing large amounts of volcanogenic sediments (Robinson *et al.*, 1995b; Yilmaz *et al.*, 1997). Middle Eocene-top Eocene sediments (45-33.9 Ma) are dominantly siliclastic turbidites (Yilmaz *et al.*, 1997) with some carbonate and terrigenous deposits (Zonenshain & Lepichon, 1986). The Maikop formation, top Eocene-Early Miocene (33.9-20.5 Ma), comprises mud rich in organic carbon (Robinson *et al.*, 1996). Samples offshore showing very little sand within this formation (10%, Shillington *et al.*, 2008), and its low seismic reflectivity suggests homogeneity in physical properties (Zonenshain & Lepichon, 1986). Early Miocene-Middle Miocene (20.5-13 Ma) sediments are mudstones and turbidites (Meredith & Egan, 2002; Robinson *et al.*, 1995a). The Sarmatian, Middle Miocene-Late Miocene (13-11Ma), comprises terrigenous sediments (Nikishin *et al.*, 2003). Late Miocene-top Pliocene (11-1.8 Ma) sediments comprise sands, conglomerates (Robinson *et al.*, 1995b), chalks, siderites, clays and limestones (Hsü & Giovanoli, 1980; Ross, 1978). Top Pliocene-Present (1.8-0 Ma) sediments, comprise mostly clays but they also include marls and occasional turbidites (Hiscott & Aksu, 2002; Hsü & Giovanoli, 1980; Ross, 1978). Shillington *et al.* (2008) present a more detailed lithological description of the sediments and how they were identified.

Mud volcanoes are the surface response of an overpressured layer and they may indicate compressional deformation, since compression squeezes the sediment laterally and may generate overpressure in low permeability sediments if the fluids cannot escape rapidly enough. In the EBSB they are found along the continental shelf (Kruglyakova *et al.*, 2004), with the largest density located in the compressional zone to the south of the Crimean Peninsula within the Sorokin Trough (Dimitrov, 2002; Ivanov *et al.*, 1996) (Fig. 4.1).

4.5.2 Assumptions, Modelling Parameters and Boundary Conditions

In the EBSB we have well-constrained layer thicknesses and V_p. However, our objective function (Eq. 4.22) also requires density and V_p in hydrostatic conditions. We have estimated ρ^{Obs} values from V_p^{Obs} values using the Hamilton's (1978) relationship and the V_p^{Norm} using the method explained in section 4.4. A 3% error in the data has been considered for $s\left(V_p^{Obs}\right)$, $s\left(V_p^{Norm}\right)$ and $s\left(z_b^{Obs}\right)$, and a 5% error for $s\left(\rho^{Obs}\right)$ to account for the scattering in the Hamilton's (1978) relationship. A 3% error corresponds to an error for the observed V_p of between 0.05-0.1 km s^{-1}, which is within the V_p perturbation applied for the Maikop formation in Scott *et al.* (2009). Below the layer L5-Maikop, where the LVZ was identified (Scott *et al.*, 2009), a rapid increase in V_p is at 5900-6750 mbsf using a set of 1D V_p profiles (Fig. 4.4). To effectively model this rapid increase in V_p, the layer below the Maikop formation has been subdivided into two sublayers, the upper layer L6u and the lower L6l. In the 1D model, we use a final mesh of 125 cells and 300 data points

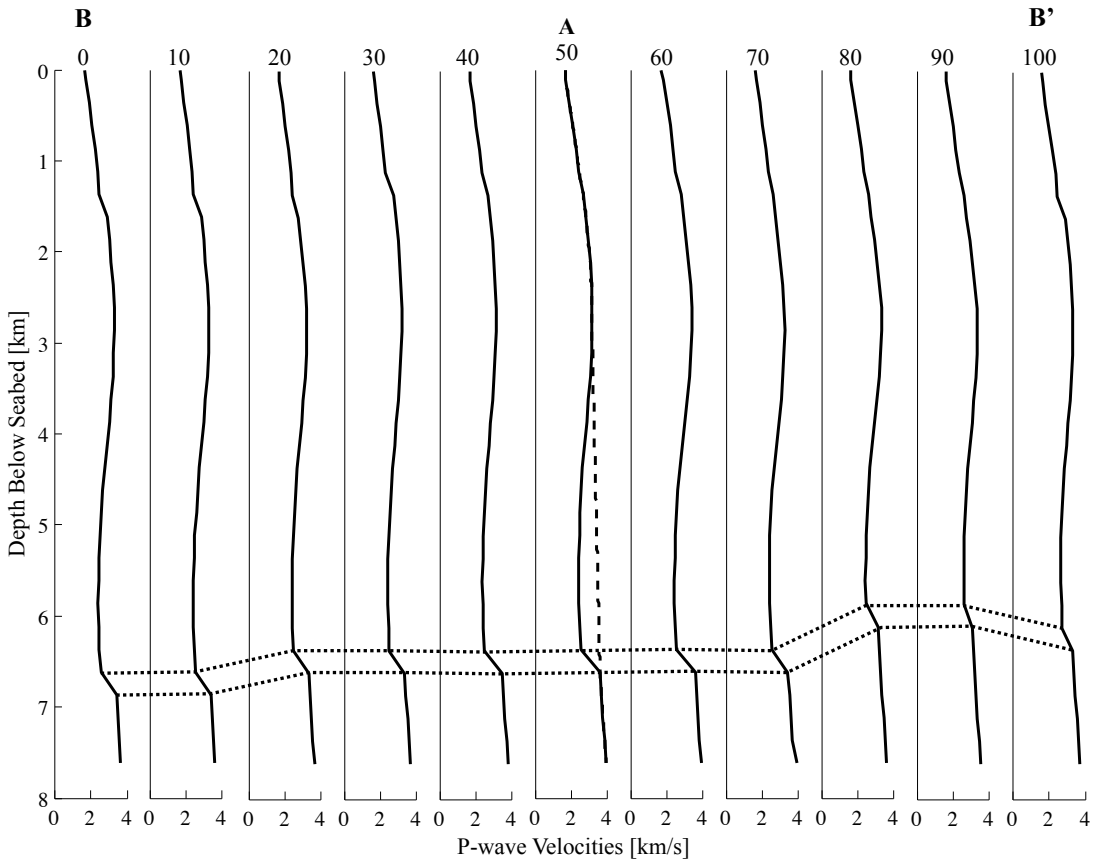

Figure 4.4: 1D profiles of observed V_p variation with depth (solid lines) inferred from wide-angle seismic data along B-B'. The profiles are separated by a distance of 10 km. Dotted lines mark the transition from the LVZ to normal V_p. Our 1D inverse analysis is for profile A-50. This profile shows the observed V_p (solid line) and the estimated V_p in hydrostatic conditions (dashed line).

for each of the first three terms in Eq. 4.22, and 8 data points for the fourth term, which gives a total of 908 data points. In the 2D model, we use a final mesh of 125x15 cells and 13620 data points in Eq. 4.22 (4500 data points for each of the first three terms and 120 for the last term).

The initial inputs and upper and lower bounds of the model parameters used in the inversion are given in Table 4.1. Other modelling parameters are given in Table 4.2.

Our inverse model (Eq. 4.22) drives the solution to relate changes in V_p to changes in pore pressure and the results of the forward model are significantly influenced by the imposed boundary conditions. For these reasons, in the 1D model, where horizontal flow is not allowed, the bottom boundary condition is imposed as $P^* = 0$ to represent the increase in V_p below L6u. If instead we use $\Delta P^*/\Delta\zeta = 0$, the overpressure below L6u would be controlled by the maximum overpressure of the sediments above, and it would not be physically possible to represent the observed increase in V_p by reducing the overpressure. In the 2D model, we can study both bottom boundary conditions $P^* = 0$ and $\Delta P^*/\Delta\zeta = 0$, and in theory, still represent the higher V_p at the bottom. As described in section two, the top boundary condition is imposed as $P^* = 0$ and the left and right boundary conditions are imposed as $P^* = 0$. The lithological parameters used in the inversion (Table 4.1) are constant within a layer because there are no data to justify their variation, because any lateral variation is likely to be minor, and to reduce the computational cost of the calculation.

Table 4.1: Initial input and lower and upper bounds for the model parameters used in the inversion: surface porosity, compaction factor, initial intrinsic permeability, intrinsic permeability evolution parameter, horizontal to vertical permeability ratio, and uncompacted thickness. The symbol H is the observed present-day thickness of stratigraphic layers.

Parameters	Initial Inputs	Lower Bound	Upper Bound	References for Initial Inputs
ϕ_0	0.55	0.30	0.70	Robinson et al. (1995a)
c [km^{-1}]	0.55	0.10	1	Robinson et al. (1995a)
k_{i0} [m^2]	1E-17	1E-13	1E-22	this study
γ	14	11.50	17.50	Audet & McConnell (1994)
α	10	1	1E4	Harrison & Summa (1991)
H_0 [km]	1.3*H	H	3*H	this study

Although in the 2D model the lithological parameters are fixed for each layer, we allow lateral variations in uncompacted layer thickness (and hence the sedimentation rate). This lateral variation of sedimentation rate balances the extra compaction that may arise from lateral fluid flow. Although the sedimentation rate varies laterally, the present-day layer

thicknesses are held laterally uniform. The layers are flat and horizontal in this part of the basin (Fig. 4.1) and variable layer thicknesses and lateral variation of the sedimentation rate would generate horizontal stress that our forward model does not consider.
The lateral bounds of the model are kept within the centre of the EBSB to avoid the effects of the compressional tectonic regime to the east and the effects of the MBSH to the west.

Table 4.2: Model parameters. Symbols T_0 and ρ_f^0 are the temperature and fluid density at seabed conditions.

Parameters	Value	References
g [m/s^2]	9.80	Robinson et al. (1995a)
Seabed depth [km]	2.13	Scott et al. (2009)
T_0 [$^\circ$C]	9	Minshull & Keddie (2010)
Thermal gradient [$^\circ$C/km]	26	Minshull & Keddie (2010)
ρ_f^0 [kg/m^3]	1030	Cloetingh et al. (2003)
ρ_s [kg/m^3]	2700	Scott et al. (2009)

4.5.3 Results

1D Results

The 1D results presented here are for location A (Figs. 4.1 and 4.4). Convergence was achieved with 2300-3500 evaluations of the objective function (Eq. 4.22). The velocities and densities obtained with our inverse model show a good match to the observed data (Fig. 4.5a; b). The misfit between the observed and calculated V_p within the Maikop formation reaches a maximum of ∼0.2 m/s, 8% misfit, which is higher than the 3% seismic velocity error assumed in the data. This may arise from either variations in lithology that are not accounted for by our model, inherent smoothing in the tomographic velocity model, or deviations from the Hamilton's (1978) V_p-density relationship in this layer. Nevertheless, our inverse model successfully finds a set of parameters that reproduce the observed velocities and indirectly validate other outputs from our forward model (Figs. 4.5c-e and 4.6). We infer the presence of overpressure mainly located in the Maikop formation at ∼3500-6500 mbsf. This overpressure is associated with a V_p decrease of ∼1 km s^{-1}, a density decrease of ∼250 kg m^{-3}, a porosity increase of ∼0.15, a compressibility increase of ∼0.5x10^{-8} Pa^{-1}, and a permeability increase of ∼3x10^{-13} m s^{-1}, with respect to the values under hydrostatic conditions (Fig. 4.5). Since density, compressibility, and permeability are functions of porosity (Eqs. 4.3, 4.12 and 4.17), which varies little within the Maikop formation, these parameters change little within this layer (Fig. 4.5).

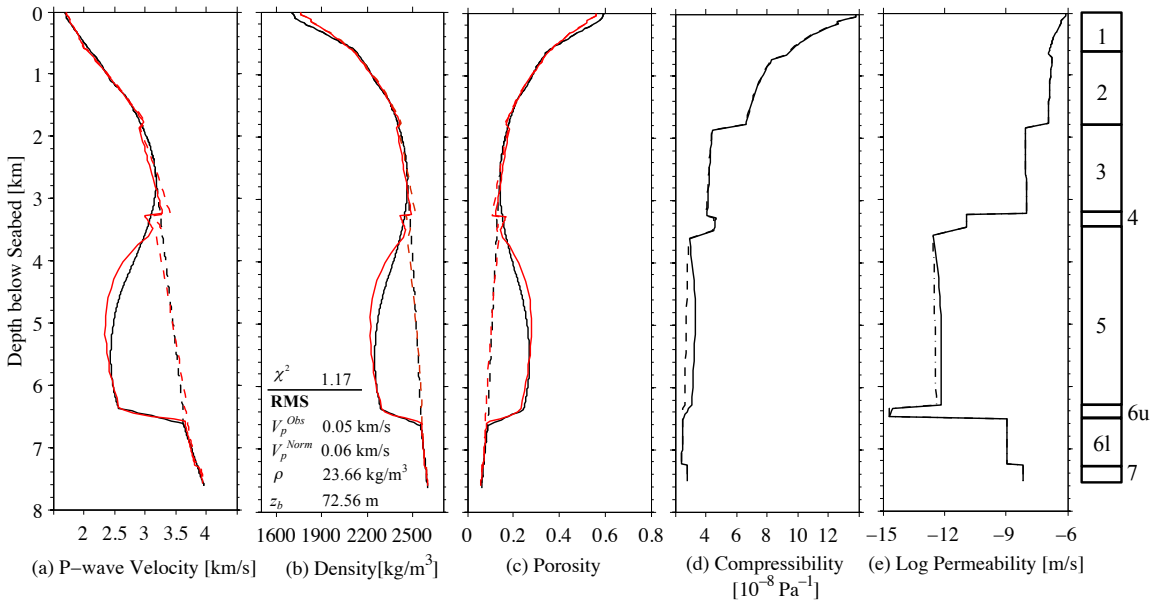

Figure 4.5: Parameter variation with depth at site A (Fig. 4.1). (a-c) Results from wide-angle seismic data (black line; Scott *et al.* (2009)) compared to those obtained with the best-fitting parameters of our inverse model (red line). The inset on the bottom right corner of (b) shows the χ^2 error and RMS error of each term in the misfit function (Eq. 4.22). (d-e) Results obtained with the best-fitting parameters from our inverse model. Solid lines represent observed conditions, and dashed lines hydrostatic conditions. The column on the left side shows the stratigraphic layers.

In the Maikop formation, a compressibility value of ∼3.5x10^{-8} Pa^{-1} (Fig. 4.5d) for a layer with 90% shale and 10% sandstone (Shillington *et al.*, 2008) is consistent with published values for the bulk compressibility of clays, for which β can vary from 2x10^{-6} Pa^{-1} for plastic clay to 6.9x10^{-8} Pa^{-1} for medium hard clay (Domenico & Mifflin, 1965). For layer L5 (the Maikop) we have obtained a permeability of ∼5x10^{-13} m s^{-1} and for layer L6u a permeability of ∼3x10^{-15} m s^{-1} (Fig. 4.5e). The implications of the significantly reduced permeability for layer L6u are discussed in the next section. Our pore pressure and λ^* (Eq. 4.26) values agree with those estimated using the Eaton method with an exponential factor of 3, and are lower than those obtained using the equivalent depth method (Fig. 4.6).

$$\lambda^* = \frac{P - P_h}{\sigma'_h} \tag{4.26}$$

In Eq. 4.26 σ'_h is the vertical effective stress in hydrostatic conditions. We have calculated with our inverse model a maximum overpressure of ∼44 MPa at ∼6400 mbsf, of which 94% is due to disequilibrium compaction and 6% due to aquathermal pressuring and a maximum λ^* of ∼0.62 at ∼5200 mbsf associated with an overpressure of ∼42 MPa.

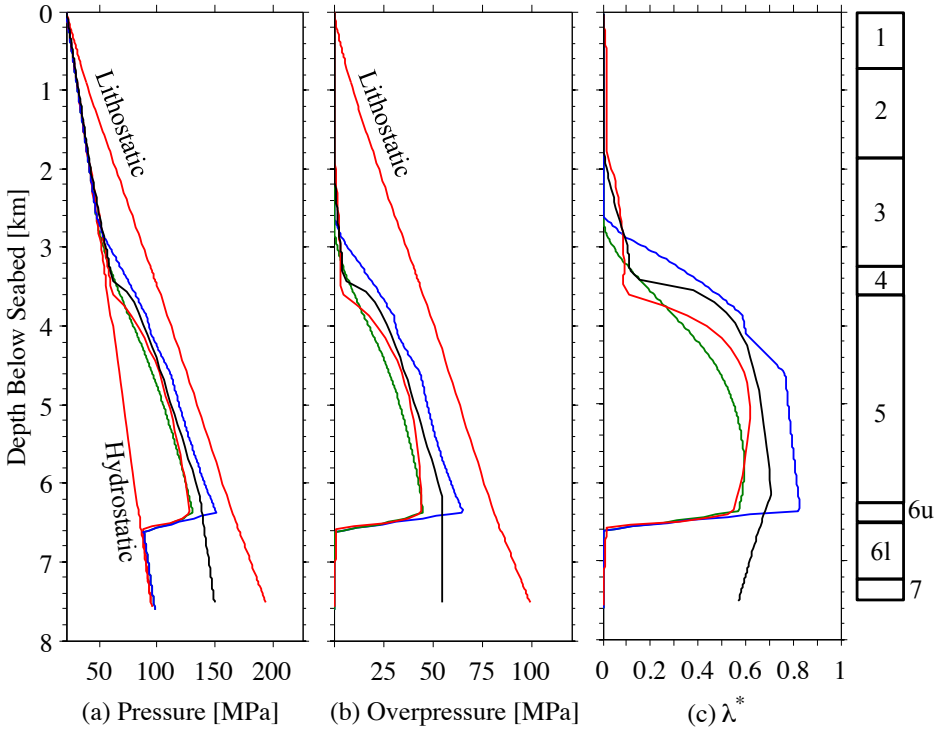

Figure 4.6: Pressure and λ^* (Eq. 4.26) variation with depth at site A (Fig. 4.1). Red lines are results using the best-fitting parameters from our inverse model, blue and green lines are results calculated using the V_p model of Scott *et al.* (2009), and the equivalent depth and the Eaton (with E=3) methods (Eqs. 4.24 and 4.25), respectively, and black lines results from Marín-Moreno *et al.* (2013a). The column on the left side shows the stratigraphic layers.

In this analysis we have assumed a constant thermal gradient of 26 °C km^{-1} that is consistent with measurements to ∼2500 m depth in the HPX-1 borehole (Fig. 4.1; Menlikli *et al.*, 2009; Minshull & Keddie, 2010). However, the thermal gradient in sediments from measurements to ∼625 m depth ranges from 32-44 °C km^{-1} at site 379 (Fig. 4.1; Erickson & Von Herzen, 1978). Variations in thermal gradient affect viscosity, which affects permeability and also fluid density. Figure 4.7 shows that a variation of ±50% of the thermal gradient (39 °C km^{-1} and 13 °C km^{-1}) generates a decrease and increase of the maximum overpressure of ∼11% and of ∼15%, respectively. This result implies that, for the thermal gradient perturbations considered, permeability changes resulting from changes in viscosity dominate over changes in fluid density. In these circumstances, changes in overpressure generated by disequilibrium compaction are greater than those generated by aquathermal pressuring.

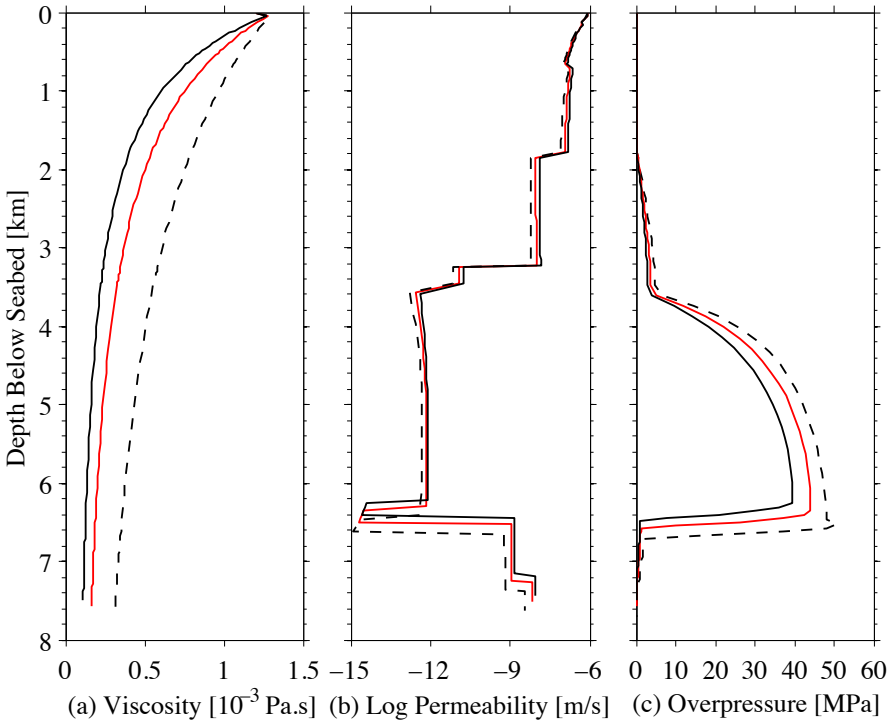

Figure 4.7: Parameter variation with depth at site A (Fig. 4.1) using a ±50% perturbation in the thermal gradient (DT/Dz) 26 °C km^{-1} applied in the forward model. Results using a DT/Dz of 26 °C km^{-1} (red lines), of 39 °C km^{-1} (black-solid lines), and of 13 °C km^{-1} (black-dashed lines).

Sensitivity Analysis of the 1D Inverse Model Parameters

We used a Monte Carlo error propagation technique to estimate the posteriori covariance matrix of the model parameters. This technique applies the inverse problem to a range of random noisy data inputs. We consider the forward problem given by

$$G\left(\mathbf{m}_k\right) = \mathbf{d} + \delta_k \tag{4.27}$$

where G is our forward model, $\mathbf{m}_k$ is a range of model parameters vectors, $\mathbf{d}$ is the noise-free data vector and δ_k is a range of imposed random noise vectors. Then, we apply the inverse model to obtain $\mathbf{m}_k$, and the posteriori covariance matrix $\mathbf{C}_\mathrm{M}$ can be estimated by

$$\mathbf{C}_\mathrm{M} \approx \frac{1}{A}\sum_{k=1}^{A}\left(\mathbf{m}_k - \mathbf{m}^*\right)\left(\mathbf{m}_k - \mathbf{m}^*\right)^\mathrm{T} \tag{4.28}$$

where $\mathbf{m}^*$ is the noise-free model and A is the number of models used. The evolution of the standard deviation of model parameters $\mathbf{s}_\mathrm{m} = \sqrt{\mathrm{diag}\left(\mathbf{C}_\mathrm{M}\right)}$ with increasing number of models is shown in Fig. 4.8.

The 95% confidence intervals for individual parameters are given by (Aster *et al.*, 2005)

$$\mathbf{m}^* \pm t_{\nu,1-0.05/2}\mathbf{s}_\mathrm{m} \tag{4.29}$$

where $t_{\nu,1-0.05/2}$ is the student's distribution t-value for ν degrees of freedom (number of data points minus number of model parameters). As mentioned above, we have used 908 data points and the number of model parameters per layer is 5, which gives a total of 40 model parameters. Therefore, the value of $t_{868,1-0.05/2}$ is 1.96 (Draper & Smith, 1998). As $\mathbf{C}_\mathrm{M}$ is not diagonal, the principal axes are not aligned with the m_i axis directions. However, we can project the 95% error ellipses onto the m_i axes to provide a conservative joint confidence interval for any pair of model parameters (Aster *et al.*, 2005).

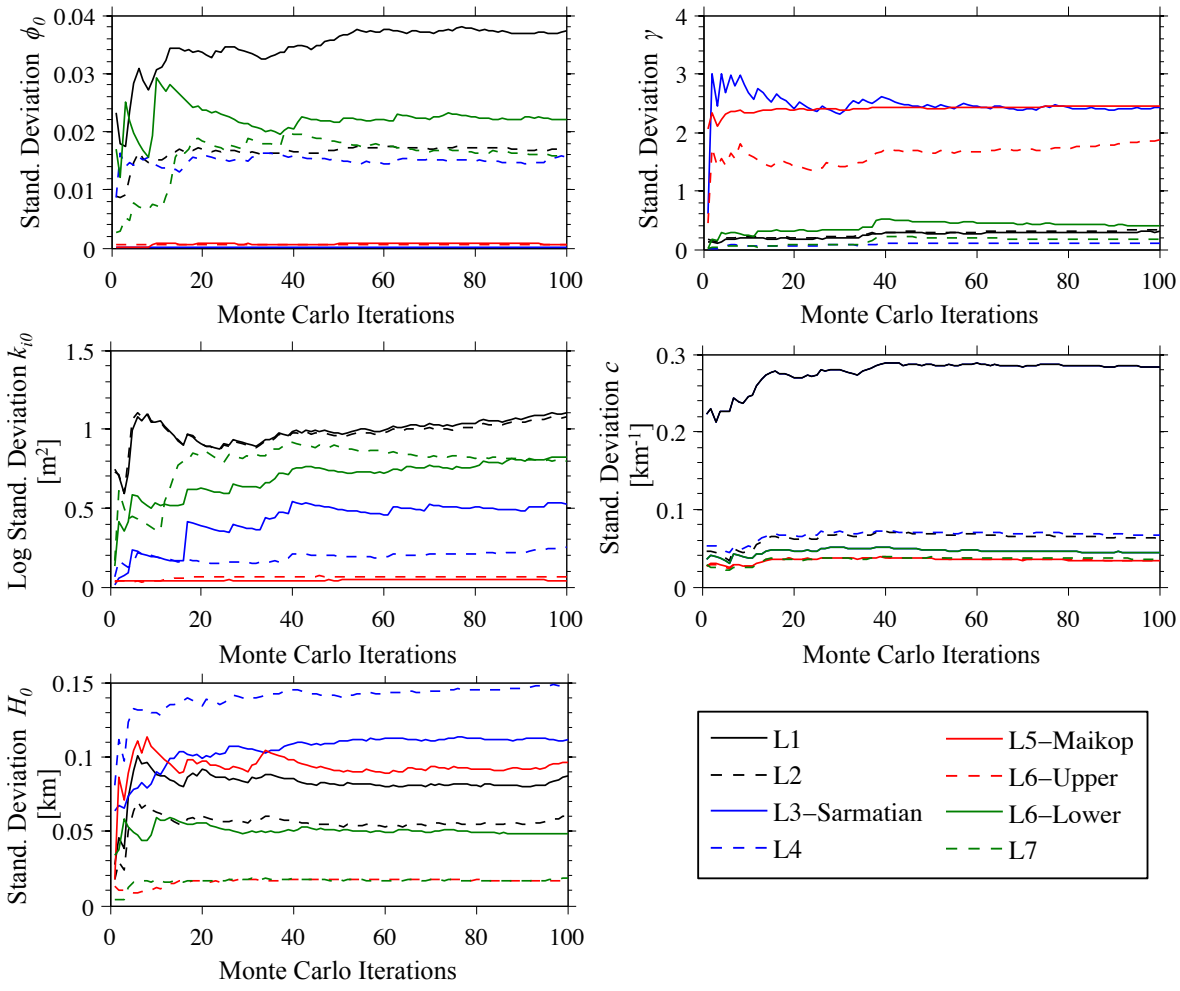

Figure 4.8: Evolution of the standard deviation of inverse model parameters $\mathbf{s}_\mathrm{m}$ with number of Monte Carlo iterations, i.e. number of noisy data vectors tested (Eq. 4.27), at site A (Fig. 4.1).

The joint 95% confidence interval ellipse for a pair of model parameters with unknown

data uncertainties is given by

$$x = m_i + \left(\sqrt{2 \cdot F_{\nu,2,0.95}}\left(\sqrt{\eta_{(1,1)}} \cdot \mathbf{\Psi}_{(1,1)}\cos(\theta) + \sqrt{\eta_{(2,2)}} \cdot \mathbf{\Psi}_{(1,2)}\sin(\theta)\right)\right)$$
$$y = \underset{j \neq i}{m_j} + \left(\sqrt{2 \cdot F_{\nu,2,0.95}}\left(\sqrt{\eta_{(1,1)}} \cdot \mathbf{\Psi}_{(2,1)}\cos(\theta) + \sqrt{\eta_{(2,2)}} \cdot \mathbf{\Psi}_{(2,2)}\sin(\theta)\right)\right)$$
$$i = j = 1, 2, \ldots, M \tag{4.30}$$

where x and y are the coordinates of the ellipse, M is de number of model parameters, $F_{\nu,2,0.95}$ is the Fisher's distribution F-value for, ν degrees of freedom, a 2D ellipse and 95% confidence, $\eta_{(,)}$ and $\mathbf{\Psi}_{(,)}$ are the eigenvalue and eigenvector, respectively, of $\mathbf{C}_{\mathrm{M}}^{*} = \begin{pmatrix} \mathbf{C}_{\mathrm{M}}(i,i) & \mathbf{C}_{\mathrm{M}}(i,j) \\ \mathbf{C}_{\mathrm{M}}(j,i) & \mathbf{C}_{\mathrm{M}}(j,j) \end{pmatrix}$ 2x2 submatrices of $\mathbf{C}_{\mathrm{M}}$ with parameters m_i and m_j, and θ varies between 0 and 2π. Each eigenvector of $\mathbf{C}_{\mathrm{M}}$ points along one of the axes of the ellipse and its associated eigenvalue scales the ellipse in the eigenvector direction. The value of $F_{\nu,2,0.95}$ is given by (Draper & Smith, 1998; Paradowski, 1997)

$$F_{\nu,2,0.95} = \frac{\nu}{2}\left((1 - 0.95)^{-2/\nu} - 1\right) \tag{4.31}$$

and therefore the value of $F_{868,2,0.95}$ is 3.01. The inclination of the error ellipses axes with respect to the parameter axes is associated with the correlation coefficient of its parameters pairs. The correlation coefficient for a pair of model parameters $r(m_i, m_j)$ is given by

$$r(m_i, m_j) = \frac{\mathbf{C}_{\mathrm{M}}(m_i, m_j)}{\mathbf{s}_{\mathrm{m}}(m_i)\,\mathbf{s}_{\mathrm{m}}(m_j)} \tag{4.32}$$

Values of $r(m_i, m_j)$ approaching +1 and -1 mean maximum correlation of the parameters and a highly eccentric error ellipse projection with a positive and negative slope, respectively. As $r(m_i, m_j)$ for the principal axes approaches zero, parameters are less correlated. The 95% confidence values for the model parameters are shown in Table 4.3.

Table 4.3: 95% confidence interval values of inverse model parameters.

Strat. Layers	ϕ_0	c [km^{-1}]	log k_{i0} [m^2]	γ	H_0 [km]
1	0.56±0.07	0.99±0.55	-13.00±2.16	11.16±0.59	0.83±0.17
2	0.52±0.03	0.90±0.12	-13.00±2.11	10.93±0.65	1.78±0.12
3-Sarmatian	0.40±0.00	0.59±0.09	-14.37±1.03	16.81±4.74	2.07±0.22
4	0.66±0.03	0.64±0.13	-16.07±0.49	12.75±0.22	0.59±0.29
5-Maikop	0.40±0.00	0.41±0.06	-19.39±0.08	10.50±4.82	3.58±0.19
6u	0.40±0.00	0.39±0.07	-21.57±0.13	12.35±3.67	0.27±0.03
6l	0.41±0.04	0.39±0.09	-15.70±1.61	13.94±0.80	1.16±0.09
7	0.48±0.03	0.45±0.07	-14.51±1.57	13.81±0.33	0.51±0.04

In Fig. 4.9 we show the error ellipses and the correlation coefficients of model parameters for layer L5 (the Maikop). Table 4.3 shows smaller 95% confidence intervals of k_{i0} for layers L4, L5 and L6u than for other layers. This result is consistent with the presence of overpressure, which adds another physical constraint to the range of possible k_{i0} able to model the observed data. High values of k_{i0} with large 95% confidence intervals, ranging from ∼2 to ∼4.3 orders of magnitude, are obtained for the non-overpressured layers (layers L1, L2, L3, L6l and L7). These confidence intervals are large because a large range of possible intrinsic permeabilities could result in hydrostatic pore pressure. Besides, in the layers close to model boundaries, the effects of the imposed boundary conditions dominate and k_{i0} is poorly constrained.

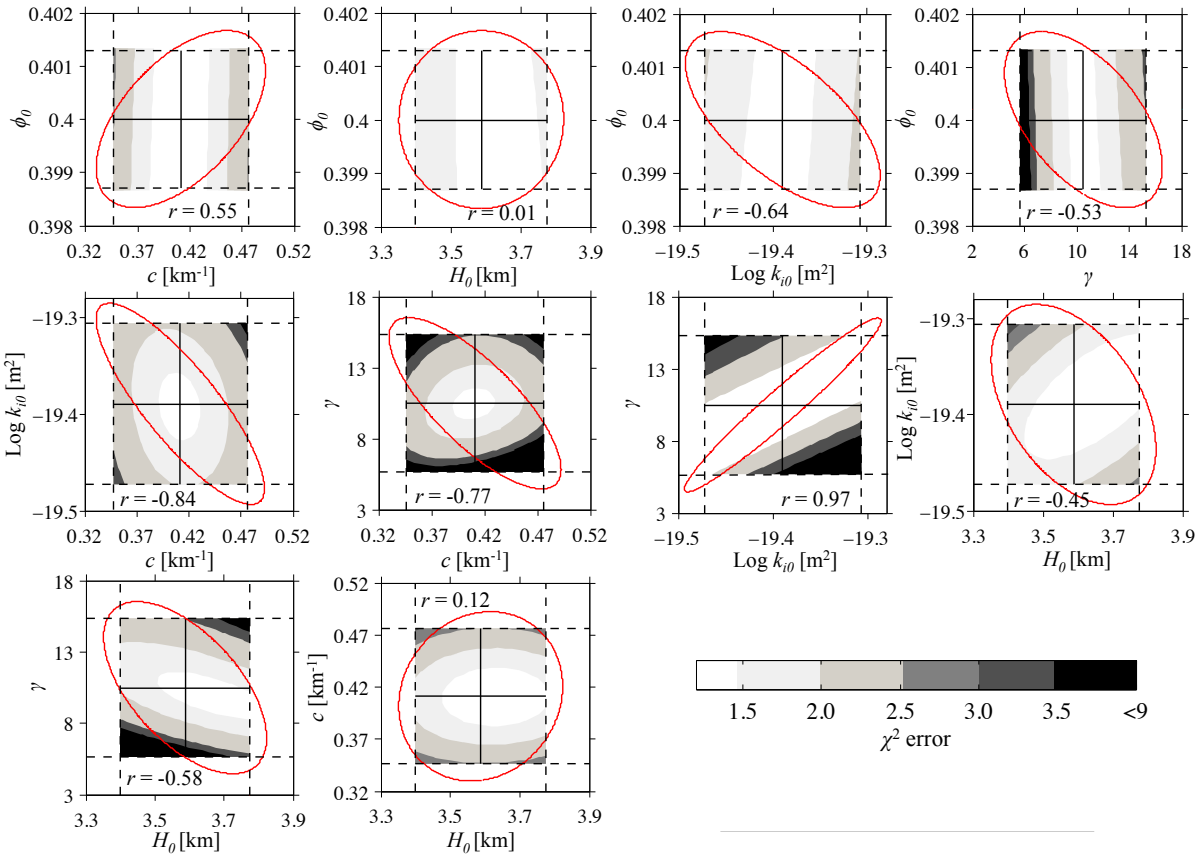

Figure 4.9: Projections of the 95% error ellipses onto parameters axes (red solid lines) and individual 95% confidence interval (dashed lines) for layer L5-Maikop best-fitting parameters (centre of the black cross) at site A (Fig. 4.1). The numbers on the panels show the correlation parameters. Contour plots, sensitivity of the χ^2 error to the 95% confidence parameter space of layer L5-Maikop best-fitting individual parameters.

The high c values in layers L1 and L2 may indicate inadequacies in the exponential porosity-effective stress law at shallower depths (Allen & Allen, 2005). The sign of the correlation

coefficients, except $r(c, k_{i0})$, is consistent with the imposed constitutive relationships in section 2. The large negative value of $r(c, k_{i0})$ may be explained by the fact that, for a given ϕ_0 and depth, a small c will result in porosities higher than expected with a normal c, and therefore an undercompacted sediment. In this situation, the undercompaction is not caused by the presence of overpressure but rather by a high stiffness of the sediment. This undercompacted sediment will have low densities and low V_p without the existence of overpressure. Therefore, a decrease in V_p can result from either a decrease in c or an increase in overpressure driven by a decrease in k_{i0} and these parameters must be strongly negatively correlated.

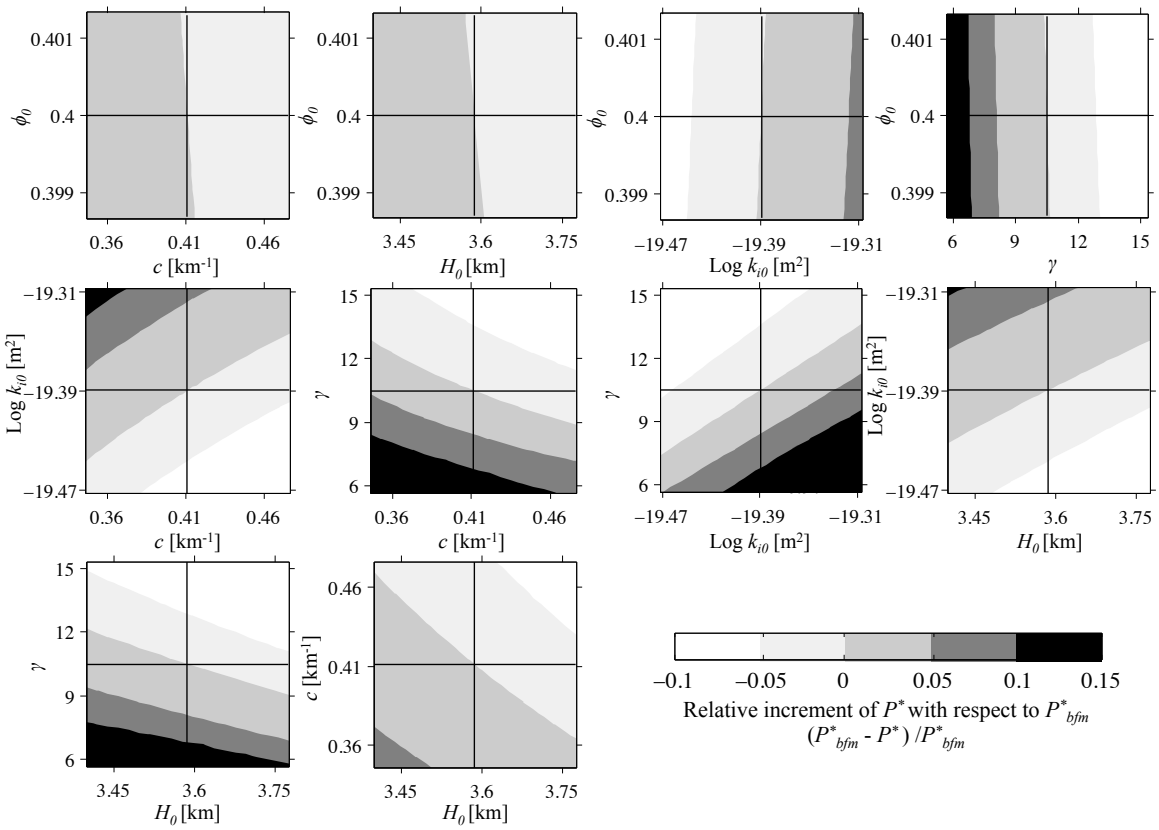

Figure 4.10: Sensitivity of the maximum overpressure obtained with the 95% confidence interval of layer L5-Maikop individual parameters relative to the maximum overpressure obtained with the best-fitting parameters P^*_{bfm} (centre of the black cross) at site A (Fig. 4.1).

Figures 4.9 and 4.10 show the sensitivity of χ^2 and maximum overpressure, respectively, to the model parameters of layer L5-Maikop within their 95% individual confidence interval. Most of the contours in the sensitivity plots of Fig. 4.9 are ellipses or elongated ellipses indicating that the model has a single local (and so a single global) minimum. The lack of a clear minimum for some parameters indicates that these parameters are poorly constrained

with the available data. From Fig. 4.10 we infer that the maximum overpressure ranges from ∼40-51 MPa (∼10% below to ∼15% above the maximum overpressure found with the optimum parameters), with a 95% confidence. We apply the 1D inversion to several 1D velocity depth profiles along the 2D section (Fig. 4.1). The small variability of best-fitting values in this quasi-2D study (Fig. 4.11) confirms the robustness of the parameter estimates.

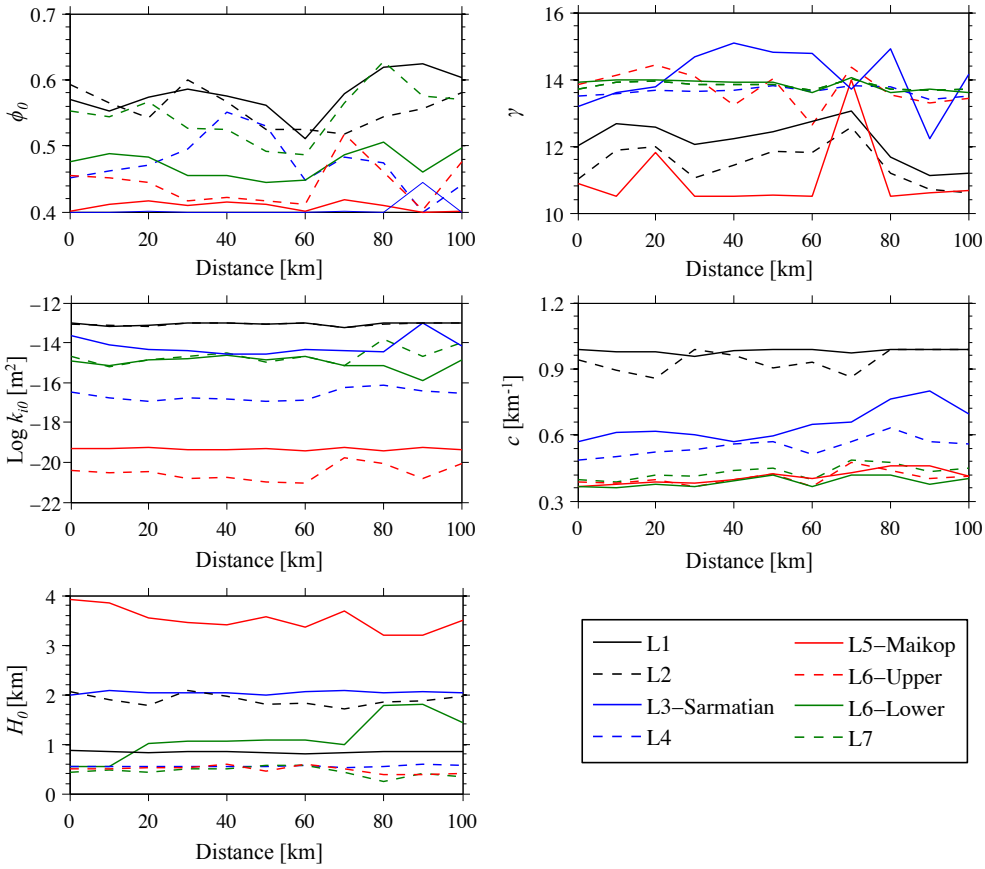

Figure 4.11: Quasi-2D analysis of lateral variation of the best-fitting inverse model parameters calculated using data from the 1D profiles shown in Fig. 4.4.

2D Results

In the 1D model we imposed a zero overpressure bottom boundary to reproduce the assumed V_p^{Norm} below L5-Maikop, but this V_p^{Norm} may also be due to a high horizontal fluid flow. To account for this possibility, we extend our analysis into two dimensions and allow horizontal fluid flow through the zero overpressure lateral boundaries. Convergence was achieved with ∼7000 evaluations of the objective function (Eq. 4.22), for both boundary conditions. We can reproduce the assumed V_p^{Norm} below layer L6u with the zero overpressure boundary condition (Fig. 4.12d), whereas with the zero flow we cannot because the

side boundary conditions only have significant influence within ∼25 km of the sides of the model. Therefore, high lateral fluid flow is not likely to be the mechanism decreasing the overpressure below L6u and, close to the side boundaries, the results are not representative of the hydrodynamic behaviour of the system.

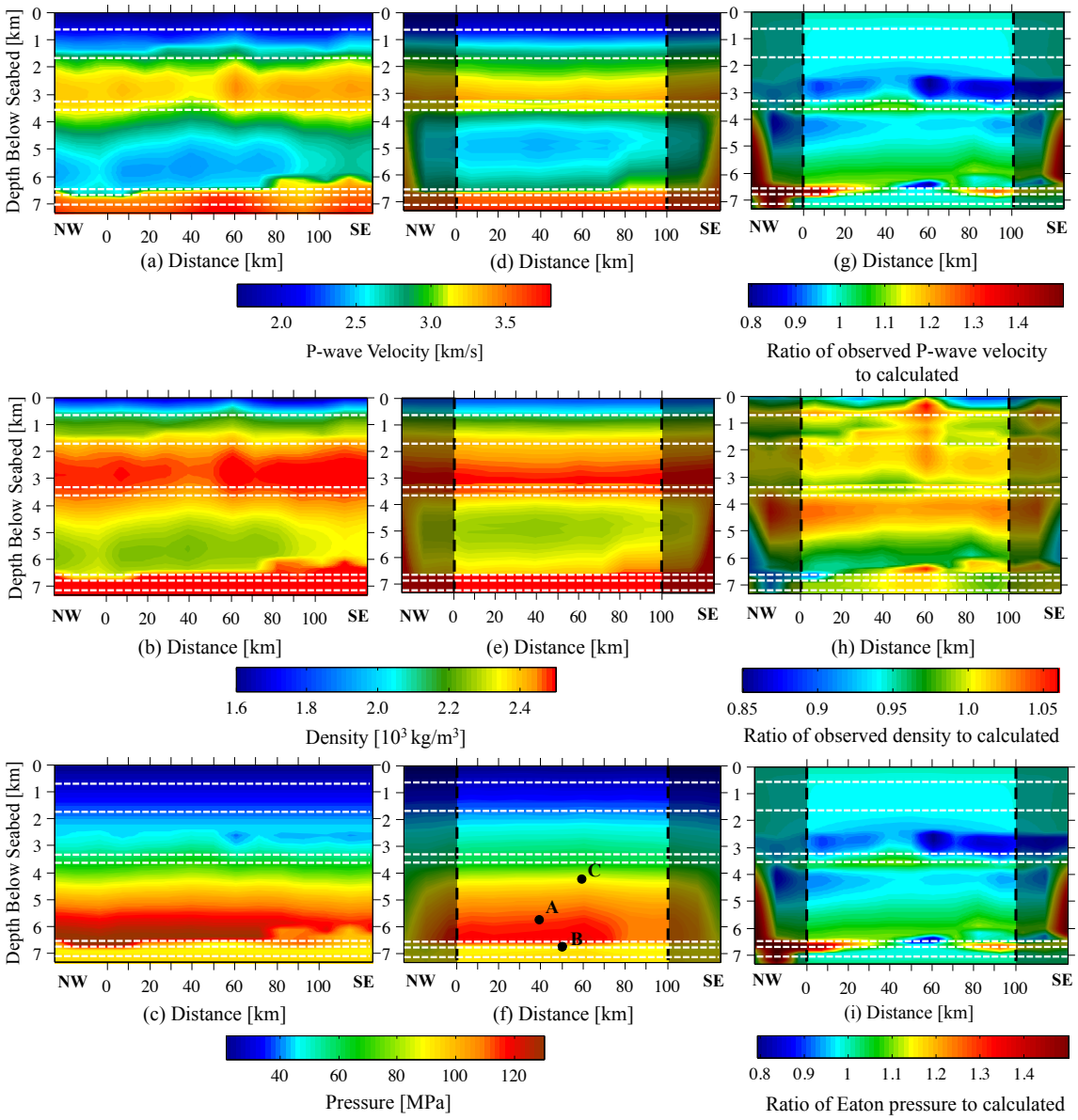

Figure 4.12: 2D parameter variation for the zero overpressure lower boundary condition along B-B' (Fig. 4.1). (a) Velocities from wide-angle seismic data. (b) Corresponding densities from the Hamilton's (1978) relationship (Eq. 4.23). (c) Pore pressure from the Eaton method (with an E of 3) (Eq. 4.25). (d-f) Results obtained with our inverse model. (g-i) Ratio between the (a-c) and (d-f). The areas outside the dashed lines in (d-i) are influenced by the lateral boundary conditions. Dashed-white lines show the layer interfaces and black circles (A, B and C) in (f) show the points for the analysis in Fig. 4.14.

The difference in fit below layer L6u results in a lower χ^2 error obtained with the zero overpressure bottom boundary condition (Table 4.4).

Table 4.4: Root mean square error of each term in the misfit function for the 2D model using the zero flow (BC-1) and zero overpressure (BC-2) bottom boundary conditions.

	BC-1	BC-2
χ^2	9.82	7.75
RMS		
V_p^{Obs} [km/s]	0.23	0.19
V_p^{Norm} [km/s]	0.16	0.11
ρ [kg/m^3]	58.57	55.67
z_b [m]	190	210

The relatively high χ^2 obtained for both 2D models, in comparison with the 1D model χ^2 error, may be due to the assumption of laterally constant lithological parameters within a layer. For both boundary conditions, the extremely high α values obtained for layers L1, L2 and L3 (Table 4.5) are due to hydrostatic pressure. In hydrostatic conditions α is not constrained and varying it by three orders of magnitude causes an increase of the χ^2 error of only 5%. As in the 1D analysis above, the high compaction factors for layers L1 and L2 (Table 4.5) may indicate inadequacies in the exponential porosity-effective stress law at shallower depths (Allen & Allen, 2005).

Table 4.5: Parameters found with our 2D inverse model using two bottom boundary conditions, zero flow (BC-1) and zero overpressure (BC-2).

	ϕ_0		c [km^{-1}]		log k_{i0} [m^2]		γ		α		H_0 [km]$^{(1)}$	
Strat. Layers	BC-1	BC-2	BC-1	BC-2	BC-1	BC-2	BC-1	BC-2	BC-1	BC-2	BC-1	BC-2
1	0.57	0.55	0.96	0.86	-13.20	-14.00	10.91	12.42	8331.11	809.32	0.82-0.88	0.80-0.86
2	0.56	0.51	0.93	0.87	-13.30	-13.81	11.21	12.14	7054.45	2653.48	1.84-2.00	1.64-1.80
3-Sarmatian	0.40	0.41	0.60	0.62	-14.19	-14.78	13.05	14.90	6556.90	1737.17	1.91-2.09	2.07-2.20
4	0.43	0.49	0.49	0.53	-16.71	-17.12	11.37	12.68	3.34	2.00	0.48-0.54	0.38-0.48
5-Maikop	0.50	0.40	0.42	0.39	-18.27	-19.29	15.75	14.33	1.36	15.12	3.97-4.64	3.58-3.94
6u	0.41	0.58	0.38	0.46	-17.20	-19.49	13.81	14.71	3.69	1.57	0.24-0.57	0.21-0.50
6l	0.40	0.48	0.39	0.38	-14.79	-15.41	14.45	14.00	4.26	123.32	0.81-1.07	0.81-0.93
7	0.40	0.56	0.41	0.42	-15.31	-15.52	14.46	14.11	4.17	159.34	0.36-0.60	0.29-0.51

(1) Minimum and maximum H_0

For the zero overpressure condition, the inferred initial intrinsic permeability k_{i0}, and permeability K_{zz} of layer L6u are ∼2 and ∼1 orders of magnitude higher, respectively, than values obtained from the 1D analysis above (Tables 4.3 and 4.5; Fig. 4.13c). This higher K_{zz} drives higher downwards fluid flow, but this is balanced by the increase in excess fluid dissipation through the zero overpressure side boundaries and due to the high horizontal permeability of layers L6l and L7 (Table 4.5). Other parameters are similar

to those for the 1D analysis (Tables 4.3 and 4.5). Most of our calculated results match those obtained directly using the wide-angle data, the Hamilton's (1978) relationship and the Eaton method (with an exponential factor of 3) within ±10% (Fig. 4.12g-i) but our contours are smoother (Fig. 4.12d-f). The smoothing arises because our model cannot simulate small lateral changes in V_p, because we do not allow the lithological parameters to change laterally.

We have obtained a maximum overpressure at 50 km distance and ~6500 mbsf of ~43 MPa, of which ~93% is due to disequilibrium compaction and ~7% due to aquathermal pressuring. The maximum λ^* of ~0.61 at 50 km distance and ~5200 mbsf is associated with an overpressure value of ~42 MPa. These values are similar to those obtained for the 1D analysis above (Fig. 4.13a; b). We have calculated a vertical and horizontal permeability for layer L5 (the Maikop) of ~5x10^{-13} m s^{-1} and of ~7.5x10^{-12} m s^{-1}, respectively, and for L6u of ~1.3x10^{-14} m s^{-1} and of ~2x10^{-14} m s^{-1}, respectively (Fig. 4.13c).

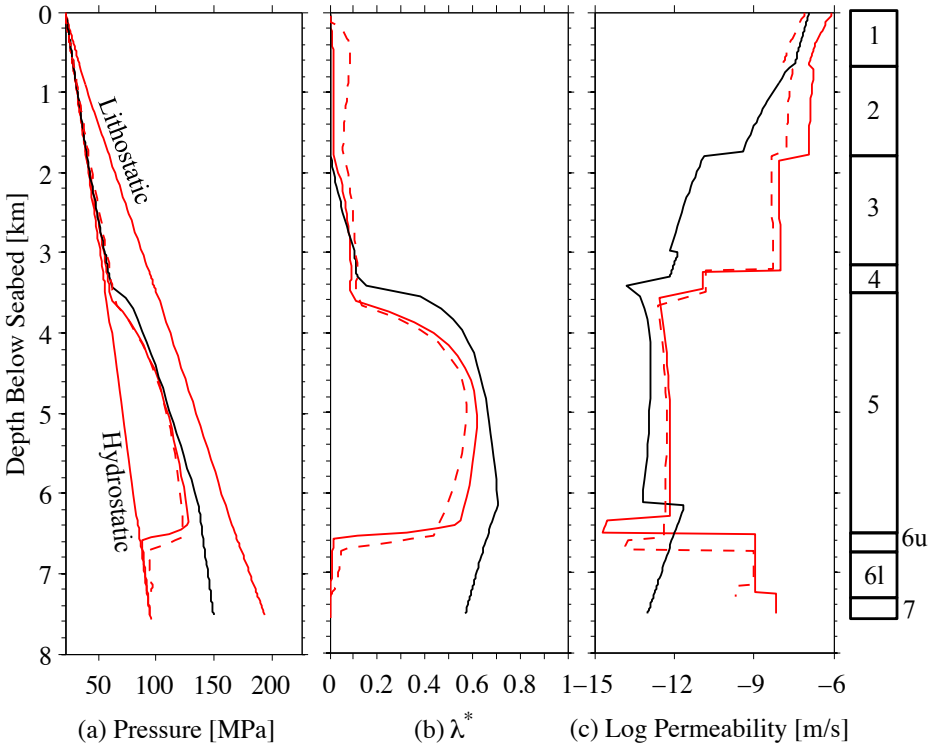

Figure 4.13: Parameter variation with depth at site A (Fig. 4.1). Comparison of the results obtained with the 1D analysis (solid lines), the 2D analysis (dashed lines) and the analysis presented by Marín-Moreno *et al.* (2013a) (black lines) using a disequilibrium compaction forward model with a zero flow bottom boundary. The column on the left side shows the stratigraphic layers with interfaces taken from the 2D analysis.

Rapid increases in overpressure are associated with the periods of relatively high sedimentation rates of 0.28-0.29 m ka^{-1} at 33.9-20.5 Ma and of 0.91-0.94 m ka^{-1} at 13-11 Ma (Fig. 4.14a). The present-day maximum fluid flow rates escaping upwards from the top of the overpressured zone (the Maikop) and downwards from the top of L6l are ∼0.02 m My^{-1} and of ∼8x10^{-3} m My^{-1}, respectively (Fig. 4.14b). Fluid flow is generally upwards at the top of the Maikop and downwards at the top of L6l (Fig. 4.14c).

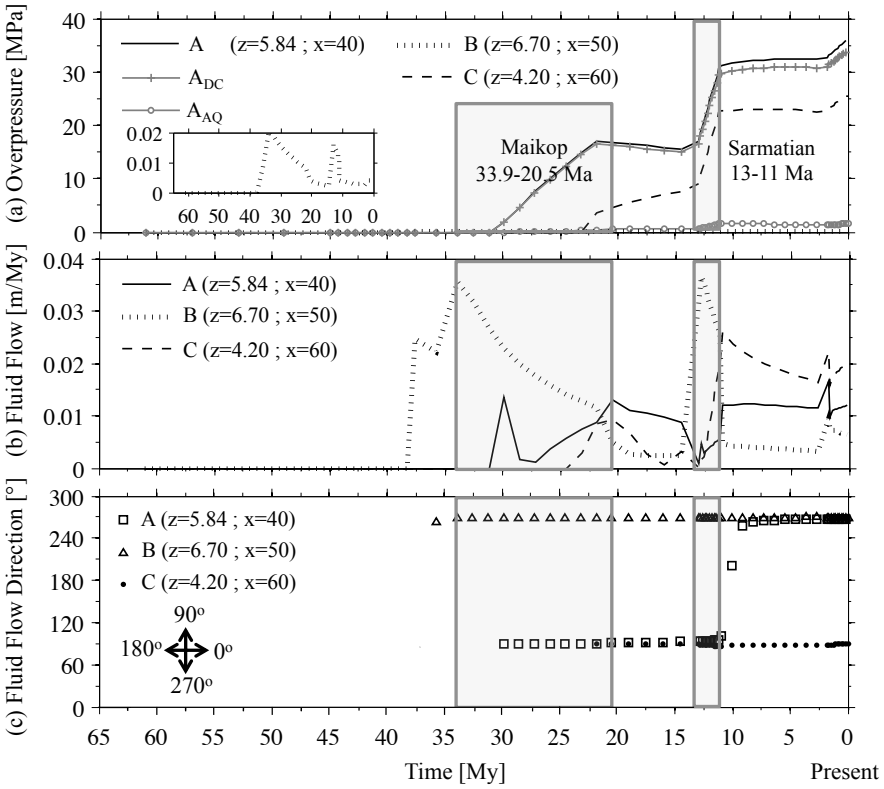

Figure 4.14: Evolution of overpressure, fluid flow (per m^2 of area) and fluid flow direction with time for the three study points, A, B and C (x and z coordinates in km) in Fig. 4.12. (a) Shows in grey the overpressure contribution from disequilibrium compaction (A_{DC}) (pluses) and the overpressure contribution from aquathermal pressuring (A_{AQ}) (circles) at point A. The graph inserted on (a) shows the overpressure evolution with time for point C. In (c) 0° represents the horizontal-East direction and 90° the vertical-North direction.

4.6 Discussion

We have presented an inverse approach to understand the hydrodynamics of a sedimentary basin by using the constraints imposed by seismic and geological data and the physical principles governing the generation of overpressure due to disequilibrium compaction and aquathermal pressuring.

The main limitations associated with geomechanical modelling of pore pressure generation are the determination of the input parameters and the validation of the results. The main input parameters controlling overpressure are sedimentation rate, permeability (e.g, Bethke, 1986) and compressibility (e.g, Hart *et al.*, 1995). Correct values of these parameters are required to model pore pressure accurately and permeability and compressibility are commonly based on literature values used in other locations (e.g, Chi *et al.*, 2010). A single sedimentation rate for the whole sediment column is commonly used in 1D models (e.g, Gutierrez & Wangen, 2005) while 2D models usually consider a different sedimentation rate for each stratigraphic layer. Models that do consider different sedimentation rates, commonly calculate them using the current thickness of the layers (e.g, Hustoft *et al.*, 2009), i.e. their compacted thickness, instead of using the uncompacted thickness, i.e. thickness at the time of deposition. In highly compressible sediment layers, use of the compacted thickness can lead to significant underestimation of overpressure. Sedimentation rates are also underestimated, which can result in significant underestimation of the permeability required to generate overpressure. Use of a decompaction model (Sclater & Christie, 1980) allows the calculation of decompacted layer thickness (Marín-Moreno *et al.*, 2013a). However, the decompaction model assumes hydrostatic conditions, and is sensitive to the layer discretisation, as it does not consider compaction because of a layer's own weight. If a layer is overpressured, assuming hydrostatic conditions will result in a greater decompacted thickness and therefore overestimation of the sedimentation rate and overpressure. If a layer is thick, the underestimated decompacted thickness and sedimentation rate will result in underestimation of the overpressure.
Empirical methods relating wire-line, seismic or drilling data to pore pressure, indirectly validate the overpressure calculated. However, as they do not represent the hydrodynamics and usually consider only a single lithology, their use can lead to incorrect and unphysical estimates of overpressure. For example, if a sediment layer is less compressible than the overlying layers, a downward decrease in V_p could exist without the existence of overpressure. Incorrectly attributing a decrease in V_p to overpressure, may result in an overestimate of the necessary drilling mud weight and in fracturing of the formation (Sarker & Batzle, 2008).

Our inverse approach provides a step forward towards overcoming the limitations of the two above-mentioned approaches for overpressure prediction. It could be applied with more sophisticated geomechanical models and considering other overpressure generation mechanisms. Other observational constraints, such as S-wave velocity or electrical resistivity, could also be added to the misfit function (Eq. 4.22).
One of the drawbacks of our inverse model is inherited from the forward model. A wide range of forward models is calculated until convergence is achieved, and so the forward

model computational cost is an extremely important aspect. The model resolution is directly linked to model discretisation and thereby to the computational cost. To limit this cost, our inverse model is best applied in basins where horizontal changes in V_p are relatively smooth and stratigraphic layers are thick. Therefore, for higher resolution studies, our inverse model should be complemented with estimates of pore pressure using empirical methods. Where possible, overpressure estimates should always be validated with direct pore pressure measurements.

Our inverse model has another three intrinsic drawbacks: (1) we need to impose a V_p-density relationship to obtain the V_p structure from our density output, (2) if the V_p structure in hydrostatic conditions is not known we need to assume it (as in the empirical methods), and (3) the permeability parameters, k_{i0}, γ and α, cannot be determined for hydrostatically pressured layers. The use of a V_p-density relationship should be fairly reliable for saturated conditions and high effective stress (Mavko *et al.*, 2009). We have used the Hamilton's (1978) relationship for marine sediments, because it is adequate for the observed lithologies in our case study, but another empirical relationship or a rock physics model could be used.

In our EBSB case study, the inferred LVZ is linked to overpressure primarily generated by disequilibrium compaction (>90%), with aquathermal pressuring acting as a secondary mechanism (<10%). Our overpressure match this obtained with the Eaton method, with an exponential factor of 3, and is slightly lower than this using the equivalent depth method. An E value of 3 is similar to that of 3.5 estimated for the same area (Marín-Moreno *et al.*, 2013a) and to those of 2.6-3 in the Gulf of Mexico (Ebrom *et al.*, 2003; Kao, 2010). The equivalent depth method assumes that the effective stress of sediments in an overpressured zone is equal to that in shallower sediments when the V_p is the same but the pressure is hydrostatic. However, this assumption may not be valid when, as here, the lithology varies between the two depths. The equivalent depth method may overestimate the overpressure if the reference hydrostatically pressured sediments are more compressible than those within the overpressured zone. Here, the V_p in the LVZ (L5-Maikop) is equal to that within layers L2 and L3-Sarmatian, but the compressibility of those layers, 4-8x10^{-8} Pa^{-1}, is higher than that of L5-Maikop, 3x10^{-8} Pa^{-1}.

The justification of disequilibrium compaction as the main mechanism generating overpressure in the centre of the EBSB is discussed extensively in Marín-Moreno *et al.* (2013a). However, they considered a zero flow bottom boundary and the increased velocities below the Maikop formation were not explained. Here, to represent the observed rapid increase in V_p below the Maikop formation, we introduced a zero overpressure bottom boundary condition and an additional layer boundary. Such a condition is consistent with suggestions that the acoustic basement of the EBSB, dominated by shallow water carbonates, is

karstified (Okay *et al.*, 1994) and/or fractured. Both processes increase the permeability and allow fluids to escape downwards. The pore fluids in the Maikop formation have not escaped downwards because of the presence of a ∼200 m lithological layer (L6u) with low permeability ∼0.3-1.3x10^{-14} m s^{-1} at ∼5900-6750 mbsf. This layer acts as a seal, retaining the pore fluids in the Maikop formation and allowing the generation of overpressure due to the relatively high sedimentation rates at 33.9-20.5 Ma and at 13-11 Ma. This seal layer could be associated with the high amplitude reflector below the Maikop formation (Fig. 4.1).

Deep overpressured zones between hydrostatically pressured zones have been previously explained using the pressure compartment concept (Bradley, 1975), and identified in basins such as the Rocky Mountains Basin (Powley, 1990). The pressure compartment concept considers the completely hydrodynamic isolation of the overpressured layers. Isolation of a layer requires intrinsic permeabilities of 10^{-25} m^2 (Roberts & Nunn, 1995) or less, which is two orders of magnitude lower than the lowest observed shale intrinsic permeability (Neuzil, 1994). In our model, the upper and lower parts of the overpressured zone are hydrodynamically connected with the sediments above and below the Maikop formation, but the low permeabilities of the Maikop and layer L6u have not allowed the pressure to equilibrate within the Maikop. Layer L6u plays a similar role to a basal seal in the pressure compartment literature (e.g, Tigert & Al-Shaieb, 1990).

Our sedimentation rates and the Maikop formation and L4 permeabilities are similar to those obtained by Marín-Moreno *et al.* (2013a) (Fig. 4.13c). Permeability in other layers is significantly higher, but in these layers the permeability is not constrained because we penalise non-hydrostatic models. The permeabilities of Marín-Moreno *et al.* (2013a) were based on the approach of Gordon & Flemings (1998), developed for the Eugene Island basin, offshore Louisiana, and permeabilities are poorly constrained by experimental data and likely varies between shale types (Fig. 4.15). However, the similar result from our inverse model suggests that the permeability parameters used by Marín-Moreno *et al.* (2013a) are appropriate for the Maikop formation and that their permeability is consistent wit a composition of approximately 90% shale and 10% sand (Shillington *et al.*, 2008), as they assumed. To obtain our permeability using Gordon & Flemings (1998) approach we would need a composition of 86% shale and 14% sand. The large differences in λ^* observed in Fig. 4.13b, despite similar overpressure, are due to differences in porosity between the two models, which therefore yield different effective stress in hydrostatic conditions.

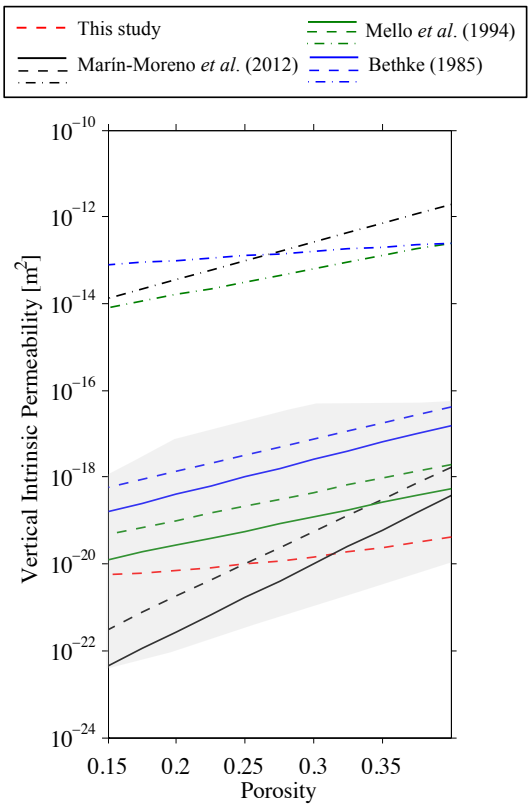

Figure 4.15: Permeability models for shale (solid lines), for sand (dotted-dashed lines), and for a layer composed of 10% sand and 90% shale (dashed lines) and using Gordon & Flemings (1998) approach for permeabilities with mixed lithologies. Permeability models used in this study for the Maikop formation (red-dashed line), from Marín-Moreno *et al.* (2013a) (black lines), from Mello *et al.* (1994) (green lines), and from Bethke (1985) (blue lines). The grey area is the experimentally determined range of shale intrinsic permeabilities (Neuzil, 1994).

4.7 Conclusions

From the application of our inverse model to the centre of the EBSB, we conclude that:

i) Overpressure generated mainly (more than 90%) by disequilibrium compaction can explain the observed LVZ in the centre of the EBSB.

ii) The maximum overpressure in our study area is ∼44 MPa at ∼6400 mbsf and the maximum λ^* is ∼0.62 at ∼5200 mbsf associated with an overpressure of ∼42 MPa.

iii) The existence of a seal layer, of ∼200 m thickness and permeability of ∼0.3-1.3x10^{-14} m s^{-1}, below the Maikop formation and the relatively high sedimentation rates of 0.28-0.29 m ka^{-1} at 33.9-20.5 Ma and of 0.91-0.94 m ka^{-1} at 13-11 Ma explain the development of overpressure in the Maikop formation.

iv) Downward escape of pore fluids can explain the inferred V_p^{Norm} and the associated hydrostatic pressure in the layers below the seal layer; this process requires a fractured and permeable acoustic basement.

From the results of our inverse modelling and comparison with other pore pressure prediction methods, we conclude that:

i) Our inverse model provides a powerful approach to understanding the hydrodynamics and sedimentation history of a basin.

ii) We have overcome the limitations of determining lithological parameters and sedimentation rates, and of validating overpressure obtained from forward geomechanical modelling, by combining the constraints imposed by the seismic structure and geological data, with physical principles governing the disequilibrium compaction and aquathermal pressuring mechanisms.

However, our inverse model has drawbacks:

i) Our 2D inverse model has a significant computational cost and therefore we need to establish a balance between computational cost and model resolution.

ii) We need to assume a V_p-density relationship to convert our density output into V_p, and the V_p structure in hydrostatic conditions if this is not known.

4.8 Acknowledgements

Héctor Marín Moreno was supported by the Graduate School of the National Oceanography Centre Southampton. We thank the Turkish Petroleum Company (TPAO) for giving permission to show their seismic reflection data. We thank the two anonymous reviewers for their constructive and thoughtful comments, which greatly improved the clarity of the manuscript.

Chapter 5

The Response of Methane Hydrate Beneath the Seabed Offshore Svalbard to Ocean Warming during the Next Three Centuries

Methane is a potent greenhouse gas and large-scale rapid release of methane from hydrate may have contributed to past abrupt climate change inferred from the geological record. The discovery in 2008 of over 250 plumes of methane gas escaping from the seabed of the West Svalbard continental margin at ∼400 m water depth (mwd) suggests that hydrate is dissociating in the present-day Arctic. Here we model the dynamic response of hydrate-bearing sediments over a period of 2300 yr and investigate ocean warming as a possible cause for present-day and likely future dissociation of hydrate, within 350-800 mwd, west of Svalbard. Future temperatures are given by two climate models, HadGEM2 and CCSM4, and scenarios, Representative Concentration Pathways (RCPs) 8.5 and 2.6. Our results suggest that over the next three centuries 5.3-29 Gg yr^{-1} of methane may be released to the Arctic Ocean on the West Svalbard margin.

5.1 Introduction

Significant amounts of methane carbon are contained in hydrate-bearing sediments along continental margins, and 100-600 Gt may be stored in the Arctic (Archer *et al.*, 2009). Hydrate forms at low temperature-high pressure conditions and if the dissolved methane concentration in the sediments within the gas hydrate stability zone (GHSZ) is at saturation value. Hydrate is most sensitive to global warming at high latitudes and in shallow

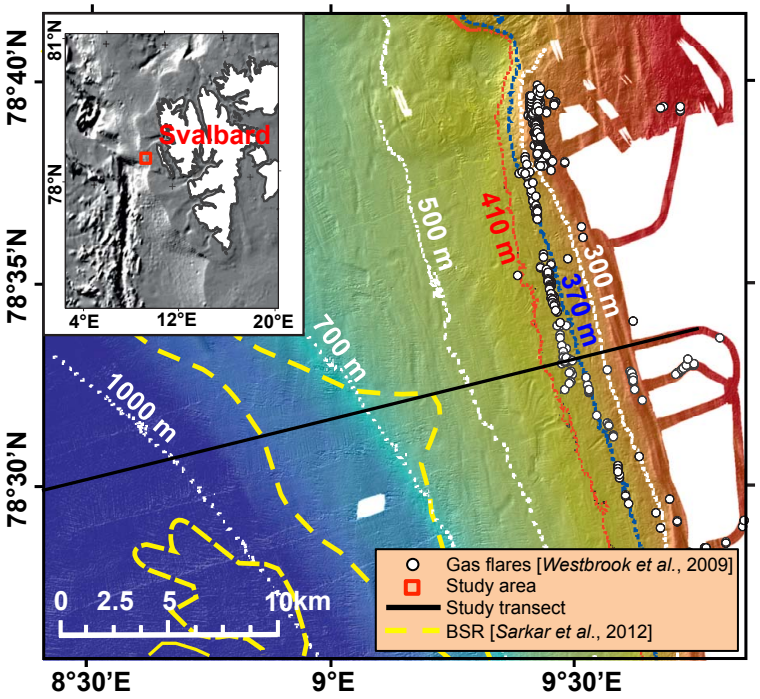

Figure 5.1: Map of the study area with bathymetry derived from multibeam echo-sounding data acquired on Cruise JR211. The dotted blue and red bathymetric contours represent the upper limit of the modelled steady state bottom of the gas hydrate stability zone (GHSZ) at 2°C and 3°C seabed water temperatures, respectively, and assuming a 3.5 wt% salinity, pure methane hydrate, and hydrostatic pressures (Sarkar *et al.*, 2012).

water depths (e.g, Hunter *et al.*, 2013). Previous modelling studies of hydrate dissociation at continental margins, using simple future climate-change scenarios, suggest that increasing temperature will liberate significant amounts of methane from hydrate to the oceans (e.g, MacDonald, 1990; Nisbet, 1989; Reagan *et al.*, 2011), as may have happened during past warm periods (e.g, Dickens, 2011).

West of Svalbard (Fig. 5.1), modelling studies indicate that methane bubble plumes observed at 340-400 m water depth (mwd) (Westbrook *et al.*, 2009) could originate from warming-induced hydrate dissociation (Reagan *et al.*, 2011; Westbrook *et al.*, 2009). Rates of warming of 1-3 °C per hundred years could yield gas at the seabed 70-100 yr after the onset of warming (Reagan *et al.*, 2011), but gas flow at the seabed could have been caused by a 1.0 °C increase of the bottom water over the last three decades due to the increase in the temperature of the West Spitsbergen current in response to Atlantic warming. The timescale of response depends upon the effective permeability and upon the initial distribution of hydrate, which is itself dependent upon the history of hydrate formation and dissociation (Thatcher *et al.*, 2013). Here, we model the future dynamic behaviour of hydrates west of Svalbard using temperature series over the next three centuries given by two climate models, HadGEM2 (Collins *et al.*, 2011; Jones *et al.*, 2011) and CCSM4 (Gent *et al.*, 2011), and two future climate-forcing scenarios, Representative Concentration Pathways (RCPs) 8.5 and 2.6 (Moss *et al.*, 2010), which represent high and low greenhouse emissions, respectively. The models employ the TOUGH+HYDRATE code (Moridis *et al.*,

2012), with constraints on input parameters from seismic observations.

5.2 Modelling Approach

We generated eight different 1D models for water depths of 350, 400, 420, 450, 500, 600, 700 and 800 m. Each model was initialised with the seabed temperature at 1 CE, hydrostatic pressure, a constant heat flow in the entire column, hydrate-free sediment in the top 7 m to approximate the sulphate reduction zone, and saturations of hydrate within and gas below the GHSZ of 5% and 3-4% of pore space, respectively. We imposed a constant heat flow, instead of a constant geothermal gradient, because the gradient changes with the phase (hydrate, water or gas) occupying the pore space. Seabed temperature series for the period 1-2300 yr (Fig. 5.2a; b, and supplementary material A, Temperature Series Construction Fig. SM-A 5.4a) were constructed for each water depth modelled using mean annual seabed temperatures given by climate models HadGEM2 and CCSM4 under RCPs scenarios 8.5 and 2.6 for the period 2005-2300, except for that from CCSM4 model RCP 8.5 which ends at 2250, from oceanographic measurements for the period 1900-2005 and from foraminifera proxy data for the period 1-1900. For the time frame of our analysis, changes in global sea level (e.g, Grinsted *et al.*, 2010) and isostatic rebound (Forman *et al.*, 2004) affecting the gas hydrate system are likely to be minor compared to ocean warming, and so they are not considered here.

Our initial hydrate saturation of 5% of the pore space lies between the 6-13%, estimated for the same area from P and S wave velocities in water depths of ∼1285-1500 m and less than 5%, estimated in water depths of 480-866 m (Chabert *et al.*, 2011). Initial gas saturation below the GHSZ of 3-4% of pore space is consistent with values of 1-7% calculated for the same area within water depths of 480-1285 m (Chabert *et al.*, 2011). We assumed a gas composition of 100% methane in our models, consistent with gas samples collected at the seabed from bubble plumes in the water column, showing a hydrocarbon composition of 99.9% methane (less than 0.01% ethane; James *et al.*, 2011). During the production runs, we introduced a source of basal heat flow that is constant over time, but varies with water depth, equal to the heat flow used as an initial condition. The imposed heat flows are such that the calculated depths of the base of the GHSZ for the initial models at 600, 700 and 800 mwd, assuming a constant thermal conductivity for water saturated sediments of 1.4 W m^{-1} K^{-1}, are similar to the depths of the bottom-simulating reflector (BSR) at those water depths, interpreted from nearby seismic reflection data (Sarkar *et al.*, 2012). At water depths shallower than 600 m the BSR cannot be identified, and we set the heat flow at 500-350 mwd equal to that at 600 mwd. Also, based on seismic velocities (Chabert *et al.*, 2011; Sarkar *et al.*, 2012) we limited the thickness of the zone containing hydrate

to be less than ∼100 m, and used a simplified two-layer model of glaciogenic sediments on top of marine sediments for water depths shallower than 600 m, and a one-layer model comprising just marine sediments in deeper water. We imposed a porosity of 0.3 for the glaciogenic sediments, to account for their very poor sorting (Thatcher *et al.*, 2013), and of 0.5 for the marine sediments. Using Budiansky's (1970) method, a sediment porosity of 0.5 corresponds to a thermal conductivity for water-saturated sediments of 1.4 W m^{-1} K^{-1}. Recently measured values in the top few meters of sediment in the plume area are 1.8-2.1 W m^{-1} K^{-1} (*T. Feseker, personal communication*), but such high values lead to over-estimation of the depth of the base of the GHSZ, interpreted from seismic data to be about 20 m below seafloor (mbsf) at 400 mwd. Therefore, we used a thermal conductivity of 1.4 W m^{-1} K^{-1} for both sediment types.

We tested intrinsic permeabilities of 10^{-16}-10^{-12} m^2, and for values greater than 10^{-14} m^2 the rate of free methane gas transport from dissociated hydrate to the seabed was similar and limited by the rate at which the latent heat required to dissociate the hydrate could be supplied. The extent to which fracture permeability enhances the effective permeability in this setting is not clear, but in models with a low permeability (10^{-16} m^2) the pore pressure exceeded the lithostatic load only a few years after the dissociation of hydrate commenced and the effective permeability required for the system to respond in the time frame of the most recent period of warming of the seabed (about 30 yr) is ∼10^{-13} m^2 (Thatcher *et al.*, 2013). Therefore, following them, we used an intrinsic permeability of 10^{-13} m^2, which is two orders of magnitude higher than used by other authors (Reagan *et al.*, 2011). We also accounted for changes in intrinsic permeability and capillary pressure arising from changes in the degrees of hydrate and ice saturation in the pore space. The irreducible gas saturation was 2%, consistent with other modelling studies in water-gas-hydrate systems and with laboratory measurements (Reagan *et al.*, 2011; Thatcher *et al.*, 2013). We imposed a constant methane flow at the bottom of the model that approximately matched the rate of flow of gas already in the column. We included multiphase molecular diffusion and, hence, methane could be transported by gas flow, by advection of dissolved methane in the aqueous phase, and by molecular diffusion of methane in the aqueous and gas phases. Methane flux by molecular diffusion is slow compared with the other two mechanisms, but for the long time periods considered here it becomes important. A summary of the physical properties of the gas hydrate system and seismic constraints is shown in the supplementary material B (Table SM-B 5.2).

5.3 Results and Discussion

There are several aspects of modelling of the response of methane-hydrate system west of Svalbard to increasing ocean temperature presented here that have not been undertaken in previous published modelling studies. The predictions of future changes in climate come from published global climate models. The initial model was chosen so that, when "grown" over the past 2000 yr and driven by a model of changing ocean temperature, it provided a present-day sub-seabed distribution of gas and hydrate that is close to that indicated by seismic data, that image the BSR in water depths of more than 580 m and the upper limit of gas-related reflectors in shallower water. Therefore, our predictions regarding the future behaviour of the gas hydrate system and on methane emissions from dissociated hydrate are driven by present-day observations rather than assumptions about initial conditions (supplementary material C, Model Uncertainties).

The resulting initial conditions produce no hydrate 2000 yr ago at 350 mwd. At 400 mwd, methane hydrate would have started to dissociate at about 850 CE, and dissolved methane would have been transported to the seabed by advection at a rate of about 0.1-0.3 mol yr^{-1} m^{-2} until ~1930 CE (supplementary material A, Temperature Series Construction Fig. SM-A 5.4b). Then, due to the increase in temperature over the Industrial Period, gas hydrates would have destabilised at 400 mwd and, ~15 yr later, free methane gas would have started to be released to the Arctic Ocean with a maximum methane flow of 100 mol yr^{-1} m^{-2} (supplementary material A, Temperature Series Construction Fig. SM-A 5.4a; b). However, very few of the acoustically imaged bubble plumes reach the sea surface (Westbrook *et al.*, 2009). Even if the bubbles could reach the seabed with significant size, for water depths deeper than 100 m most of the original methane may be dissolved into the water column and replaced by other gases (McGinnis *et al.*, 2006), increasing ocean acidification. Once there is a constant amount of free gas above the irreducible gas saturation within the GHSZ, the pulses of seabed methane are directly correlated with changes in temperature with no time delay (see insets in supplementary material A, Temperature Series Construction Fig. SM-A 5.4a; b). By ~2050 CE, most hydrate dissociates (Fig. 5.3 and supplementary material D, Fig. SM-D 5.7) but it takes ~30 yr more for all of the liberated methane to migrate to the ocean (Fig. 5.2c; d).

The timing differences between the models at 400-500 mwd result from lower temperatures estimated by the CCSM4 model over the next century. At water depths deeper than ~500-600 m, hydrate remains stable for the time period considered (Fig. 5.3 and supplementary material D, Fig. SM-D 5.7). At water depths were there are methane emissions, the period of high rate emissions increases with increasing water depth (Fig. 5.2c; d) because the amount of hydrate beneath the seabed in the models increases with increasing water

depth and the magnitude of high rate emissions is similar at different water depths and limited by enthalpy (Thatcher *et al.*, 2013).

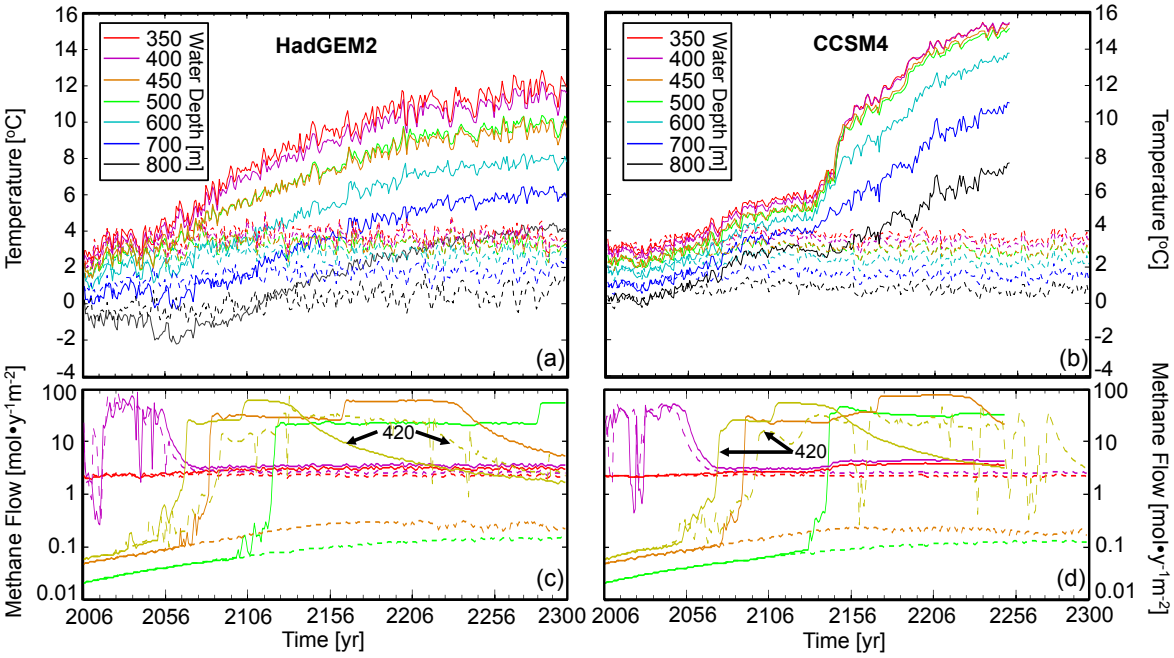

Figure 5.2: Results using temperatures from climate models HadGEM2 (a and c) and CCSM4 (b and d) at our study transect (Fig. 5.1) for the period 2006-2300 yr. Solid lines show results using the climate-forcing scenario RCP 8.5 and dashed lines using RCP 2.6. (a and b) Future temperature for 800, 700, 600, 500, 450, 400 and 350 m water depth (mwd). (c and d) Methane flow at the seabed for 350 (red lines), 400 (purple lines), 420 (yellow-green lines), 450 (brown lines), and 500 (green lines) mwd. Note that the first jump in methane outflow observed at 420, 450, and 500 mwd for both climate models and RCP 8.5 is due to dissociation from the top part of the gas hydrate layer, and the second jump occurs when methane from dissociated hydrate at the base of the GHSZ reaches the seabed, and contributes to the methane outflow.

We estimated the methane flow in the area where gas hydrate dissociation occurs, between latitudes of 78°26'N-78°40'N (~25 km length), assuming a constant continental slope of 1.5°, between the 370-500 mwd contours in Fig. 5.1, to calculate the across-margin distance. The time averaged methane flows at 400, 420, 450 and 500 and 600 mwd over a time period and per m^2 of area, were calculated from the total methane liberated over that period at each water depth, and the time averaged methane flows between the water depths modelled were estimated assuming a linear interpolation. Over the next century, the gas hydrate dissociation front may retreat an across-margin distance of 2860 m from ~400 to ~480 mwd (Fig. 5.2c). Therefore, within this depth range, the methane release per meter wide strip across-margin will be 0.11-0.33 Mg yr^{-1} and for the 25 km long dissociation area will be 3.9-6.6 Gg yr^{-1} (2.4-7.2 mol yr^{-1} m^{-2}) if using RCP 2.6 or RCP 8.5, respectively. Over the next three centuries, the active gas hydrate dissociation area may occupy 134

km^2 (seabed range of ~400-550 mwd) releasing 5.3-29 Gg yr^{-1} (2.5-13.5 mol yr^{-1} m^{-2}) if using RCP 2.6 or RCP 8.5, respectively. Although the flux per square meter is limited by enthalpy, the total flux over the next three centuries increases with time because the active area of methane emission increases.

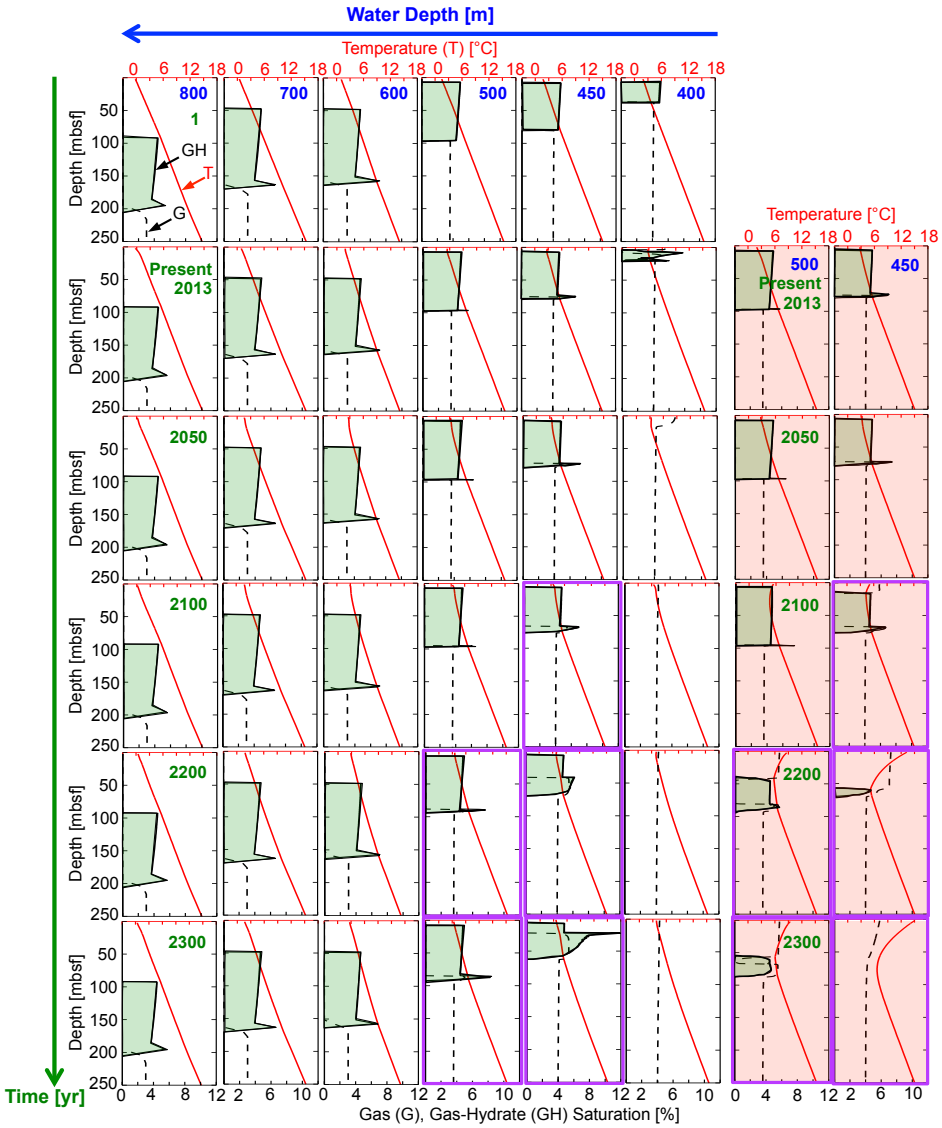

Figure 5.3: Left: grid of results showing the variations in temperature (T, solid red lines), and saturations of gas hydrate (GH, solid black lines enclosing green areas) and gas (G, dashed black lines) with time (rows) and water depth (columns), using the climate model HadGEM2 and climate-forcing scenario RCP 2.6. Each individual plot in the grid shows the variation of T, and of GH and G saturations with depth for a specific water depth and time. Right: plots with red backgrounds show the results using the climate model HadGEM2 and RCP 8.5. The plots outlined in purple show that, at 2100-2300 yr and at 450-500 mwd, the differences between the results from using RCP 2.6 and RCP 8.5 are significant.

If our calculations for the next three centuries can be extended to an area of seabed within 400-550 mwd of ~41400 km^2 along the Svalbard archipelago (73°N-85°N; 0-40.4°E), and to an area of ~152350 km^2 along the entire Eurasian Margin (Jakobsson *et al.*, 2008), the potential methane release from marine hydrate over the next three centuries may be ~1.7-9 Tg yr^{-1} and ~6.1-33 Tg yr^{-1}, respectively. Such extrapolations should be treated with caution because current ocean temperatures (colder further east, so involving hydrate in shallower waters), slopes (more gentle in shallow waters, so dissociation perhaps affecting a larger area) and future temperature changes, will vary along the margin. However, even considering the entire Eurasian Margin, the maximum potential methane release from hydrate is about five times smaller than global methane emissions from all natural wetlands, which are currently ~150 Tg yr^{-1} (Dlugokencky *et al.*, 2011), the same order of magnitude as the 8-29 Tg yr^{-1} from Arctic tundra (McGuire *et al.*, 2012), and about two orders of magnitude smaller than the 5000 Tg yr^{-1} from the East Siberian Arctic Shelf recently assumed by Whiteman *et al.* (2013).

5.4 Acknowledgements

This work was supported by the UK Department of Energy and Climate Change through a supplement to Natural Environment Research Council grants NE/H002732/1 and NE/H022260/1. We thank Kate Thatcher for her help initialising the T+H models, and Matt Hornbach and an anonymous reviewer for their detailed and constructive comments.

5.5 Supplementary Material A. Temperature Series Construction

To arrive at appropriate starting conditions for modelling the next three centuries, we preconditioned the model of the present-day gas hydrate system, using a combination of measured and estimated records of temperature for the past two millennia. Temperature series were constructed for a period of 2005 yr at 350, 400, 420, 450, 500, 600, 700 and 800 m water depth (mwd) (Fig. SM-A 5.4a) on a transect across the margin (Fig. 5.1). To model the period 1975-2005, we used near-seabed temperature means at the above water depths, given by May-to-October CTD measurements in our study area, from Westbrook *et al.* (2009, Fig. 3b) and the temperature anomalies, temperature deviations from the mean at that period, at 400 mwd from Thatcher *et al.* (2013). The temperature anomalies for the other water depths were calculated by scaling the variation in temperature measured at 400 mwd in proportion to the ratio between the standard deviation from the

mean at each depth and the standard deviation from the mean at 400 mwd. We took the variation of standard deviation of temperature with depth from the profiles of Polyakov *et al.* (2003, Fig. 2) and, assuming that the temperature variability with depth at the profile location, 82.85°N 25.79°E, is the same as that in our study site, scaled these standard deviations to be appropriate to our study transect using the ratio between the standard deviation of the temperature anomalies at 400 mwd at the study transect and 400 mwd at Polyakov *et al.*'s 2003 profile. For the period 1950-1975, we used mean values for the period 1975-2005 from Westbrook *et al.* (2009), and the anomalies from Ocean Station Mike at 50 mwd (Holliday *et al.*, 2008). These anomalies were scaled to match the standard deviation of the anomalies for the period 1975-2005 for each water depth. For the period 1900-1950, we used the mean temperature and 15-year-running mean anomalies at 150-300 mwd for region 4 from Polyakov *et al.* (2004). For each water depth, these anomalies were scaled to match the standard deviation of the anomalies for the period 1950-1975, and the temperatures were offset to make the temperature at 1950 the same as the mean for the period 1950-2005. For the period 1-1900, we used 50-year-running summer temperature means at 50 mwd, obtained from planktic foraminifera proxy data in a borehole nearby our study area and using the SINMAX modern analog technique (Spielhagen *et al.*, 2011), and scaled them to our location and water depths by applying a linear regression between the near-surface temperatures at the site of Spielhagen *et al.* (2011) and the temperatures at the water depths along our transect given by the ocean/sea-ice model NEMO (Madec, 2012) at 1/12° resolution (ORCA12). The temperatures for this period were offset to make the temperature at 1900 the same as the mean for the period 1900-1950.

The temperatures for the period 2005-2300 were mean annual seabed temperatures given by climate models HadGEM2 (Collins *et al.*, 2011; Jones *et al.*, 2011) and CCSM4 (Gent *et al.*, 2011) under climate-forcing scenarios Representative Concentration Pathways (RCPs) 8.5 and 2.6 (Moss *et al.*, 2010), except for that from CCSM4 model RCP 8.5 which goes from 2005-2250 (Fig. 5.2a; b). These temperatures were interpolated to our study location and offset (Table SM-A 5.1) to make the temperature at 2005 the same as the mean temperature for the period 1975-2005 given by CTD measurements in our study area.

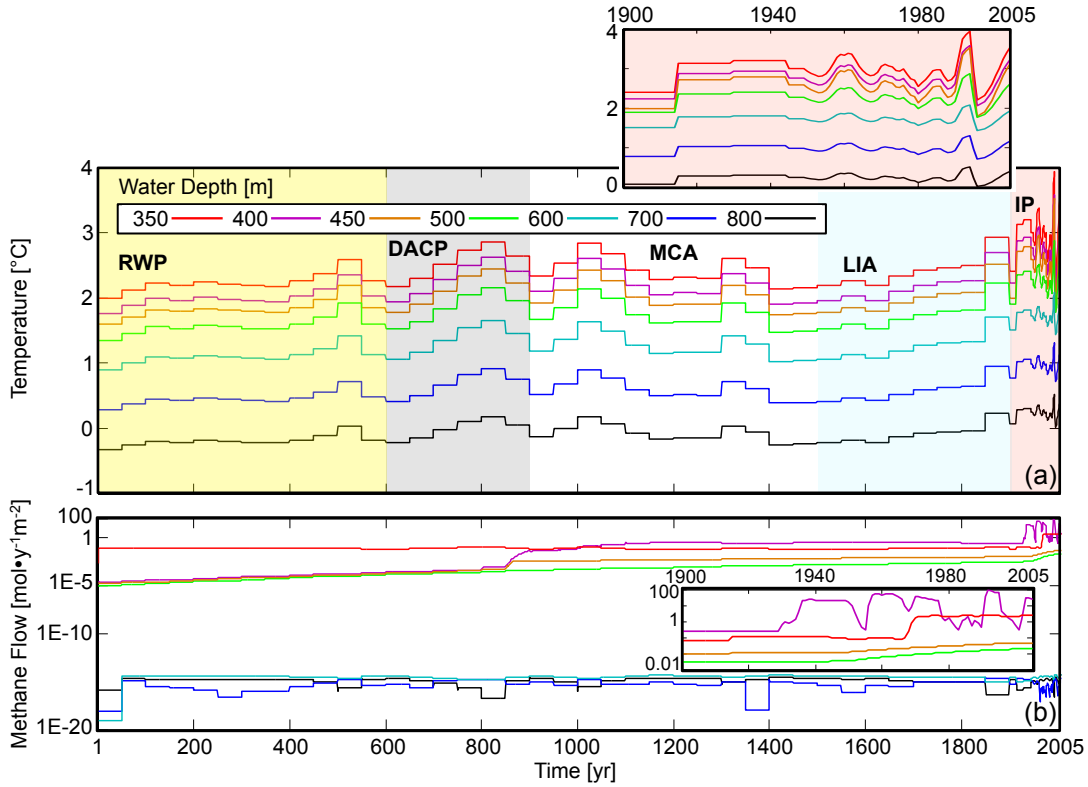

Figure SM-A 5.4: (a) Past temperature constructed for our study transect (Fig. 5.1) for the period 1-2005 yr and for 800, 700, 600, 500, 450, 400, 350 m water depth (mwd). This period is subdivided into the Roman Warm Period (RWP, until ~600 CE), the Dark Ages Cold Period (DACP, ~600 to ~900 CE), the Medieval Climate Anomaly (MCA, ~900 to ~1500 CE), the Little Ice Age (LIA, ~1500 to ~1900 CE), and the Industrial Period (IP)(Spielhagen *et al.*, 2011). Temperature data were obtained from Spielhagen *et al.* (2011) for the period 1-1900, from Polyakov *et al.* (2004) for 1900-1950, from Holliday *et al.* (2008) for 950-1975, and from Westbrook *et al.* (2009) and Thatcher *et al.* (2013) for 1975-2005. (b) Methane flow at the seabed. The insets in (a-b) show details for the period 1900-2005. Note that at 350 mwd (red line), the increase in methane outflow at ~1967 yr is due to free methane gas coming from the deeper part of the model contributing to the methane outflow in the upper part.

Table SM-A 5.1: Temperature bias at 2005 yr given by the climate models with respect to the mean seabed temperature for the period 1975-2005 given by CTD measurements in our study area (Westbrook *et al.*, 2009). Positive temperature offsets indicate higher temperatures predicted by the climate models.

		Offsets applied [°C] for each water depth [m]							
Climate Model	RCP	350	400	420	450	500	600	700	800
HadGEM2	8.5	3.32	3.54	3.55	3.56	3.64	3.56	3.46	3.94
CCSM4	8.5	-0.26	-0.06	0.00	0.09	0.35	0.82	1.49	2.15
HadGEM2	2.6	3.09	3.31	3.29	3.26	3.31	3.25	3.08	3.49
CCSM4	2.6	-0.35	0.13	0.06	0.05	0.32	0.82	1.55	2.26

5.6 Supplementary Material B. Physical Properties of the Gas Hydrate System and Seismic Constraints

Table SM-B 5.2: Table with physical properties of the gas hydrate system and seismic constraints.

Parameter	Value
Initial salinity [wt%]	3.5
Initial hydrate saturation [%]	5
Initial gas saturation below GHSZ [%]	3-4
Initial thickness of SRZ [m]	7
Gas composition	100% CH_4
Gas flow [kg s^{-1}]	10^{-13}
Water saturated thermal conductivity [W $m^{-1}K^{-1}$]	1.4
Solid grain density [kg m^{-3}]	2600
Intrinsic permeability [m^2]	10^{-13}
Initial diffusivity [m^2 s^{-1}]	
CH_4: aqueous phase, gas phase	$2x10^{-9}$, $2x10^{-5}$
H_2O: aqueous phase, gas phase	$1x10^{-9}$, $3x10^{-5}$
NaCl: aqueous phase, gas phase	$1.5x10^{-9}$, 0
Porosity [%]	
Glaciogenic sediments	30
Hemipelagic sediments	50
Relative permeability model	$k_{rA} = \max\left\{0, \min\left\{\left[\frac{S_A - S_{irA}}{1 - S_{irA}}\right]^n, 1\right\}\right\}$,
Modified version of Stone's first three phase relative permeability method [*Stone*, 1970]	$k_{rG} = \max\left\{0, \min\left\{\left[\frac{S_G - S_{irG}}{1 - S_{irA}}\right]^{n_G}, 1\right\}\right\}$, $S_{irA} = 0.12$, $S_{irG} = 0.02$, $n = n_G = 4$
Capillary pressure model [*van Genuchten*, 1980]	$P_{cap} = -P_0\left[\left(S^*\right)^{-1/\lambda} - 1\right]^{-\lambda}$, $-P_{max} \le P_{cap} \le 0$, $S^* = \frac{\left(S_A - S_{irA}\right)}{\left(S_{mxA} - S_{irA}\right)}$, $\lambda = 0.254$, $S_{irA} = 0.11$, $P_0 = 12500$ MPa, $P_{max} = 10^6$ MPa, $S_{mxA} = 1$
Heat flow [W m^{-2}]	
From 350-600 mwd	$7.7x10^{-2}$
At 700 mwd	$8.5x10^{-2}$
At 800 mwd	$8.8x10^{-2}$
Seismic constraints	
Initial gas hydrate thickness [m]	≤100
Present day gas hydrate thickness at 400 mwd [m]	20
Depth of glaciogenic sediments [mbsf]	
From 350-500 mwd	65-50 with a negative gradient of 10%
From 600-800 mwd	0
Depth of BSR [mbsf], [*Sarkar et al.*, 2012]	
From 350-500 mwd	Not identified
At 600 mwd	160
At 700 mwd	160
At 800 mwd	190

GHSZ, gas hydrate stability zone; BSR, bottom-simulating reflector; SRZ, sulphate reduction zone; mwd, meters water depth; mbsf, meters below seafloor; k_{rA} and k_{rG} are relative permeabilities for aqueous and gas phases, respectively; S_A and S_G are saturations for aqueous and gas phases; S_{irA} and S_{irG} are irreducible aqueous and gas saturations; S_{mxA} is the maximum water saturation; P_{cap} is the capillary pressure; P_{max} is the maximum value of capillary pressure; P_0 is the capillary entry pressure; n, n_G and λ are fitting parameters.

5.7 Supplementary Material C. Model Uncertainties

Here, we discuss the impacts of hydrate concentration, heat flow, mesh size, and climate model uncertainties to our results.

Hydrate saturation in the pore space is one of the least certain parameters in our models. For our default model we used a hydrate saturation of the pore space of 5%, which lies between the 6-13%, estimated for the same area from P and S wave velocities in water depths of ∼1285-1500 m (Chabert *et al.*, 2011; Westbrook *et al.*, 2008) and less than 5%, estimated in water depths of 480-866 m (Chabert *et al.*, 2011). Thatcher *et al.* (2013) showed that for our intrinsic permeability value of 10^{-13} m^2, the time for methane to reach the seabed is independent of the hydrate saturation for values between 5-30% (their Fig. 6b). Figure SM-C 5.5a supports the results of Thatcher *et al.* (2013), but shows that for a hydrate concentration of 2.5% there is a delay of ∼50 yr, due to the limited amount of methane from dissociated hydrate to reach the irreducible gas saturation. The maximum rate of seabed methane outflow and the time period over which it is emitted increases with increasing hydrate saturation. With the 20% model there is still significant methane in the system by 2300 yr (Fig. SM-C 5.5a). For hydrate saturations of the pore space within 2.5-20%, the maximum rate of seabed methane outflow is between 29-120 mol yr^{-1} m^{-2}. Importantly, because the period of gas emission increases with increasing hydrate concentration, the magnitude of total gas emission from the area increases, because gas emission is active simultaneously from a greater range of depths and, therefore, from a larger area.

In our modelling approach, we decided to impose a constant heat flow instead of a constant geothermal gradient, because the gradient changes with the phase (hydrate, water or gas) occupying the pore space. For a given thermal conductivity, our heat flows were estimated by an iterative process of varying them until our present-day seabed distribution of gas and hydrate (for a 100% methane hydrate) matched current seismic data that image BSR depth in water depths of more than 580 m and the depth of the upper limit of gas-related reflectors in shallower waters. We were more confident about the range of possible thermal conductivities in our study area than about heat flow values, based on the type of sediments, published measurements (Table SM-C 5.3) and recent measurements on the top few meters of sediment in the plume area (1.8-2.1 W m^{-1} K^{-1}, *T. Feseker, personal communication*), and hence we iterated over the heat flow. If the real thermal conductivity of the sediment is over/underestimated, the heat flow will be over/underestimated by the same relative amount, and so, the temperature profile with depth will remain the same as that which gives a present-day seabed distribution of gas and hydrate consistent with the seismic observations. In our models, uncertainties in heat flow arising from uncertainties

in thermal conductivity (within a range of ±30%) do not significantly affect the time for methane to reach the seabed (Fig. SM-C 5.5b). However, they do influence the maximum rate of methane outflow, ranging from 46-74 mol yr^{-1} m^{-2}, and the time for methane from dissociation at the base of the GHSZ to contribute to the methane outflow from dissociation in the upper part, which produces the second significant increase in methane outflow (Fig. SM-C 5.5b).

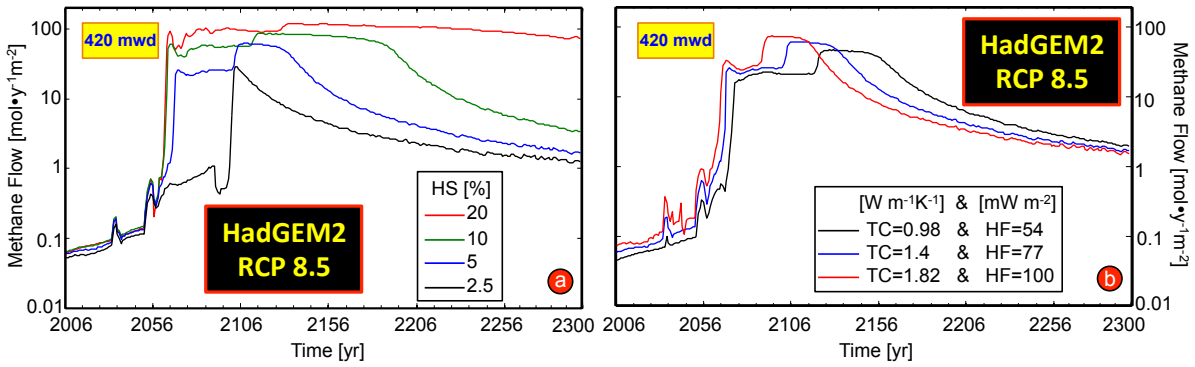

Figure SM-C 5.5: Rate of flow of methane from the seabed at 420 m water depth (mwd), using HadGEM2 climate model and climate-forcing scenario RCP 8.5. (a) Results for hydrate saturations (HS) of 2.5, 5,10, and 20% of pore space. All other parameters are identical to those for the default model (supplementary material B Table SM-B 5.2). (b) Results for thermal conductivity (TC) of 0.98 W m^{-1} K^{-1} and (HF) heat flow of 54 mW m^{-2}, TC of 1.4 W m^{-1} K^{-1} and HF of 54 mW m^{-2}, and TC of 1.82 W m^{-1} K^{-1} and HF of 100 mW m^{-2}. All other parameters are identical to those for the default model.

Table SM-C 5.3: Thermal gradient (TG), thermal conductivity (TC) and heat flow (HF) values west of Svalbard.

Water Depth [m]	Thermal Gradient [°C km^{-1}]	Thermal Conductivity [W $m^{-1}K^{-1}$]	Heat Flow [mW m^{-2}]	Reference	Observations
>2200	115	1.2	102.5	Vanneste et al., [2005]	BSR-derived TG
>900	85-122	1.0-1.2	85-122	Crane et al., [1991]	TG, TC, and HF data in the top ~5 m
850	70	1.2	102.5	Vanneste et al., [2005]	BSR-derived TG
840	113	1.16	131	Crane et al., [1991]	TG, TC, and HF data in the top ~5 m
820	73	1.09	80	Eldholm et al., [1999]	TG and TC data in the top ~5 m
813	119	1.16	138	Crane et al., [1991]	TG, TC, and HF data in the top ~5 m
800		1.4	88	This study	TC and HF constrained by data
700		1.4	85	This study	TC and HF constrained by data
688	108	1.6	102.5	Crane et al., [1991]	TG, TC, and HF data in the top ~5 m
600-350		1.4	77	This study	TC and HF constrained by data
560	97	1.14	110	Crane et al., [1991]	TG, TC, and HF data in the top ~5 m
~400	53-61			Sarkar et al., [2012]	Inferred TG from BSR at other water depths
~250	44			Rajan et al., [2012]	Inferred TG from BSR at other water depths

In Fig. 5.2d the model at 420 m water depth shows a "spiky" behaviour. This behaviour may be due to either a physical phenomena, where the system a few meters below the seabed responds quasi-instantaneously to temperature perturbations at the seabed, or due to numerical instabilities derived from a coarse mesh. To test this, the model at 420 mwd using the climate model CCSM4 and scenario RCP 2.6 has been re-run using three finer meshes (Table SM-C 5.4). At 420 mwd, the base of the GHSZ is located at ∼56 m below seabed, and hence we have considered the top 100 m as the potential zone where the mesh size may influence the results. The time step for the three models varies automatically within 10-10^6 seconds depending on the stability of the convergence procedure.

Table SM-C 5.4: Table with the depth discretisation applied for the three model runs at 420 mwd using the climate model CCSM4 and scenario RCP 2.6.

Depth Interval [m]	Default-Mesh(1) [m]	Mesh-2 [m]	Mesh-3 [m]	Mesh-4 [m]
0-0.001	0.001	0.001	0.001	0.001
0.001-20	0.5	0.1	0.05	0.01
20-62.5	0.5	0.1	0.05	0.05
62.5-100	0.5	0.1	0.05	2.5
100-600	$1.1*\Delta z^{Previous}$	0.5	0.5	2.5
>600	$1.1*\Delta z^{Previous}$	2.5	2.5	2.5
Computational Time [h]	0.75	3	5	25

(1) At depths deeper than 100 m the mesh size increases by a factor of 1.1 with respect to the previous depth z-interval.
Note: the used T+H version allows a maximum of 3000 grid cells.

Figure SM-C 5.6 shows an extremely similar behaviour and values of the seabed methane flow for the four meshes. The models with finer meshes (Mesh-3 and Mesh-4 models) have a centimetric resolution for a size domain of 100 m, hence it is likely that their response is consistent with the physical response of the system.

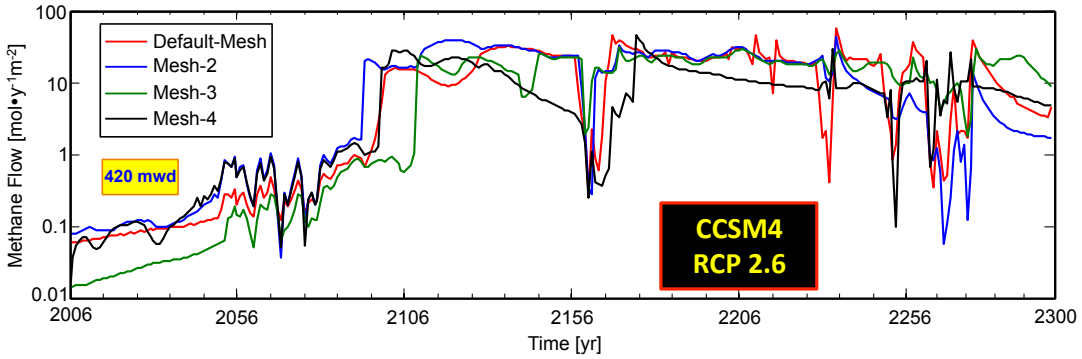

Figure SM-C 5.6: Sensitivity analysis of the influence of the mesh size to the behaviour of the methane flow at the seabed.

The model (or structural) uncertainty was captured by using two different climate models, HadGEM2 and CCSM4, and the scenario-related uncertainty was examined by using the two most extreme scenarios, RCPs 8.5 and 2.6, which represent high and low greenhouse emissions, respectively, to cover the full range of possible future scenarios. The temperatures predicted by these global climate models were offset to make the temperature at 2005 yr the same as the mean temperature for the period 1975-2005 given by CTD measurements in our study area (supplementary material A, Table SM-A 5.1). By this means, the bias in the temperatures given by the global climate models was normalised to our study location. The parametric uncertainty of climate models, which is an active area of research in its own right, is beyond the scope of this work. A detailed discussion on climate model uncertainty is given by Hawkins & Sutton (2009).

5.8 Supplementary Material D. Evolution of Temperature, Gas and Gas Hydrate Saturations with Time and Water Depth Using CCSM4 Climate Model

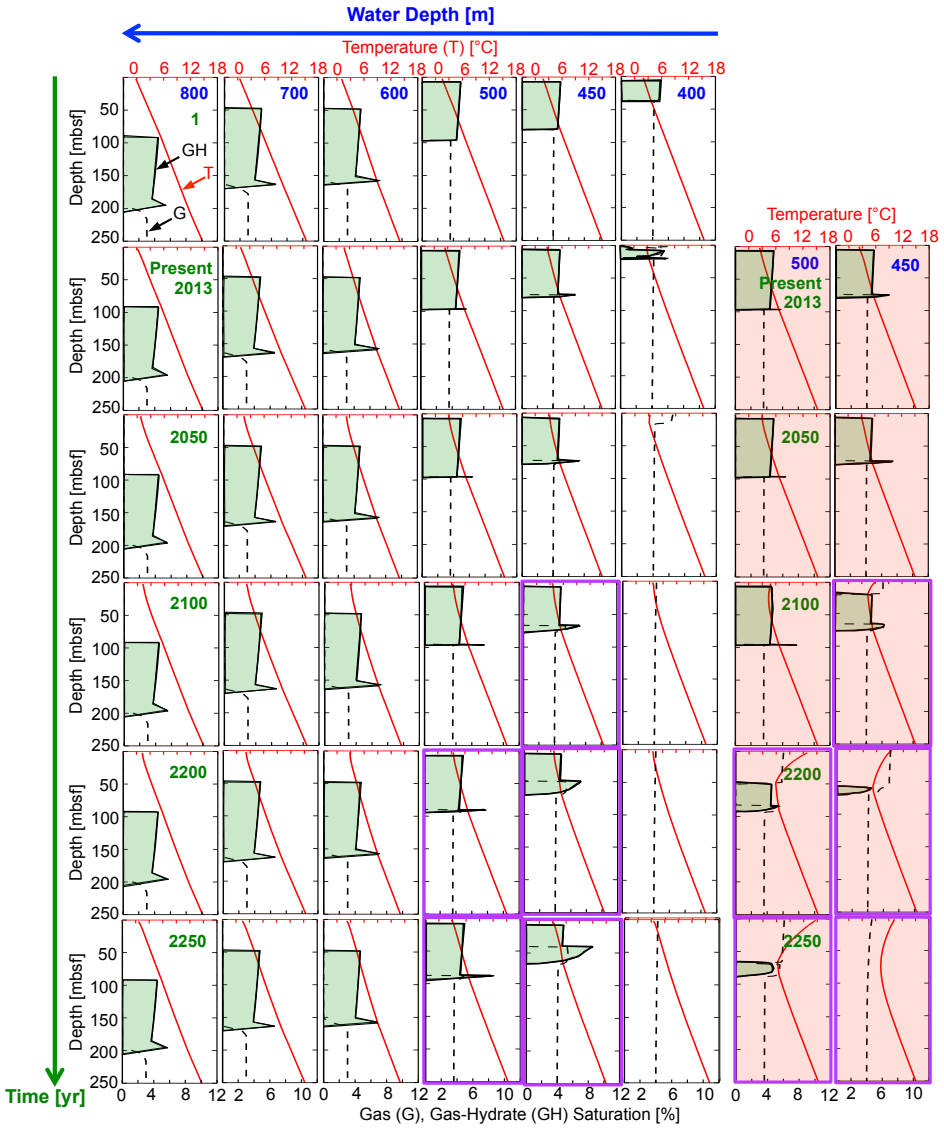

Figure SM-D 5.7: Left: grid of results showing the variations in temperature (T, solid red lines), and saturations of gas hydrate (GH, solid black lines enclosing green areas) and gas (G, dashed black lines) with time (rows) and water depth (columns), using the climate model CCSM4 (Gent *et al.*, 2011), and climate-forcing scenario Representative Concentration Pathway (RCP) 2.6 (Moss *et al.*, 2010). Each individual plot in the grid shows the variation of T, and of GH and G saturations with depth for a specific water depth and time. Right: plots with red backgrounds show the results using the climate model CCSM4 and RCP 8.5. The plots outlined in purple show that, at 2100-2300 yr and at 450-500 m water depth, the differences between the results from using RCP 2.6 and RCP 8.5 are significant.

Chapter 6

Reducing Uncertainty on Warming-Induced Methane Emissions from Hydrate Beneath the Seabed Offshore West Svalbard over the Next Century

Oceans are warmer than they have been in millions of years and hence, gas hydrates have the potential to release more methane than in the past. The discovery in 2008 of over 250 plumes of methane gas escaping from the seabed of the West Svalbard continental margin, at the landward limit of the hydrate stability, suggests that hydrate is dissociating in the present-day Arctic. Here, we investigate ocean warming as a trigger mechanism for gas hydrate dissociation offshore of west Svalbard over the next century, and study the sensitivity of its response to future temperatures given by seven different climate models, CCSM4, GFDL, HadGEM2, IPSL, MPI, MRI and NorESM1, and climate-forcing scenarios, Representative Concentration Pathways (RCPs) 2.6 and 8.5. The different climate models used here predict different patterns of temperature change in our study region and so different magnitude of methane emissions. The predicted future temperatures are significantly more sensitive to the RCP scenario than to the climate model but the estimated methane emissions are sensitive to both factors. Over the next century between 400 to 480 m water depth, the average seabed temperature increase will be of $\sim$0.008$\pm$0.003 ^{o}C yr^{-1} releasing 2.4$\pm$1.43 Gg yr^{-1} of methane from dissociated hydrate to the Arctic Ocean and of $\sim$0.0315$\pm$0.005 ^{o}C yr^{-1} releasing 7.08$\pm$3.22 Gg yr^{-1}, if using scenario RCP 2.6 and 8.5, respectively.

6.1 Introduction

Gas hydrates in marine sediments may contain ∼500-2500 Gt (e.g, Piñero *et al.*, 2013) of methane carbon globally of which ∼100-600 Gt may be stored in the Arctic (Archer *et al.*, 2009). Gas hydrate forms at low temperature-high pressure conditions and if the dissolved methane concentration in the sediments within the gas hydrate stability zone (GHSZ) is at saturation value. Hydrate is most sensitive to global warming at high latitudes and in shallow water depths (e.g, Hunter *et al.*, 2013) and Arctic hydrate may be affected more rapidly by global warming that hydrate at lower latitudes because the most intense warming is predicted in the Arctic (Hassol, 2004). Previous modelling studies of hydrate dissociation at continental margins, using simple future climate-change scenarios, suggest that increasing temperature will liberate significant amounts of methane from hydrate to the oceans (MacDonald, 1990; Nisbet, 1989; Reagan & Moridis, 2008; Reagan *et al.*, 2011) as may have happened during past warm periods (e.g, Dickens *et al.*, 1995; Nisbet, 1990).

Recent transient numerical modelling studies offshore West Svalbard indicate that the observed bubble plumes (Fig. 6.1; Westbrook *et al.*, 2009), at 340-400 m water depth (mwd), could originate from warming-induced hydrate dissociation (Marín-Moreno *et al.*, 2013c; Reagan & Moridis, 2009; Reagan *et al.*, 2011; Thatcher *et al.*, 2013). Marín-Moreno *et al.* (2013c) estimated that offshore West Svalbard, the GHSZ may retreat from ∼400 to ∼480 mwd over the next century, and so 3.9-6.6 Gg yr^{-1} (2.4-7.2 mol $yr^{-1}m^{-2}$) of methane may be release from the active area of hydrate dissociation within those depths (∼71.5 km^2). To explore how uncertainties in climate models (structural uncertainty) impacted their results, they assumed that this uncertainty was captured by using two climate models: the Community Climate System model (CCSM4; Gent *et al.*, 2011) and the Met Office Hadley Centre model (HadGEM2; Collins *et al.*, 2011; Jones *et al.*, 2011). However, these two climate models may not capture the range of possible behaviours. The scenario-related uncertainty, is likewise assumed to be examined by using a number of different climate-forcing scenarios for each model. Marín-Moreno *et al.* (2013c) used the two most extreme scenarios, Representative Concentration Pathways (RCPs) 8.5 and 2.6 (Moss *et al.*, 2010), which represent high and low greenhouse emissions respectively, to cover the full range of possible future scenarios. A detailed discussion on climate model uncertainty is given by Hawkins & Sutton (2009).

Here we study warming-induced gas hydrate dissociation in a transect offshore west of Svalbard (Fig. 6.1) over the next century and for water depths from 400-500 m, which is the depth range of potential gas hydrate dissociation over the next century (Marín-Moreno *et al.*, 2013c). We focus on how climate model uncertainties impact our results, in terms of predictions of future response of the gas hydrate system and future methane emissions.

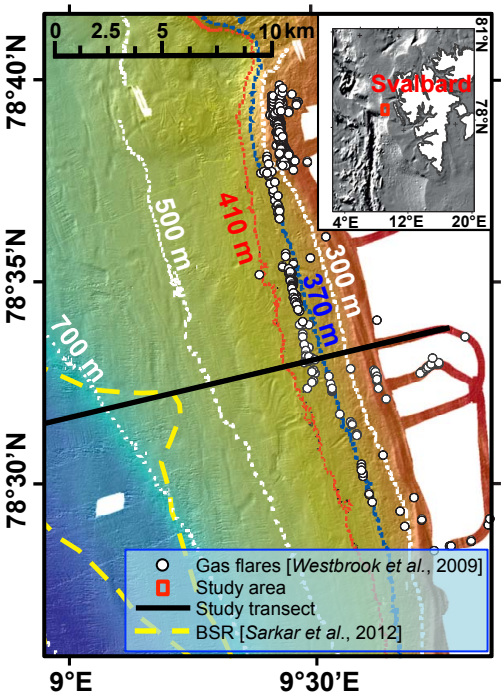

Figure 6.1: Map of the study area with bathymetry derived from multibeam echosounding data acquired on Cruise JR211. The dotted blue and red bathymetric contours represent the upper limit of the modelled steady state bottom of the gas hydrate stability zone (GHSZ), using Moridis' (2003) phase boundary, at 2 °C and 3 °C seabed water temperatures, respectively, and assuming a 3.5 wt% salinity, pure methane hydrate (James *et al.*, 2011), and hydrostatic pressures (Sarkar *et al.*, 2012).

To understand the range of possible future temperature behaviours and asses environmental impacts, we use seven different climate models: the CCSM4, the Geophysical Fluid Dynamics Laboratory model (GFDL; Gordon & Stern, 1982), the HadGEM2 model, the Institute Pierre-Simon Laplace model (IPSL; Marti *et al.*, 2010), the Max-Plank Institute model (MPI; Marsland *et al.*, 2003), the Meteorological Research Institute model (MRI; Yukimoto *et al.*, 2001) and, the Norwegian Climate Centre model (NorESM1; Bentsen *et al.*, 2012; Iversen *et al.*, 2012). We thus build on Marín-Moreno *et al.* (2013c) by providing further constraints to potential future methane emissions from marine hydrate-bearing sediments in the Arctic.

6.2 Modelling Approach and Future Temperatures

We generated four different 1D models for water depths of 400, 420, 450 and 500 m. Model assumptions and uncertainties in parameters are discussed by Marín-Moreno *et al.* (2013c). The applied physical properties of the gas and hydrate system, imposed seismic constraints, and the method used to construct the temperature series for the period 1-2005 are described in their electronic supplementary material. Here we focus on the period 2005-2100, for which a broader range of climate models can be explored. For this period, we used mean annual seabed temperatures given by the global climate models CCSM4, GFDL, HadGEM2, IPSL, MPI, MRI, and NorESM1, under RCP scenarios 8.5 and 2.6, and

interpolated them to our study location. Some models predict poorly the current temperatures; we therefore use the models to predict the magnitude of future changes rather than the actual temperature values. To tie the constructed past temperature series with the future temperatures, some overlapping should exist between both series around the tying time and the future temperatures may be offset by the difference in mean temperatures over the overlapping period. CTD measurements in the study area were compiled for the period 1975-2008 (Westbrook *et al.*, 2009), so we had only three years of overlap and we offset the future temperatures to make the temperature at 2005 the same as the mean over the period 1975-2005 (Table 6.1). Only CTD data from May to October were compiled (Westbrook *et al.*, 2009), and we considered future mean annual seabed temperatures, so this difference could have added some second-order differences between past and future temperature values. However, Table 6.1 shows that the applied offsets are within ±1 °C (Table 6.1), except for the HadGEM2 and MPI models, which is about the temperature perturbation of all the models around 2005 (Fig. 6.2a-d and 6.3a-d). This observation suggests that the offsets would not change significantly if we applied a more rigorous approach to calculate them, and that the temperatures directly given by these global climate models are similar to those measured in our study area. In contrast, the HadGEM2 and MPI models show offsets of more than 3 °C (Table 6.1) and so, the uncorrected temperatures from both models significantly overestimate those measured.

Table 6.1: Temperature biases at 2005 yr given by the climate models with respect to the mean seabed temperature over the period 1975-2005 given by CTD measurements in our study area (Westbrook *et al.*, 2009), which are: at 400 m water depth (mwd) 2.69 °C, at 420 mwd 2.61 °C, at 450 mwd 2.51 °C, and at 500 mwd 2.23 °C (Marín-Moreno *et al.*, 2013c; supplementary material). Positive temperature offsets indicate higher temperatures predicted by the climate models.

		Offsets applied [°C] for each water depth [m]			
Climate Model	RCP	400	420	450	500
CCSM4	8.5	-0.06	0.00	0.09	0.35
CCSM4	2.6	0.13	0.06	0.05	0.32
GFDL	8.5	0.45	0.51	0.61	0.85
GFDL	2.6	0.45	0.51	0.61	0.87
HadGEM2	8.5	3.54	3.55	3.56	3.64
HadGEM2	2.6	3.31	3.29	3.26	3.31
IPSL	8.5	-0.97	-0.88	-0.76	-0.45
IPSL	2.6	-0.73	-0.63	-0.49	-0.16
MPI	8.5	3.20	3.24	3.31	3.49
MPI	2.6	3.12	3.27	3.24	3.44
MRI	8.5	-0.94	-0.87	-0.77	-0.50
MRI	2.6	-0.94	-0.88	-0.77	-0.49
NorESM1	8.5	0.57	0.61	0.66	0.83
NorESM1	2.6	0.55	0.58	0.63	0.79

6.3 Results and Discussion

In our study area and over the next century, temperatures are significantly more sensitive to the RCP scenario than to the climate model (Fig. 6.4a-c; g-i; m). A linear regression of the mean future temperatures for scenario RCP 2.6, gives an increase of 0.008±0.003 °C yr^{-1}. For RCP 8.5 the corresponding increase is 0.032±0.005 °C yr^{-1} at 400 mwd and of 0.031±0.005 °C yr^{-1} at 500 mwd (Table 6.2 and supplementary material A Table SM-A 6.3). For all climate models and for each water depth, temperatures over the first quarter of the century are similar and independent of the scenario RCP used (Table 6.2 and Fig. 6.4a-c; g-i; m). Temperature differences between the scenarios start to be important at ~2050 yr (Fig. 6.4a-c; h; i; m), and in the last quarter of the century, the differences between mean temperatures are ~1.8 °C (Table 6.2). The temperature evolution over the next century using scenario RCP 2.6 can be well described by a linear increase, and that using RCP 8.5 by a quadratic. This is indicated by the norm of the residuals between the temperatures from the models and those from the regression curves (Table 6.2 and supplementary material A Table SM-A 6.3).

Table 6.2: Mean temperatures ± one standard deviation for the first and last quarter of the century and regression parameters to approximate the evolution of the mean temperature series for the period 2000-2100 yr. Note that quadratic fits for scenario RCP 2.6 are not presented because a linear regression gives a good fit.

				Regression parameters to approximate the evolution of the mean temperature series [°C] for the period 2000-2100						
				Linear $T = at + b$			Quadratic $T = at^2 + bt + c$			
Water depth [m]	RCP	2000-2025 [yr] Mean ± σ [°C]	2075-2100 [yr] Mean ± σ [°C]	a [°C yr^{-1}]	b [°C]	$\Sigma (T_i^m - T_i)^2$	a [°C yr^{-2}]	b [°C yr^{-1}]	c [°C]	$\Sigma (T_i^m - T_i)^2$
400	8.5	2.68 ± 0.23	5.09 ± 0.48	0.032	-61.51	3.00	3.29E-4	-1.31	1323.5	1.65
400	2.6	2.71 ± 0.22	3.25 ± 0.11	0.007	-12.08	1.64				
420	8.5	2.62 ± 0.24	5.00 ± 0.48	0.031	-61.24	2.98	3.24E-4	-1.20	1299.8	1.66
420	2.6	2.64 ± 0.23	3.19 ± 0.11	0.007	-12.34	1.66				
450	8.5	2.51 ± 0.25	4.88 ± 0.49	0.031	-60.82	2.94	3.15E-4	-1.26	1264.3	1.69
450	2.6	2.53 ± 0.24	3.01 ± 0.11	0.007	-12.74	1.70				
500	8.5	2.22 ± 0.19	4.55 ± 0.43	0.031	-59.97	2.71	2.98E-4	-1.19	1195.2	1.46
500	2.6	2.23 ± 0.19	2.83 ± 0.10	0.008	-13.59	1.52				

σ, standard deviation; T and T^m, temperatures from the regression and from the climate models mean series, respectively [°C]; t, time [yr].

The time taken for methane gas to reach the seabed is controlled by the temperature changes given by the climate models (in the absence of other differences between the models), and the higher the rate of change the sooner gas emissions occur (Fig. 6.5). Seabed gas emissions from dissociated hydrate at 400 mwd started in the second quarter of the 20th century (Marín-Moreno *et al.*, 2013c), at 420 mwd they start after 2080 CE and between 2060 and 2085 CE, if using RCP 2.6 or 8.5, respectively (Fig. 6.5). At 450 mwd they occur only if using RCP 8.5 and these start between 2074 and 2096 CE (or not at all

with MPI and NorESM1; Figs. 6.2g and 6.3g). At 500 mwd none of the models predict gas emissions (Figs. 6.2h and 6.3h).

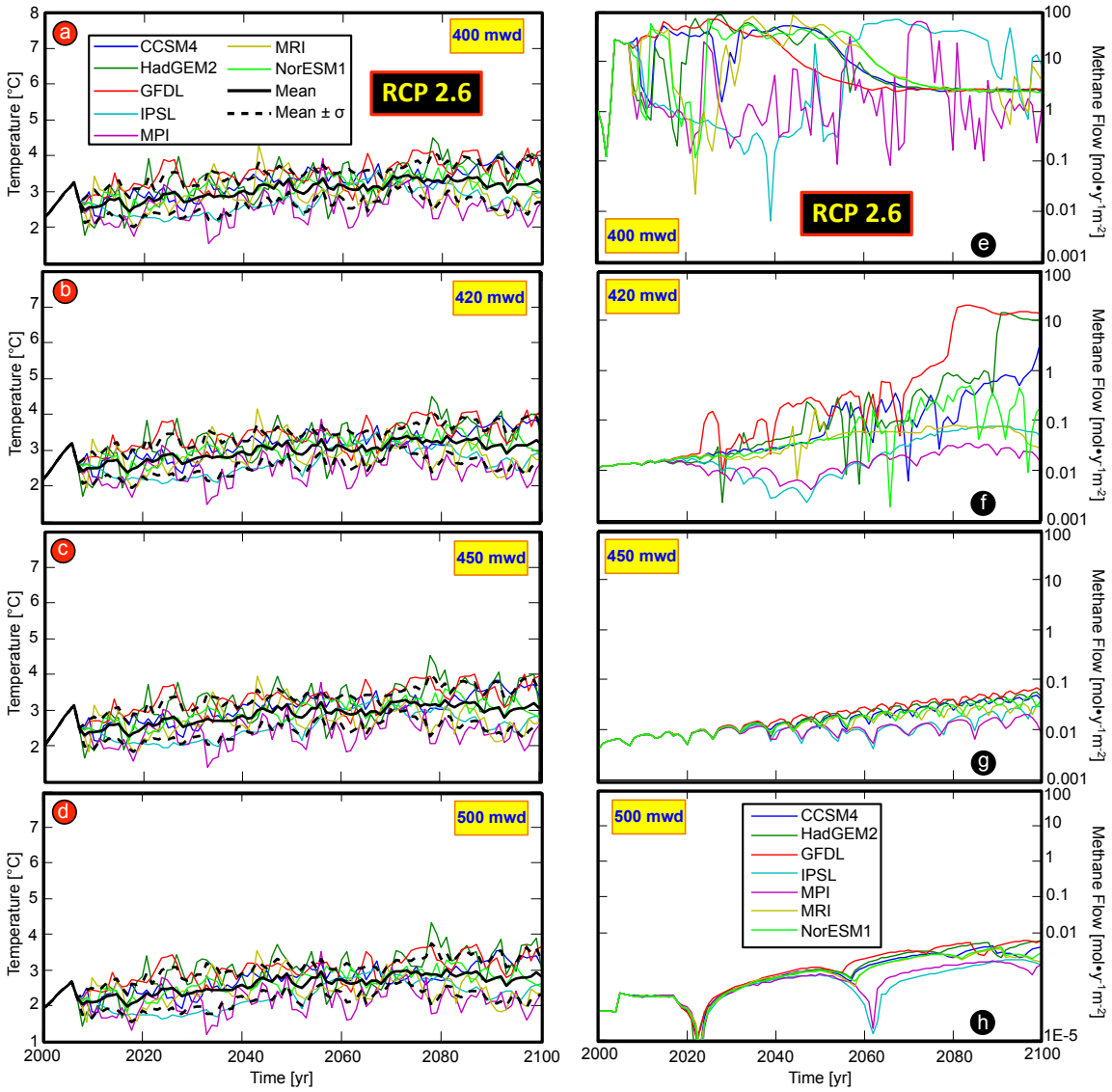

Figure 6.2: Results at our study transect from climate models CCSM4, HadGEM2, GFDL, IPSL, MPI, MRI, NorESM1 under climate-forcing scenario RCP 2.6 over the next century and for 400, 420, 450 and 500 m water depth. (a-d) Future temperature and (e-h) methane flow at the seabed. Note that the temperatures on the first part of (a-d) plots collapse into one line because the temperature at that time period (2000-2005 yr) is not given by the climate models. In the legend, σ is standard deviation.

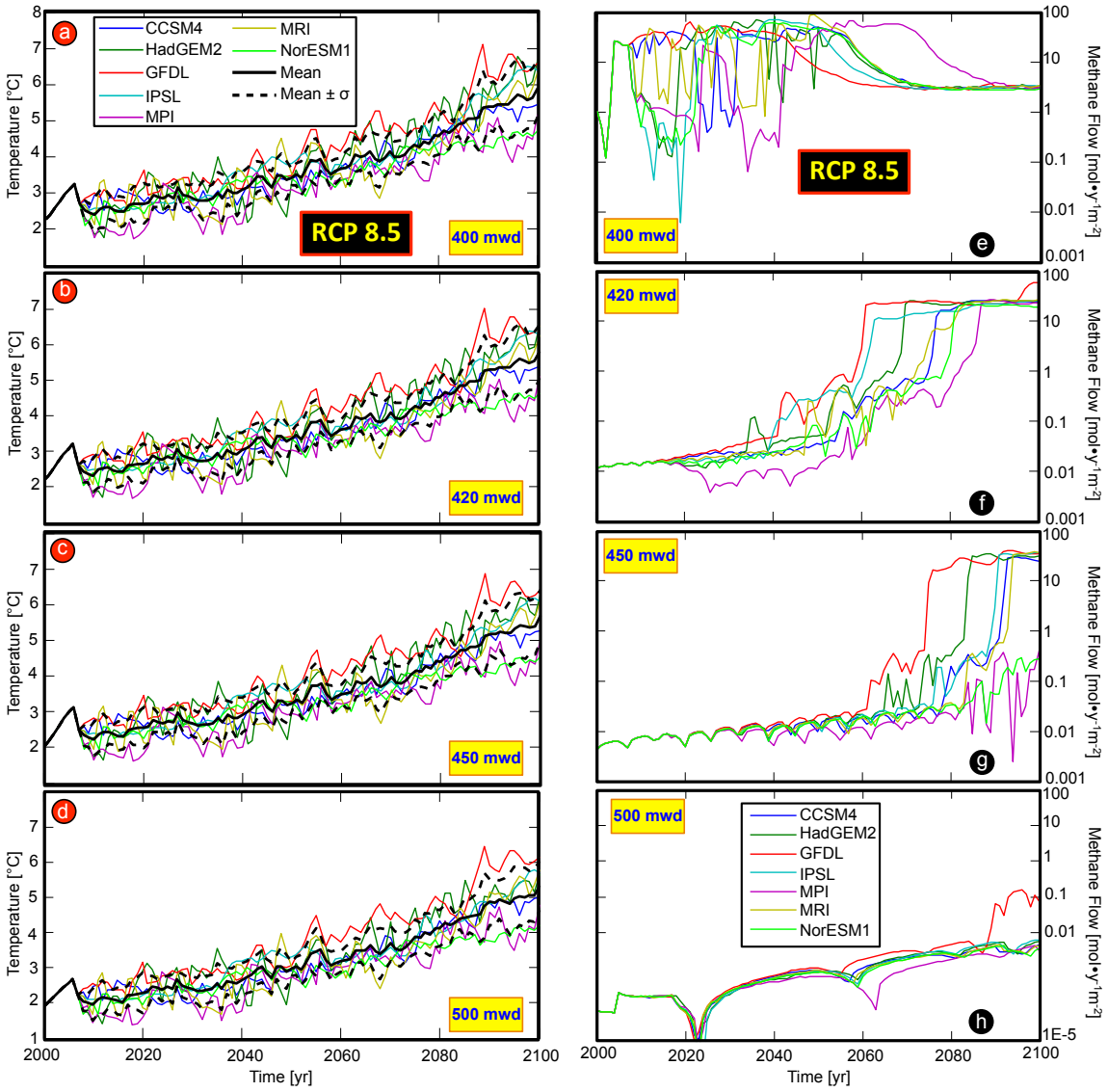

Figure 6.3: Results at our study transect from climate models CCSM4, HadGEM2, GFDL, IPSL, MPI, MRI, NorESM1 under climate-forcing scenario RCP 8.5 over the next century and for 400, 420, 450 and 500 m water depth. (a-d) Future temperature and (e-h) methane flow at the seabed. Note that the temperatures on the first part of (a-d) plots collapse into one line because the temperature at that time period (2000-2005 yr) is not given by the climate models. In the legend, σ is standard deviation.

At 400 mwd the future response of the system is not very sensitive to which climate model and RCP scenario are used, with the exception of climate models IPSL and MPI (Fig. 6.4d-f; j-l; n). This supports Marín-Moreno *et al.*'s (2013c) result that, at the present-day, most of the system is out of the GHSZ and that the uncertainty in its future response to ocean warming is small.

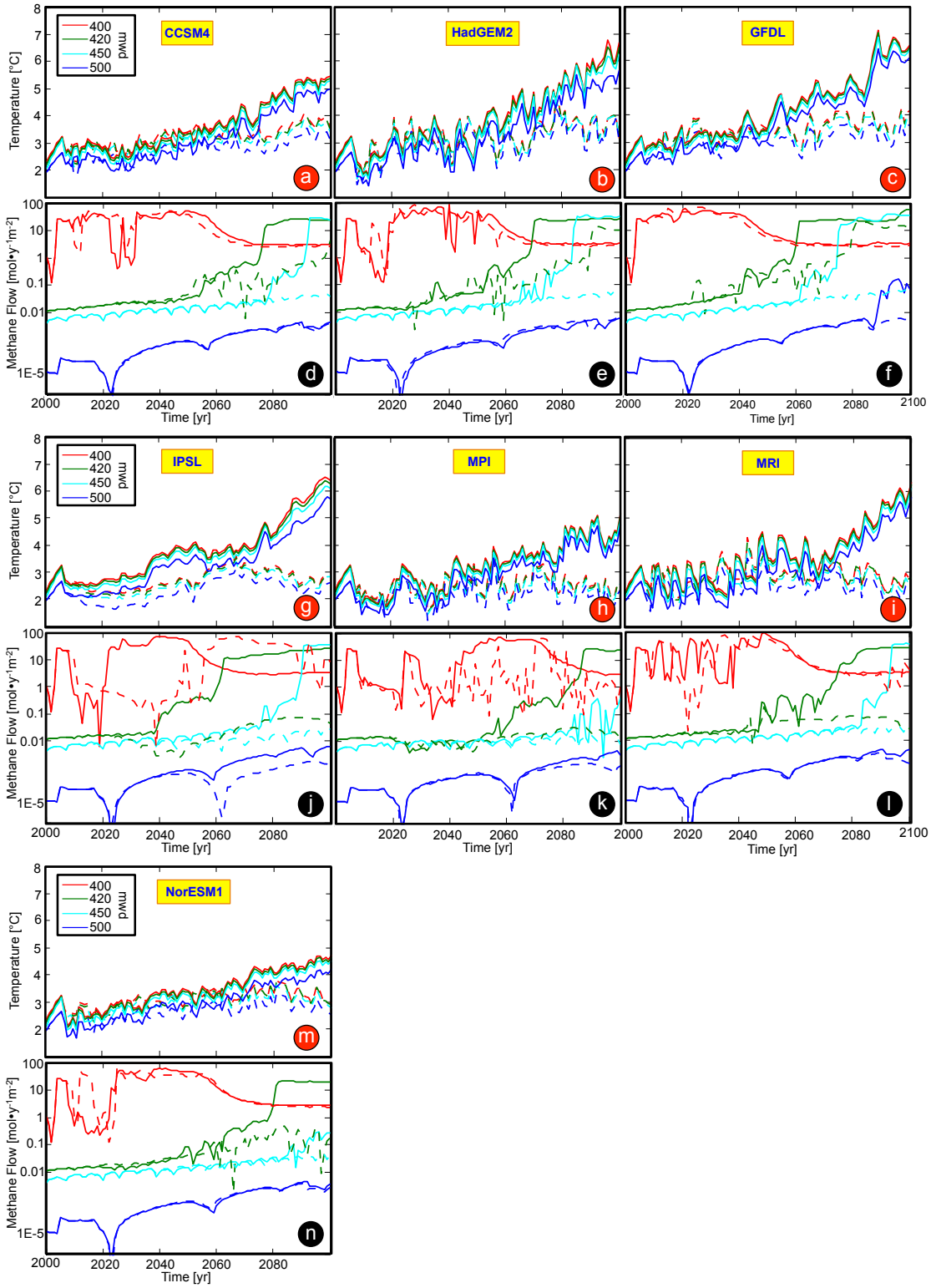

Figure 6.4: Results at our study transect from climate models CCSM4, HadGEM2, GFDL, IPSL, MPI, MRI, NorESM1 over the next century and for 400, 420, 450 and 500 m water depth. Solid lines show results using the climate-forcing scenario RCP 8.5 and dashed lines using RCP 2.6. (a-c, g-i and m) Future temperature and (d-f, j-l and n) methane flow at the seabed.

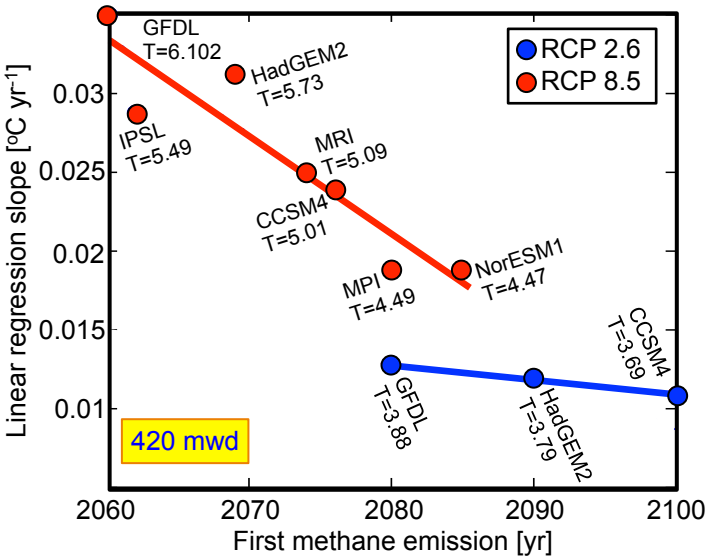

Figure 6.5: Year of first methane emission vs slope of a linear fit to the temperature series. Results at 420 m water depth for RCPs 2.6 (blue dots) and 8.5 (red dots), and for the climate models that predict methane emissions. The number in each dot shows the temperature (T, ºC) when the first methane emission occurs.

At that depth, for the climate models that give a sub-seabed temperature profile (supplementary material B, Figure SM-B 6.7) a bit lower than the temperature profile for dissociation, the perturbations in temperature about the trend move the gas hydrate system in and out its stability field and seabed methane pulses are directly correlated with those perturbations (e.g, Fig. 6.4h-i; k-l). The MPI climate model under RCP 2.6 at 400 mwd, shows the most "spiky" seabed methane emissions behaviour of all the climate models (Figs. 6.2e) because its long-term average temperature is below the temperature of dissociation over the whole century and so, methane emissions are completely controlled by temperature perturbations around this average. At 420 mwd, although temperature perturbations are in the same order of magnitude, at about ±1.5 ºC, as those at 400 mwd, significant pulses of methane are not observed. The magnitude of temperature perturbations is not enough to affect the gas hydrate system at 420 mwd and hence, for water depths deeper than ∼420 m, an average increase in temperature due to global warming is required to affect the system. Different behaviours at 400 and 420 mwd may suggest that the present-day gas hydrate system at 400 mwd may be responding to temperature perturbations of about ±1-2 ºC due to seasonality (Beszczynska-Möller *et al.*, 2012; Biastoch *et al.*, 2011), where in summer gas hydrate would dissociate and in winter would reform. However, if seasonality is what controls the system, and assuming that this has not changed significantly in the past two millennia, methane from dissociated hydrate should has been emanating from the seabed at that depth, at least, over the past two millennia at periods where temperatures are similar to the mean over the last century, that is ∼2.6 ºC (Marín-Moreno *et al.*, 2013c; supplementary material). To account for seasonality as a trigger mechanism for gas hydrate dissociation in our study area, a constant source of gas charging the GHSZ needs to be explained. At 400 mwd, all climate models show a

similar maximum rate of methane emission of 65-75 mol yr^{-1} m^{-2} (Figs. 6.2e and 6.3e), which is limited by enthalpy (Thatcher *et al.*, 2013). At 420 mwd for scenario RCP 2.6, the maximum rate of emission is 10-20 mol yr^{-1} m^{-2} (Fig. 6.2f) and for RCP 8.5 at 420 and 450 mwd, it is 25-35 mol yr^{-1} m^{-2} (Fig. 6.3f; g). Although the magnitude of methane emissions is limited by enthalpy, these different values are driven by a different response of the system at different water depths. At day and over the next century, at 400 mwd most of the hydrate system is out of its GHSZ but at 420 and 450 mwd there are two unconnected dissociation fronts, the top part of the hydrate layer and the base of the GHSZ (Figs. SM 6.13 and SM 6.14). Methane emissions over the next century at 400 mwd come from dissociation of the complete hydrate layer, and at 420 and 450 mwd come from dissociation only at the top. At some future time beyond 2100 CE, at 420 and 450 mwd methane from dissociated hydrate at the base of the GHSZ will contribute to the methane outflow from dissociation at the top part of the hydrate layer and the maximum methane outflow will be similar to that at 400 mwd (Marín-Moreno *et al.*, 2013c). Figure 6.3f for climate model GFDL (red line), which is the model that predicts the earliest seabed methane emissions (Figs. 6.2e-f and 6.3e-g), shows that methane from dissociation at the base of the GHSZ will start to contribute to the total methane outflow by the end of this century, and this will be of ~60 mol yr^{-1} m^{-2}. Our calculated magnitude of high rate emissions is slightly lower than that recorded close to vents on the South Hydrate Ridge (Heeschen *et al.*, 2005) and similar to that of Reagan *et al.* (2011), but we predict high fluxes extending into significantly deeper water.

We follow Marín-Moreno *et al.*'s (2013c) approach to estimate the methane outflow in the area where gas hydrate dissociation occurs, between latitudes of 78°26'N-78°40'N (~25 km length). Over the next century, using scenario RCP 2.6 the active seabed area of methane emissions may be of ~26.8 km^2, from 400 to 430 mwd (Figs. 6.2e-h), releasing between 0.97-3.3 Gg yr^{-1} (2.3-7.8 mol yr^{-1} m^{-2}) of methane to the Arctic Ocean. For RCP 8.5, methane emissions may occupy a seabed area of ~71.4 km^2, from 400 to 480 mwd (Fig. 6.3e-h), releasing between 3.9-10.3 Gg yr^{-1} (3.4-9.0 mol yr^{-1} m^{-2}). Therefore, and assuming the maximum potential seabed area of future methane emissions (~71.4 km^2), over the next century between 0.97-10.3 Gg yr^{-1} (0.85-9.0 mol yr^{-1} m^{-2}) of methane may be emitted to the Arctic Ocean. The rate of methane emissions is not constant over the next century (Fig. 6.6). Over the first half of the century, differences in average methane emissions between both RCP scenarios are minor, except for the IPSL climate model, because, as mentioned above, both RCPs scenarios predict similar temperatures over that period. In contrast, for the period 2050-2100 those differences are significant (Fig. 6.6). Although future temperatures are more sensitive to the RCP scenario chosen than to the climate model, methane emissions from hydrate dissociation over the next century are sensitive to

both RCP scenario and climate model (Fig. 6.6). However, the estimated methane emissions for the second half of the century (Fig. 6.6) suggest that if extending the calculations beyond 2100 CE, where the rates of increasing temperature change drastically between the two RCP scenarios and methane emissions from dissociated hydrate at deeper water depths start to be important (Marín-Moreno *et al.*, 2013c), future methane emissions are likely to be significantly more influenced by the choice of RCP scenario than by the choice of climate model.

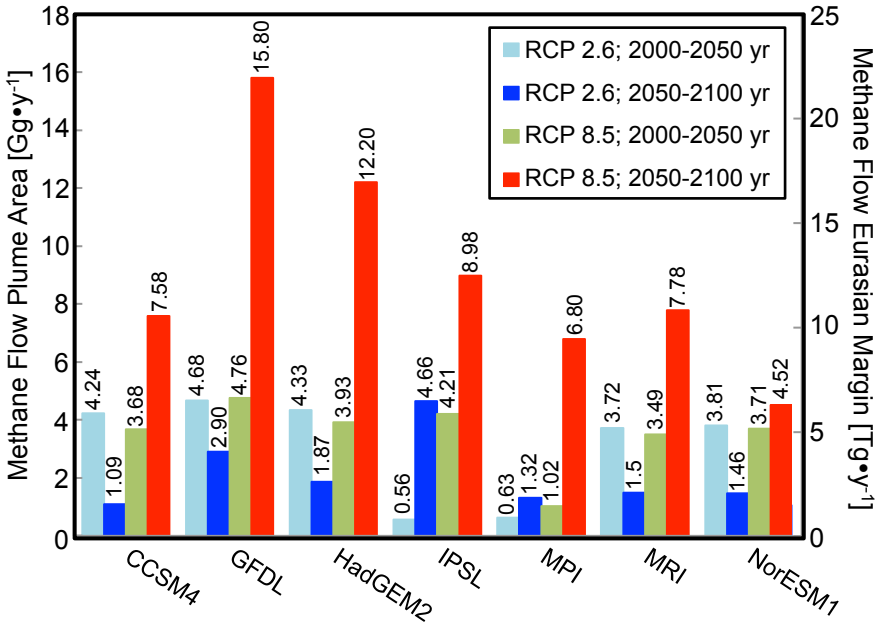

Figure 6.6: Average methane flow at the seabed between 400 to 480 m water depth for the periods 2000-2050 and 2050-2100, along the plume area (~71.4 km^2) and along the entire Eurasian Margin (73°N-85°N; 0°-160°N, going eastward, ~98475 km^2; Jakobsson *et al.*, 2008). Results for RCPs 2.6 and 8.5 and for climate models CCSM4, GFDL, HadGEM2, IPSL, MPI, MRI, and NorESM1. An scaling factor of 1377 has been used (ratio between both areas) to estimate the methane outflow in the entire Eurasian Margin. The number above each bar shows the average methane outflow in the plume area.

6.4 Acknowledgements

This work was supported by the UK Department of Energy and Climate Change through a supplement to Natural Environment Research Council grants NE/H002732/1 and NE/H022260/1.

6.5 Supplementary Material A. Regression Parameters

Table SM-A 6.3: Regression parameters to approximate the evolution of the mean ± standard deviation time series for the period 2000-2100 yr. Note that quadratic fits for scenario RCP 2.6 are not presented because a linear regression gives a good fit.

		Regression parameters to approximate the evolution of the **mean plus standard deviation** temperature series [°C] for the period 2000-2100						
		Linear $T = at + b$			Quadratic $T = at^2 + bt + c$			
Water depth [m]	RCP	a [°C yr^{-1}]	b [°C]	$\Sigma (T_i^m - T_i)^2$	a [°C yr^{-2}]	b [°C yr^{-1}]	c [°C]	$\Sigma (T_i^m - T_i)^2$
400	8.5	0.037	-71.90	3.387	3.39E-4	-1.36	1355.9	2.18
400	2.6	0.011	-18.21	1.89				
420	8.5	0.037	-71.46	3.30	3.30E-4	-1.32	1315.7	2.13
420	2.6	0.011	-18.50	1.92				
450	8.5	0.036	-70.84	3.19	3.16E-4	-1.26	1256.8	2.09
450	2.6	0.011	-18.94	1.98				
500	8.5	0.036	-69.64	2.90	2.94E-4	-1.17	1164.8	1.84
500	2.6	0.011	-19.65	1.90				

		Regression parameters to approximate the evolution of the **mean minus standard deviation** temperature series [°C] for the period 2000-2100						
		Linear $T = at + b$			Quadratic $T = at^2 + bt + c$			
Water depth [m]	RCP	a [°C yr^{-1}]	b [°C]	$\Sigma (T_i^m - T_i)^2$	a [°C yr^{-2}]	b [°C yr^{-1}]	c [°C]	$\Sigma (T_i^m - T_i)^2$
400	8.5	0.027	-51.10	3.42	3.19E-4	-1.28	1291.1	2.40
400	2.6	0.004	-5.94	2.54				
420	8.5	0.026	-51.00	3.40	3.17E-4	-1.28	1283.9	2.39
420	2.6	0.004	-6.19	2.55				
450	8.5	0.026	-50.81	3.39	3.14E-4	-1.26	1271.8	2.39
450	2.6	0.004	-6.53	2.57				
500	8.5	0.026	-50.3	3.17	3.03E-4	-1.21	1225.6	2.18
500	2.6	0.005	-7.54	2.42				

T and T^m, temperatures from the regression and from the climate models mean series, respectively [°C]; t, time [yr].

6.6 Supplementary Material B. Variations in Sub-Seabed Distribution of Temperature, Pressure and, Gas Hydrate and Gas Saturations with Time and Water Depth

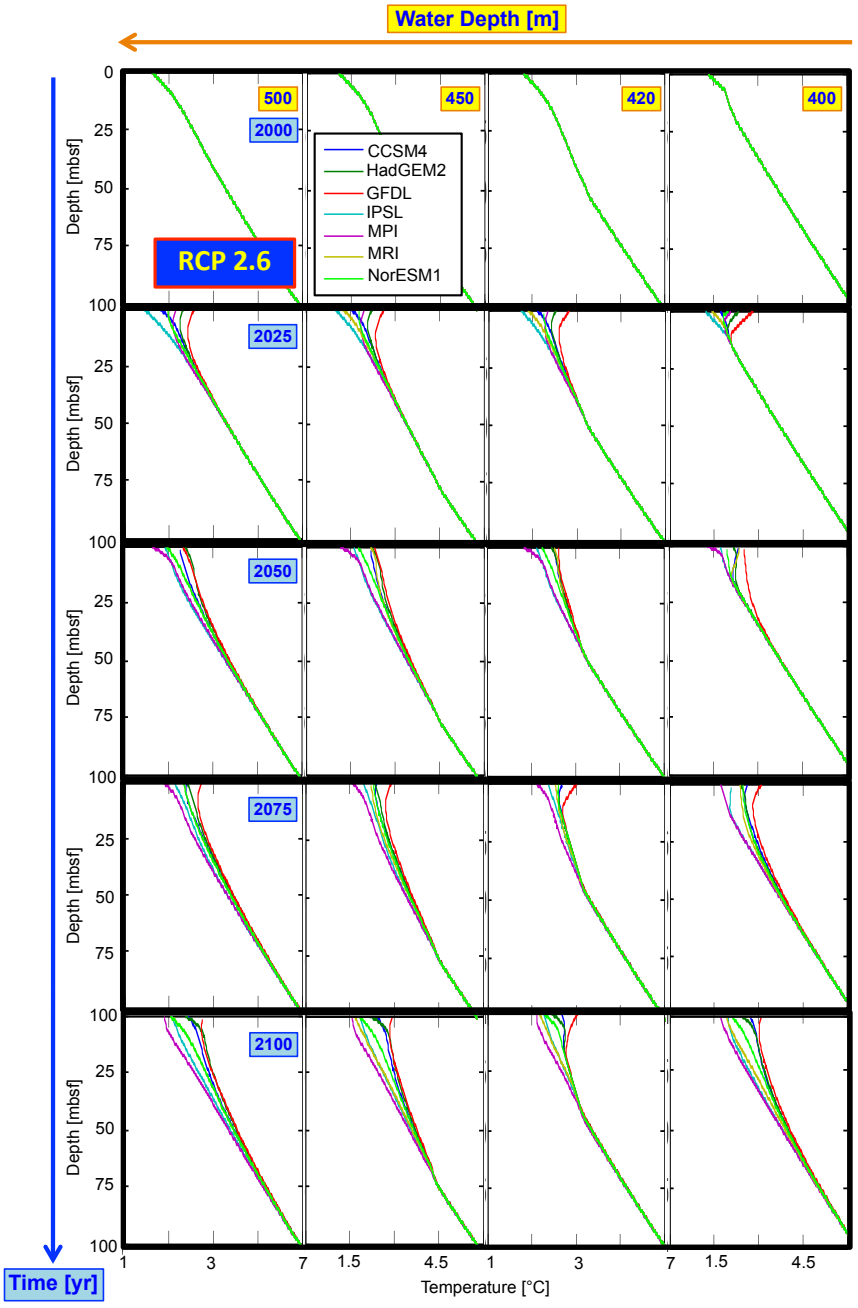

Figure SM-B 6.7: Grid of results showing the variation in temperature with time (rows) and water depth (columns), using the climate-forcing scenario RCP 2.6 and climate models CCSM4, GFDL, HadGEM2, IPSL, MPI, MRI, and NorESM1.

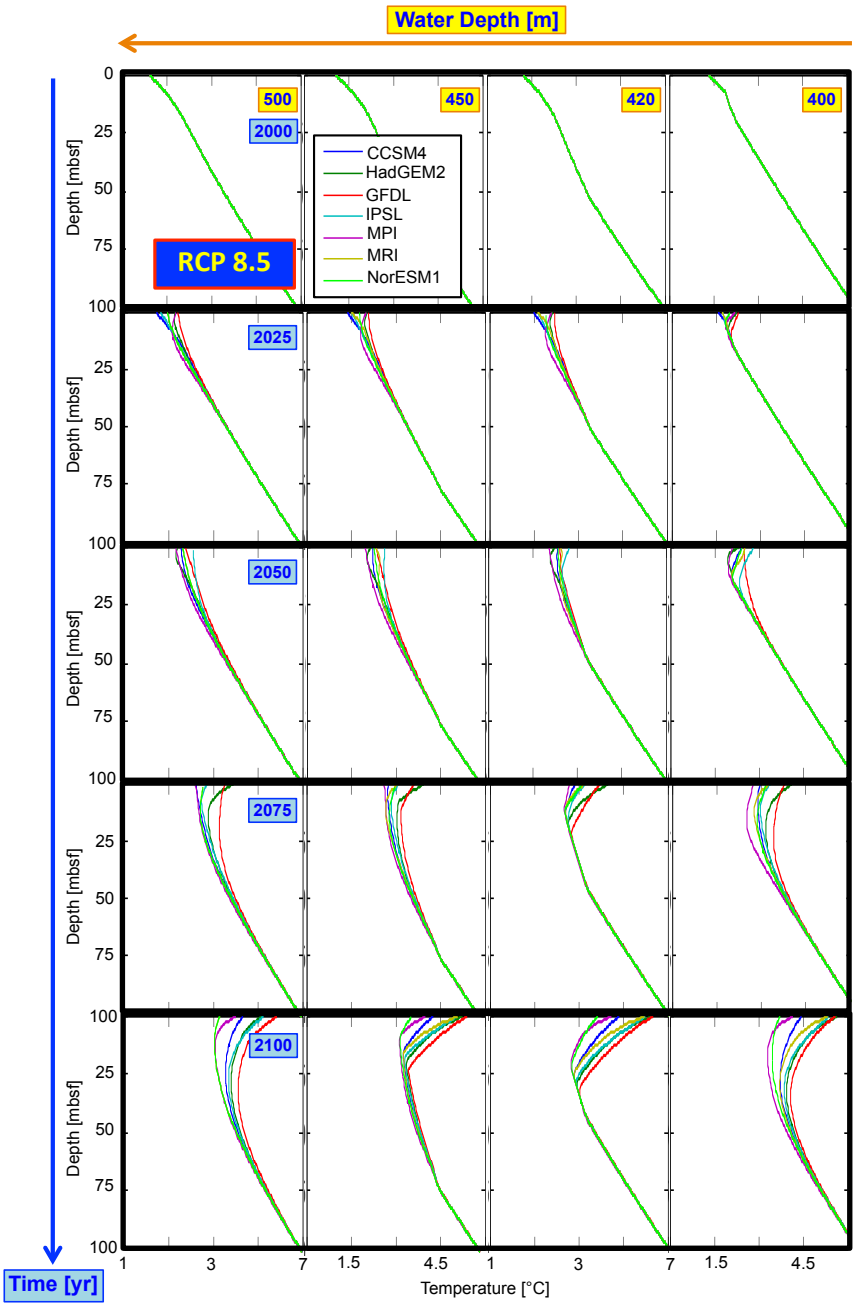

Figure SM-B 6.8: Grid of results showing the variation in temperature with time (rows) and water depth (columns), using the climate-forcing scenario RCP 8.5 and climate models CCSM4, GFDL, HadGEM2, IPSL, MPI, MRI, and NorESM1.

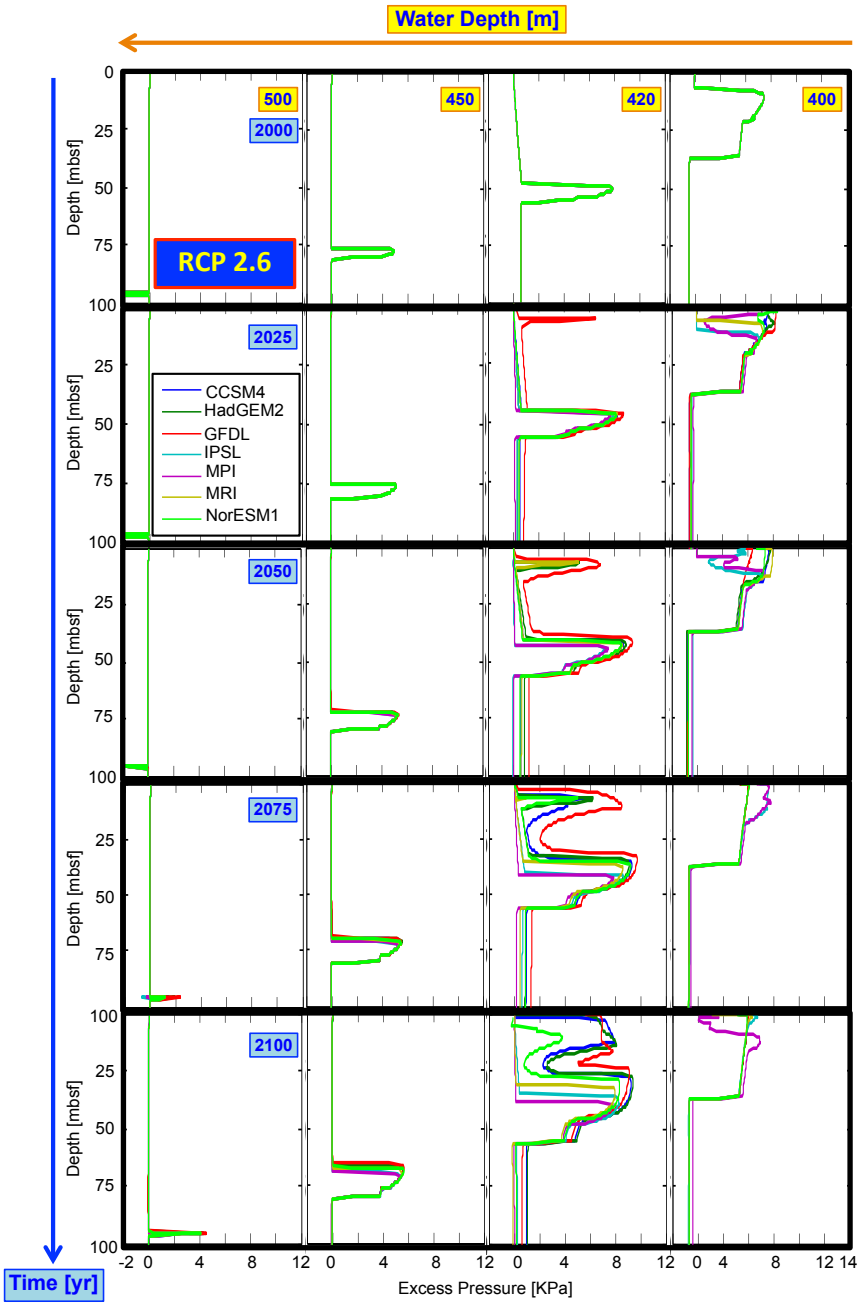

Figure SM-B 6.9: Grid of results showing the variation in excess pressure with time (rows) and water depth (columns), using the climate-forcing scenario RCP 2.6 and climate models CCSM4, GFDL, HadGEM2, IPSL, MPI, MRI, and NorESM1.

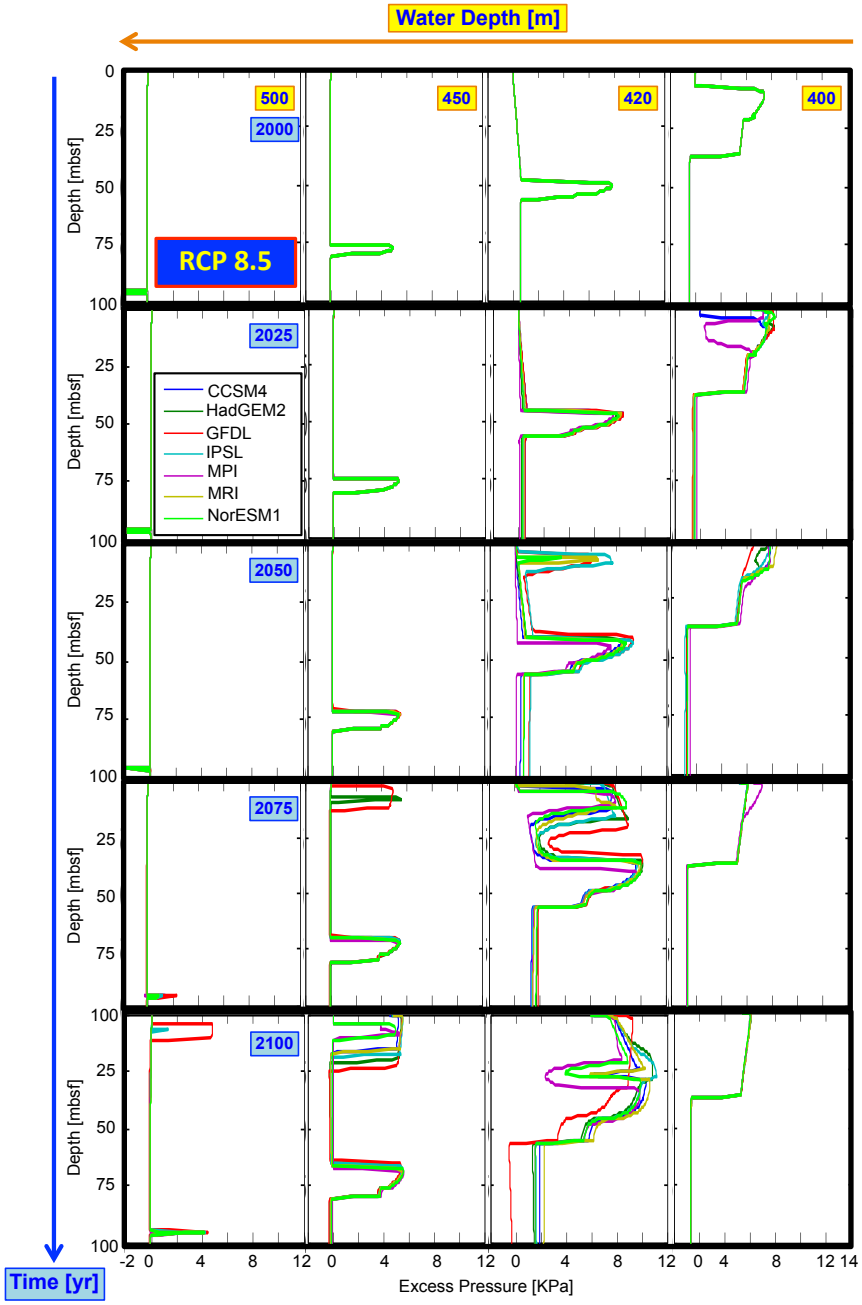

Figure SM-B 6.10: Grid of results showing the variation in excess pressure with time (rows) and water depth (columns), using the climate-forcing scenario RCP 8.5 and climate models CCSM4, GFDL, HadGEM2, IPSL, MPI, MRI, and NorESM1.

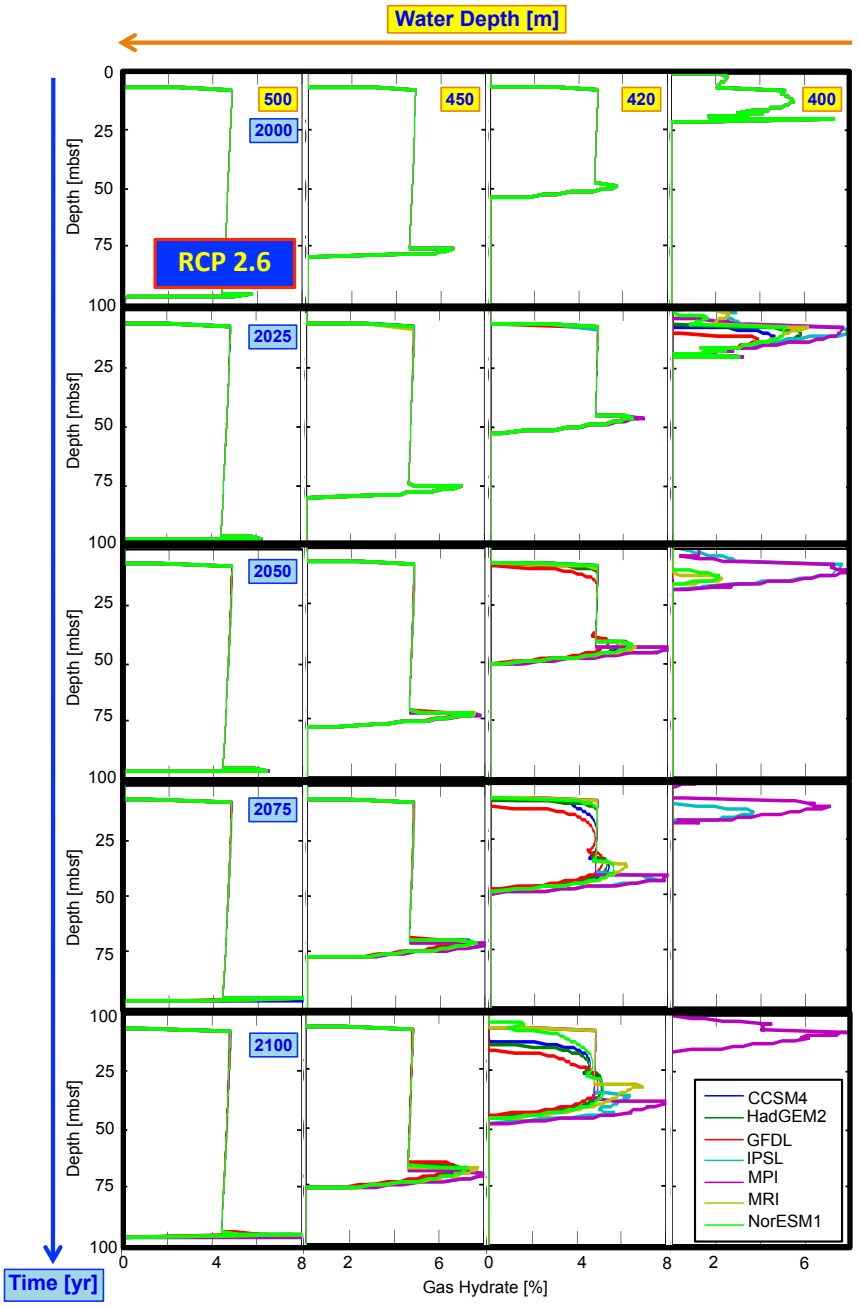

Figure SM-B 6.11: Grid of results showing the variation in gas hydrate saturation with time (rows) and water depth (columns), using the climate-forcing scenario RCP 2.6 and climate models CCSM4, GFDL, HadGEM2, IPSL, MPI, MRI, and NorESM1.

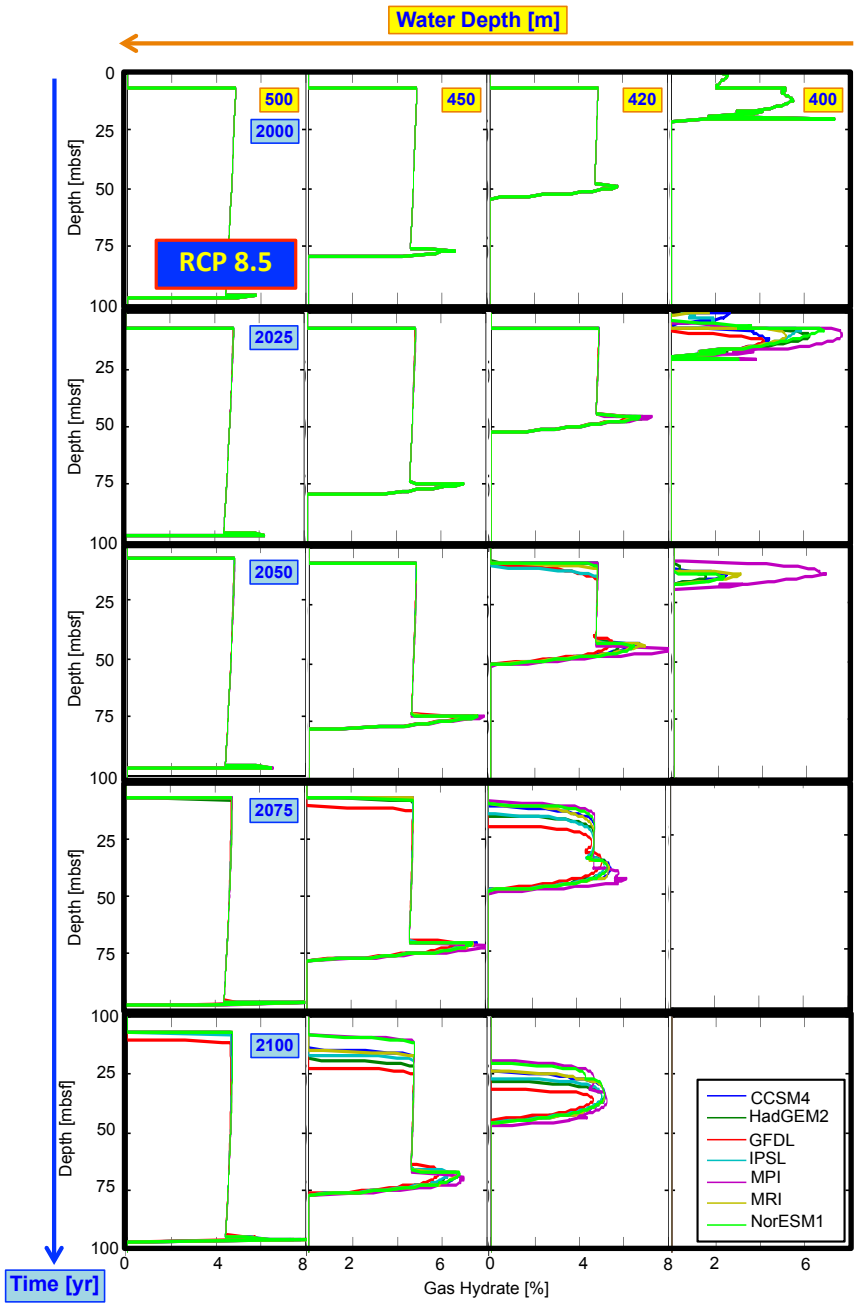

Figure SM-B 6.12: Grid of results showing the variation in gas hydrate saturation with time (rows) and water depth (columns), using the climate-forcing scenario RCP 8.5 and climate models CCSM4, GFDL, HadGEM2, IPSL, MPI, MRI, and NorESM1.

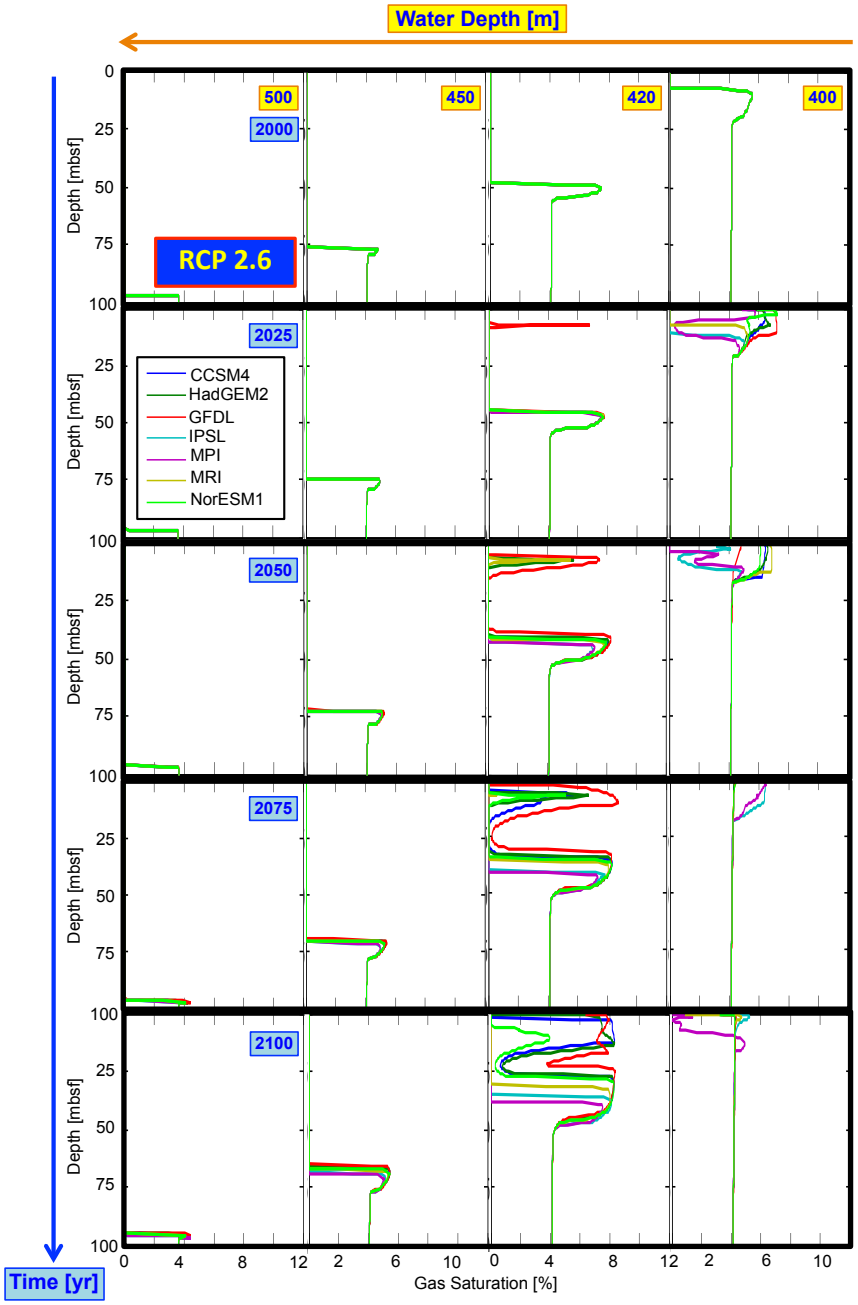

Figure SM-B 6.13: Grid of results showing the variation in gas saturation with time (rows) and water depth (columns), using the climate-forcing scenario RCP 2.6 and climate models CCSM4, GFDL, HadGEM2, IPSL, MPI, MRI, and NorESM1.

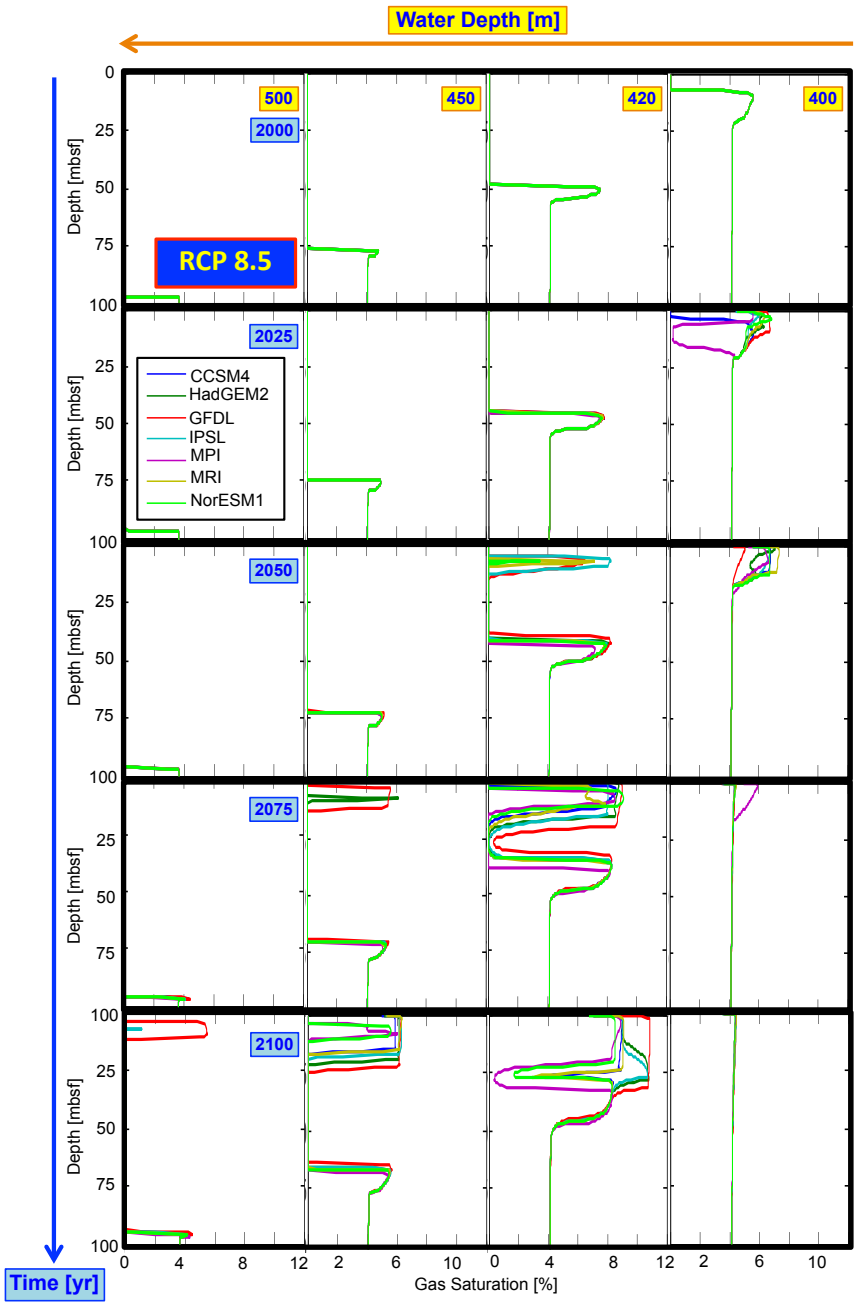

Figure SM-B 6.14: Grid of results showing the variation in gas saturation with time (rows) and water depth (columns), using the climate-forcing scenario RCP 8.5 and climate models CCSM4, GFDL, HadGEM2, IPSL, MPI, MRI, and NorESM1.

Chapter 7

Final Conclusions and Future Work

7.1 Overpressure Development in Deep Basins. Final Conclusions

This thesis concludes that low velocity zones (LVZ) in deep basins can be linked to overpressure generated by disequilibrium compaction. Semi-empirical methods constrained by geophysical data can estimate the amount and distribution of overpressure. However, these methods may result in inaccurate estimates in complex geological settings and they do not provide a consistent physical explanation for the inferred overpressure. Hydromechanical numerical models, consider the physics of overpressure generation but their results are difficult to validate, especially in deep and/or large basins, and the accuracy of their results is completely dependent on the selection of the initial input parameters. Bringing together numerical models, able to describe the mechanisms governing the generation of overpressure, with observed geophysical constraints, such as using an inverse model, provides further insights into the hydrodynamic behaviour of the system. The inverse model presented here is a powerful tool that allows estimation of the overpressure, and determination of lithological parameters and sedimentation rates. These parameters will help the understanding of possible fluid migration pathways in the past and provide essential information for possible future hydrocarbon exploration campaigns.

The key findings of this part of the thesis are summarised here:

i) Two methods for overpressure prediction have been developed to constrain the overpressure generated by a 1D/2D disequilibrium compaction (DC) and aquathermal expansion (AE) forward model with seismic and geological data. The first method,

presented in Chapter 3, estimates the overpressure generated by DC and model parameters: sedimentation rate, surface porosity, and compaction factor for each modelled layer. It does not require any assumption regarding the P-wave velocity V_p of normally compacted sediments (hydrostatic conditions), as do the semi-empirical methods. However, it uses both a decompaction model and a V_p-density relationship that incorporate more relationships between variables and assumptions in the model. The inverse model, presented in Chapter 4, estimates the overpressure generated by DC and AE, and model parameters: surface porosity, compaction factor, intrinsic permeability at surface conditions, a parameter controlling the evolution of intrinsic permeability with porosity, the ratio between horizontal and vertical permeability and sedimentation rate (assuming a known time interval) for each layer. The relatively large number of different model parameters explored by the inverse model requires further constraints on the misfit function from assuming the V_p of normally compacted sediments (if this is not known). It also requires bounds within which the inverse model parameters can evolve and a V_p-density relationship.

ii) The above methods have been applied successfully to the centre of Eastern Black Sea Basin. The observed LVZ modelled from wide-angle seismic data in the centre of the basin, located within the Maikop formation at ∼3500-6500 mbsf, has been linked to overpressured sediments. Overpressure was mainly generated by DC (more than 90%) with AE acting as a secondary mechanism. A maximum overpressure of ∼40-51 MPa (with a 95% confidence) at ∼6400 mbsf and λ^* (ratio of excess pore pressure above hydrostatic to the effective stress in hydrostatic conditions) value of ∼0.62 at ∼5200 mbsf may exist in the basin at the present-day. These results match those obtained using the semi-empirical method, Eaton's method, with an Eaton exponent between 3-3.5. An Eaton exponent of 3 is the recommended value in basins where disequilibrium compaction is thought to be the dominant mechanism generating overpressure.

iii) DC occurred because of the relative high sedimentation rates of 0.28-0.29 m ka^{-1} at 33.9-20.5 Ma, during the deposition of the Maikop formation, and of 0.91-0.94 m ka^{-1} at 13-11 Ma, during the deposition of the Sarmatian. The relatively low vertical and horizontal permeabilites of the Maikop formation sediments of ∼1-5x10^{-13} m s^{-1} and of ∼7.5x10^{-12} m s^{-1}, respectively, and the presence of a significantly low permeability layer of ∼0.3-1.3x10^{-14} m s^{-1}, with a thickness of ∼200 m, below the Maikop formation, limited the escape of pore fluids, hence allowing the development of overpressure within the Maikop formation. The inferred normal V_p velocities and the associated hydrostatic pressures below the Maikop formation were explained by downward escape of pore fluids, which may be supported by the presence of a fractured and/or karstified basement.

7.2 Future Response of Gas Hydrate to Ocean Warming Offshore West Svalbard. Final Conclusions

This thesis concludes that significant amounts of methane may be released to the Arctic Ocean over the next three centuries from warming-induced dissociation of marine hydrate-bearing sediments offshore West Svalbard. A well constrained model of the evolution of the gas hydrate system for the period 1-2300 CE and between 350-800 m water depth (mwd) was created. The gas hydrate model was "grown" over the past ∼2000 yr driven by a model of changing ocean temperature to provide a present-day sub-seabed distribution of gas and hydrate that is close to that indicated by seismic data, that image the BSR in water depths of more than 580 m and the upper limit of gas-related reflectors in shallower water. Future temperatures came from seven published global climate models, CCSM4, GFDL, HadGEM2, IPSL, MPI, MRI, and NorESM1, and climate-forcing scenarios Representative Concentration Pathways (RCPs) 2.6 and 8.5. This work is the first numerical modelling study that uses the predictions of future changes in climate to provide well constrained estimates of methane emissions from dissociated hydrate on a continental margin.

The key findings of this part of the thesis are summarised here:

i) The dissociation reaction of hydrate acts as a heat sink to the increases in temperature of the overlaying ocean, and the more hydrate present the longer it takes for the subsurface to warm. At the pressure and temperature conditions of the phase boundary, dissociation of hydrate will produce gas at a rate determined by the rate at which heat is supplied to overcome the latent heat. The resulting products of gas hydrate dissociation, gas and pure water, increase the pressure and decrease the salinity of the system and hence, increase its stability. Therefore, the sub-seabed temperature gently increases to move the system again to the phase boundary. Depending on the amount of heat supply and the hydrate saturation of the pore space, gas and hydrate phases can coexist at the same depth.

ii) For intrinsic permeabilities greater than $\sim 10^{-13}$ m^2, further increases in permeability make no difference to the rate of gas transport to the seabed. This is because the process is limited by the rate at which heat can be taken into the hydrate to supply the latent heat required for the dissociation reaction to occur.

iii) Over the next century offshore West Svalbard, the climate models show an increase in temperatures of $\sim 0.008 \pm 0.003$ °C yr^{-1} for RCP 2.6. Using RCP 8.5, they show a temperature increase of $\sim 0.032 \pm 0.005$ °C yr^{-1} at 400 mwd and of $\sim 0.031 \pm 0.005$ °C yr^{-1} at 500 mwd. For all climate models used in this thesis and for each water depth, over the first quarter of this century temperatures are similar and independent of the

scenario RCP used. Temperature differences between scenarios start to be important at ∼2050 CE, and in the last quarter of the century, the differences between mean temperatures are ∼1.8 ^{o}C.

iv) The observed bubble plumes of methane gas escaping from the seabed of the West Svalbard continental margin at ∼400 mwd, may be driven by warming-induced gas hydrate dissociation. At that depth, dissociation would have started at ∼1930 CE, due to the increase in temperature over the Industrial Period, and ∼15 yr later, methane emissions would have started and may be active until ∼2060-2100 CE with a magnitude of high rate emissions of 65-75 mol yr^{-1} m^{-2}, limited by enthalpy. At 400 mwd, the future response of the system is not very sensitive to which climate model and RCP scenario is used and so, the uncertainty in its future response to ocean warming is small. Most of the present-day system at 400 mwd is out of the gas hydrate stability zone (GHSZ), or close to the temperature of dissociation and hence, perturbations in temperature about the main temperature trend move the gas hydrate system in and out its stability field and seabed methane pulses are directly correlated with those perturbations. Temperature perturbations about the main temperature trend have a magnitude of ±1.5 ^{o}C for all climate models, which is similar to the temperature changes due to seasonality in the area of ±1-2 ^{o}C. This model behaviour indicates that the gas hydrate system at 400 mwd may be responding to seasonal temperature changes as well as to ocean warming. However, such temperature perturbations do not affect the system beyond 420 mwd, so seasonality, if does not significantly vary during the future, will not be a dominant factor controlling the future response of the system there.

v) At 420 mwd, seabed methane emissions may start after 2080 CE and between ∼2060-2085 CE, if using RCP 2.6 or 8.5, respectively, and may be active for the next three centuries. If using RCP 8.5, seabed methane emissions may start at ∼2074-2096 CE at 450 mwd, and at 500 mwd, at ∼2100-2130 CE. At water depths deeper than ∼500-600 m, no methane emissions are predicted, and hydrate remains stable for the next three centuries. At water depths where there are methane emissions, the duration of high rate emissions increases with increasing water depth. This is because the amount of hydrate beneath the seabed in the models increases with increasing water depth and the magnitude of high rate emissions is similar at different water depths and limited by enthalpy. Over the next century, the potentially active seabed area of methane emissions may be within the depth range of ∼400-480 mwd (71.4 km^2) realising 0.97-10.3 Gg yr^{-1} (0.85-9.0 mol yr^{-1} m^{-2}) of methane to the Arctic Ocean. The rate of methane emissions is not constant over the next century and future potential methane emissions in the Arctic, beyond ∼2100 CE, are likely to be much more sensitive to the

choice of RCP scenario than to the choice of climate model. For the first half of this century differences in average methane emissions between RCP scenarios are minor but for the period 2050-2100 those differences are significant. Over the next three centuries, methane emissions may extend further offshore to water depths between ~400-550 m (seabed area of 134 km^2) emitting between 5.3-29 Gg yr^{-1} (2.5-13.5 mol yr^{-1} m^{-2}). The total flux over the next three centuries increases with time because the active area of methane emission increases. The percentage of methane that may reach the atmosphere from those bubble plumes is still unknown. Very few of the acoustically imaged bubble plumes at ~400 mwd reach the sea surface, and even for those that could reach the seabed with significant size, for water depths deeper than 100 m most of the original methane may be dissolved into the water column and replaced by other gases. However, the increase in methane concentration is itself important because its oxidation in the water column causes ocean acidification and deoxigenation.

vi) If the future gas hydrate response offshore West Svalbard can be extended along the Svalbard archipelago and along the entire Eurasian Margin, over the next century, ~0.5-4.8 Tg yr^{-1} and ~1.3-14.2 Tg yr^{-1} of methane may be released to the Arctic Ocean, respectively. Over the next three centuries, ~1.7-9 Tg yr^{-1} and ~6.1-33 Tg yr^{-1} of methane may be released along the Svalbard archipelago and along the entire Eurasian Margin, respectively. Over the next three centuries, the maximum potential methane release from hydrate in the entire Eurasian Margin will be about five times smaller than global present-day methane emissions from all natural wetlands, which are currently 150 Tg yr^{-1} (Dlugokencky *et al.*, 2011), the same order of magnitude as the 8-29 Tg yr^{-1} from Arctic tundra (McGuire *et al.*, 2012), and about two orders of magnitude smaller than the 5000 Tg yr^{-1} between 2015-2025, recently assumed in the East Siberian Arctic Shelf (Whiteman *et al.*, 2013).

7.3 Future Work

In this thesis, I have presented a 1D/2D forward model to calculate the overpressure generated by the disequilibrium compaction (DC) and aquathermal expansion (AE) mechanisms, and an inverse model to constrain the overpressure calculated with seismic data.

- Only mechanical compaction, as a function of changes in effective stress, was considered in the forward model. Chemical compaction is mainly controlled by time, temperature and mineralogy (Bjørlykke & Høeg, 1997) and dominates over mechanical compaction in unlithified sediments at temperatures above 80-100 °C (Mondol *et al.*, 2007) in basins older than ~100 Ma (Schneider *et al.*, 1996). In the Eastern Black Sea

Basin (EBSB), the Maikop formation (33.9-20.5 Ma) has temperatures within 90-170 ^{o}C (assuming a constant thermal gradient in the EBSB of 26 ^{o}C km^{-1}; Minshull & Keddie, 2010). The overpressured sediments are significantly younger than 100 Ma, however and due to the high temperatures within the Maikop formation, chemical compaction may have occurred in the past and may be still active at the present-day in the basin. Including chemical compaction in the forward model will better represent the compaction history of the basin. Besides, in Marín-Moreno *et al.* (2013b) we inferred a significantly low permeability layer of ∼200 m below the Maikop formation that would not have allowed the pore fluids, within the Maikop formation, to escape downwards through the permeable basement. However, we did not give any explanation regarding its possible origin, which could be related to chemical compaction. Because the Maikop formation is a clay layer rich in organic matter, other processes such as hydrocarbon generation and smectite dehydration to illite may also contribute to overpressure generation, and could be added to the other two processes in the forward model.

- The accuracy of the inverse model result is influenced significantly by the number of misfit terms. The inverse model presented in this thesis minimises the error between observed and calculated values of: P-wave velocity V_p, normal V_p (hydrostatic conditions), sediment density, and depth of layer interfaces. Pore pressure variations have a greater effect on S-wave velocities V_s than V_p and so, they are a better indicator of pore pressure changes (Carcione & Helle, 2002). Electrical resistivity is also sensitive to changes in porosity (Archie, 1942). Therefore, two new terms containing the misfits in V_s and electrical resistivity could be added to the objective function. These parameters are not direct outputs from the forward model and adequate empirical relationships could be used to relate those parameters to porosity (e.g, Castagna *et al.*, 1985 for V_s; Archie, 1942 for electrical resistivity).
  To solve the inverse problem and as the misfit function increases in complexity (more misfit terms), direct search algorithms, such as Monte Carlo type techniques, are recommended over linearised search techniques (Sambridge & Mosegaard, 2002) such as the trust-region reflective method used in Marín-Moreno *et al.* (2013b). Therefore, if incorporating the above two new terms into the misfit function, the inverse problem should be solved using Monte Carlo type methods. Besides, even in the current version of the inverse model, applying a Monte Carlo type method will ensure that the global minima has been found. However, if the V_p resolution increases considerably, with respect to the smooth V_p structure used in Marín-Moreno *et al.* (2013b), the number of model layers should increase correspondingly to accurately model the V_p structure, and so will do the number of parameters to invert (the number of inversion parameters is equal to five in 1D or six in 2D times the number of

layers). If the number of parameters is greater than a few hundred and depending on computing power, a Monte Carlo type method may become impractical (Sambridge & Mosegaard, 2002).

- The inverse model uses a V_p relationship to transform the density output of the forward model into V_p. In our EBSB case study, we used Hamilton's (1978) relation for a silt, clay and turbidite lithology, because it was adequate for the type of sediments in the basin. For comparison, we also used Gardner *et al.*'s (1974) relation and the results were similar. However, adding more terms, such as the V_s and electrical resistivity, would require the introduction of more empirical relationships and the uncertainty in model outputs driven by uncertainty in the empirical relations selected would increase. Ideally, in areas where log data are available, including either density or porosity, V_p, V_s and resistivity, local relationships could be stablished between those parameters. However, if no data are available, global relationships still apply, but these could be better used by considering end member relationships for the type of material observed in the study area. This approach will give a range for overpressure and an idea of the sensitivity of the model to changes in the empirical relationships. To assess how uncertainties in the forward physical model (which includes the empirical relations mentioned above) propagate to the estimated model parameters statistically, the Monte Carlo error propagation technique (e.g, Tarantola, 2005) could be employed. In Marín-Moreno *et al.* (2013b) we used it to assess how data uncertainties impact the estimated model parameters but not to assess how those are impacted by uncertainties in the forward physical model. Estimating this uncertainty will provide further insights into the robustness of the inverse model presented in this thesis, and for each study area, into the robustness of the parameter estimates.

- The methods presented in Chapters 3 and 4 have been successfully applied to the centre of the EBSB. However, the lack of direct pore pressure measurements and density data in the centre of the basin does not allow complete validation of the results. Therefore, the methods should be applied elsewhere where borehole density data and direct pore pressure measurements indicating overpressure, mainly generated by DC or AE (considering the model at its present-day version), are available in addition to seismic data. Some preliminary results of applying the inverse model in the Ursa Basin, Gulf of Mexico, where direct pore pressure measurements are available, the time periods and thicknesses for each layer are known (Flemings *et al.*, 2008; Long *et al.*, 2011; Integrated Ocean Drilling Program, IODP site U1322), and the *a-priori* state of information in the model parameters is also known (Long *et al.*, 2008; Reece *et al.*, 2012) show some encouraging results (Figs. 7.1 and 7.2). However, no seismic

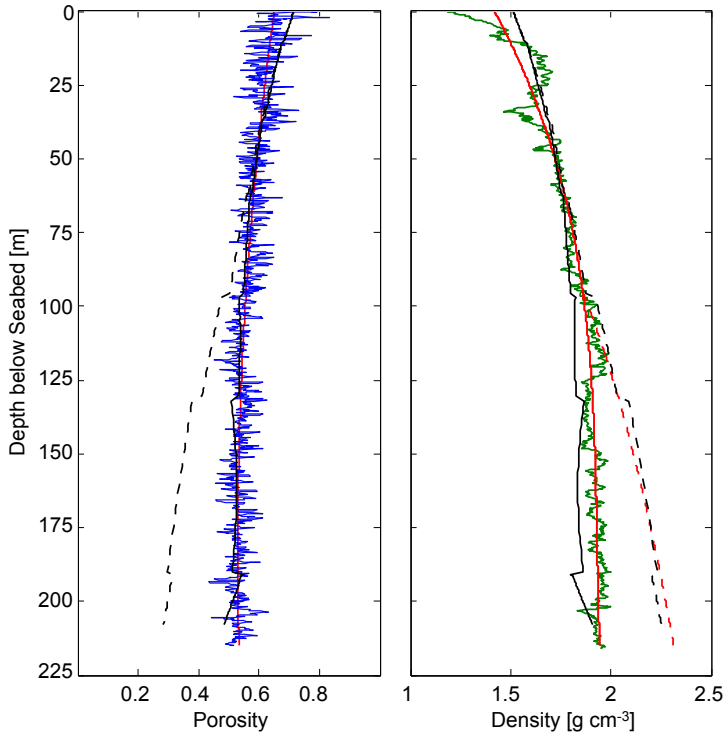

Figure 7.1: Porosity (blue solid line) and density (green solid line) vs depth profiles at site U1322 and their approximated (red lines) and calculated with the inverse model (black lines) profiles. Solid lines indicate observed conditions and dashed lines assumed hydrostatic conditions. Note that solid red lines are second order polynomial approximations to the observed data. The approximation to the assumed density in hydrostatic conditions is formed by a second order polynomial for the density data at depths shallower than ∼100 m and a linear extrapolation for deeper depths. The inverse model uses these polynomial fits as data.

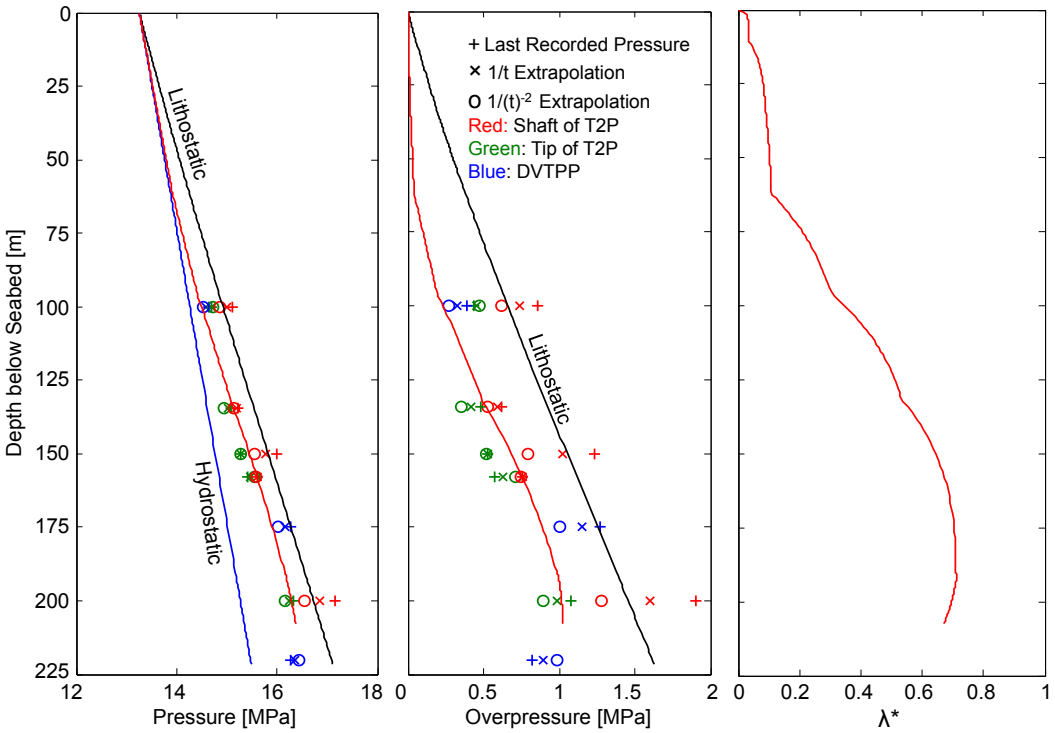

Figure 7.2: Pore pressure, overpressure and λ^* (ratio of excess pore pressure above hydrostatic to the effective stress in hydrostatic conditions) vs depth profiles from the inverse model at site U1322 (red lines). Direct pore pressure measurements come from Flemings *et al.* (2008).

velocity data are available and the data used for inversion were density, porosity and depth of the layer interfaces (from the observed density data, a density profile assuming hydrostatic conditions was also used in the inverse model). This is ongoing work, that should be improved using a better approximation to the logged porosity and density depth profiles (Fig. 7.1).

In this thesis I have studied the response of marine hydrate-bearing sediments to ocean warming offshore West of Svalbard for the period 1-2300 CE.

- Several 1D models have been proposed at water depths of 350, 400, 420, 450, 500, 600, 700 and 800 m. A 1D approach was used because the computational cost of a 2D model was too high for the large time series of the analysis and for the wide range of ocean models to be considered, and because for the low hydrate saturations and slopes in the study area, not significant lateral heat and fluid transport were anticipated. However, and although a previous modelling study in the area suggests that the error in the 1D approximation is small (Reagan *et al.*, 2011), this should be tested in these models. Therefore, a logical next step in this work would be to develop a 2D model of the gas hydrate system offshore West Svalbard. This may give some new insights regarding the hypothesis that methane emissions at water depths shallower than the present-day top of the gas hydrate stability zone (GHSZ) are driven by dissociated hydrate at deeper water depths flowing laterally up slope (Westbrook *et al.*, 2009) through layers of high lateral permeability. To capture well the likely lateral gas migration, the model should include the heterogeneity of the sediments by using as many different layers as the current seismic data can resolve.

- In Chapter 6, I discussed the hypothesis that gas hydrate at 400 m water depth (mwd) may be dissociating due to temperature changes because of seasonality, but that seasonality at water depths deeper than 420 m is not likely to be a dominant factor affecting hydrate stability in the next three centuries. To test this hypothesis, monthly seabed temperatures (in this thesis I have used mean annual seabed temperatures) given by the global climate models should be used to study the response of the gas hydrate system at 400 mwd and 420 mwd. Three different scenarios should be considered: (1) the scenario presented here, which does not consider seasonality, (2) a scenario where the mean temperature at those depths is kept constant at the mean temperature value for the period 1975-2005, which is 2.69 ^{o}C at $\sim$400 mwd and 2.61 ^{o}C at $\sim$420 mwd, and the response of the system is just controlled by seasonality and (3) a scenario that includes seasonality and the global trend in temperature. Comparing and analysing the outputs from those scenarios will allow the identification of the impacts of seasonal changes in temperature in the present-day and future response of the gas hydrate system offshore West Svalbard.

- The seabed temperatures offshore West Svalbard at the water depths of our models are significantly higher than in other places in the Arctic due to the Atlantic Water inflow through its prolongation, the West Spitsbergen Current (WSC). Therefore, the observed methane bubble plumes at ~400 mwd (Westbrook *et al.*, 2009) could have been caused by a 1.0 °C increase of the bottom water over the last three decades due to the increase in the temperature of the WSC in response to Atlantic warming (Thatcher *et al.*, 2013). This suggests that the gas hydrate system offshore West Svalbard may be more prone to dissociation than other gas hydrate systems in the Arctic. We selected the Beaufort Sea, north Alaska, to study how future ocean warming affects the hydrate system elsewhere in the Arctic, because:

  1) Hydrate is known to be widespread from observations of a characteristic bottom simulating reflector (BSR) that marks the base of the region where hydrate is stable (Andreassen *et al.*, 1995, 1997) and from direct sampling and exploitation of methane hydrate nearby (e.g, Boswell *et al.*, 2011; Collett *et al.*, 2011).

  2) Sufficient geophysical and geological data exist to estimate the thickness of the hydrate and gas layers, saturations of hydrate and gas in the pore space (Andreassen *et al.*, 1995, 1997), and other important parameters such as heat flow, thermal conductivity and porosity from land measurements nearby (Lachenbruch *et al.*, 1982). A summary of the physical properties of the gas hydrate system and seismic constraints is shown in Table 7.1.

  3) A temperature model for water depths of 350, 400, 450, 500 m for the period 800-2300 could be constructed (Fig. 7.3) using a similar approach to that used offshore West Svalbard (supplementary material in Marín-Moreno *et al.*, 2013c).

  No BSR is observed at the water depths of the models and so, their heat flow is an average of those calibrated at water depths of 1000 and 1450 m, where the BSR is clearly identified (Andreassen *et al.*, 1995). To estimate the heat flow at both water depths, I assumed a thermal conductivity of 1.5 W m^{-1} K^{-1} (which is consistent with a porosity of 0.4 according to Budiansky's, 1970 relationship) and a seabed temperature at each depth equal to the mean of the measured temperatures over the period 1950-2008.
  This is ongoing work, but some preliminary results show no present-day methane emissions from dissociated hydrate at the modelled water depths (Figs. 7.4d; h, 7.5d; h, 7.6d; h, and 7.4d; h), consistent with the lack of observed bubble plumes in the area (according to my current state of knowledge). Over the next three centuries, only the models at 350 mwd show methane emissions. For scenario RCP 2.6, no methane emissions occur using the climate model CCSM4 (Fig. 7.4d), and if using HadGEM2 they start by ~2260CE (Fig. 7.4h) with a maximum rate of emissions of ~23 mol

yr^{-1} m^{-2}. For RCP 8.5, methane emissions would start by ~2200 CE and by ~2170 CE if using CCSM4 and HadGEM2 (Figs. 7.6d; h), respectively, with a maximum rate of emissions of ~55 mol yr^{-1} m^{-2}. One important reason why no methane emissions occur at models deeper than 350 mwd for the time period considered, is because the gas hydrate layer is limited to a thickness of ~24 m above the base of the GHSZ (Figs. 7.4c; g, 7.5c; g, 7.6c; g, and 7.7c; g), based on results at deeper waters (Andreassen *et al.*, 1995). Therefore, the time it takes for methane from dissociated hydrate to reach the seabed is higher than that at the models offshore West Svalbard.

Table 7.1: Table with physical properties of the gas hydrate system and seismic constraints.

Parameter	Value
Initial salinity [wt%]	3.5
Gas composition	100% CH_4
Water saturated thermal conductivity [W $m^{-1}K^{-1}$]	1.5
Solid grain density [kg m^{-3}]	2600
Intrinsic permeability [m^2]	10^{-14}
Initial diffusivity [m^2 s^{-1}]	
CH_4: aqueous phase, gas phase	$2x10^{-9}$, $2x10^{-5}$
H_2O: aqueous phase, gas phase	$1x10^{-9}$, $3x10^{-5}$
NaCl: aqueous phase, gas phase	$1.5x10^{-9}$, 0
Porosity [%]	40
Relative permeability model	$k_{rA} = \max\left\{0, \min\left\{\left[\frac{S_A - S_{irA}}{1 - S_{irA}}\right]^n, 1\right\}\right\}$,
Modified version of Stone's first three phase relative permeability method [*Stone*, 1970]	$k_{rG} = \max\left\{0, \min\left\{\left[\frac{S_G - S_{irG}}{1 - S_{irA}}\right]^{n_G}, 1\right\}\right\}$, $S_{irA} = 0.12$, $S_{irG} = 0.02$, $n = n_G = 4$
Capillary pressure model [*van Genuchten*, 1980]	$P_{cap} = -P_0\left[\left(S^*\right)^{-1/\lambda} - 1\right]^{-\lambda}$, $-P_{max} \le P_{cap} \le 0$, $S^* = \frac{(S_A - S_{irA})}{(S_{mxA} - S_{irA})}$, $\lambda = 0.254$, $S_{irA} = 0.11$, $P_0 = 12500$ MPa, $P_{max} = 10^6$ MPa, $S_{mxA} = 1$
Heat flow [W m^{-2}]	
From 350-500 mwd	$7.85x10^{-2}$
Seismic constraints [*Andreassen et al.*, 1995]	
Initial gas hydrate layer thickness [m]	24
Initial gas layer thickness below GHSZ [m]	14
Initial hydrate saturation [%]	8
Initial gas saturation below GHSZ [%]	3
Depth of BSR [mbsf]	
From 350-500 mwd	Not identified
At 1025 mwd	222
At 1450 mwd	341

GHSZ, gas hydrate stability zone; BSR, bottom-simulating reflector; mwd, meters water depth; mbsf, meters below seafloor; k_{rA} and k_{rG} are relative permeabilities for aqueous and gas phases, respectively; S_A and S_G are saturations for aqueous and gas phases; S_{irA} and S_{irG} are irreducible aqueous and gas saturations; S_{mxA} is the maximum water saturation; P_{cap} is the capillary pressure; P_{max} is the maximum value of capillary pressure; P_0 is the capillary entry pressure; n, n_G and λ are fitting parameters.

These preliminary results suggest that, over the next three centuries, the active seabed area of gas hydrate dissociation will be at water depths between ~300-400 m. The imposed initial conditions produced no hydrate at 300 mwd, hence I propose to generate ten 1D models to cover water depths between 310-400 m every 10 mwd. These ten models should be applied with a larger number of global climate models, and using adequate combinations of thermal conductivity and heat flow, while keeping the thermal gradient to that calibrated, which is ~52 °C km^{-1}. The Beaufort Sea is a current study area for gas hydrate, and the models developed here are significantly driven by seismic data acquired two decades ago. Therefore, the new models should used the most recent seismic observations, mainly, in terms of depth of BSR, thickness of the gas hydrate layer, and hydrate saturation in the pore space.

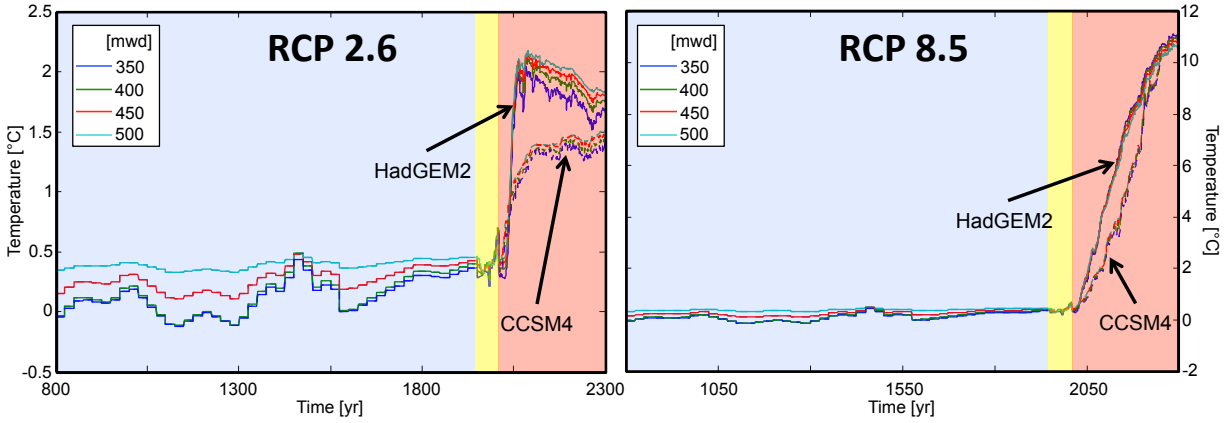

Figure 7.3: Constructed temperature series for the period 800-2300 at 350, 400, 450 and 500 m water depth (mwd). The temperature series are divided into the three different data sets used: 1) for the period 800-1950 (coloured in blue), sea surface temperatures from foraminifera proxy data (Farmer *et al.*, 2011, core site GGC-19), 2) for the period 1950-2008 (coloured in yellow), oceanographic measurements from the World Ocean Database 2009 (WOD09, http://www.nodc.noaa.gov/ OC5/WOD09/pr_wod09.html), and 3) for the period 2008-2300 (coloured in orange), mean annual seabed temperatures given by climate models HadGEM2 and CCSM4 under climate-forcing scenarios RCPs 8.5 and 2.6 (the CCSM4 model under RCP 8.5 ends at 2250 CE).

- Global climate models do not consider methane emissions from dissociated hydrate, and our results show that those may be important in the future in the Arctic. Although the amount of methane that reaches the atmosphere may be small, the increase in methane concentration in the Arctic Ocean increases ocean acidification with consequent implications for marine biodiversity (Riebesell, 2008; Valentine *et al.*, 2001).

  In Chapters 5 and 6, estimates of future methane emissions from dissociated hydrate for the entire Eurasian Margin were given. It was assumed that the calculated

seabed methane emissions offshore West Svalbard could be extrapolated to the entire Eurasian Margin and the caveats of this extrapolation were explained. To predict the total amount of methane emissions from dissociated hydrate in the entire Arctic, these should be calculated using similar approaches to that used in this thesis at different Arctic locations, where there are enough geophysical and geological data to constrain the models. The calculated local methane emissions could then be interpolated and/or extrapolated to create Arctic maps of methane emissions from dissociated hydrate over time. These maps would be an interesting tool for scientists working in the Arctic and may be used as a base line, using adequate transformations, towards maps of: contribution of methane emissions from dissociated hydrate to Arctic Ocean acidification, and atmospheric methane emissions in the Arctic from dissociated marine hydrate.

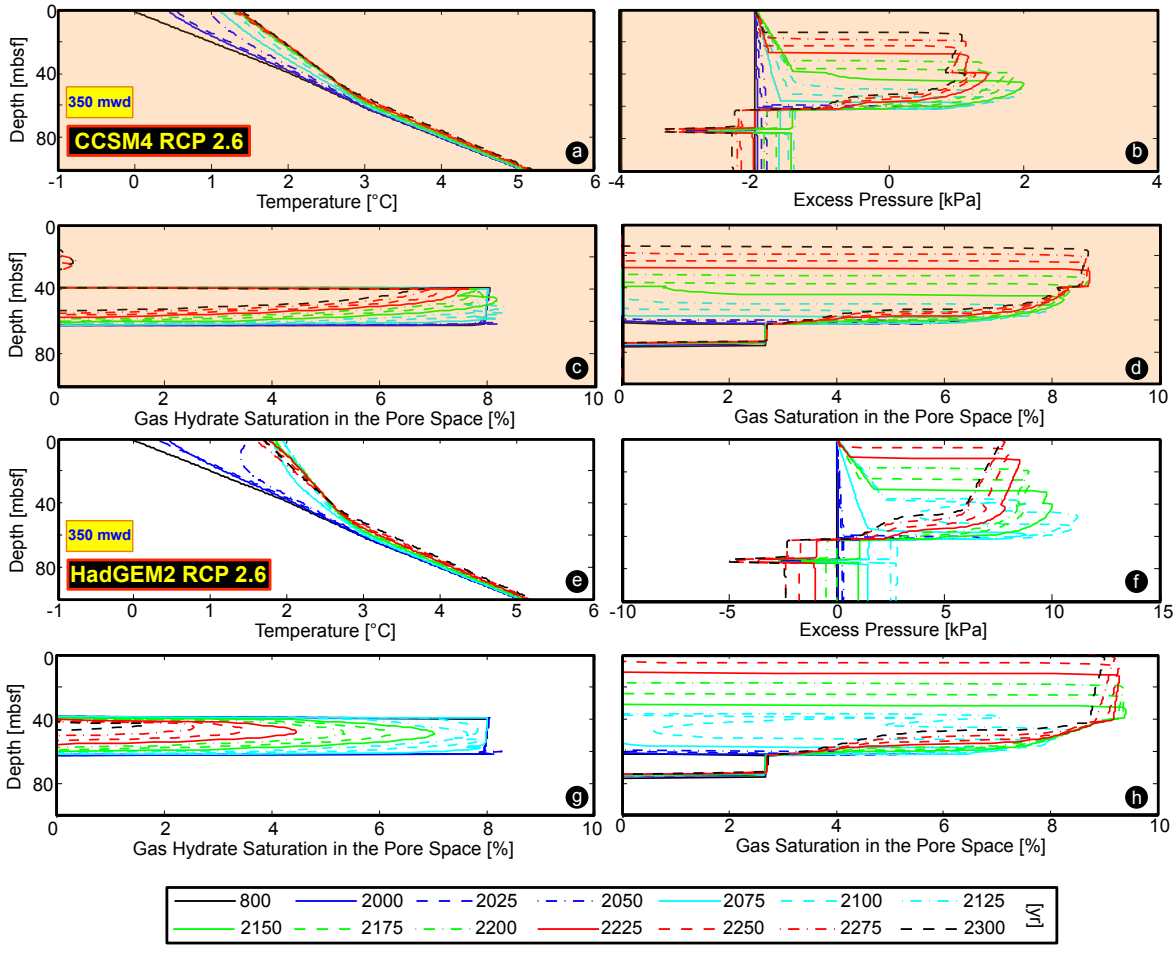

Figure 7.4: Time evolution of temperature, excess pressure, and saturations of gas hydrate and gas in the pore space vs depth (in meters below seafloor, mbsf) at 350 m water depth (mwd) using climate-forcing scenario RCP 2.6 for climate models CCSM4 (coloured in orange) and HadGEM2. Note that the initial model is at 800 CE.

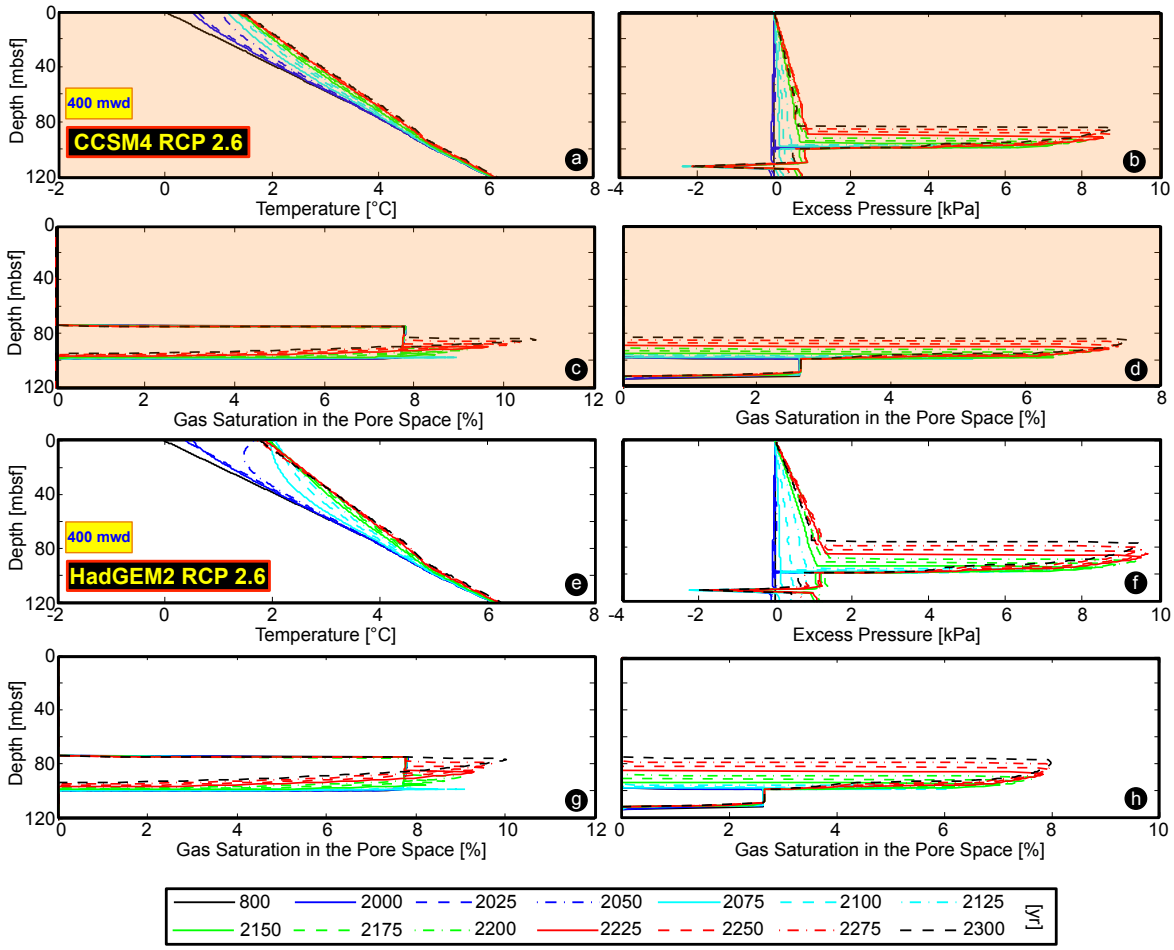

Figure 7.5: Time evolution of temperature, excess pressure, and saturations of gas hydrate and gas in the pore space vs depth (in meters below seafloor, mbsf) at 400 m water depth (mwd) using climate-forcing scenario RCP 2.6 for climate models CCSM4 (coloured in orange) and HadGEM2. Note that the initial model is at 800 CE.

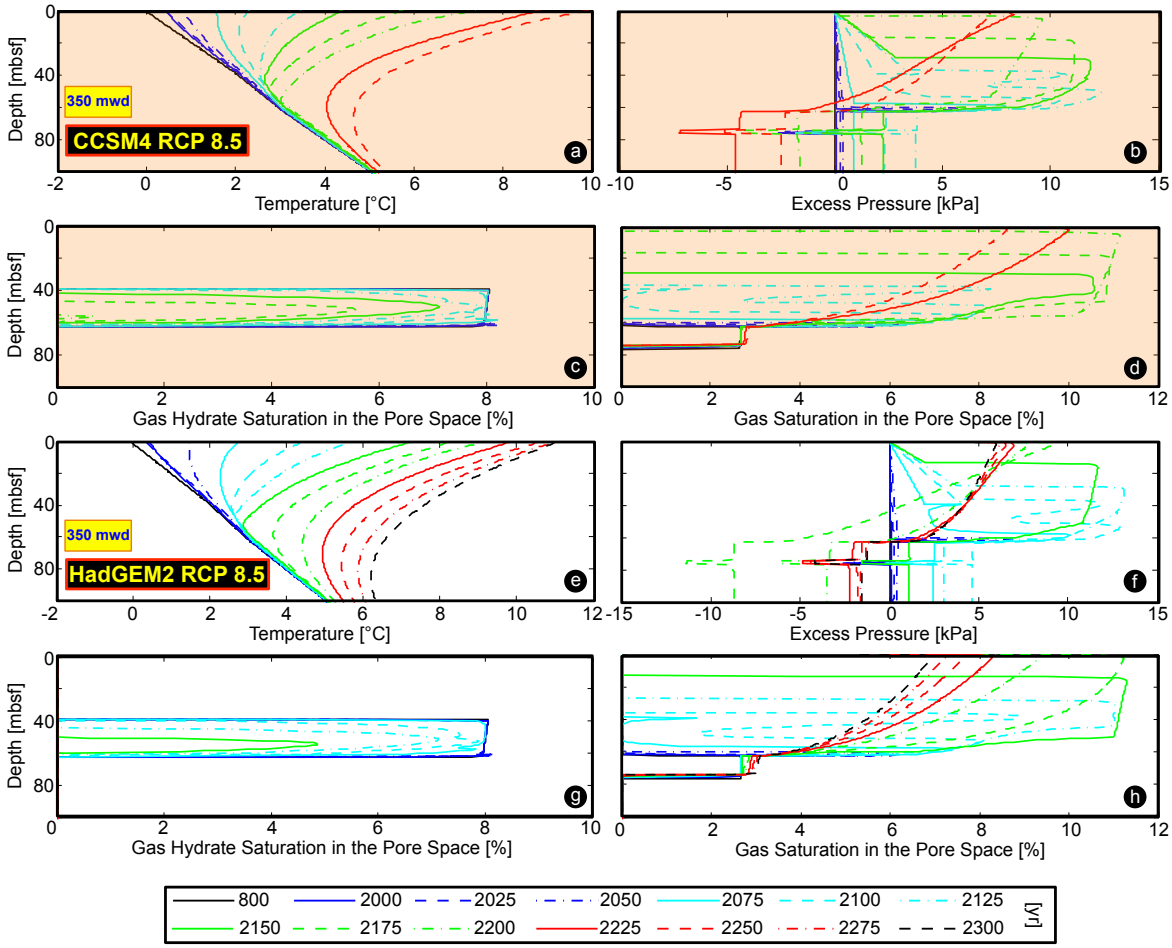

Figure 7.6: Time evolution of temperature, excess pressure, and saturations of gas hydrate and gas in the pore space vs depth (in meters below seafloor, mbsf) at 350 m water depth (mwd) using climate-forcing scenario RCP 8.5 for climate models CCSM4 (coloured in orange) and HadGEM2. Note that the initial model is at 800 CE.

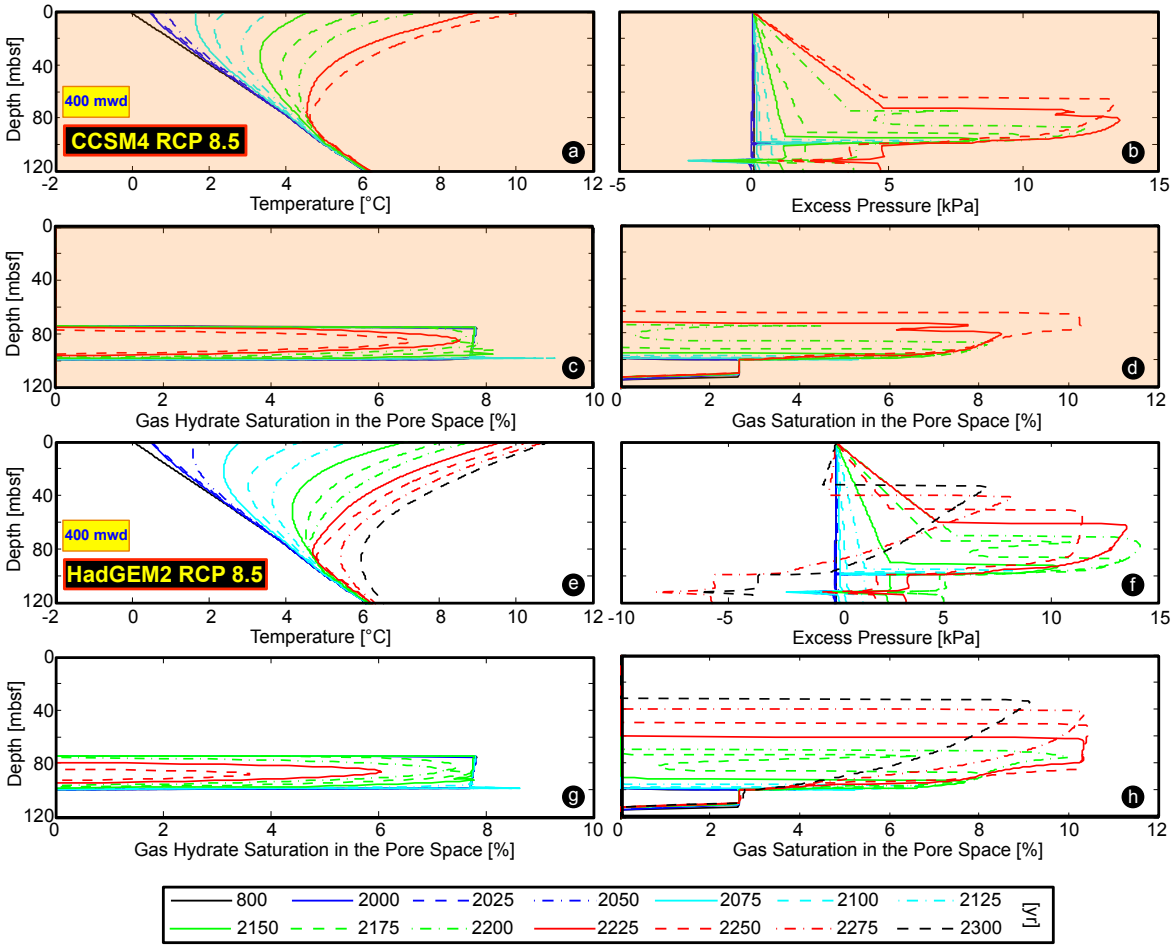

Figure 7.7: Time evolution of temperature, excess pressure, and saturations of gas hydrate and gas in the pore space vs depth (in meters below seafloor, mbsf) at 400 m water depth (mwd) using climate-forcing scenario RCP 8.5 for climate models CCSM4 (coloured in orange) and HadGEM2. Note that the initial model is at 800 CE.

Appendix. Matlab 7.8.0 Functions

A.1 Implementation of the Overpressure Models with Matlab 7.8.0

The main functions coded in Matlab 7.8.0 for the overpressure methods are described here. These functions are included in the electronic material EM.1 for those used in Chapter 3, in EM.2 for those used in Chapter 4, and in EM.3 for those used in the Ursa Basin case study. Each function description has been ordered according to its approximate appearance in the code.

A.1.1 Main Functions for the Analysis in Chapter 3

main.m: main script of the code for the method explained in section 2.1.2. It also includes plotting functions and the possibility of carrying out a sensitivity analysis of overpressure to variable sedimentation rates and permeabilities.

userInputs.m: includes all the initial input parameters that the user needs to introduce to run the method (spatial and temporal discretisation, top and bottom depth boundary and sedimentation time interval of each layer, type of material, seafloor depth, lithological parameters, etc.).

Decompaction.m: contains the Sclater & Christie's (1980) model to calculate a decompacted layer thickness or thickness at the time of deposition.

matParam.m: calculates the initial permeability, compressibility and porosity of each layer as a function of the type of material imposed.

Hr1.m and **Hr2.m**: contain the algorithm to calculate the compaction factor that gives a sediment thickness similar to that observed within a tolerance. In **Hr1.m** all compaction factors are updated per iteration and in **Hr2.m** one compaction factor is updated per iteration.

RhoMu.m: includes the International Association for the Properties of Water and Steam's

(2007; 2008) fluid density and viscosity models.

oneDDCM.m, **Diffusion.m**, and **Coefficients.m**: include the algorithm to calculate the overpressure generated by a 1D disequilibrium compaction model assuming a zero flow and zero overpressure bottom and top boundary conditions, respectively, and hydrostatic pressure as a initial condition.

matUpdated.m: updates the parameters, sediment density, compressibility, porosity and permeability at each time step.

GeophyMeth.m: reads a text file of P-wave velocity data and applies the geophysical based methods, depth equivalent method (e.g, Westbrook, 1991) and Eaton's method (den Boer *et al.*, 2006; Eaton, 1969, 1975), to estimate the overpressure.

A.1.2 Main Functions for the Analysis in Chapter 4

main.m: main script of the code for the method explained in section 2.1.3. It includes plotting functions and functions to carry out statistical analysis of some forward model parameters.

userInputs.m: contains all the initial input parameters that the user needs to introduced to run the method (spatial and temporal discretisation, number of sampling points, top and bottom depth boundary and sedimentation time interval of each layer, type of material, seafloor depth, lithological parameters, etc.). It also includes two parameters to select the type of model, 1D or 2D, and the type of boundary conditions imposed, and some statistical parameters.

realData.m: reads a text file of P-wave velocity data and applies the geophysical based method, depth equivalent method (e.g, Westbrook, 1991), to calculate the overpressure. It also interpolates the observed V_p structure, and the estimated density, porosity and pressure (hydrostatic, lithostatic and total pore pressure) to the sampling x and z points.

optAlg.m: includes all the functions involved in the application of the inverse method.

objFunc1.m: includes the misfit function to be minimised.

forwardModel.m: includes the functions involved in the calculation of the overpressure generated by a 1D/2D disequilibrium compaction and aquathermal expansion model.

CompactionModel.m, **Diffusion.m**, **EqSystem(1-2)D(1-4).m**, **KcoefH.m**, **KcoefV.m** and **place.m**: include the algorithm to calculate the overpressure depending on the model selected, 1D or 2D, and the boundary conditions imposed. The imposed top boundary condition is zero overpressure and the bottom, right and left boundary conditions are selected by the user. **EqSystem1D1.m** and **EqSystem1D2.m** are for a 1D model with a zero flow and zero overpressure bottom boundary, respectively. **EqSystem2D1.m** and

EqSystem2D2.m are both for a 2D model with a zero flow bottom boundary and a zero overpressure right boundary conditions, and for a zero flow and zero overpressure left boundary conditions, respectively. **EqSystem2D3.m** and **EqSystem2D4.m** are both for a 2D model with a zero overpressure bottom boundary and a zero overpressure right boundary conditions, and for a zero flow and zero overpressure left boundary conditions, respectively.

VpHamilton.m and **rhoHamilton.m**: include the calculation of the V_p and sediment density using Hamilton's (1978) relationship.

DensityViscosityCal.m: includes the International Association for the Properties of Water and Steam's (2007; 2008) fluid density and viscosity models.

paramMupdated.m: updates the parameters, sediment density, compressibility, porosity and permeability at each time step.

MCEP.m: calculates the approximate *a-posteriori* covariance matrix of the inverse model parameters using the Monte Carlo Error Propagation Technique (Tarantola, 2005). It also calculates the correlation matrix of those parameters.

empCovCorrM.m: calculates the approximate *a-posteriori* covariance matrix of the inverse model parameters using Eq. 9.38 in Aster *et al.* (2005) and considering a 4^{th} order numerical approximation to the Jacobian (for each mesh cell, partial derivative of the forward model with respect each of the model parameters used in the inversion). It also calculates the correlation matrix of those parameters.

statistics.m: includes the calculation of the 95% confidence interval of individual model parameters and the joint 95% confidence interval ellipse for a pair of model parameters.

postProReal.m: includes the geophysical based method, Eaton Method (den Boer *et al.*, 2006; Eaton, 1969, 1975), to calculate the overpressure.

A.2 Inputing Variable Seabed Temperature and Extracting Results in T+H v1.2 Code with Matlab 7.8.0

The functions coded in Matlab 7.8.0 to study the response of Arctic hydrate to ocean warming are described here and included in the electronic material EM.4, for those used in Chapters 5 and 6, and EM.5 for those used in the Beaufort Sea case study. Each function description has been ordered according to their order of use in the method.

PaleoTempSeries_(Svalbard, BeaufortSea).m: creates the past temperature series at the study location.

ClimateModel_(Svalbard, BeaufortSea).m: interpolates the temperature data ex-

tracted from climate models to the study location and water depths. It includes the functions **TfutureCal.m**, **LatLonInterp.m**, **LevelSeabed.m** and **DepthInterp.m**.

main_(Svalbard, BeaufortSea).m: main script of the code for the method explained in section 2.2.1. It acts as an interface between T+H and the temperature series constructed. It creates the past and future temperature series, and calls the function **ChangeTime.m**, to annually change the time in the T+H input file "initT", and the function **ChangeTemp.m** to change the temperature of the top boundary cell in the T+H input file "INCON". It creates a folder that contains all the input and output files needed and generated, respectively, by T+H.

Output_(Svalbard, BeaufortSea).m: extracts the results of interest from the T+H text output files, "Plot_Data_Conx", "Plot_Data_Elem" and "initT.out", and generates four matrices with these results. These matrices are then used, in this function, to plot.

Output2_Svalbard.m: includes the function **PostProcess.m** and generates a series of plots using the matrices generated by **Output_Svalbard.m** for the seven climate models.

Output3_Svalbard.m: includes the function **TwoDContours.m** and generates a series of contour plots using the matrices generated by **Output_Svalbard.m**.

IBCAO.m: it uses the one minute resolution IBCAO bathymetric grid (http://www.ngdc.noaa.gov/mgg/bathymetry/arctic/grids/version2_23/IBCAO_ver2_23_GEO_netCDF_1min.grd) to calculate the seabed area of the Arctic Ocean within a giving range of water depths.

Bibliography

Allen, P. A. & Allen, J. R. (2005). *Basin analysis: principles and applications*. Malden, MA: Blackwell Pub, 2nd edition.

Andreassen, K., Hart, P., & Grantz, A. (1995). Seismic studies of a bottom simulating reflection related to gas hydrate beneath the continental margin of the Beaufort Sea. *Journal of Geophysical Research*, 100(B7), 12659–12673.

Andreassen, K., Hart, P. E., & MacKay, M. (1997). Amplitude versus offset modeling of the bottom simulating reflection associated with submarine gas hydrates. *Marine Geology*, 137(1), 25–40.

Archer, D. (2005). Fate of fossil fuel CO_2 in geologic time. *Journal of Geophysical Research: Oceans*, 110(C9), C09S05.1–C09S05.6, doi: 10.1029/2004jc002625.

Archer, D. (2007). Methane hydrate stability and anthropogenic climate change. *Biogeosciences Discussions*, 4(2), 993–1057.

Archer, D. & Brovkin, V. (2008). The millennial atmospheric lifetime of anthropogenic CO_2. *Climatic Change*, 90(3), 283–297.

Archer, D., Buffett, B., & Brovkin, V. (2009). Ocean methane hydrates as a slow tipping point in the global carbon cycle. *Proceedings of the National Academy of Sciences*, 106(49), 20596–20601.

Archie, G. (1942). The electrical resistivity log as an aid in determining some reservoir characteristics. *Transactions of the AIME*, 146(1), 54–62.

Aster, R. C., Thurber, C. H., & Borchers, B. (2005). *Parameter estimation and inverse problems*. Amsterdam; Boston: Elsevier Academic Press.

Athy, L. (1930). Density, porosity, and compaction of sedimentary rocks. *AAPG Bulletin*, 14, 1–22.

Audet, D. M. & Fowler, A. C. (1992). A mathematical model for compaction in sedimentary basins. *Geophysical Journal International*, 110(3), 577–590.

Audet, D. M. & McConnell, J. D. C. (1994). Establishing resolution limits for tectonic subsidence curves by forward basin modelling. *Marine and Petroleum Geology*, 11(3), 400–411.

Barker, C. (1972). Aquathermal pressuring-role of temperature in development of abnormal pressure zones. *AAPG Bulletin*, 56(10), 2068–2071.

Bekele, E. B., Johnson, M. D., & Higgs, W. G. (2001). Numerical modelling of overpressure generation in the Barrow Sub-Basin, Northwest Australia. *APPEA Journal*, 41, 595–607.

Bentsen, M., Bethke, I., Debernard, J., Iversen, T., Kirkevåg, A., Seland, Ø., Drange, H., Roelandt, C., Seierstad, I., & Hoose, C. (2012). The Norwegian Earth System Model, NorESM1-M-Part 1: Description and basic evaluation of the physical climate. *Geoscientific Model Development*, 6(3), 687–720.

Berhmann, J., Flemings, P. B., & John, C. (2006). Rapid sedimentation, overpressure, and focused fluid flow, Gulf of Mexico continental margin. *Scientific Drilling*, 3, 12–17.

Berry, F. A. (1973). High fluid potentials in california coast ranges and their tectonic significance. *AAPG Bulletin*, 57(7), 1219–1249.

Beszczynska-Möller, A., Fahrbach, E., Schauer, U., & Hansen, E. (2012). Variability in Atlantic water temperature and transport at the entrance to the Arctic Ocean, 1997-2010. *ICES Journal of Marine Science: Journal du Conseil*, 69(5), 852–863.

Bethke, C. M. (1985). A numerical-model of compaction-driven groundwater-flow and heat-transfer and its application to the paleohydrology of intracratonic sedimentary basins. *Journal of Geophysical Research-Solid Earth and Planets*, 90(NB8), 6817–6828.

Bethke, C. M. (1986). Inverse hydrologic analysis of the distribution and origin of Gulf Coast-type geopressured zones. *Journal of Geophysical Research-Solid Earth and Planets*, 91(B6), 6535–6545.

Bethke, C. M. (1989). Modeling subsurface flow in sedimentary basins. *Geologische Rundschau*, 78(1), 129–154.

Biastoch, A., Treude, T., Rüpke, L. H., Riebesell, U., Roth, C., Burwicz, E. B., Park, W., Latif, M., Böning, C. W., Madec, G., & Wallmann, K. (2011). Rising arctic ocean temperatures cause gas hydrate destabilization and ocean acidification. *Geophysical Research Letters*, 38(8), L08602, doi: 10.1029/2011gl047222.

Bjørlykke, K. & Høeg, K. (1997). Effects of burial diagenesis on stresses, compaction and fluid flow in sedimentary basins. *Marine and Petroleum Geology*, 14(3), 267–276.

Borowski, W. S., Paull, C. K., & Ussler, W. (1996). Marine pore-water sulfate profiles indicate in situ methane flux from underlying gas hydrate. *Geology*, 24(7), 655–658.

Boswell, R. & Collett, T. S. (2011). Current perspectives on gas hydrate resources. *Energy and environmental science*, 4(4), 1206–1215.

Boswell, R., Rose, K., Collett, T. S., Lee, M., Winters, W., Lewis, K. A., & Agena, W. (2011). Geologic controls on gas hydrate occurrence in the Mount Elbert prospect, Alaska North Slope. *Marine and Petroleum Geology*, 28(2), 589–607.

Bradley, J. S. (1975). Abnormal formation pressure. *AAPG Bulletin*, 59(6), 957–973.

Bredehoeft, J. D. (2002). The water budget myth revisited: why hydrogeologists model. *Ground Water*, 40(4), 340–345.

Bredehoeft, J. D. & Hanshaw, B. B. (1968). On the maintenance of anomalous fluid pressures: I. thick sedimentary sequences. *Geological Society of America Bulletin*, 79, 1097–1106.

Bredehoeft, J. D., Neuzil, C. E., & Milly, P. (1983). Regional flow in the Dakota Aquifer: a study of the role of confining layers. *U. S. Geological Survey Water-Supply Paper 2237*, (pp. 1–45).

Bruce, C. H. (1984). Smectite dehydration - its relation to structural development and hydrocarbon accumulation in northern Gulf of Mexico Basin. *AAPG Bulletin*, 68(6), 673–683.

Brunet, M.-F., Korotaev, M. V., Ershov, A. V., & Nikishin, A. M. (2003). The South Caspian Basin: a review of its evolution from subsidence modelling. *Sedimentary Geology*, 156, 119–148.

Budiansky, B. (1970). Thermal and thermoelastic properties of isotropic composites. *Journal of Composite Materials*, 4(3), 286–295.

Buffett, B. & Archer, D. (2004). Global inventory of methane clathrate: sensitivity to changes in the deep ocean. *Earth and Planetary Science Letters*, 227(3), 185–199.

Burwicz, E. B., Ruepke, L., & Wallmann, K. (2011). Estimation of the global amount of submarine gas hydrates formed via microbial methane formation based on numerical reaction-transport modeling and a novel parameterization of Holocene sedimentation. *Geochimica et Cosmochimica Acta*, 75(16), 4562–4576.

Byrne, T. & Fisher, D. (1990). Evidence for a weak and overpressured décollement beneath sediment-dominated accretionary prisms. *Journal of Geophysical Research-Solid Earth and Planets*, 95(B6), 9081–9097.

Carcione, J. M. & Helle, H. B. (2002). Rock physics of geopressure and prediction of abnormal pore fluid pressures using seismic data. *CSEG Recorder*, 27(7), 8–32.

Castagna, J. P., Batzle, M. L., & Eastwood, R. L. (1985). Relationships between compressional-wave and shear-wave velocities in clastic silicate rocks. *Geophysics*, 50(4), 571–581.

Cathles, L. M. & Smith, A. T. (1983). Thermal constraints on the formation of Mississippi Valley-type lead-zinc deposits and their implications for episodic basin dewatering and deposit genesis. *Economic Geology*, 78(5), 983–1002.

Chabert, A., Minshull, T. A., Westbrook, G. K., Berndt, C., Thatcher, K. E., & Sarkar, S. (2011). Characterization of a stratigraphically constrained gas hydrate system along the western continental margin of Svalbard from ocean bottom seismometer data. *Journal of Geophysical Research: Solid Earth*, 116(B12), B12102, doi: 10.1029/2011JB008211.

Chapman, R. E. (1980). Mechanical versus thermal cause of abnormally high pore pressures in shales. *AAPG Bulletin*, 64(12), 2179–2183.

Charbeneau, R. J. (2006). *Groundwater hydraulics and pollutant transport*. Illinois: Waveland Press.

Chi, G., Lavoie, D., Bertrand, R., & Lee, M. K. (2010). Downward hydrocarbon migration predicted from numerical modeling of fluid overpressure in the Paleozoic Anticosti Basin, eastern Canada. *Geofluids*, 10(3), 334–350.

Christensen, T. R., Johansson, T., Åkerman, H. J., Mastepanov, M., Malmer, N., Friborg, T., Crill, P., & Svensson, B. H. (2004). Thawing sub-arctic permafrost: Effects on vegetation and methane emissions. *Geophysical Research Letters*, 31(4), L04501, doi: 10.1029/2003GL018680.

Cloetingh, S., Spadini, G., Van Wees, J. D., & Beekman, F. (2003). Thermo-mechanical modelling of Black Sea Basin (de)formation. *Sedimentary Geology*, 156(1-4), 169–184.

Coleman, T. F. & Li, Y. (1994). On the convergence of interior-reflective Newton methods for nonlinear minimization subject to bounds. *Math. Program.*, 67(2), 189–224.

Coleman, T. F. & Li, Y. (1996). An interior trust region approach for nonlinear minimization subject to bounds. *SIAM Journal on Optimization*, 6(2), 418–445.

Collett, T. S. (1993). Natural gas hydrates of the Prudhoe Bay and Kuparuk River area, North Slope, Alaska. *AAPG Bulletin*, 77(5), 793–812.

Collett, T. S., Kvenvolden, K. A., & Magoon, L. B. (1988). Geologic interrelations relative to gas hydrates within the North Slope of Alaska. *USGS Open-file report*, 150, 88–139.

Collett, T. S., Lee, M. W., Agena, W. F., Miller, J. J., Lewis, K. A., Zyrianova, M. V., Boswell, R., & Inks, T. L. (2011). Permafrost-associated natural gas hydrate occurrences on the Alaska North Slope. *Marine and Petroleum Geology*, 28(2), 279–294.

Collett, T. S., Lewis, R., & Uchida, T. (2000). Growing interest in gas hydrates. *Oilfield Review*, (pp. 42–57).

Collins, W. J., Bellouin, N., Doutriaux-Boucher, M., Gedney, N., Halloran, P., Hinton, T., Hughes, J., Jones, C. D., Joshi, M., Liddicoat, S., Martin, G., O'Connor, F., Rae, J., Senior, C., Sitch, S., Totterdell, I., Wiltshire, A., & Woodward, S. (2011). Development and evaluation of an Earth-System model-HadGEM2. *Geosci. Model Dev.*, 4(4), 1051–1075.

Crane, K., Sundvor, E., Buck, R., & Martinez, F. (1991). Rifting in the northern Norwegian-Greenland Sea: Thermal tests of asymmetric spreading. *Journal of Geophysical Research: Solid Earth*, 96(B9), 14529–14550.

Cuadros, J. (2008). Clay as sealing material in nuclear waste repositories. *Geology Today*, 24(3), 99–103.

Daigle, H. & Dugan, B. (2010). Origin and evolution of fracture-hosted methane hydrate deposits. *Journal of Geophysical Research-Solid Earth*, 115, B11103, doi: 10.1029/2010JB007492.

Davie, M. K. & Buffett, B. A. (2001). A numerical model for the formation of gas hydrate below the seafloor. *Journal of Geophysical Research: Solid Earth*, 106(B1), 497–514.

Davis, D., Suppe, J., & Dahlen, F. A. (1983). Mechanics of fold-and-thrust belts and accretionary wedges. *Journal of Geophysical Research*, 88(NB2), 1153–1172.

den Boer, L., Sayers, C., Nagy, Z., & Hooyman, P. (2006). Pore pressure prediction using well-conditioned seismic velocities. *First Break*, 24, 43–49.

Dickens, G. R. (2001). In C. K. Paull & W. P. Dillon (Eds.), *Natural gas hydrates: occurrence, distribution, and detection*, volume 124 (pp. 19–38). Washington, DC: American Geophysical Union.

Dickens, G. R. (2011). Down the rabbit hole: toward appropriate discussion of methane release from gas hydrate systems during the Paleocene-Eocene thermal maximum and other past hyperthermal events. *Climate of the Past*, 7(3), 831–846.

Dickens, G. R., Castillo, M. M., & Walker, J. C. (1997). A blast of gas in the latest Paleocene: Simulating first-order effects of massive dissociation of oceanic methane hydrate. *Geology*, 25(3), 259–262.

Dickens, G. R., O'Neil, J. R., Rea, D. K., & Owen, R. M. (1995). Dissociation of oceanic methane hydrate as a cause of the carbon isotope excursion at the end of the Paleocene. *Paleoceanography*, 10(6), 965–971.

Dimitrov, L. I. (2002). Mud volcanoes - the most important pathway for degassing deeply buried sediments. *Earth-Science Reviews*, 59(1-4), 49–76.

Dlugokencky, E. J., Nisbet, E. G., Fisher, R., & Lowry, D. (2011). Global atmospheric methane: budget, changes and dangers. *Philosophical Transactions of the Royal Society A: Mathematical, Physical and Engineering Sciences*, 369(1943), 2058–2072.

Domenico, P. A. & Mifflin, M. D. (1965). Water from low-permeability sediments and land subsidence. *Water Resources Res*, 1(4), 563–576.

Draper, N. & Smith, H. (1998). *Applied Regression Analysis (Wiley Series in Probability and Statistics)*. New York: Wiley-Interscience, 3rd edition.

Dugan, B. & Sheahan, T. C. (2012). Offshore sediment overpressures of passive margins: mechanisms, measurement, and models. *Review Geophysics*, 50(3), RG3001, doi: 10.1029/2011RG000379.

Eaton, B. (1969). Fracture gradient prediction and its application in oilfield operations. *Journal of Petroleum Technology*, 10, 1353–1360.

Eaton, B. (1975). The equation for geopressure prediction from well logs. *Society of Petroleum Engineers*, (pp. 1–11).

Eaton, B. & Eaton, T. (1997). Fracture gradient prediction for the new generation. *World Oil*, 218, 93–94, 96–100.

Ebrom, D., Heppard, P., Mueller, M., & Thomsen, L. (2003). Pore pressure prediction from S-wave, C-wave, and P-wave velocities. *SEG Expanded Abstracts*, 22, 1370–1373.

Edwards, A. (1972). *TRUMP: A Computer Program for Transient and Steady State Temperature Distributions in Multidimensional Systems.* National Technical Information Service, National Bureau of Standards, Springfield, VA.

Eldholm, O., Sundvor, E., Vogt, P. R., Hjelstuen, B. O., Crane, K., Nilsen, A. K., & Gladczenko, T. P. (1999). SW Barents Sea continental margin heat flow and Håkon Mosby Mud Volcano. *Geo-Marine Letters*, 19(1-2), 29–37.

Englezos, P. & Lee, J. D. (2005). Gas hydrates: A cleaner source of energy and opportunity for innovative technologies. *Korean Journal of Chemical Engineering*, 22(5), 671–681.

Erickson, S. N. & Von Herzen, R. (1978). Downhole temperature measurements and heat

flow data in the Black Sea-DSDP Leg 42B (1975). In D. Ross, Y. Neprochnov, & P. Supko (Eds.), *Initial Report of the Deep Sea Drilling Project*, volume 42 (pp. 985–1103). Washington: U. S. Gov. Print. Off.

Farmer, J. R., Cronin, T. M., de Vernal, A., Dwyer, G. S., Keigwin, L. D., & Thunell, R. C. (2011). Western Arctic Ocean temperature variability during the last 8000 years. *Geophysical Research Letters*, 38(24), L24602, doi: 10.1029/2011GL049714.

Fertl, W. H., Chapman, R. E., & Holtz, R. (1994). *Studies in abnormal pressures*. New York: Elsevier.

Feyzullayev, A. A. & Lerche, I. (2009). Occurrence and nature of overpressure in the sedimentary section of the South Caspian Basin, Azerbaijan. *Energy Exploration and Exploitation*, 27(5), 345–366.

Finetti, I., Bricchi, G., Del Ben, A., Pipan, M., & Xuan, Z. (1988). Geophysical study of the Black Sea area. *Bollettino di Geofisica Teorica e Applicata*, 30, 197–324.

Fischer, H., Behrens, M., Bock, M., Richter, U., Schmitt, J., Loulergue, L., Chappellaz, J., Spahni, R., Blunier, T., & Leuenberger, M. (2008). Changing boreal methane sources and constant biomass burning during the last termination. *Nature*, 452(7189), 864–867.

Fisher, R., Sriskantharajah, S., Lowry, D., Lanoisellé, M., Fowler, C., James, R., Hermansen, O., Lund Myhre, C., Stohl, A., & Greinert, J. (2011). Arctic methane sources: Isotopic evidence for atmospheric inputs. *Geophysical Research Letters*, 38(21), L21803, doi: 10.1029/2011GL049319.

Flemings, P. B., Long, H., Dugan, B., Germaine, J., John, C. M., Behrmann, J. H., Sawyer, D., & Scientists, I. E. . (2008). Pore pressure penetrometers document high overpressure near the seafloor where multiple submarine landslides have occurred on the continental slope, offshore Louisiana, Gulf of Mexico. *Earth and Planetary Science Letters*, 269(3), 309–325.

Forman, S., Lubinski, D., Ingólfsson, O., Zeeberg, J., Snyder, J., Siegert, M., & Matishov, G. (2004). A review of postglacial emergence on Svalbard, Franz Josef Land and Novaya Zemlya, northern Eurasia. *Quaternary Science Reviews*, 23(11), 1391–1434.

Foster, W. R. (1982). Smectite-illite transformation: its role in generating and maintaining geopressure. *SEG Technical Program Expanded Abstracts*, 1(1), 506–508.

Gardner, G. H. F., Gardner, L. W., & Gregory, A. R. (1974). Formation velocity and density - Diagnostic basics for stratigraphic traps. *Geophysics*, 39(6), 770–780.

Garven, G. & Freeze, R. A. (1984). Theoretical-analysis of the role of groundwater-flow in

the genesis of stratabound ore-deposits.1. Mathematical and numerical-model. *American Journal of Science*, 284(10), 1085–1124.

Gent, P. R., Danabasoglu, G., Donner, L. J., Holland, M. M., Hunke, E. C., Jayne, S. R., Lawrence, D. M., Neale, R. B., Rasch, P. J., & Vertenstein, M. (2011). The Community Climate System Model version 4. *Journal of Climate*, 24(19), 4973–4991.

Georgiopoulou, A., Masson, D. G., Wynn, R. B., & Krastel, S. (2010). Sahara Slide: age, initiation, and processes of a giant submarine slide. *Geochemistry Geophysics Geosystems*, 11, Q07014, doi: 10.1029/2010GC003066.

Gibson, R. E. (1958). The progress of consolidation in a clay layer increasing with time. *Géotechnique*, 8, 171–182.

Gordon, C. T. & Stern, W. F. (1982). A description of the GFDL global spectral model. *Monthly Weather Review*, 110(7), 625–644.

Gordon, D. S. & Flemings, P. B. (1998). Generation of overpressure and compaction-driven fluid flow in a Plio-Pleistocene growth-faulted basin, Eugene Island 330, offshore Louisiana. *Basin Research*, 10(2), 177–196.

Görür, N. (1988). Timing of opening of the Black-Sea Basin. *Tectonophysics*, 147(3-4), 247–262.

Grace, J. D. & Hart, G. F. (1986). Giant gas field of northern West Siberia. *AAPG Bulletin*, 70(6), 830–852.

Grauls, D. (2001). Gas hydrates: importance and applications in petroleum exploration. *Marine and Petroleum Geology*, 18(4), 519–523.

Grinsted, A., Moore, J. C., & Jevrejeva, S. (2010). Reconstructing sea level from paleo and projected temperatures 200 to 2100AD. *Climate Dynamics*, 34(4), 461–472.

Gutierrez, M. & Wangen, M. (2005). Modeling of compaction and overpressuring in sedimentary basins. *Marine and Petroleum Geology*, 22(3), 351–363.

Haacke, R. R., Westbrook, G. K., & Riley, M. S. (2008). Controls on the formation and stability of gas hydrate-related bottom-simulating reflectors (BSRs): A case study from the west Svalbard continental slope. *Journal of Geophysical Research: Solid Earth*, 113(B5), B05104, doi: 10.1029/2007JB005200.

Habermehl, M. A. (1980). The Great Artesian Basin, Australia. *BMR Journal of Australian Geology and Geophysics*, 5(1).

Hald, M., Ebbesen, H., Forwick, M., Godtliebsen, F., Khomenko, L., Korsun, S.,

Ringstad Olsen, L., & Vorren, T. O. (2004). Holocene paleoceanography and glacial history of the west spitsbergen area, euro-arctic margin. *Quaternary Science Reviews*, 23(20), 2075–2088.

Hamilton, E. L. (1978). Sound velocity-density relations in sea-floor sediments and rocks. *Journal of the Acoustical Society of America*, 63(2), 366–377.

Han, D.-h., Nur, A., & Morgan, D. (1986). Effects of porosity and clay content on wave velocities in sandstones. *Geophysics*, 51(11), 2093–2107.

Hanshaw, B. B. & Zen, E. (1965). Osmotic equilibrium and overthrust faulting. *Geological Society of America Bulletin*, 76, 1379–1386.

Hansom, J. & Lee, M. K. (2005). Effects of hydrocarbon generation, basal heat flow and sediment compaction on overpressure development: a numerical study. *Petroleum Geoscience*, 11(4), 353–360.

Harrison, W. J. & Summa, L. L. (1991). Paleohydrology of the Gulf of Mexico Basin. *American Journal of Science*, 291(2), 109–176.

Hart, B. S., Flemings, P. B., & Deshpande, A. (1995). Porosity and pressure - Role of compaction disequilibrium in the development of geopressures in a Gulf-Coast Pleistocene Basin. *Geology*, 23(1), 45–48.

Hassol, S. J. (2004). *Impacts of a warming Arctic - Arctic climate impact assessment.* Cambridge University Press.

Hawkins, E. & Sutton, R. (2009). The potential to narrow uncertainty in regional climate predictions. *Bulletin of the American Meteorological Society*, 90(8), 1095–1107.

Heard, H. C. & Rubey, W. W. (1966). Tectonic implications of gypsum dehydration. *Geological Society of America Bulletin*, 77, 741–760.

Heeschen, K. U., Collier, R. W., de Angelis, M. A., Suess, E., Rehder, G., Linke, P., & Klinkhammer, G. P. (2005). Methane sources, distributions, and fluxes from cold vent sites at hydrate ridge, cascadia margin. *Global Biogeochemical Cycles*, 19(2), GB2016, doi: 10.1029/2004GB002266.

Hiscott, R. N. & Aksu, A. E. (2002). Late Quaternary history of the Marmara Sea and Black Sea from high-resolution seismic and gravity-core studies. *Marine Geology*, 190(1-2), 261–282.

Hobro, J. W., Singh, S. C., & Minshull, T. A. (2003). Three-dimensional tomographic inversion of combined reflection and refraction seismic traveltime data. *Geophysical Journal International*, 152(1), 79–93.

Holder, G., Angert, P. F., John, V., & Yen, S. (1982). A thermodynamic evaluation of thermal recovery of gas from hydrates in the Earth. *Journal of Petroleum Technology*, 34(5), 1127–1132.

Holliday, N. P., Hughes, S., Bacon, S., Beszczynska-Möller, A., Hansen, B., Lavin, A., Loeng, H., Mork, K., Østerhus, S., & Sherwin, T. (2008). Reversal of the 1960s to 1990s freshening trend in the northeast North Atlantic and Nordic Seas. *Geophysical Research Letters*, 35(3), L03614, doi: 10.1029/2007GL032675.

Holtzman, R. & Juanes, R. (2011). Thermodynamic and hydrodynamic constraints on overpressure caused by hydrate dissociation: A pore-scale model. *Geophysical Research Letters*, 38(14), L14308, doi: 10.1029/2011GL047937.

Hsü, K. & Giovanoli, F. (1980). Messian event in the Black Sea. *Palaeogeography, Palaeoclimatology, Palaeoecology*, 29, 75–83.

Hubbert, M. K. & Rubey, W. W. (1959a). Role of fluid pressure in mechanics of overthrust faulting: I. Mechanics of fluid-filled porous solids and its application to overthrust faulting. *Geological Society of America Bulletin*, 70, 115–166.

Hubbert, M. K. & Rubey, W. W. (1959b). Role of fluid pressure in mechanics of overthrust faulting: II. Overthrust belt in geosynclinal area of Western Wyoming in light of fluid pressure hypothesis. *Geological Society of America Bulletin*, 70, 167–206.

Hunter, S. J., Goldobin, D. S., Haywood, A. M., Ridgwell, A., & Rees, J. G. (2013). Sensitivity of the global submarine hydrate inventory to scenarios of future climate change. *Earth and Planetary Science Letters*, 367(0), 105–115.

Hustoft, S., Dugan, B., & Mienert, J. (2009). Effects of rapid sedimentation on developing the Nyegga pockmark field: constraints from hydrological modeling and 3-D seismic data, offshore mid-Norway. *Geochemistry Geophysics Geosystems*, 10, Q06012, doi: 10.1029/2009GC002409.

International Association for the Properties of Water and Steam (2007). *Revised Release on the IAPWS Industrial Formulation 1997 for the Thermodynamic Properties of Water and Steam*. Lucerne, Switzerland.

International Association for the Properties of Water and Steam (2008). *Release on the IAPWS Formulation 2008 for the Viscosity of Ordinary Water Substance*. Berlin, Germany.

Isaksen, I. S., Gauss, M., Myhre, G., Anthony, W., Katey, M., & Ruppel, C. (2011). Strong atmospheric chemistry feedback to climate warming from Arctic methane emissions. *Global Biogeochemical Cycles*, 25(2), GB2002, doi: 10.1029/2010GB003845.

Ivanov, M. K., Limonov, A. F., & vanWeering, T. C. E. (1996). Comparative characteristics of the Black Sea and Mediterranean Ridge mud volcanoes. *Marine Geology*, 132(1-4), 253–271.

Iversen, T., Bentsen, M., Bethke, I., Debernard, J., Kirkevåg, A., Seland, Ø., Drange, H., Kristjánsson, J., Medhaug, I., & Sand, M. (2012). The Norwegian Earth System Model, NorESM1-M-Part 2: Climate response and scenario projections. *Geoscientific Model Development Discussions*, 5(3), 2933–2998.

Jakobsson, M., Macnab, R., Mayer, L., Anderson, R., Edwards, M., Hatzky, J., Schenke, H. W., & Johnson, P. (2008). An improved bathymetric portrayal of the Arctic Ocean: Implications for ocean modeling and geological, geophysical and oceanographic analyses. *Geophysical Research Letters*, 35(7), L07602, doi: 10.1029/2008GL033520.

James, R. H., Connelly, D., Graves, C., Alker, B., Cole, C., Wright, I., & Kolomijeca, A. (2011). Fate of methane released from Arctic shelf and slope sediments and implications for climate change. In *AGU Fall Meeting 2011*.

Jones, C. D., Hughes, J. K., Bellouin, N., Hardiman, S. C., Jones, G. S., Knight, J., Liddicoat, S., O'Connor, F. M., Andres, R. J., Bell, C., Boo, K. O., Bozzo, A., Butchart, N., Cadule, P., Corbin, K. D., Doutriaux-Boucher, M., Friedlingstein, P., Gornall, J., Gray, L., Halloran, P. R., Hurtt, G., Ingram, W. J., Lamarque, J. F., Law, R. M., Meinshausen, M., Osprey, S., Palin, E. J., Parsons Chini, L., Raddatz, T., Sanderson, M. G., Sellar, A. A., Schurer, A., Valdes, P., Wood, N., Woodward, S., Yoshioka, M., & Zerroukat, M. (2011). The HadGEM2-ES implementation of CMIP5 centennial simulations. *Geosci. Model Dev.*, 4(3), 543–570.

Judd, A. G. (2004). Natural seabed gas seeps as sources of atmospheric methane. *Environmental Geology*, 46(8), 988–996.

Kao, J. (2010). Estimating pore pressure using compressional and shear wave data from multicomponent seismic nodes in Atlantis Field, deepwater Gulf of Mexico. *SEG Expanded Abstracts*, (pp. 1641–1645).

Karig, D. E. & Hou, G. (1992). High-stress consolidation experiments and their geologic implications. *Journal of Geophysical Research-Solid Earth*, 97(B1), 289–300.

Kennett, J. P., Cannariato, K. G., Hendy, I. L., & Behl, R. J. (2000). Carbon isotopic evidence for methane hydrate instability during Quaternary interstadials. *Science*, 288(5463), 128–133.

Kennett, J. P., Cannariato, K. G., Hendy, I. L., & Behl, R. J. (2003). *Methane hydrates*

in Quaternary climate change: The clathrate gun hypothesis, volume 54. American Geophysical Union.

Kerr, R. A. (2004). Gas hydrate resource: smaller but sooner. *Science*, 303(5660), 946–947.

Knapp, C. C., Knapp, J. H., & Connor, J. A. (2004). Crustal-scale structure of the South Caspian Basin revealed by deep seismic reflection profiling. *Marine and Petroleum Geology*, 21(8), 1073–1081.

Krastel, S., Spiess, V., Ivanov, M., Weinrebe, W., Bohrmann, G., Shashkin, P., & Heidersdorf, F. (2003). Acoustic investigations of mud volcanoes in the Sorokin Trough, Black Sea. *Geo-Marine Letters*, 23(3-4), 230–238.

Kruglyakova, R. P., Byakov, Y. A., Kruglyakova, M. V., Chalenko, L. A., & Shevtsova, N. T. (2004). Natural oil and gas seeps on the Black Sea floor. *Geo-Marine Letters*, 24(3), 150–162.

Kvenvolden, K., Ginsburg, G., & Soloviev, V. (1993). Worldwide distribution of subaquatic gas hydrates. *Geo-Marine Letters*, 13(1), 32–40.

Kvenvolden, K. A. (1988). Methane hydrate- a major reservoir of carbon in the shallow geosphere? *Chemical Geology*, 71(1), 41–51.

Kvenvolden, K. A. (1993). Gas hydrates- geological perspective and global change. *Reviews of Geophysics*, 31(2), 173–187.

Kvenvolden, K. A. (1999). Potential effects of gas hydrate on human welfare. *Proceedings of the National Academy of Sciences*, 96(7), 3420–3426.

Kvenvolden, K. A. (2002). Methane hydrate in the global organic carbon cycle. *Terra Nova*, 14(5), 302–306.

Kvenvolden, K. A. & Lorenson, T. D. (2001). The global occurrence of natural gas hydrate. In C. K. Paull & W. P. Dillon (Eds.), *Natural Gas Hydrates- Ocurrence, Distribution and Detection*, volume 124. Geophysical Monograph.

Kwon, T. H., Cho, G. C., & Santamarina, J. C. (2008). Gas hydrate dissociation in sediments: pressure-temperature evolution. *Geochemistry Geophysics Geosystems*, 9, Q03019, doi: 10.1029/2007GC001920.

Lachenbruch, A. H., Sass, J. H., Marshall, B. V., & Moses, T. H. (1982). Permafrost, heat flow, and the geothermal regime at Prudhoe Bay, Alaska. *Journal of Geophysical Research: Solid Earth*, 87(B11), 9301–9316.

Lahann, R. W. & Swarbrick, R. E. (2011). Overpressure generation by load transfer

following shale framework weakening due to smectite diagenesis. *Geofluids*, 11(4), 362–375.

Lee, S., Shaw, J., Ho, R., Burger, J., Singh, S., & Troyer, B. (1999). Illuminating the shadows: tomography, attenuation and pore pressure processing in the South Caspian Sea. *Journal of Petroleum Science and Engineering*, 24(1), 1–12.

Leynaud, D., Sultan, N., & Mienert, J. (2007). The role of sedimentation rate and permeability in the slope stability of the formerly glaciated Norwegian continental margin: The Storegga slide model. *Landslides*, 4, 297–309.

Long, H., Flemings, P. B., Germaine, J., & Saffer, D. (2008). Data report: consolidation characteristics of sediments from IODP Expedition 308, Ursa Basin, Gulf of Mexico. In *Proc. IODP 308, Integrated Ocean Drilling Program Management International, Inc.,* College Station, Tx.

Long, H., Flemings, P. B., Germaine, J. T., & Saffer, D. M. (2011). Consolidation and overpressure near the seafloor in the Ursa Basin, deepwater Gulf of Mexico. *Earth and Planetary Science Letters*, 305(1), 11–20.

Luo, X. & Vasseur, G. (1992). Contributions of compaction and aquathermal pressuring to geopressure and the influence of environmental conditions. *AAPG Bulletin*, 76(10), 1550–1559.

Luo, X., Wang, Z., Zhang, L., Yang, W., & Liu, L. (2007). Overpressure generation and evolution in a compressional tectonic setting, the southern margin of Junggar Basin, northwestern China. *AAPG Bulletin*, 91(8), 1123–1139.

MacDonald, G. J. (1990). The future of methane as an energy resource. *Annual Review of Energy*, 15(1), 53–83.

Madec, G. (2012). *NEMO ocean engine. Note du Pole de Modélisation.* Technical report, Inst. Pierre-Simon Laplace (IPSL), Paris.

Marín-Moreno, H., Minshull, T. A., & Edwards, R. A. (2013a). A disequilibrium compaction model constrained by seismic data and application to overpressure generation in The Eastern Black Sea Basin. *Basin Research*, 25(3), 331–347.

Marín-Moreno, H., Minshull, T. A., & Edwards, R. A. (2013b). Inverse modelling and seismic data constraints on overpressure generation by disequilibrium compaction and aquathermal pressuring: application to the Eastern Black Sea Basin. *Geophysical Journal International*, 194(2), 814–833.

Marín-Moreno, H., Minshull, T. A., Westbrook, G. K., Sinha, B., & Sarkar, S. (2013c).

The response of methane hydrate beneath the seabed offshore svalbard to ocean warming during the next three centuries. *Geophysical Research Letters*, 40, doi: 10.1002/grl.50985.

Marine, I. W. & Fritz, S. J. (1981). Osmotic model to explain anomalous hydraulic heads. *Water Resources Research*, 17(1), 73–82.

Marsland, S., Haak, H., Jungclaus, J., Latif, M., & Röske, F. (2003). The Max-Planck-Institute global ocean/sea ice model with orthogonal curvilinear coordinates. *Ocean Modelling*, 5(2), 91–127.

Marti, O., Braconnot, P., Dufresne, J. L., Bellier, J., Benshila, R., Bony, S., Brockmann, P., Cadule, P., Caubel, A., Codron, F., Noblet, N., Denvil, S., Fairhead, L., Fichefet, T., Foujols, M. A., Friedlingstein, P., Goosse, H., Grandpeix, J. Y., Guilyardi, E., Hourdin, F., Idelkadi, A., Kageyama, M., Krinner, G., Lévy, C., Madec, G., Mignot, J., Musat, I., Swingedouw, D., & Talandier, C. (2010). Key features of the IPSL ocean atmosphere model and its sensitivity to atmospheric resolution. *Climate Dynamics*, 34(1), 1–26.

Martin, P. A., Lea, D. W., Rosenthal, Y., Shackleton, N. J., Sarnthein, M., & Papenfuss, T. (2002). Quaternary deep sea temperature histories derived from benthic foraminiferal Mg/Ca. *Earth and Planetary Science Letters*, 198(1), 193–209.

Maslin, M., Owen, M., Betts, R., Day, S., Jones, T. D., & Ridgwell, A. (2010). Gas hydrates: past and future geohazard? *Philosophical Transactions of the Royal Society A: Mathematical, Physical and Engineering Sciences*, 368(1919), 2369–2393.

Mavko, G., Mukerji, T., & Dvorkin, J. (2009). *The Rock Physics Handbook*. Tools for Seismic Analysis of Porous Media. New York: Cambridge University Press, 2nd edition.

McClusky, S., Balassanian, S., Barka, A., Demir, C., Ergintav, S., Georgiev, I., Gurkan, O., Hamburger, M., Hurst, K., Kahle, H., Kastens, K., Kekelidze, G., King, R., Kotzev, V., Lenk, O., Mahmoud, S., Mishin, A., Nadariya, M., Ouzounis, A., Paradissis, D., Peter, Y., Prilepin, M., Reilinger, R., Sanli, I., Seeger, H., Tealeb, A., Toksoz, M. N., & Veis, G. (2000). Global positioning system constraints on plate kinematics and dynamics in the eastern Mediterranean and Caucasus. *Journal of Geophysical Research-Solid Earth*, 105(B3), 5695–5719.

McGinnis, D., Greinert, J., Artemov, Y., Beaubien, S., & Wüest, A. (2006). Fate of rising methane bubbles in stratified waters: How much methane reaches the atmosphere? *Journal of Geophysical Research: Oceans*, 111(C9), C09007, doi: 10.1029/2005JC003183.

McGuire, A. D., Christensen, T. R., Hayes, D., Heroult, A., Euskirchen, E., Kimball, J. S., Koven, C., Lafleur, P., Miller, P. A., Oechel, W., Peylin, P., Williams, M., & Yi, Y. (2012). An assessment of the carbon balance of Arctic tundra: comparisons

among observations, process models, and atmospheric inversions. *Biogeosciences*, 9(8), 3185–3204.

McPherson, B. J. & Garven, G. (1999). Hydrodynamics and overpressure mechanisms in the Sacramento Basin, California. *American Journal of Science*, 299(6), 429–466.

Meinshausen, M., Smith, S. J., Calvin, K., Daniel, J. S., Kainuma, M., Lamarque, J., Matsumoto, K., Montzka, S., Raper, S., & Riahi, K. (2011). The RCP greenhouse gas concentrations and their extensions from 1765 to 2300. *Climatic Change*, 109(1-2), 213–241.

Mello, U. T., Karner, G. D., & Anderson, R. N. (1994). A physical explanation for the positioning of the depth to the top of overpressure in shale-dominated sequences in the Gulf-Coast Basin, United-States. *Journal of Geophysical Research-Solid Earth*, 99(B2), 2775–2789.

Menlikli, C., Demirer, A., Sipahioğlu, O., Körpe, L., & Aydemir, V. (2009). Exploration plays in the Turkish Black Sea. *The Leading Edge*, 28(9), 1066–1075.

Meredith, D. J. & Egan, S. S. (2002). The geological and geodynamic evolution of the eastern Black Sea Basin: insights from 2-D and 3-D tectonic modelling. *Tectonophysics*, 350(2), 157–179.

Meyer, C., McClintock, R., Silvestri, G., & Spencer, R. (1963). *ASME Steam Tables*. New York: American Society of Mechanical Engineering, 2nd edition.

Milkov, A. V. (2004). Global estimates of hydrate-bound gas in marine sediments: how much is really out there? *Earth-Science Reviews*, 66(3), 183–197.

Milkov, A. V. (2005). Molecular and stable isotope compositions of natural gas hydrates: A revised global dataset and basic interpretations in the context of geological settings. *Organic Geochemistry*, 36(5), 681–702.

Minshull, T. & White, R. (1989). Sediment compaction and fluid migration in the Makran Accretionary Prism. *Journal of Geophysical Research-Solid Earth and Planets*, 94(B6), 7387–7402.

Minshull, T. A. & Keddie, A. (2010). Measuring the geotherm with gas hydrate bottom-simulating reflectors: a novel approach using three-dimensional seismic data from the eastern Black Sea. *Terra Nova*, 22(2), 131–136.

Mondol, N. H., Bjørlykke, K., Jahren, J., & Høeg, K. (2007). Experimental mechanical compaction of clay mineral aggregates—changes in physical properties of mudstones during burial. *Marine and Petroleum Geology*, 24(5), 289–311.

Moore, J. C. & Tobin, H. (1997). Estimated fluid pressures of the Barbados accretionary prism and adjacent sediments. In T. Shipley, Y. Ogawa, P. Blum, & J. Bahr (Eds.), *Proceedings of the Ocean Drilling Program, Scientific Results*, volume 156.

Moridis, G. (2003). Numerical studies of gas production from methane hydrates. *SPE Journal*, 8(4), 359–370.

Moridis, G. & Pruess, K. (1995). *Flow and transport simulations using T2CG1, a package of conjugate gradient solvers for the TOUGH2 family of codes*. Lawrence Berkeley Lab., Berkeley, California.

Moridis, G. J., Kowalsky, M., & Pruess, K. (2012). *TOUGH+HYDRATE v1.2 user's manual: A code for the simulation of system behaviour in hydrate-bearing geological media*. Per. LBNL-0149E, Lawrence Berkeley Natl. Lab., Berkeley, California.

Moridis, G. J. & Pruess, K. (1998). T2SOLV: An enhanced package of solvers for the TOUGH2 family of reservoir simulation codes. *Geothermics*, 27(4), 415–444.

Moss, R. H., Edmonds, J. A., Hibbard, K. A., Manning, M. R., Rose, S. K., van Vuuren, D. P., Carter, T. R., Emori, S., Kainuma, M., & Kram, T. (2010). The next generation of scenarios for climate change research and assessment. *Nature*, 463(7282), 747–756.

Narasimhan, T. & Witherspoon, P. (1976). An integrated finite difference method for analysing fluid flow in porous media. *Water Resources Research*, 12(1), 57–64.

Neuzil, C. E. (1994). How permeable are clays and shales? *Water Resources Research*, 30(2), 145–150.

Neuzil, C. E. (1995). Abnormal pressures as hydrodynamic phenomena. *American Journal of Science*, 295(6), 742–786.

Nikishin, A. M., Korotaev, M. V., Ershov, A. V., & Brunet, M. F. (2003). The Black Sea Basin: Tectonic history and Neogene-Quaternary rapid subsidence modelling. *Sedimentary Geology*, 156(1-4), 149–168.

Nisbet, E. (1989). Some northern sources of atmospheric methane: production, history, and future implications. *Canadian Journal of Earth Sciences*, 26(8), 1603–1611.

Nisbet, E. (1990). The end of the Ice Age. *Canadian Journal of Earth Sciences*, 27(1), 148–157.

Nisbet, E. G. (2002). Have sudden large releases of methane from geological reservoirs occurred since the Last Glacial Maximum, and could such releases occur again? *Philosophical Transactions of the Royal Society of London. Series A: Mathematical, Physical and Engineering Sciences*, 360(1793), 581–607.

Noble, E. A. (1963). Formation of ore deposits by water of compaction. *Economic Geology*, 58, 1145–1156.

Okay, A. I., Sengor, A. M. C., & Görür, N. (1994). Kinematic history of the opening of the Black-Sea and its effect on the surrounding regions. *Geology*, 22(3), 267–270.

Osborne, M. J. & Swarbrick, R. E. (1997). Mechanisms for generating overpressure in sedimentary basins; a reevaluation. *AAPG Bulletin*, 81(6), 1023–1041.

Osborne, M. J. & Swarbrick, R. E. (1999). Diagenesis in North Sea HPHT elastic reservoirs - consequences for porosity and overpressure prediction. *Marine and Petroleum Geology*, 16(4), 337–353.

Palciauskas, V. V. & Domenico, P. A. (1989). Fluid pressures in deforming porous rocks. *Water Resources Research*, 25(2), 203–213.

Paradowski, L. R. (1997). Uncertainty ellipses and their application to interval estimation of emitter position. *Aerospace and Electronic Systems, IEEE Transactions on*, 33(1), 126–133.

Paull, C. K., Ussler III, W., Dallimore, S. R., Blasco, S. M., Lorenson, T. D., Melling, H., Medioli, B. E., Nixon, F. M., & McLaughlin, F. A. (2007). Origin of pingo-like features on the Beaufort Sea shelf and their possible relationship to decomposing methane gas hydrates. *Geophysical Research Letters*, 34(1), L01603, doi: 10.1029/2006GL027977.

Peaceman, D. W. (1977). *Fundamentals of numerical reservoir simulation.* Amsterdam, The Netherlands: Elsevier.

Piñero, E., Marquardt, M., Hensen, C., Haeckel, M., & Wallmann, K. (2013). Estimation of the global inventory of methane hydrates in marine sediments using transfer functions. *Biogeosciences*, 10(2), 959–975.

Platt, L. (1962). Fluid pressure in thrust faulting, a corollary. *American Journal of Science*, 260, 107–114.

Polyakov, I., Alekseev, G., Timokhov, L., Bhatt, U., Colony, R., Simmons, H., Walsh, D., Walsh, J., & Zakharov, V. (2004). Variability of the intermediate Atlantic water of the Arctic Ocean over the last 100 years. *Journal of Climate*, 17(23), 4485–4497.

Polyakov, I., Walsh, D., Dmitrenko, I., Colony, R. L., & Timokhov, L. A. (2003). Arctic Ocean variability derived from historical observations. *Geophysical Research Letters*, 30(6), 1298, doi: 10.1029/2002GL016441.

Pooladi-Darvish, M. (2004). Gas production from hydrate reservoirs and its modeling. *Journal of Petroleum Technology*, 56(6), 65–71.

Powell, M. J. D. (1970). A Fortran subroutine for solving systems of nonlinear algebraic equations. In P. Rabinowitz (Ed.), *Numerical Methods for Nonlinear Algebraic Equations*. New York: Gordon & Breach.

Powley, D. E. (1990). Pressures and hydrogeology in petroleum basins. *Earth-Science Reviews*, 29, 215–226.

Pruess, K., Oldenburg, C., & Moridis, G. (1999). *TOUGH2 user's guide - version 2.0, Lawrence Berkeley Laboratory report*. LBL-43134, Berkeley, California.

Rajan, A., Mienert, J., & Bünz, S. (2012). Acoustic evidence for a gas migration and release system in Arctic glaciated continental margins offshore NW-Svalbard. *Marine and Petroleum Geology*, 32(1), 36–49.

Ramdhan, A. M. & Goulty, N. R. (2010). Overpressure-generating mechanisms in the Peciko Field, Lower Kutai Basin, Indonesia. *Petroleum Geoscience*, 16(4), 367–376.

Rangin, C., Bader, A., Pascal, G., Ecevitoglu, B., & Görür, N. (2002). Deep structure of the Mid Black Sea High (offshore Turkey) imaged by multi-channel seismic survey (BLACKSIS cruise). *Marine Geology*, 182, 265–278.

Reagan, M. T. & Moridis, G. J. (2008). Dynamic response of oceanic hydrate deposits to ocean temperature change. *Journal of Geophysical Research: Oceans*, 113(C12), C12023, doi: 10.1029/2008JC004938.

Reagan, M. T. & Moridis, G. J. (2009). Large-scale simulation of methane hydrate dissociation along the West Spitsbergen Margin. *Geophysical Research Letters*, 36(23), L23612, doi: 10.1029/2009GL041332.

Reagan, M. T., Moridis, G. J., Elliott, S. M., & Maltrud, M. (2011). Contribution of oceanic gas hydrate dissociation to the formation of Arctic Ocean methane plumes. *Journal of Geophysical Research*, 116(C9), C09014, doi: 10.1029/2011JC007189.

Reece, J. S., Flemings, P. B., Dugan, B., Long, H., & Germaine, J. T. (2012). Permeability-porosity relationships of shallow mudstones in the Ursa Basin, northern deepwater Gulf of Mexico. *Journal of Geophysical Research: Solid Earth*, 117(B12), B12102, doi: 10.1029/2012JB009438.

Riebesell, U. (2008). Climate change: Acid test for marine biodiversity. *Nature*, 454(7200), 46–47.

Roberts, S. J. & Nunn, J. A. (1995). Episodic fluid expulsion from geopressured sediments. *Marine and Petroleum Geology*, 12(2), 195–204.

Robertson, A. H. F., Ustaomer, T., Pickett, E. A., Collins, A. S., Andrew, T., & Dixon,

J. E. (2004). Testing models of Late Palaeozoic Early Mesozoic orogeny in Western Turkey: support for an evolving open-Tethys model. *Journal of the Geological Society*, 161, 501–511.

Robinson, A., Spadini, G., Cloetingh, S., & Rudat, J. (1995a). Stratigraphic evolution of the Black-Sea- inferences from basin modeling. *Marine and Petroleum Geology*, 12(8), 821–835.

Robinson, A. G., Banks, C. J., Rutherford, M. M., & Hirst, J. P. P. (1995b). Stratigraphic and structural development of The Eastern Pontides, Turkey. *Journal of the Geological Society*, 152, 861–872.

Robinson, A. G., Rudat, J. H., Banks, C. J., & Wiles, R. L. F. (1996). Petroleum geology of the Black Sea. *Marine and Petroleum Geology*, 13(2), 195–223.

Ross, D. (1978). Summary of results of Black Sea drilling. *Inititial Report DSDP 42*, (pp. 1149–1177).

Saffer, D. M. (2003). Pore pressure development and progressive dewatering in underthrust sediments at the Costa Rican subduction margin: comparison with northern Barbados and Nankai. *Journal of Geophysical Research-Solid Earth*, 108(B5), 2261, doi: 10.1029/2002JB001787.

Saffer, D. M. & McKiernan, A. W. (2009). Evaluation of in situ smectite dehydration as a pore water freshening mechanism in the Nankai Trough, offshore southwest Japan. *Geochemistry Geophysics Geosystems*, 10, Q02010, doi: 10.1029/2008GC002226.

Saffer, D. M. & Tobin, H. J. (2011). Hydrogeology and mechanics of subduction zone forearcs: fluid flow and pore pressure. *Annual Review of Earth and Planetary Sciences*, 39(1), 157–186.

Sambridge, M. & Mosegaard, K. (2002). Monte Carlo methods in geophysical inverse problems. *Reviews of Geophysics*, 40(3), 1009, doi: 10.1029/2000RG000089.

Sarkar, S., Berndt, C., Minshull, T. A., Westbrook, G. K., Klaeschen, D., Masson, D. G., Chabert, A., & Thatcher, K. E. (2012). Seismic evidence for shallow gas-escape features associated with a retreating gas hydrate zone offshore West Svalbard. *Journal of Geophysical Research: Solid Earth*, 117(B9), B09102, doi: 10.1029/2011JB009126.

Sarker, R. & Batzle, M. (2008). Effective stress coefficient in shales and its applicability to Eaton's equation. *The Leading Edge*, (pp. 798–804).

Sayers, C. M. (2006). An introduction to velocity-based pore-pressure estimation. *The Leading Edge*, 25(12), 1496–1500.

Schneider, F., Potdevin, J., Wolf, S., & Faille, I. (1996). Mechanical and chemical compaction model for sedimentary basin simulators. *Tectonophysics*, 263(1), 307–317.

Sclater, J. G. & Christie, P. A. F. (1980). Continental stretching - an explanation of the Post-Mid-Cretaceous Subsidence of the Central North-Sea Basin. *Journal of Geophysical Research*, 85(NB7), 3711–3739.

Scott, C. (2009). *PhD thesis. Formation and evolution of the Eastern Black Sea Basin: Constraints from wide-angle seismic data.* Southampton, UK: University of Southampton.

Scott, C. L., Shillington, D. J., Minshull, T. A., Edwards, R. A., Brown, P. J., & White, N. J. (2009). Wide-angle seismic data reveal extensive overpressures in the Eastern Black Sea Basin. *Geophysical Journal International*, 178(2), 1145–1163.

Screaton, E. J., Wuthrich, D. R., & Dreiss, S. J. (1990). Permeabilities, fluid pressures, and flow rates in the Barbados Ridge Complex. *Journal of Geophysical Research: Solid Earth*, 95(B6), 8997–9007.

Shakhova, N., Semiletov, I., & Panteleev, G. (2005). The distribution of methane on the Siberian Arctic shelves: Implications for the marine methane cycle. *Geophysical Research Letters*, 32(9), L09601, doi: 10.1029/2005GL022751.

Shakhova, N., Semiletov, I., Salyuk, A., Yusupov, V., Kosmach, D., & Gustafsson, O. (2010). Extensive methane venting to the atmosphere from sediments of the East Siberian Arctic Shelf. *Science*, 327, 1246–1250.

Sharp, J. M. (1978). Energy and momentum transport model of Ouachita Basin and its possible impact on formation of economic mineral-deposits. *Economic Geology*, 73(6), 1057–1068.

Sharp, J. M. (1983). Permeability controls on aquathermal pressuring. *AAPG Bulletin*, 67(11), 2057–2061.

Sharp, J. M. & Domenico, P. A. (1976). Energy-transport in thick sequences of compacting sediment. *Geological Society of America Bulletin*, 87(3), 390–400.

Shi, Y. L. & Wang, C. Y. (1986). Pore pressure generation in sedimentary basins - overloading versus aquathermal. *Journal of Geophysical Research-Solid Earth and Planets*, 91(B2), 2153–2162.

Shillington, D. J., White, N., Minshull, T. A., Edwards, G. R. H., Jones, S. A., Edwards, R. A., & Scott, C. L. (2008). Cenozoic evolution of the eastern Black Sea: a test of

depth-dependent stretching models. *Earth and Planetary Science Letters*, 265(3-4), 360–378.

Shipley, T. H., Houston, M. H., Buffler, R. T., Shaub, F. J., McMillen, K. J., Ladd, J. W., & Worzel, J. L. (1979). Seismic evidence for widespread possible gas hydrate horizons on continental slopes and rises. *AAPG Bulletin*, 63(12), 2204–2213.

Sloan, E. D. (2004). Introductory overview: Hydrate knowledge development. *American Mineralogist*, 89(8-9), 1155–1161.

Solheim, A., Bryn, P., Sejrup, H., Mienert, J., & Berg, K. (2005). Ormen lange- an integrated study for the safe development of a deep-water gas field within the Storegga Slide Complex, NE Atlantic continental margin; executive summary. *Marine and Petroleum Geology*, 22(1), 1–9.

Sowers, T. (2006). Late Quaternary atmospheric CH_4 isotope record suggests marine clathrates are stable. *Science*, 311(5762), 838–840.

Spahni, R., Chappellaz, J., Stocker, T. F., Loulergue, L., Hausammann, G., Kawamura, K., Flückiger, J., Schwander, J., Raynaud, D., & Masson-Delmotte, V. (2005). Atmospheric methane and nitrous oxide of the late Pleistocene from Antarctic ice cores. *Science*, 310(5752), 1317–1321.

Spielhagen, R. F., Werner, K., Sørensen, S. A., Zamelczyk, K., Kandiano, E., Budeus, G., Husum, K., Marchitto, T. M., & Hald, M. (2011). Enhanced modern heat transfer to the Arctic by warm Atlantic water. *Science*, 331, 450–453.

Stone, H. (1970). Probability model for estimating three-phase relative permeability. *Journal of Petroleum Technology*, 22(2), 214–218.

Stouffer, R. & Manabe, S. (2003). Equilibrium response of thermohaline circulation to large changes in atmospheric CO_2 concentration. *Climate Dynamics*, 20(7-8), 759–773.

Sultan, N., Cochonat, P., Foucher, J.-P., & Mienert, J. (2004). Effect of gas hydrates melting on seafloor slope instability. *Marine Geology*, 213(1), 379–401.

Swarbrick, R. E. (2002). Challenges of porosity-based pore presessure prediction. *Canadian Society of Exploration Geophysicists Recorder*, (pp. 74–77).

Swarbrick, R. E. & Hillis, R. (1999). The origin and influence of overpressure within reference to the North West Shelf, Australia. *APPEA Journal*, 39(1), 64–72.

Swarbrick, R. E. & Osborne, M. J. (1998). Mechanisms that generate abnormal, pressures: an overview. In Law, B. E., Ulmishek G. F. & Slavin V. I. (Ed.), *Abnormal pressures in hydrocarbon environments*, volume 70 of *AAPG Memoirs* (pp. 13–34).

Swarbrick, R. E., Osborne, M. J., & Yardley, G. (2002). The magnitude of overpressure from generating mechanisms under realistic basin conditions. *American Association of Petroleum Geologists*, Memoir 76, 1–12.

Tarantola, A. (2005). *Inverse problem theory and methods for model parameter estimation.* Philadelphia, PA: Society for Industrial and Applied Mathematics.

Terzaghi, K. (1943). *Theoretical soil mechanics.* New York: Wiley.

Thatcher, K. E., Westbrook, G. K., Sarkar, S., & Minshull, T. A. (2013). Methane release from warming-induced hydrate dissociation in the West Svalbard continental margin: Timing, rates, and geological controls. *Journal of Geophysical Research: Solid Earth*, 118(1), doi: 10.1029/2012JB009605.

Tigert, V. & Al-Shaieb, Z. (1990). Pressure seals: their diagenetic banding patterns. *Earth-Science Reviews*, 29(1), 227–240.

Tobin, H. J. & Saffer, D. M. (2009). Elevated fluid pressure and extreme mechanical weakness of a plate boundary thrust, Nankai Trough subduction zone. *Geology*, 37(8), 679–682.

Tsuji, T., Tokuyama, H., Pisani, P. C., & Moore, G. (2008). Effective stress and pore pressure in the Nankai accretionary prism off the Muroto Peninsula, southwestern Japan. *Journal of Geophysical Research-Solid Earth*, 113, B11401, doi: 10.1029/2007JB005002.

Tsuru, T., Park, J.-O., Kido, Y., Ito, A., Kaneda, Y., Yamada, T., Shinohara, M., & Kanazawa, T. (2005). Did expanded porous patches guide rupture propagation in 2003 Tokachi-oki earthquake? *Geophysical Research Letters*, 32(20), L20310, doi: 10.1029/2005GL023753.

Valentine, D. L., Blanton, D. C., Reeburgh, W. S., & Kastner, M. (2001). Water column methane oxidation adjacent to an area of active hydrate dissociation, eel river basin. *Geochimica et Cosmochimica Acta*, 65(16), 2633–2640.

Van Genuchten, M. T. (1980). A closed-form equation for predicting the hydraulic conductivity of unsaturated soils. *Soil Science Society of America Journal*, 44(5), 892–898.

Vanneste, M., Guidard, S., & Mienert, J. (2005). Bottom-simulating reflections and geothermal gradients across the western Svalbard margin. *Terra Nova*, 17(6), 510–516.

Wallace Jr, R., Kraemer, T., Taylor, R., & Wesselman, J. (1979). Assessment of geopressured-geothermal resources in the northern Gulf of Mexico basin. *US Geological Survey Circular*, 790, 132–155.

Wallmann, K., Piñero, E., Burwicz, E., Haeckel, M., Hensen, C., Dale, A., & Ruepke, L.

(2012). The global inventory of methane hydrate in marine sediments: A theoretical approach. *Energies*, 5(7), 2449–2498.

Wangen, M. (1992). Pressure and temperature evolution in sedimentary basins. *Geophysical Journal International*, 110(3), 601–613.

Westbrook, G., Chand, S., Rossi, G., Long, C., Bünz, S., Camerlenghi, A., Carcione, J., Dean, S., Foucher, J.-P., & Flueh, E. (2008). Estimation of gas hydrate concentration from multi-component seismic data at sites on the continental margins of NW Svalbard and the Storegga region of Norway. *Marine and Petroleum Geology*, 25(8), 744–758.

Westbrook, G. K. (1991). Geophysical evidence for the role of fluids in accretionary wedge tectonics. *Philosophical Transactions of the Royal Society of London Series a-Mathematical Physical and Engineering Sciences*, 335(1638), 227–242.

Westbrook, G. K., Thatcher, K. E., Rohling, E. J., Piotrowski, A. M., Pälike, H., Osborne, A. H., Nisbet, E. G., Minshull, T. A., Lanoisellé, M., & James, R. H. (2009). Escape of methane gas from the seabed along the West Spitsbergen continental margin. *Geophysical Research Letters*, 36(15), L15608, doi: 10.1029/2009GL039191.

Whiteman, G., Hope, C., & Wadhams, P. (2013). Climate science: Vast costs of Arctic change. *Nature*, 499, 401–403.

Xu, W. & Germanovich, L. N. (2006). Excess pore pressure resulting from methane hydrate dissociation in marine sediments: A theoretical approach. *Journal of Geophysical Research: Solid Earth*, 111(B1), B01104, doi: 10.1029/2004JB003600.

Yang, S., Zhang, H., Wu, N., Su, X., Schultheiss, P., Holland, M., Zhang, G.-X., Liang, J., Lu, J., & Rose, K. (2008). High concentration hydrate in disseminated forms obtained in Shenhu area, North Slope of South China Sea. In *Proceedings of the 6th International Conference on Gas-Hydrates (ICGH July 6-10, 2008),* Vancouver, British Columbia, Canada.

Yassir, N. (2003). The role of shear stress in mobilizing deep-seated mud volcanoes: geological and geomechanical evidence from Trinidad and Taiwan. In VanRensbergen, P. , Hillis, R. R., Maltman, A. J. & Morley, C. K. (Ed.), *Subsurface Sediment Mobilization*, volume 216 of *Geological Society Special Publication* (pp. 461–474).

Yilmaz, Y., Tuysuz, O., Yigitbas, E., Genc Can, S., & Sengor, A. (1997). Geology and tectonic evolution of the Pontides. In A. G. Robinson (Ed.), *Regional and petroleum geology of the Black Sea and surrounding region*, volume 68 of *AAPG Memoirs* (pp. 183–226).

Yukimoto, S., Noda, A., Kitoh, A., Sugi, M., Kitamura, Y., Hosaka, M., Shibata, K.,

Maeda, S., & Uchiyama, T. (2001). The new Meteorological Research Institute coupled GCM(MRI-CGCM 2)- model climate and variability. *Papers in Meteorology and Geophysics*, 51(2), 47–88.

Zonenshain, L. P. & Lepichon, X. (1986). Deep basins of the Black-Bea and Caspian Sea as remnants of Mesozoic back-arc basins. *Tectonophysics*, 123(1-4), 181–211.